LA-6510-PR
PROGRESS REPORT

UC-21
Issued: November 1976

Laser Fusion Program

by
EUGENE STARK

January 1—June 30, 1976

los alamos
scientific laboratory
of the University of California
LOS ALAMOS, NEW MEXICO 87545

UNITED STATES
ENERGY RESEARCH AND DEVELOPMENT ADMINISTRATION
CONTRACT W-7405-ENG. 36

The four most recent reports in this series, unclassified, are LA-5739-PR, LA-5919-PR, LA-6050-PR, and LA-6245-PR.

This work was supported by the US Energy Research and Development Administration, Division of Laser Fusion.

Printed in the United States of America. Available from
National Technical Information Service
U.S. Department of Commerce
5285 Port Royal Road
Springfield, VA 22161
Price: Printed Copy $6.00 Microfiche $3.00

CONTENTS

Progress Report on

LASER-FUSION PROGRAM AT LASL

January 1 – June 30, 1976

by

Eugene Stark and the Laser Division Staff

Edited by

Frederick Skoberne

ABSTRACT

Progress in the development of high-energy short-pulse CO_2 laser systems for fusion research is reported. The Single-Beam System continued to be used in target experiments at a peak intensity of 7×10^{14} W/cm^2, and the system was improved. The status of the Two-Beam System, on which target experiments have begun with 300-J, 1-ns pulses in one beam, is described. Construction and checkout of the Eight-Beam System is continuing. Further design studies for the High-Energy Gas Laser Facility and the initiation of a prototype program are reported.

The rare-gas oxides and dimeric mercury were emphasized in investigations into new lasers for fusion research. Experimental kinetics studies, a study of heat-pipe containment of metal vapors, theoretical support, and optical-damage investigations are described.

Significant experimental and theoretical results are reported on the question of wavelength-scaling in laser-plasma interaction physics. Studies of vacuum insulation as a means of preventing target preheat by hot electrons are also summarized. Analyses of the ponderomotive force in laser-plasma interactions and of the relationship between x-ray spectrum and suprathermal electron distribution are described. Improvements to the MCRAD and LASNEX design codes are outlined, and a LASNEX analysis of a target heated by laser-generated fast ions is discussed. Improved methods of screening, characterizing, and fabricating microballoons and more complex targets are described, and progress in applying uniform layers of DT ice on the inside of a microballoon is reported. Improvements in diagnostics include x-ray streak photographs, the fabrication of x-ray microscope systems, and x-ray film imaging.

New results in our feasibility and systems studies are presented, including the wetted-wall and magnetically protected reactor concepts, the effect of ionized debris on cavity walls, the fusion-fission breeder concept, and the production of synthetic fuels by fusion radiation.

SUMMARY AND PROGRAM OVERVIEW

INTRODUCTION

The Laser-Fusion Program was established at Los Alamos in 1969, with the initiation of research into high-pressure CO_2 laser systems. Within the next few years, we developed the electron-beam-controlled CO_2 laser amplifier, and expanded our efforts into a complete, balanced research program of laser fusion for energy and military applications.

Our long-range goal is the completion of a comprehensive set of experimental and theoretical studies to test the scientific and engineering feasibility of using laser-induced microexplosions of small fusion pellets to produce heat for commercial electric-power generation and other applications.

Basic elements of this work include: the development of efficient, short-pulse, high-energy laser systems to illuminate small fuel pellets; advanced laser research; the design and fabrication of fusion pellets; the conduct, diagnosis, and analysis of laser-target interaction experiments; theoretical studies of the physics of laser-matter interactions; and systems and applications studies.

Significantly, our Laser-Fusion Program has contributed to the initiation of other important programs, ranging from a large laser-isotope separation effort and a joint development program with Union Carbide Corp.'s Y-12 plant on mirror fabrication by micromachining -- expected to have a wide impact on the optics industry -- to a small project on basic research into photosynthesis.

Highlights of the past six months include the initiation of wavelength-scaling experiments at 7×10^{14} W/cm^2 in the single-beam CO_2 laser system, and the start of target experiments at 300 J in a single beam in the two-beam CO_2 laser system. Results of these experiments, and related work on our Nd:glass laser system, have been compared with theory and have led to a significant new understanding of the wavelength-scaling question. In contrast to theoretical predictions of the past several years, which have ignored such important effects as the laser ponderomotive force, our new results indicate that the laser absorption and the hot-electron spectra inside the target plasma are very similar for 1- and 10-μm light at equal intensities.

CO_2 LASER PROGRAM

It is generally agreed that the high energies (several hundred kilojoules), short pulse lengths (0.25 to 1.0 ns), and smooth, focusable beams required for laser fusion can be achieved efficiently only by gas laser systems. Economical systems require large-aperture beams to avoid laser damage to the optical components. Only gas lasers can operate in such a large-aperture configuration. Historically, the CO_2 laser has received major emphasis in our development effort because of its high efficiency and its well-developed short-pulse generation and amplification technology. We have chosen a sequence of progressively more powerful CO_2 laser systems, with each new system requiring a reasonable extension of the state of the art while providing the capability for important new target experiments. Our existing and planned CO_2 laser systems include the following.

Single-Beam System (SBS)

This system includes an oscillator and four electron-beam-controlled amplifiers. Three amplifiers were used in the first 10.6-μm laser-target experiments early in 1973, delivering 10 J in a 1-ns pulse. Since then, the SBS has been upgraded to generate 250 J in 1-ns pulses and to deliver 180 J to a target with a peak intensity of 7×10^{14} W/cm^2. The SBS also serves as a developmental testbed for new laser-system components, e.g., oscillators, isolation schemes, and optical systems. Progress is summarized as follows:

- Substantial upgrading of the fourth amplifier was initiated. Power-supply modifications now permit reliable operation at a higher excitation voltage resulting in significantly increased output pulse energy.

- A spatial filter was installed in the system to smooth the transverse profile of the laser pulses. This modification reduces intensity spikes in the pulse profile, helping to prevent optical damage to mirrors and windows, as well as increasing the focusability of the beam.

- Target experiments were performed at a peak intensity of 7×10^{14} W/cm^2. At this intensity, important target experiments have been conducted, especially those related to wavelength scaling of laser-plasma interactions.

Two-Beam System (TBS)

The heart of this system is a dual-beam amplifier module, in which two gain chambers share one cold-cathode electron-beam ionization gun. The oscillator pulse is split into two beams, each of which is amplified in three passes through a single gain chamber. The TBS was originally intended only as a prototype for the Eight-Beam system. However, the need for additional laser capability at higher intensities became apparent, and the TBS program was enlarged to include a target irradiation capability. The design point for the TBS is a total output of 2 to 4 TW, or 1.25 kJ per beam in a 1-ns pulse. Specifically, the following progress was made:

- Target experiments began in May, 1976, with a 300-J, 1-ns, single-beam pulse. Initial target results monitored with a time-of-flight ion detector indicate that the beam is well focused to a spot of ~175 μm diameter. The system is expected to reach 1200 J in two beams in early 1977 and should meet its design point later in 1977.

- The optical diagnostic system as well as the computer-control, data-acquisition, and processing system are functioning. A prototype system for precise alignment of the beams onto targets has been checked out.

- A major discovery was the fact that laser light reflected from the target creates a region of optical gas breakdown in the amplifier, which then absorbs the reflected light. This absorption protects optical components earlier in the amplifier chain from the severe, damaging light intensities that would otherwise occur.

Eight-Beam System (EBS)

This system will include an oscillator, preamplifiers, and four dual-beam amplifiers, with a design-point performance of 10 to 20 TW in a 0.25- to 1-ns multiline pulse (maximum energy output, 10 kJ in 1 ns). This design point should be reached in 1977, with target experiments to begin in 1978. Progress is summarized as follows:

- The EBS is being assembled. The oscillator-preamplifier system is nearly operational and the computer-control and data-acquisition systems are functional. Assembly of one of the four dual-beam amplifier modules is nearly complete.

- The power supplies have been installed and tested successfully.

High-Energy Gas Laser Facility (HEGLF)

The HEGLF, planned for completion in 1981, represents a major step in laser-fusion research. This system is expected to demonstrate scientific breakeven (i.e., fusion yield equal to incident laser-pulse energy) and will serve as a major testbed for the study of a variety of target designs. It will be subsequently available for laser engineering-optimization studies for a prototype reactor. The power stage of this system will consist of six large annular amplifiers, which will yield a total energy of 100 kJ in a 1-ns pulse, or 100 to 200 TW -- the latter value is for a 0.25-ns pulse. The associated target irradiation facility will permit the symmetric irradiation of a fusion pellet by the six beams.

We feel that this program represents a least risk path to scientific breakeven. The system represents a reasonable extrapolation of existing technology and engineering. Major subsystems will

be evaluated in a prototype program. Progress is summarized as follows:

- Analysis and prototype activities are proceeding well. Power-amplifier module physics have been studied in detail, aimed at achieving uniform gain in an annular medium and determining the required oscillator pulse energy.

- Prototype programs have been initiated to study the cold-cathode electron gun, a scaled power-amplifier module prototype, a high-voltage test module, and a prototype pulse-forming-network power supply.

- Design studies, based on a 4:1::CO_2:N_2 gas mixture for the power amplifiers were completed.

CO_2 Laser Technology

Scientific support for our CO_2 system development programs includes studies of short optical-pulse generation techniques, system isolation to prevent parasitic oscillations, laser-system diagnostics, and other work to improve and optimize system performance. For example, oscillator pulses containing multiple rotational transitions will increase both pulse energy and peak intensity significantly and will reduce the risetime. Target deposition of only 50 μJ by parasitic oscillations or by laser precursor pulses can melt the target prior to the arrival of the main pulse. System isolation must prevent this unwanted energy deposition as well as alleviate the problem of optical damage by amplified reflections from the target. Extensive efforts in temporal and spatial beam diagnostics and in beam improvements are under way to achieve a small focused spot size. The following progress is significant.

- We have built multiline and single-line laser oscillators that produce temporally smooth pulses. Outputs as short as 250 ps can be switched out electro-optically from these pulses.

- A reliable system for the production of 50-ps pulses has been developed using the optical analog of free-induction decay.

- We have improved the laser-pulse transverse profiles by using spherical-optics spatial filters, and we have developed a cylindrical-optics spatial filter concept, which represents a major advancement.

- Several promising system-isolation schemes have been analyzed. Basically, we wish to use a bleachable or switchable absorber (gas, solid, or plasma) to absorb any prepulse energy, and thus to help prevent both system self-oscillation and the amplification of target reflections. The most promising candidates are p-type germanium, and hot, low-pressure CO_2; others include saturable tri- and polyatomic gases, gases whose infrared absorption bands can be switched by external excitation, and electrically driven plasma curtains.

- We have developed a CO_2 laser pulse-driven Kerr-shutter streak-camera system that can detect our 50-ps pulses, and a 5-GHz oscilloscope which, in combination with a pyroelectric detector, yields a detection-system risetime of 70 ps.

- Damage studies of antireflection-coated NaCl windows indicate a damage threshold of 10 J/cm^2. We have developed an optical analysis capability to evaluate our major systems for wavefront error, correction, and alignment sensitivity.

- A theoretical method for calculating collisional dynamics in a CO_2 laser medium was verified by experimental results of Ar-CO_2 collision measurements.

NEW LASER RESEARCH

In the early years of laser-fusion research, it was felt that the "ideal" short-pulse laser for fusion research had not yet been invented. Its desired characteristics included high efficiency, visible or near-uv output, and a small-gain cross section coupled with high-density energy storage. However, recent experimental and theoretical results at CO_2 laser wavelengths may relax the projected requirement for a shorter wavelength.

Our efforts in new lasers are concentrated in three areas: fundamental investigations of kinetic

processes and laser excitation methods, investigation of related technology areas, and establishment of a general experimental capability in electrical discharges and high-energy electron beams. Our major emphasis has been on Hg_2 and on rare-gas oxides (to produce the green auroral line of atomic oxygen). The following progress is noteworthy:

- To investigate intermediate reactions in the formation of the rare-gas oxides, we have used optical pumping techniques in our kinetics studies of high-pressure ArO, and recently of pure krypton and xenon. Xenon data from 10 to 30 000 torr have yielded rates for several important processes.

- A new, large electron-beam machine has been purchased for kinetics studies and laser parameter investigations at useful volumetric scales. This machine produces a 2-MeV beam from a cathode with a 50- or 100-cm transverse dimension, in pulses of 20- to 40-ns duration (risetime, 11 ns), and delivers an energy of 15 kJ. The associated high-pressure experimental chamber is being fabricated, and a gas purification system is being built to reduce operating expenses.

- An electron-beam-controlled electrical-discharge system has been built for the study of kinetic processes and instability mechanisms in high-pressure electrical discharges. Electron-beam control has been demonstrated at a pressure of 10 atm, with a current density of 80 A/cm^2 and a current risetime of 50 ns.

- The first milestone in the study of Hg_2 was the operation of a self-sustained discharge at a density of 10^{19} cm^{-3}, with a discharge current of 6 A/cm^2 and a duration of 1.4 μs.

- Heat-pipe containment of metal vapors is expected to provide a laser medium of uniform temperature and density. Studies carried out with Hg, Na, and H_2O indicated that the diameter of state-of-the-art heat pipes is limited to 2 to 3 cm.

- Electron-collision-induced transitions to higher energy states are important in the rare gases, leading to competing loss channels for excited-state energy storage, to less efficient pumping, and to instabilities in the electrical discharge. In particular, we studied electron-collision excited-state kinetics in argon and mercury. These effects do not appear to be as serious in mercury.

- We analyzed excited-state electron-impact cross sections for argon and krypton. Measured differential cross sections are used to identify the inelastic channels in the energy-loss spectra and to determine a total integral electron impact cross section as a function of electron energy.

- Earlier ab initio calculations on electronic-state properties of ArO have been extended to KrO and XeO. The emission of the $O(^1S) \rightarrow O(^1D)$ line at 0.558 μm, induced by collision with the rare gases, is of particular importance. We have determined potential-energy curves for the repulsive ground state as well as for the several repulsive and bound excited states of KrO and XeO.

- The development of optical components with high damage thresholds for use in the visible and near uv is very important for high-power laser systems at these wavelengths. Testing is now under way at 0.532 μm. We have evaluated SiO_2 and TiO_2 rf-sputtered films, and have determined the superiority of rf-sputtered coatings.

LASER FUSION--THEORY, EXPERIMENTS, AND TARGET DESIGN

The laser-fusion program is a coordinated effort in theory, experiment, and target design. Because the interaction of high-intensity laser pulses with target plasmas represents a new regime of physics not previously studied in detail, there have been many uncertainties in modeling the relevant processes. Experimentally, we require precise spatial and temporal resolution, the spectra of emitted particles and radiation, as well as a complete characterization of the incident laser pulse. These experiments are conducted to test theoretical models and often lead to major modifications of theory. Theoretical efforts examine, for example, the various light-absorption mechanisms, hydrody-

namic motion and instabilities, energy-transport mechanisms, and the deposition of nuclear reaction products. In turn, target design efforts must take account of our present theoretical understanding and of problems that may have arisen with previous designs. Significant progress was made in various areas:

- Wavelength scaling of laser-plasma interaction phenomena has received great attention, both theoretically and experimentally. Prior theoretical descriptions and experimental interpretations have usually ignored the effect of the laser-pulse electric field (ponderomotive force) on the plasma density profile, but recent developments have shown that profile modification is important. In fact, the short interaction lengths produced in the plasma by the laser electric field may be the dominant factor in determining the absorption and electron energy distribution, independent of laser wavelength. Recent experiments and theoretical results indicate that this indeed is the case. Measurements of ion and electron spectra produced by the interaction of 1.06- and 10.6-μm laser pulses on thin foils gave similar results.

- Studies of ion emission from single- and double-foil targets have shown correlations between the risetime of the ion time-of-flight signal and the quality of microballoon implosions. This correlation has been traced to the presence of laser prepulses; we have, in fact, shown that the fast-ion signal is a sensitive indicator of laser pulse quality. Experiments with multiple foils have given information on the applicability to target design of vacuum insulation in which space charge stops the fast electrons. Our theoretical design studies indicate that a vacuum insulation layer is effective in reducing electron preheat substantially. Experiments have shown that the shielding obtained for realistic targets is effective long enough to make this technique important in target design. In fact, LASNEX calculations show that targets can be designed which exceed breakeven, even in the presence of an extreme hot-electron spectrum.

- Plasma simulations of identical experiments at 1.06 and 10.6 μm are difficult due to limitations on computer time, but we have reached general conclusions that agree qualitatively with experiments. The steepening of the plasma-density profile by the ponderomotive force softens the electron spectrum. However, the steepened profile is unstable and the resulting surface ripples produce a 30 to 50% laser-pulse absorption over a wide angular range, in agreement with experiment.

- We continued theoretical studies of the relationship between the x-ray spectrum and the suprathermal electron distribution, and found important omissions in earlier published work.* A more accurate description of the bremsstrahlung process showed that the x-ray spectrum is more sensitive to the electron distribution than had been concluded earlier. Our result enables us to obtain more information from the x-ray spectrum, although it is not possible to obtain the total suprathermal electron energy in a manner that is independent of spectral details.

- Further development has been done on the MCRAD and LASNEX target design codes. Although LASNEX studies of implosions driven by laser-generated fast ions have given yields as high as 1%, it has not yet been determined that optimization of an ion-driven target can yield breakeven.

LASER-FUSION TARGET FABRICATION

Fabrication and characterization of target pellets are important areas of supporting technology in our laser-fusion program. Small, often complex, target pellets must be fabricated to strict specifications, e.g., filling a sphere to several hundred atmospheres with DT and depositing a uniform DT-ice layer on the inside of a microballoon. The characterization of completed pellets is also an important and challenging task. Our progress in this effort included the following:

*K. A. Brueckner, "Energy Deposition in Laser-Heated Plasmas," Phys. Rev. Lett. 36, 677 (1976).

- We continued our development of techniques to select and measure glass microballoons (GMBs) via optical interferometry. The selection process was improved by developing a tilting GMB holder that fits on our interference microscope and allows rapid examination of the GMBs in two orthogonal views.

- A new ray-trace-type computer program permits us to simulate interferograms of GMBs with defects such as nonconcentricity, ellipticity, and bumps. This program will improve our knowledge of the types and magnitudes of defects that can be detected by our interferometric inspection.

- Our capabilities in plastic fabrication were improved in two areas. We developed a technique to fabricate thin films of normal or deuterated polyethylene over a thickness range of at least 20 nm to 1 μm. We also developed processes to fabricate plastic microballoons that can be lined and/or coated with a wide range of metals. These targets are assembled from pairs of hemishells, allowing DT-filled glass or metal microballoons to be supported within the plastic microballoon, followed by any number of concentric plastic microballoons to form a multishelled target.

- We continued our development of methods to deposit high-strength metal pusher shells onto spherical substrates. Chemical vapor deposition received considerable emphasis, devoted primarily to improving our control of process variables and to evaluating deposition conditions with $Mo(CO)_6$ in an attempt to obtain 10-μm-thick, smooth-surfaced, stress-free coatings of molybdenum carbide and of molybdenum metal. In addition, we began experiments with MoF_6 and WF_6 for the deposition of molybdenum and tungsten, respectively. In a related experiment we found that a gas-fluidized bed of substrated particles can be coated by sputtering.

- Our electroless and electrolytic metal-coating capabilities were expanded. Electroless nickel coatings were applied to GMB substrates, and experiments have been started to develop an electroless nickel-iron alloy coating capability.

- To improve our ability to evaluate coatings quickly, we are developing a rapid technique in which we measure the tensile strength of coated microballoons by gluing the microballoon to a fixture and bursting it with pressurized oil via a hole in the microballoon.

- Initial experiments have demonstrated the feasibility of counting visible-light photons from tritium-filled GMBs as a nondestructive fuel-gas assay technique.

- We have made considerable progress in our study of methods to condense DT fuel into a uniform deposit on the inside of GMBs. In a series of experiments employing a combination of cooling methods, we have demonstrated that we can condense a layer of DT that is either thicker on the bottom, thicker on the top, or reasonably uniform throughout the GMB, depending on the speed of the heat-transfer technique employed.

TARGET DIAGNOSTICS

Measurements of laser-plasma interactions, which may last from 50 ps to 1 ns, impose severe constraints on the diagnostics, requiring much equipment to be designed in-house, and pacing the state of the art in many areas. Progress in diagnostics development included the following:

- Recent theoretical and experimental results, which indicate a much weaker wavelength dependence of laser-plasma interaction than believed earlier, imply the presence of a very steep density gradient at the critical surface. To measure the scale length of strong laser-plasma interactions, we designed a high-resolution interferometer, which will be synchronized with the laser pulse in the two-beam CO_2 system (TBS) to give a temporal resolution of 5 to 10 ps and a spatial resolution of 3 to 5 μm. We are also developing techniques for analyzing these interferograms.

- Time-resolved x-ray photographs of ball-and-disk targets were made with a temporal resolu-

tion of ~3 ps and a spatial resolution of 25 μm. Only the central compression was observed, with poor statistics, but analysis of experimental conditions indicates that earlier estimates of sensitivity and temporal resolution are correct.

- Design and surface-error studies were performed on x-ray microscope systems, and a replicated Wolter microscope was fabricated at UCC's Y-12 plant. Preliminary measurements indicate a spatial resolution of less than 25 μm, and tests are continuing. Improved fabrication techniques should produce inexpensive microscopes for target experiments.

- We completed studies of grazing-incidence transport systems and of ir sensitivity to impurity deposits. Analysis showed that a layer of carbon (simulating vacuum-pump oil) as thin as 30 Å can affect the reflectivity of x-ray optics at photon energies below 2 keV. This sensitivity requires that x-ray microscopes be recalibrated periodically.

- The imaging characteristics of x-ray film have been improved successfully. Our calibration of Kodak RAR 2490 film for soft x rays was completed; the spatial resolution is higher than for no-screen medical x-film and there is less fog, but the absolute sensitivity is lower. As a result, effective image sensitivity for RAR 2490 is higher than for the no-screen film.

- Development of automated data-analysis and-acquisition techniques continued. Ion calorimeters, which measure total ion energy and ion angular distribution, have been coupled to the NOVA-840 computer to provide accurate measurements of absorbed laser energy immediately after the experiment. The reliability and accuracy of these ion calorimeters have been demonstrated earlier.

- Tests have shown that the 10.6-μm light from a CO_2 laser-system oscillator can be used to align the beam on target. Recent improvements in pyroelectric vidicons have made this possible. An improved camera for these vidicons is being developed for us, and a dynamic range greater than 100 seems attainable.

APPLICATIONS OF LASER FUSION -- FEASIBILITY AND SYSTEMS STUDIES

Our feasibility and systems studies are performed to analyze the various commercial and military applications of laser fusion, and to identify technological problems requiring long-term development. Analysis, optimization, and tradeoff studies are performed on conceptual power-plant designs, and alternative applications of laser fusion are investigated. Progress was made in recent studies that have included the following:

- We have analyzed in greater detail the flow of lithium which protects the cavity wall in a spherical wetted-wall laser-fusion reactor. Gravity flow of a thin film of lithium, with variations in the lithium source, was considered. Indications are that lithium films ≥1 mm in thickness can be obtained.

- Our investigation has continued to determine the behavior of ionized fusion-pellet debris in a magnetically protected reactor. Analytic expressions to predict sputtering of solid materials by energetic ions were derived in parallel to the determination of ion fluences on cavity component surfaces. Energy deposition, both from energetic particles in the fusion-pellet debris and from radiation sources, is a second source of erosion of reactor-cavity component surfaces. We have modeled the problem of calculating surface-temperature time histories and evaporation rates in a general way, which permits us to specify volume sources, the arbitrary time dependence of energy deposition, and finite shell thicknesses. We will use these computer programs to investigate reactor-cavity designs for structured fusion pellets.

- We have reevaluated the operating characteristics and the performance of a laser-fusion central-station generating plant based on the magnetically protected reactor concept. A recalculation of the blanket energy-multiplication factor due to exoergic nuclear reactions and from an updated model of a potassium topping cycle indicated significant changes in the performance and capital costs of current designs. A survey of available

data did not change our previous estimate of maximum permissible total neutron fluences for determining laser-fusion reactor-cavity component lifetimes.

- Our evaluation of the ^{239}Pu burner-^{233}U breeder hybrid concept is continuing. This fusion-fission breeder concept, producing large amounts of thermal power and fuel for thermal-fission reactors, may be attractive as a direct substitute for the liquid-metal fast-breeder reactor, but retains essentially all the environmental disadvantages of the latter.

- The investigation of synthetic-fuel production by using the radiation from fusion-pellet microexplosions to decompose H_2O or CO_2 radiolytically into H_2 or CO was continued, and we have updated our estimates of product costs from such processes. Radiolysis would require high-energy neutrons, and tritium for the fuel cycle would have to be purchased from an outside source. An optimistic economic analysis of a production-plant model indicates a cost between 2 and 2.5 dollars per million Btu of neutron energy. Synthetic-fuel production from laser-fusion reactors dedicated to this purpose would not be competitive with standard coal-gasification processes in the context of 1973 market values. These conclusions could be reversed by dramatic changes in relative market values or by scarcities of feed materials.

- We have performed some theoretical calculations to investigate the possibilities of imploding cylindrical shells with high-power lasers. Cylindrical geometry was chosen to allow the viewing of geometrical convergence effects along the inside surface of the shell. Preliminary results indicate that a 100-kJ, 1-ns, 10-μm laser pulse might produce pressures of 30 to 40 Mbar in a gold cylinder with a diameter of 0.39 cm and a length of 0.78 cm.

These and other results of our efforts during the first half of 1976 are discussed in detail in the following sections.

I. CO_2 LASER PROGRAM

The research and development programs on high-energy short-pulse CO_2 lasers were begun at LASL in 1969. Three large systems are now either operating or are being installed. The Single-Beam System (SBS), a four-stage prototype, was designed in 1971 and has been in operation since 1973 with an output energy of 250 J in a 1-ns pulse with an on-target intensity of 7.0×10^{14} W/cm^2. Target experimentation has begun on the Two-Beam System (TBS), which will ultimately generate pulses of 2 to 4 TW for target-irradiation experiments. Construction is under way on all subsystems of the Eight-Beam System (EBS), which is scheduled for completion in early 1977 and will begin target experiments at 10 to 20 TW in 1978. A fourth system, the High-Energy Gas Laser Facility (HEGLF), is in the design and prototype stage. This system will generate laser pulses of 100 to 200 TW.

SINGLE-BEAM SYSTEM (SBS)

Introduction

The Single-Beam System (SBS) is operated both as a service facility for single-beam laser target-interaction experiments at 10.6 μm with a 1.0-ns pulse as well as a developmental system for many aspects of operating and controlling high-energy CO_2 laser systems for target experiments. The SBS consists of a gated oscillator and four electron-beam-sustained amplifiers (see Fig. 1). The system delivers on target a maximum intensity of 7×10^{14} W/cm^2 and yields new information for fusion-target design development.

In addition to using the SBS as a target-irradiation facility, we are continuing to upgrade

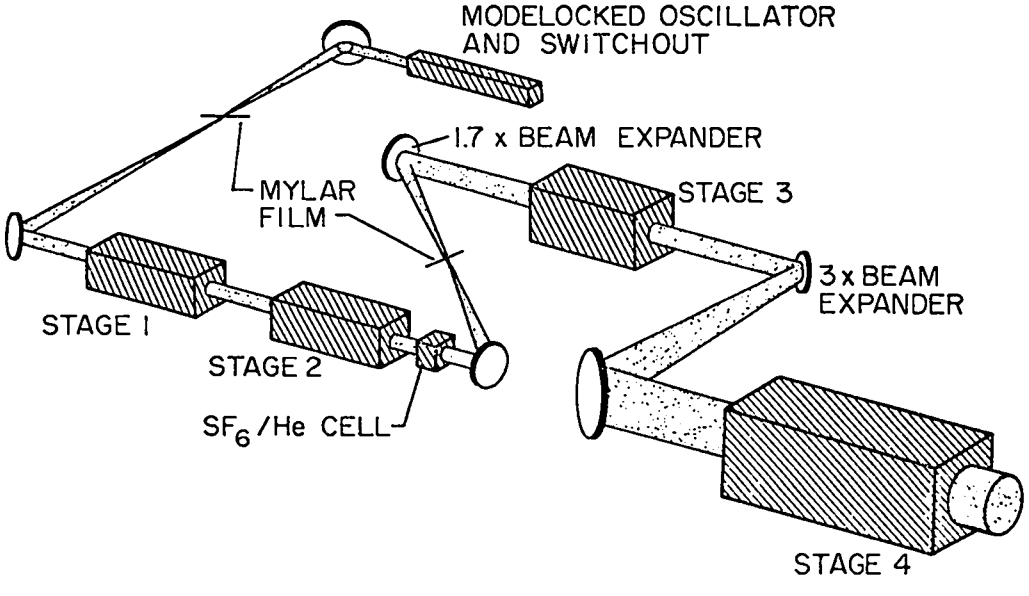

Fig. 1. Schematic of Single-Beam System.

the SBS to produce higher target irradiances. This upgrading involves reducing the problems of laser-pulse feedthrough, self-lasing, and retroreflected pulses; and improving the beam quality. Specific improvements included:

- The installation of a more powerful oscillator and of two subsequent electro-optic switches to provide a peak power of 5 MW and an extinction ratio of 4.5×10^5.
- The addition of SF_6 and Freon isolator cells after Amplifier 2 to increase the system self-oscillation threshold.
- The addition of a NaCl prism after the oscillator switchout to help prevent system oscillation at 9 μm and to protect the oscillator from any 9-μm retropulses from the target.
- The addition of a telescopic spatial filter after Amplifier 2; and the addition of a 50-mW He:Ne laser for easier beam and target alignment.

The combined application of these techniques has allowed us to perform many useful flat-target irradiation experiments with a high-quality beam at energies up to 180 J in a 1-ns pulse. These flat-target experiments were performed without self-lasing or damage due to high-energy target reflections. Full power output of the laser is 250 J/ns (without isolators or targets) indicating that over 70% of the available energy can be focused onto a target. Efforts to upgrade Amplifier 4 to deliver still higher energies on target are under way and will be implemented after the target-irradiation experiments.

Upgrading of Amplifier 4

The output energy of Amplifier 4 has been limited to ~250 J, partly because of the 200-kV maximum safe operating level of the power supply for the pumping chamber. This power supply is designed for ~300 kV (nearly twice the present level of energy deposition). Past experience has shown that operation above 200 kV involves a risk of high voltage breakdown, and correction of this voltage limitation requires crowbarring the pumping-chamber power supply just before terminating the electron-beam current. A commercially procured five-stage graded vacuum switch designed to crowbar the capacitor bank has failed to function properly. The triggering electrode will have to be modified for proper operation under these conditions.

To minimize the probability of foil damage caused by occasional internal arcs, we have added a diverter switch across the Amplifier-4 pumping chamber so that the large voltage generated at electron-beam turnoff will cause this switch to close should the vacuum switch fail. The excess power-supply energy is diverted to the load resistors.

The implementation and verification of these system upgrades will be completed on a schedule compatible with the ongoing target experiments.

Salt-Prism Isolation

A NaCL prism has been installed in the optical path prior to Amplifier 1 to help avoid system oscillation at 9 μm and to ensure that any returning 9-μm light would be prevented from reaching the damage-sensitive CdTe electro-optic switch. This prism is mounted in a temperature-controlled unit because temperature drifts will steer the beam by 17 μrad/K. The prism causes an insertion loss of ~ 20% due to Fresnel reflections for the 10.6-μm gated pulse.

Prevention of Self-Lasing

To upgrade the energy delivered on target, we have also had to improve our techniques for suppression of self-lasing. New absorption data we obtained on SF_6 and two fluorocarbons demonstrate that self-lasing can be prevented more efficiently than in the past. Figure 2 shows the small-signal absorption spectra for these compounds. Employing these new isolators to control self-lasing, an average of ~ 180 J can be delivered to the target. This represents a twofold increase in energy over that used during the last series of target experiments.

In the present configuration, two 6-cm-long absorption cells are placed immediately after Amplifier 2. The first cell contains 40 torr of FC-115 (CF_3CF_2Cl), which absorbs in the 10-μm

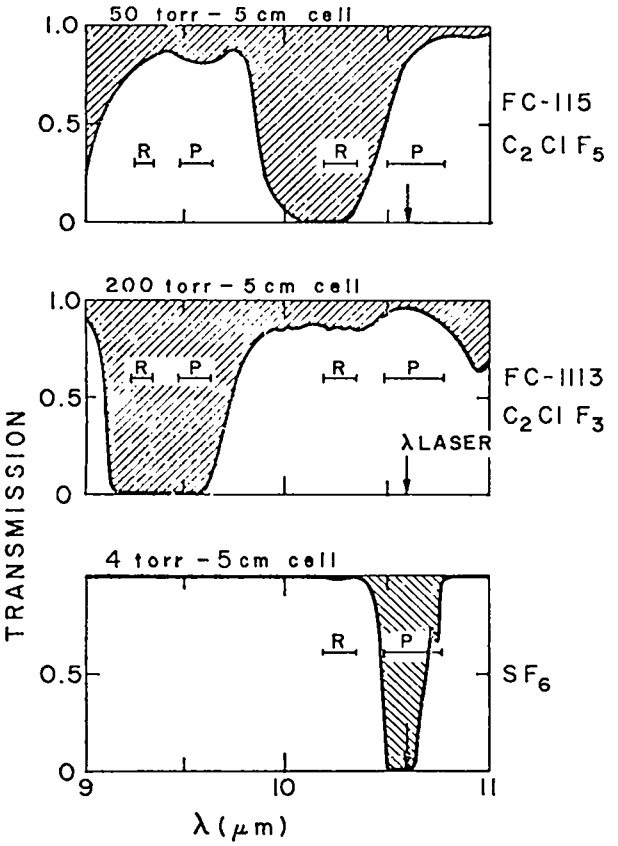

Fig. 2. Small-signal absorption spectra of SF_6 and two fluorocarbons.

R-branch, and 200 torr of FC-1113 (CF_2:CFCl), which absorbs in both the 9-μm P- and R-branches. The second cell contains 5 torr of SF_6, which absorbs in the 10-μm P-branch. With this combination of absorbers, the system is conditionally stable; any self-lasing seen can be classified as "post"-lasing, i.e., it occurs in time after the main pulse is normally switched out from the oscillator. When a pulse is switched out, no self-lasing is observed. Such a system is not fail-safe, because self-lasing could occur if the oscillator failed to switch out a pulse. To prevent possible damage to the oscillator, a standard Mylar-foil blast shutter is placed in the beam just after the oscillator.

TWO-BEAM SYSTEM (TBS)

Introduction

The two major functions of the Two-Beam Laser System (TBS) are to serve as a developmental prototype for the dual-beam modules of the Eight-Beam Laser System (EBS), and to provide a facility for target irradiation experiments for military and laser-fusion applications. All major components of the TBS have been installed. Numerous improvements to the operating system and to laser diagnostics have been made. Use of the system computer for diagnostics and for control functions continues to expand.

In our experimental program we have concentrated on achieving operational status for target experiments in the next quarter. The following progress is particularly significant:

- The problem of damage due to target-reflected pulses has been resolved. The mechanism of optical breakdown has been shown experimentally to provide adequate protection for all components in the dual-beam module.
- We have identified a feedback mechanism in the triple-pass optical system which results in self-oscillation at less than full gain. A modified optical system that eliminates this problem has been designed for the EBS and will be installed in the TBS late in 1976.
- The energy-extraction performance of each beam has been measured to be $\gtrsim 800$ J in a 1.2-ns pulse. The measured performance is in good agreement with the predicted performance, thus verifying our current CO_2 kinetics models for the design of large CO_2 laser devices.
- Experiments have been initiated to measure and to reduce system self-oscillation with flat targets. As part of these experiments we have conducted single-beam target irradiation experiments at energies up to 300 J. Fast-ion signals from the plane targets indicate a focal-spot intensity of $> 10^{14}$ W/cm^2.

System Development

Oscillator-Preamplifier Subsystem -- The optical train for both beams has been completed. We have tested, under a variety of operating and tar-

get experimental conditions, the spatial filters incorporated into the optical system to protect the oscillator from damage by energy feedback from the dual-beam module. This entirely passive system performed excellently. No damage has occurred, even during system oscillations that sent > 20 J back toward the oscillator.

The laser-triggered spark-gap switch, a critical component in the oscillator switchout, has been modified to provide more reliable triggering and less jitter. Switchout reliability is now greater than 99% and the jitter is less than 1 ns.

Dual-Beam Module (DBM) -- With the installation of the optical system in one of the pumping chambers, and the installation of the 40.5-cm-diam NaCl output windows early this year, we completed the assembly of the DBM. Subsequent additions and modifications included new mirror mounts, which provide greater rigidity in both beam lines. These mirror mounts are provided with stepping motors for adjustments about two rotational axes and along one translational axis. The control system for these stepping motors, which provides an operator with remote pushbutton selection and independent operation of any mirror in the DBM, has been in operation for several months. This mirror-control system has greatly facilitated routine alignment of the triple-pass optical system.

Control Systems -- No major modifications have been made to the operating system. Use of the NOVA-840 computer continues to increase as more routine tasks are added to the software. To cope with this increased usage, a second disk storage unit has been added, and an additional 16k of memory are on order.

Typical of the tasks added to the computer programming are subroutines to analyze small-signal gain and to calculate electrical parameters of the DBM after each shot. The small-signal gain calculation is particularly useful because the gain coefficient is an important diagnostic of DBM performance.

The computer data-collection system will be extended to the target diagnostics screen room so that computer-assisted data collection and analysis can begin.

Laser Diagnostics -- A small-signal gain-measuring apparatus has been installed on both beam lines; it enables us to measure the gain coefficient for each shot. Additional diagnostics, implemented for routine use, include monitors of pulse energy entering the target chamber, of reflected pulse energy, and of input pulse shape, as well as an oscillation monitor which detects any significant self-oscillation.

The energy-measuring system is calibrated with an in-house-built 38-cm-diam calorimeter. Repeated calibrations and comparisons indicate a relative accuracy of $\pm$ 3% and an absolute accuracy of $\pm$ 6%.

Target Alignment System -- We have installed a prototype beam-alignment system that uses a modified Hartman test and works as follows: A Hartman mask containing an array of apertures shaped into a "cross" is placed into the beam line just upstream of the target chamber, and the CO_2 oscillator-preamplifier system is used to irradiate, through the Hartman mask, a special surrogate spherical ball-bearing target in the target chamber. When the target-chamber optics are perfectly aligned, the array of small beams generated by the mask will retroreflect exactly and will be autocollimated back onto the Hartman mask. By viewing the target side of the mask with an ir vidicon, we can discern the proper alignment condition.

The results obtained with this prototype system are encouraging. One channel of the ir vidicon display has been assembled by EG&G and has demonstrated satisfactory performance; Fig. 3 shows the TV monitor display seen by an operator during optical alignment with the prototype system. When correct alignment is obtained, the image of the five spots should form a symmetrical cross with a black circle (i.e., a hole) at the center of each spot; the hole corresponds to the opening in the Hartman mask. A pointing accuracy of < 20 μm and a focusing accuracy of $\pm$ 50 μm (depth of focus for the TBS focusing mirror is 100 to 200 μm) are feasible even in the presence of the nonzero wavefront aberration in the target optics. The components needed to implement this system on both beams of the TBS are in procurement, and the complete two-beam alignment system should be operational in August, 1976.

Target Chamber -- Installation of target chamber, shield room, and instrumentation-cable conduits has been completed. The parabolic focusing

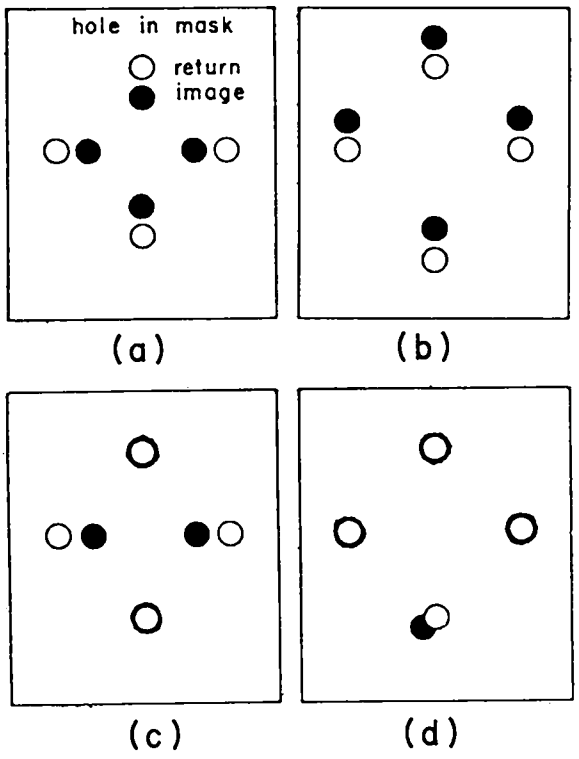

Fig. 3. Typical displays from Hartmann Mask beam-alignment system. (a) Beam focus in front of sphere center; (b) beam focus above sphere center; (c) paraboloid axis not parallel to incoming beam in horizontal plane; (d) wavefront error in beam or paraboloid.

mirrors were installed and given a preliminary alignment by using the He:Ne laser. The measured spot diameter was 150 to 180 μm at a wavelength of 0.63 μm.

A multiple-target holder has been installed and used. It typically carries one alignment target and nine experimental targets, so that we can conduct one to two days of experiments between pumpdown cycles of the target chamber.

The remote stepping-motor controls for the target pedestal, and for the parabolic and turning mirrors, have been installed and operate satisfactorily.

Experimental Program

Self-Oscillation -- Two modes of oscillation exist in the TBS, which must be distinguished: First, a total system oscillation along the optical axis involves reflection from the target and from components in the oscillator-preamplifier, and is intrinsic to the laser-target interaction system. This oscillation will be discussed below. The other oscillation occurs within the DBM. The cause of this oscillation has been traced to a feedback mechanism in the triple-pass optical system, which allows a slightly off-axis ray entering the output window of the DBM to make four passes through the amplifying region and to be returned directly upon itself. With a diffuse black surface ($R < 1\%$) at the DBM output, this four-pass oscillation occurs at a small-signal gain of $\sim 2.9\%$/cm, or at a round-trip gain of 2.5×10^{10}. We have designed a modified triple-pass optical system, which utilizes an evacuated spatial filter between the first and second amplifier passes. The aperture at the beam waist of the spatial filter blocks those ray paths that are critical to the four-pass oscillation mode and thus eliminates this mode. This aperture will be evaluated on the first DBM amplifier assembly in the EBS during September, 1976.

Energy Extraction -- The output energy of both beams has been measured for gains ranging from 1.6 to 2.9%/cm at an input energy of ~ 150 mJ. We made these measurements with a diffuse absorber at the output of the DBM. The maximum single-beam energy was 820 J in a 1.2-ns pulse at a gain of 2.9%/cm. The energy output decreased linearly with gain to $\sim 2.3\%$/cm and more rapidly thereafter due to incomplete saturation. Computer performance calculations compare satisfactorily, and the full output of 1250 J per beam should be achieved as soon as the new optical system allows operation at the design gain of 4%/cm.

The measured variation of output energy with input energy gives less than 20% change for a four-fold reduction in input, consistent with the expected strong-signal gain saturation.

Retropulse Measurements -- The first measurements we made after installation and alignment of the target-chamber optics were designed to determine whether the energy reflected from the target would damage components of the DBM. Computer calculations made to analyze the second pass of the reflected pulse in the DBM indicated that the reflected pulse on this pass is contracted in area by a factor of ~ 340, raising the question of optical damage to the convex mirror (see Fig. 4). These calculations had predicted that the large intensity

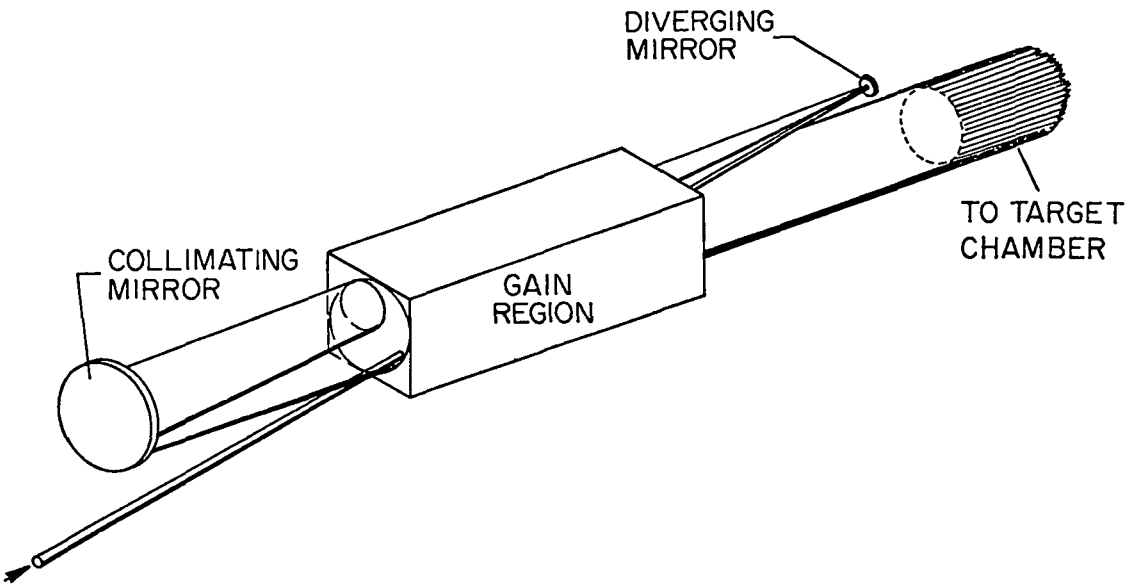

Fig. 4. Schematic of triple-pass amplification. The pulse reflected from the target causes an optical breakdown just before reaching the diverging mirror, thus protecting that mirror and other optical components from damage.

of the converging reflected pulse would raise the electron density in the laser gas to a level where optical energy loss by inverse bremsstrahlung would limit the flux density at the convex mirror surface to less than 5 J/cm^2, but that the energy density returning to the entrance window might easily exceed the design limit of 2 J/cm^2.

The energy passing back through the entrance window was measured for a range of reflected pulse energies from 10 to 30 J. In all cases, the measured energy was < 0.25 J, much less than predicted by the computer calculations. Revised calculations, which included the refractive as well as absorptive properties of the breakdown plasma, show that refraction can account for the observed small retropulse signal. Defocusing of the reflected pulse occurs after only a few hundred millijoules have passed through the breakdown region.

The occurrence of gas breakdown was verified experimentally by photographing the region in front of the convex mirror. A plasma column whose diameter equaled the beam diameter and whose length exceeded 10 cm was clearly evident. This plasma should suffice to shield the mirror against the retropulse.

The modified triple-pass optical system described earlier does not possess the characteristics of the current design, which make this gas breakdown particularly effective. We believe that the new design will still be free from retropulse damage, but to avoid any program delays in the event that damage does occur, we are continuing the development of a small electron gun, which can preionize the laser medium in a high-flux region of the new optical system and thus lower the gas breakdown threshold. The electron gun, which is being tested, should produce a 100-A, 0.25-μs pulse of 250-keV electrons, sufficient to preionize the gas to > 10^{13} electrons per cubic centimeter. The gun is compact (30-cm-diam by 76-cm-long), and provisions have been made to mount it on the new optical chambers.

Prepulse Measurements -- Prepulse energy arises from two sources, system oscillations and feedthrough energy that passes through the oscillator switchout system in its off state. Based on measurements of target damage, > 50 μJ of feedthrough energy and > 500 μJ of oscillation pulse energy are thought to cause unacceptable damage to experimental targets.

The measured contrast ratio of switched-out energy to feedthrough energy is 9 x 10^3 for our oscillator. By using a saturable absorber cell containing 14 torr of SF_6 between Preamplifiers 1 and

2, we increased the contrast ratio to 4×10^8, which should permit operation at a DBM gain of up to 2.44%/cm with less than 50 μJ of prepulse energy on target. This prediction has been tested at somewhat lower gain (1.9%/cm) by operating the system with the switchout turned off. Such operation allows the entire leakage energy to be amplified and focused onto the target. No visible breakdown nor damage to the 0.25-mil-thick Mylar target was observed. To extend operation to higher gains, we will increase the pressure in the preamplifier SF_6 cell to 20 torr; this will permit operation of the DBM up to a gain of 3.6%/cm. The final increase in contrast ratio required at a gain of 4%/cm will be obtained by adding a second saturable absorber to the new optical system.

System oscillation occurs at a DBM gain of 1.9%/cm with a flat polyethylene target oriented 16° off the beam axis. The range of threshold gains reflects the dependence on gas excitation voltage. The energy on target due to system oscillation depends on the time history of the gain and on the total time available for the growth of system oscillations (i.e., the time between the point when the gain exceeds the loss and when the short pulse enters the DBM). Operation at higher voltage reduces the time available for oscillation growth and permits short-pulse amplification at gains as high as 2.4%/cm.

These measured threshold energies are consistent with earlier results obtained on the SBS. By using this proven technique, we are installing cells for saturable-absorber gases between the target chamber and the DBM. The cell at the target-chamber window will be filled with a low-pressure mixture of SF_6 and other gases, which will reduce the round-trip gain on the 10.6-μm band. A second cell after Preamplifier 2 uses various Freons to suppress oscillation on the 9-μm band. This combination will permit the DBM gain to increase to > 3%/cm without system oscillation. At that gain, system performance will be limited only by the four-pass oscillation described earlier.

The modified optical system to be installed late this year will eliminate the four-pass oscillation. To suppress the system oscillation more effectively, we will install a gas-filled absorption cell in the DBM between Passes 1 and 2. At this location total absorption can be much greater because the gain of Passes 2 and 3 will make up for the substantial loss of energy which the primary pulse experiences in bleaching the absorber.

Target Plasma Measurements -- By using rapid pumping of the DBM, we have performed a few single-beam target experiments in conjunction with the experimental program described above. At a gain of 2.3%/cm we extracted an energy of 320 J focused onto a polyethylene film target.

An ion detector recorded the arrival-time history of the target ions. Based on this information, we estimated the target irradiance to be 6×10^{14} W/cm^2. Assuming a 1.2-ns pulse, the effective spot diameter is ~ 200 μm. This size is comparable to the spot size measured with the oscillator- preamplifier pulse only.

EIGHT-BEAM LASER SYSTEM

Introduction

The Eight-Beam Laser System (EBS) represents the next generation of high-power short-pulse CO_2 laser systems we will use to study the interaction of intense light beams with matter, with emphasis on investigating problems relating to laser fusion. This system is designed to deliver 10 to 20 TW to a target -- 10 kJ in a 1-ns pulse or 5 to 8 kJ in a 0.25-ns pulse. The EBS will consist of an oscillator-preamplifier system which generates a 0.25-ns multiline optical pulse at the several-hundred-megawatt level, and which will drive four DBMs clustered around a target chamber. Each of the eight 35-cm-diam beams will deliver ~ 650 to 1250 J (depending on pulse length) to the target chamber, which will contain an optical system to focus these beams onto a target. An artist's rendition of the EBS facility is shown in Fig. 5.

Occupancy of the facility is completed and the EBS is now in an intermediate state of assembly. The pulse-forming networks (PFNs) used to excite the laser gas have been installed and tested, and installation and test of the electron-gun-pulsed power supplies are nearly complete. Assembly of the oscillator-preamplifier system and of one dual-beam amplifier module is nearly complete, and both have been partially tested; assembly of the other DBMs has begun.

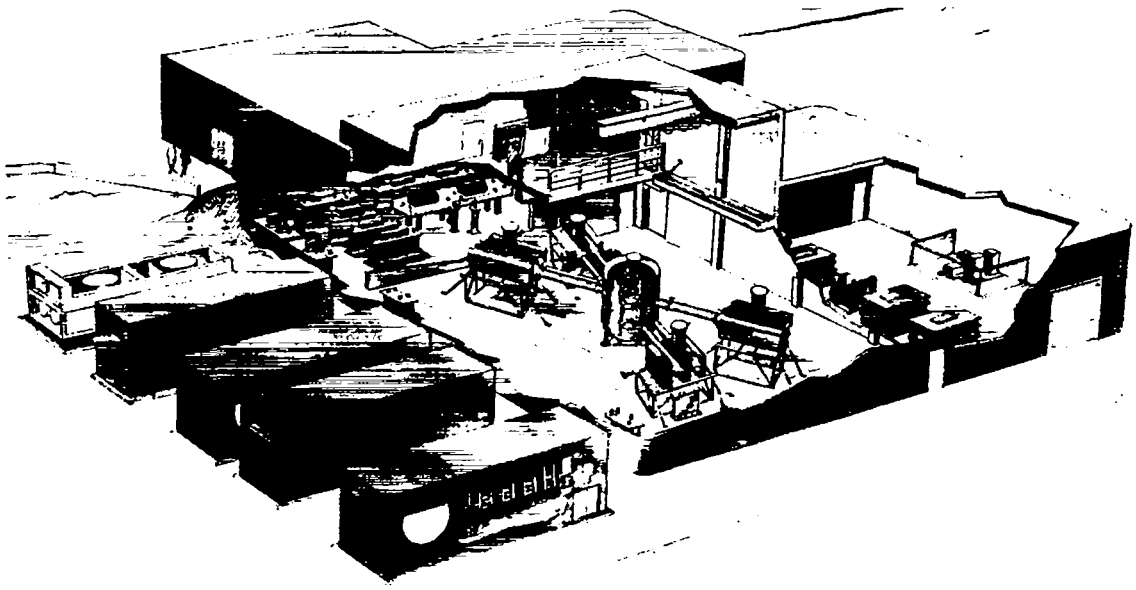

Fig. 5. Artist's rendition of Eight-Beam System. The oscillator room is in the background. The pulse-forming networks for pumping-chamber excitation are at the left, and the electron-beam power supplies are at the right.

Pulsed Power Supplies

The pulsed power supplies for the EBS consist of eight gas-discharge pulsers and four electron-gun power supplies. The discharge pulsers, Guillemin Type-C PFNs, with an efficiency of 90%, are operational and have all been tested by firing them into dummy 3-Ω loads (330 kV at 100 kA) with a reliability > 95%. The 16 high-voltage cables of each pulser have been connected to the PFN and have been pulled into the main power-amplifier area. The four electron-gun supplies (60 kJ stored energy at -330 kV) have been installed; two are operational and have been connected to their respective DBMs.

Master Oscillator and Preamplifier

This system will produce a 250-ps multiline pulse with sufficient energy (10 to 100 mJ) to drive the DBMs. The 250-ps master oscillator uses a plasma-smoothing tube to obtain a smooth gain-switched pulse, and an electro-optic pulse switch-out. The oscillator-preamplifier system and its associated beam-transport optics have been analyzed and designed to incorporate spatial filters and saturable absorbers which utilize p-doped germanium. We have chosen p-doped germanium because of the broad bandwidth required of saturable absorbers in multiline operation.

We have operated the oscillator in the smoothed gain-switched mode with a typical energy output of 500 mJ and a pulse length of 60 ns FWHM, and obtained multiline output through the use of an intracavity SF_6 absorption cell. A Pockels cell switchout using a cadmium-telluride crystal between crossed polarizers has been used to generate 1-ns pulses. We will use this pulse for initial evaluation of the DBMs; a 0.25-ns switchout system will be added later. The two preamplifiers required for this system have been constructed, tested, and are operational; they are identical to the double-discharge preamplifiers used in the TBS.

Main Power Amplifiers

A single DBM consisting of an electron gun and two power-amplifier chambers has been assembled, vacuum- and pressure-tested, and has undergone initial electrical testing. A view of this module without the triple-pass optics or gas-cooling hardware is shown in Fig. 6. We have successfully operated the cold-cathode electron gun at its design voltage of 300 kV after some initial problems with electrical breakdown in the vicinity of the electron-gun high-voltage bushings. One of the two power amplifiers has undergone initial testing and

Fig. 6. First dual-beam amplifier in Eight-Beam System.

has been operated successfully at 90% of maximum design voltage (275 kV, 100 kA at 1800 torr of 3:1/4:1::He:N_2:CO_2 laser mix).

All hardware for assembly of the DBMs has been received, with the exception of the triple-pass optics and related hardware. We will install these remaining parts in one of the DBMs by the end of July. Assembly of the second and third DBMs is proceeding on schedule.

Control System

About 80% of the control system has been fabricated, installed, and is operational in the manual mode.

The vacuum control system is operational for two of the four DBMs. The control system for the two remaining modules will become operational as the modules are assembled. We are installing a forepump rotation detector on all forepumps to prevent damage to the oil diffusion pumps due to power failure, belt breakage, or motor stalling.

Controls for three preamplifiers are complete, and oscillator-control installation should be completed early in FY 76T. These controls permit operation of the oscillator-preamplifier system from either the oscillator-preamplifier room or the control room. Installation of the oscillator and preamplifier laser-gas system is nearly complete.

Spark-gap gas-control systems for the PFNs, electron-beam pulsers, oscillators, and preamplifiers are operational.

The laser gas-mixing system for two of the four DBMs has been installed. The remaining two modules will be connected to the gas-mixing system as they are assembled. Presently, the DBMs are using bottled premixed gas; gas mixing will begin in the near future as separate gas storage tanks for He, N_2, and CO_2 are installed.

Computer-Controlled Monitoring, Diagnostic, and Control Systems

General -- The manual control system mentioned above will permit the checkout of each subsystem. For full-system operation, all the various subsystems controls are tied to and controlled by a Data General computer system. Computer operation also offers the ability to monitor and diagnose the operation of the laser system and its related components. The status of this effort is summarized below.

Computer System -- The computer system, consisting of a Data General S-200 Eclipse central processor, a disk system, tape unit, CAMAC interface and several CAMAC crates, Tektronix 4010 and 4014 graphics interface terminals, and Versatek printer is complete and operational. The central processor has been augmented with 8k of additional core memory.

Diagnostics and Monitoring -- By using the fast CAMAC digitizer and associated software for data acquisition, we have recorded transient voltage and current signals from both the electron-beam supply and the PFN pulser during the electrical testing of the first DBM. A program is being written to record data and to perform calculations for the upcoming small-signal gain measurements.

To record the relative times at which pulsed power supplies and diverter spark gaps are triggered, we have designed a three-channel interface using CAMAC timing modules, which will convert the light pulse from a spark-gap discharge into an electrical pulse that actuates the time-interval modules. The light pulse is conducted to the interface circuit by means of a 50-m-long fiber-optic cable.

A separate microprocessor-based control system will monitor area interlocks, display the safety status of all areas, and enable operation of the various high-voltage power supplies. The hardware for this system is being fabricated. The operating procedures have been defined, and the program logic is being defined by using state-transition diagrams.

Controls -- The laser control subsystems, which will be operated through the computer, are the PFN, the spark-gap, the electron-beam, and the main-amplifier gas systems. Computer control is exercised with a special subprogram dedicated to the operation of a particular subsystem, called up in turn by a master program that synchronizes operation of the entire system. The PFN subprogram is complete and the program for the spark-gap gas system is nearing completion; the remaining programs are being written.

Target-Chamber System

The target-chamber system consists of the optical elements required to focus the eight laser beams onto the target, of an optical support structure for the optical system and the target, and of a vacuum vessel and pump system.

In our target-irradiation scheme, eight beams are pointed at the target through the corners of an imaginary cube whose center coincides with the target (Fig. 7). The critical optical elements, i.e., the off-axis parabolic focusing mirrors, have been

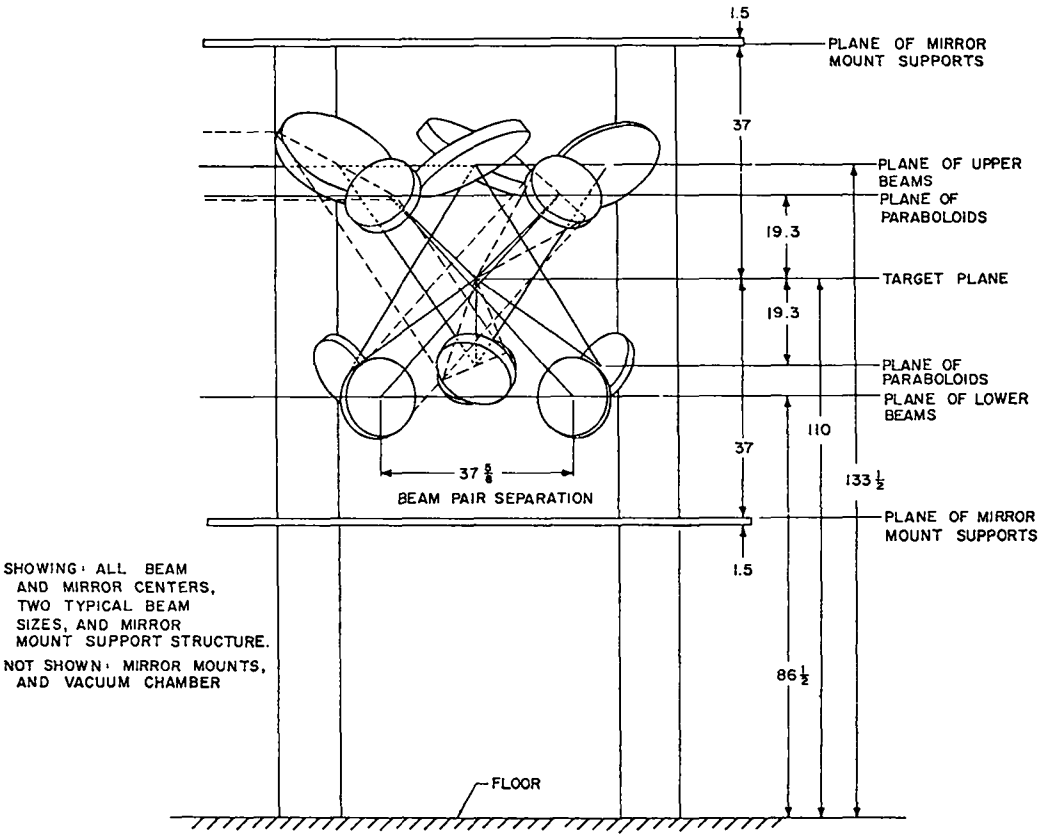

Fig. 7. Schematic of target optics system. All dimensions in inches.

designed (focal length, 68.5 cm; f-number, ~ 2.5) and are being procured. Because the optical system is rather compact, a 1/8th scale model of the target optical support structure is being built to verify component clearances.

The performance of aspheric optical elements could be degraded by even small beam misalignments; we are therefore studying the ability of the off-axis parabolas to produce satisfactory focused spots in the presence of misalignment. Preliminary results indicate that a misalignment of ~ 100 μrad (a value thought to be easily achieved with the alignment system) does not produce unacceptable degradation of the focal spot. A contract is being negotiated with Rocketdyne Corp. for an extensive design-and-analysis effort as well as for fabrication of the target-chamber system. This work includes optical sensitivity analysis; a ray-tracing analysis of the effect of spatial filters; structural design and analysis; and design and fabrication of the target optical-support structure, the target chamber, and the target-system mirror mounts.

Procurement of Optical Components

The design and specification for all optical EBS components is complete. The large-diameter mirrors are being fabricated at UCC's Oak Ridge Y-12 plant, in their micromachining facility. The flat mirrors will be made on the Moore machine and no delays in delivery are expected. Fabrication of the off-axis parabolas is being delayed to await completion of the upgrading of the Excello machine and installation of an on-line interferometric figure-determination system.

Fabrication of the 40-cm-diam by 7.6-cm-thick NaCl polycrystalline windows is in progress. Four have been made and are being shipped to us; a regular delivery of 1 to 2 per month is expected.

Vibration Analysis of the EBS Facility Floor

An extensive series of seismic measurements on the floor of the EBS facility has been completed. The results indicate that the floor is a reasonably stable optical platform with maximum displacements of 1.8×10^{-6} cm peak to peak over a frequency band of 5 to 60 Hz. These results were not affected significantly by building-equipment masses. Some wall-to-floor wind coupling exists. Empirically, the floor displacement, X (in inches), was found to be related to the wind speed, V (mph), by

$$X = 3.98 \times 10^{(0.0059\ V-7)} .$$

Beam jitter due to air-temperature fluctuations over the optical path lengths may require the use of beam tubes.

Safety System for EBS Building

The safety system for the 10-kJ EBS laser building is a microprocessor-based control system that will display the safety status and will control the access and interlocks in the building. This project will also test the susceptibility of the microprocessor hardware to the electromagnetic pulse interference generated by the laser. The system consists of an M-6800 microprocessor, of a control panel for operator input and display, of optical and CAMAC interfaces, and of various building interlocks. The single-task program, directed by the panel switches, will check all building interlocks; it will inhibit unsafe conditions, display the safety status, test itself, and provide a fail-safe output.

This project is 60% complete, with most of the hardware finished and the software defined. The system will be operational in July, 1976.

HIGH-ENERGY GAS LASER FACILITY (HEGLF)

Introduction

The objective of our High-Energy Gas Laser Facility Program (HEGLF) is to extend the present CO_2 laser capabilities to power levels at which fusion experiments can be expected to yield thermonuclear energy release in the range of scientific breakeven (defined as equality between the thermonuclear energy output and the laser-beam energy incident on target). The investigation of laser-fusion phenomena at these levels will provide more complete understanding of the physics involved and allow laser and target design-parameter requirements to be established with confidence. The program specifically calls for the construction of a

six-beam, 100- to 200-TW CO_2 laser (100 kJ in 1 ns or 50 kJ in 0.25 ns) and an associated target irradiation facility.

Norman Engineering Co. began Title-I work for the HEGLF in April 1976, with completion of this phase expected at the end of August. Cooperation between the architect-engineer and LASL has led to a more complete definition of the facility and associated supporting services. Studies by an independent firm, Mechanics Research, Inc. (MRI) provided additional insight into the problems of vibration introduced by background and cultural seismic noise, as well as vibrations initiated by mechanical equipment located within the building. As a result of the study by MRI, all floors of the facility supporting optical components will be laid on cut tuff rather than on backfill, and as much mechanical equipment as possible will be located in a separate mechanical-equipment building.

We have concentrated on analyzing and designing the power-amplifier modules and the laser train. Work on the power-amplifier modules was directed toward achieving uniform population inversion over the optical aperture by eliminating the adverse effects of magnetic pinching in the gas discharge and toward calculating the gain-length product and driver energy needed to produce the required output. In addition, we have analyzed several designs of electrical-energy storage modules for performance, efficiency, and reliability. Optical analysis and design studies developed sensitivity data on aberrations introduced by misalignment of the various telescopes which constitute the optical train.

As a result of our studies, we developed a prototype program to verify experimentally the analytical conclusions and to confirm from an engineering standpoint the design concepts before beginning procurement of the major laser hardware.

Prototype Programs

Gridded Cold-Cathode Gun -- A contract was let to Systems, Science and Software for studies of a gridded cold-cathode gun. The contractor is expected to verify, at full-scale geometry and beam energy, the concept of beam-current regulation in cold-cathode, large-area guns by adding a self-biasing grid between the cathode and the anode. The contract was to be completed by July 1976, but unanticipated difficulties in procurement have delayed completion of the work by two months. Preliminary tests at 350 kV showed that the concept worked. Efforts to achieve spatial and temporal uniformity, as well as to determine the range of grid control, are in progress.

Prototype Power-Amplifier Module -- We designed and have let a fabrication contract for a prototype power-amplifier module (PAM) that will allow verification of design criteria for gain coefficient, gain uniformity, and electrical efficiency. The prototype module will also address questions of optical stability in the presence of gain, including axial and azimuthal modes of parasitic oscillation.

Although previous designs such as the dual-beam module (DBM) have established the feasibility for a PAM of the size proposed, many new or different features are contemplated, and to a large degree are necessary, to obtain a viable 100-kJ system. For example, considerations of physical space occupied by the units and the type of optical elements that can be procured led to design of a cylindrical shape. However, the information gathered on details of large-volume discharges in the DBM is inadequate to create a design with the precision needed. Other features of the new PAM design include, e.g., an electron gun that is a cylindrical gridded cold-cathode unit. Gridded cold cathodes are relatively new and have, to date, been built only in planar geometry. Our current development contract with Systems, Science and Software covers the extension of this technology to cylindrical geometries of our size requirements. There remains, however, the further problem of integrating the cold cathodes with the complete PAM unit. Cost and efficiency considerations led to the selection of pulse-forming networks (PFNs) as the source of pulse power to drive the discharge, which requires that the impedances of the PFN and of the gas discharge be matched. The gas-discharge impedance, in turn, is controlled by the electron-gun output. At present, the uncertainties as to the influence of window structure and large discharge volume on effective gun output will require some trial-and-error adjustments to the electron gun.

The advantages of helium-free gas mixtures are well established in small devices. Their use in large devices promises improved performance and a substantial reduction in overall cost. However, helium-free mixtures require higher operating voltages and more difficult high-voltage engineering. While the voltages involved do not exceed those used by the electric utility industry, these aspects of the design must be tested before going into production.

Large discharge volumes inherently contain nonuniformities in the current and voltage distributions due primarily to nonuniformities in the ionization produced by the electron beam. The nonuniform gain may affect beam quality and may cause damage to optical elements in regions where local beam-energy excesses result from locally high gain. This problem has been addressed by calculations, but the uncertainties are too large ($\sim \pm$ 15%) to be acceptable, and direct experimental measurements are needed.

Calculations also indicate that magnetic fields produced by the gas discharge must be reduced by segmentation of the PAM into two or three axial sectors. The calculational difficulties are so great that we need a direct experimental approach to determine the optimal number of sectors.

Ideally, a prototype should be a full-scale device. However, considerations of cost, time, and experimental space have led to a program wherein the proposed unit will be full scale only in radial dimensions and about half scale in length. The gas discharge will not be created over the entire prototype, but rather over one fourth of it, reducing power-supply requirements by a factor of four.

Two modes of operation are contemplated: In the first, the discharge will fill the full length of the prototype module but only a quarter of the full annulus; whereas, in the second mode, the discharge will cover one-fourth the length but will encompass the full annular region. The first mode is intended to address problems of, e.g., high-voltage engineering, gain uniformity, gain standoff, magnetic-field effects (the remaining 270° discharge currents will be simulated by a low-voltage current source), and electron-gun performance. The second mode is intended primarily to investigate the possibility of a ring-mode parasitic oscillation. Table I lists major dimensional and operational specifications of the proposed unit.

TABLE I

SPECIFICATIONS FOR PAM PROTOTYPE

Active length, m	*1.3*
Full-size diameters, m	
Gun	*0.559*
Grid	*0.99*
Window structure	*1.42*
Anode	*1.98*
Anode-Cathode gap, m	*0.279*
Pressure vessel (central part), m	
Length	*2.23*
Diameter	*3.02*
Three full-size anodes, m	*1.30 by 0.25*
or	
Twelve quarter-length anodes	*0.325 by 0.25*
Operating conditions	
Helium-free gas mixture, torr	*1800*
Gain, cm^{-1}	*0.035*
Gain-length product	*4.55*
Energy input, J/liter	*180*
Main discharge:	
500 kV across 27.9-cm gap	
Current density, A/cm^2	*10*
Electron gun	
kV	*500*
kA	*5.8*

Controls: Primarily manual with minimum of interlocks to ensure operational safety.

As mentioned, the design of the prototype module is such that three sectors are excited to a gain-length product half that of the full module. To test for end-to-end parasitic oscillations, 45° folding mirrors are installed at one end to couple two adjacent sectors, simulating one full-length sector. Any problems due to reflections from anode and cathode structures will be identified and corrected. To examine ring modes, the three half-length sectors will be converted to twelve eighth-length sectors so that a full annulus is excited. This requires the same electrical pulser. Nonconducting, optically black vanes will be inserted between the anode plates to develop a technique for suppressing spiral-mode oscillations. The principal problems are electrical, and if arcing can be prevented, the vanes can be added to suppress spi-

ral parasitic modes. All optical designs for the PAM modules now include an off-angle input optic and focus with field stop to suppress the four-pass narcissistic parasitic mode discovered in the DMB.

The prototype module will be installed in a laboratory equipped with a 3-ton crane servicing an area large enough to accommodate the prototype. All components that need to be moved routinely can thus be handled. The laboratory is equipped with a screen room, and much of the basic support instrumentation is on hand. Only minor modifications to the existing building are anticipated.

We have begun to design the pulsed-power supply that will pump the prototype power-amplifier module. This network will be a Type-C Guillemin-Marx, similar to those built for the EBS, and similar to those being designed for the power amplifier. Because the prototype power amplifier is essentially 1/48th of a full 100-kJ system while the pulsed power supplies for the final power amplifier are being designed to drive 1/24th of the full system, the prototype design will not require the sophistication of the final system.

The oil tank has been designed, and bidding has been invited. The tank should be received by October, 1976 to be installed before the power-amplifier hardware arrives. The remainder of the hardware is being designed.

Design of the prototype module has been partially completed, with parts for the long lead-time chamber having been completed first for early fabrication bids. Anodes, cathodes, foil windows, grids, and insulator bushings are being designed according to present concepts of the components in the power amplifiers; any of these parts will be replaced with parts of improved design if test results disclose such needs.

High-Voltage Test Module -- The test module is a small electron-beam-controlled discharge system that will provide information on high-voltage breakdown before the prototype PAM is operational. This module will operate at full voltage (500 kV), but will not scale in dimensions transverse to the discharge. It may be used to obtain data on ionized laser-gas breakdown, bushing designs, cable terminations, and gas-discharge uniformity.

Because breakdown statistics and life data are important in such a test program, the pulsed power supplies must operate at a reasonable repetition rate. The gas-discharge pulser will be a 20-stage Marx generator, with an output capacitance of 0.035 μF and a peak voltage of 1 MV, and is designed for operation at a rate of 4 pulses/min at 1 MV and of up to 8 pulses/min at 500 kV.

The design of the test module has been completed and most of the hardware parts are in fabrication, with a completion date of early September 1976. The single, cylindrical pumping chamber contains an anode with a diameter of $\sim$ 25 cm and a foil-to-anode gap of $\sim$ 28 cm. A single, cylindrical electron-gun chamber is foreseen, whose cathode has the same diameter as the anode.

HEGLF Laser Design

Parameter Studies

Characterization of Helium-Free Gas Mixture -- We have prepared some gain-vs-time histories for CO_2 laser gas mixtures to assist in design tradeoff studies. In the parameter space of current density and electric field in the discharge, the gains predicted by our kinetic modeling code agree to within $\pm$ 5% with experimental data. A $4{:}1{::}CO_2{:}N_2$ gas mixture was used; absolute pressure was 600 torr. To convert the information to different pressures, the usual similarity laws must be applied, viz, current and electric field are multiplied by P/600, and the time scale is multiplied by 600/P. Results are shown in Figs. 8, 9, 10, and 11.

Gain Uniformity in Large-Aperture Amplifiers -- A calculational approach has been developed to predict the spatial and temporal gain nonuniformities encountered in large-aperture electron-beam-controlled CO_2 laser amplifiers. The spatial nonuniformity is caused by variations in discharge conditions wherein the electric fields and current densities vary throughout the discharge volume. Gain nonuniformity is normally attributed to the inability of the external electron beam to provide uniform ionization. Geometric design of the electrodes and magnetic-field effects are also involved. To improve our design capability, we have made an effort to calculate and to predict the performance of a given design.

The physics involved are relatively simple. We assume a steady-state, neutral, recombination-

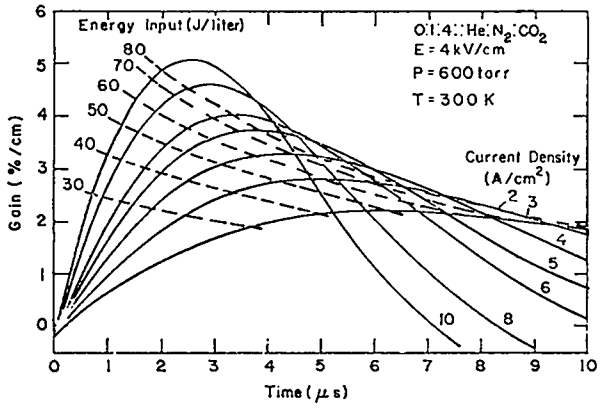

Fig. 8. Gain vs time for 0:1:4::He:N_2:CO_2 mixture at 600 torr, 4 kV/cm. Gas temperature, 300 K.

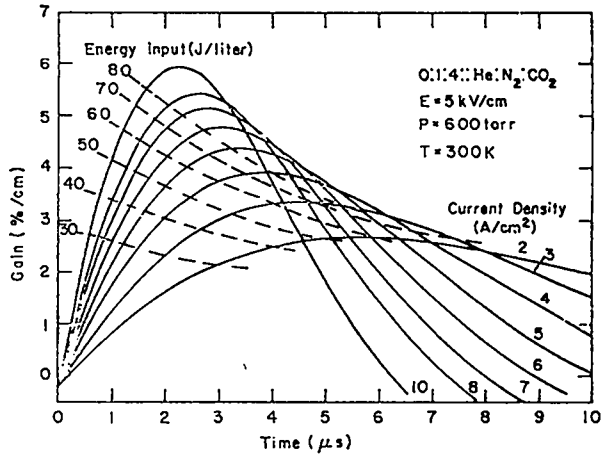

Fig. 9. Gain vs time for 0:1:4::He:N_2:CO_2 mixture at 600 torr, 5 kV/cm. Gas temperature, 300 K.

limited discharge with current flow accounted for by electrons drifting in the local field. The recombination coefficient and the drift velocity depend on the electric field. Current and electric-field distributions are then arranged in such a way as to meet boundary conditions, conserve charge, and accommodate the externally imposed ionization. Mathematically,

$$n_e = \sqrt{\frac{S(\vec{r})}{\gamma(E)}} \ , \qquad (1)$$

$$\vec{j} = e n_e \vec{v}_d(\vec{E}) \ , \qquad (2)$$

$$\nabla \cdot \vec{j} = 0 \ , \qquad (3)$$

$$\vec{E} = \nabla \phi \ , \qquad (4)$$

$$\phi \text{ fixed at boundaries} \ , \qquad (5)$$

where

n_e = electron density (electrons/cm^3),
$S(\vec{r})$ = external ionization (ion pairs/$cm^3 \cdot s$),
$\gamma(E)$ = field-dependent recombination coefficient ($cm^3\ s^{-1}$),
$\vec{v}_d(\vec{E})$ = field-dependent drift velocity (cm/s),
$\vec{j}$ = current density (A/cm^2),
e = electronic charge .

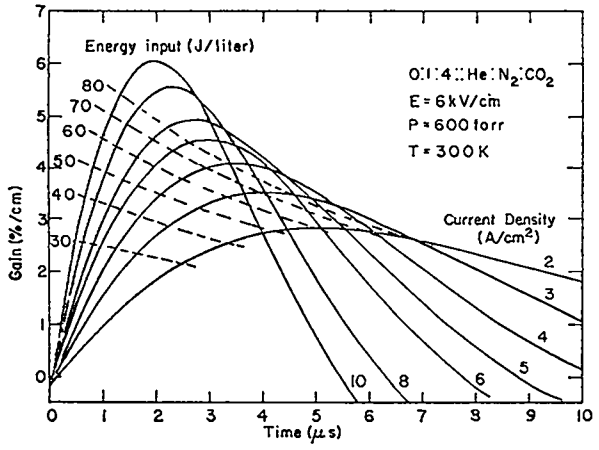

Fig. 10. Gain vs time for 0:1:4::He:N_2:CO_2 mixture at 600 torr, 6 kV/cm. Gas temperature, 300 K.

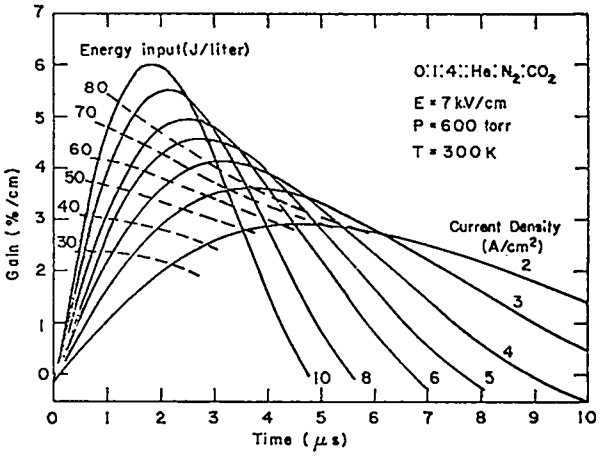

Fig. 11. Gain vs time for 0:1:4::He:N_2:CO_2 mixture at 600 torr, 7 kV/cm. Gas temperature, 300 K.

The external ionization $S(\vec{r})$ is determined by a Monte Carlo calculation which permits consideration of externally applied magnetic and electric fields.[1,2] However, a major difficulty arises in characterizing the primary electron beam injected into the discharge volume. Usually it is assumed that the uniform, monodirectional, monoenergetic beam illuminates a fixed aperture. In reality, the beam is often spatially nonuniform and directionally dispersed by magnetic effects. With cold-cathode electron guns, a further complication arises from the time variation of current inherent in gun operation.

Given these relative spatial variations of $S(\vec{r})$, a two-dimensional calculation is performed next to obtain a self-consistent solution to Eqs. (1) through (5). The resulting distributions of $\vec{J}$ and $\vec{E}$ are then used as input for the final calculational step, which involves the computation of the small-signal gain at line center of the P(20) line of the 10.4-μm CO_2 laser band.

The results of such a calculation for the experimental parameters of the DBM of the Two-Beam System are in excellent qualitative agreement with measured values of gain and agree to within $\pm$ 15% in absolute value throughout the aperture.

High-Voltage and Pulsed-Power Engineering

Pulsed Power Supplies for Pumping Chamber -- The approximate requirement for the gas pulsers is the delivery of 2.5 MJ at 500 kV in 1.5 μs. To do this efficiently, some pulse-shaping will be required; also, some parallel units will have to be used. The minimum number of parallel units is determined by the circuit used, by pulse length, switch capabilities, and by the maximum energy per capacitor that the manufacturers can attain. We had concluded previously that the Type-C Guillemin Marx network has the greatest flexibility and the least stringent inductance requirements. A Type-C Guillemin-Marx circuit is shown in Fig. 12. The loop inductance, L_s, is one of the limiting factors, because it tends to slow the rise and fall of the pulse. Loop inductance may be reduced by folding the generator, as shown in Fig. 13, with the single fold having the lowest inductance. However, folding in the Type-C network has the disadvantage that mutual inductance between L_1 in the first stage and L_2 in the last stage (Fig. 12) will affect the shape of the pulse. The pulse-shaping inductors may be shielded from each other by putting C_1 and C_2 with their associated inductors in a capacitor can, as illustrated in Fig. 14. The high-voltage network may now be formed by Marxing these "pulse-forming capacitors." Discussions with manufacturers indicate that such units can be built with energy up to 10 kJ and a discharge time as short as 1 μs.

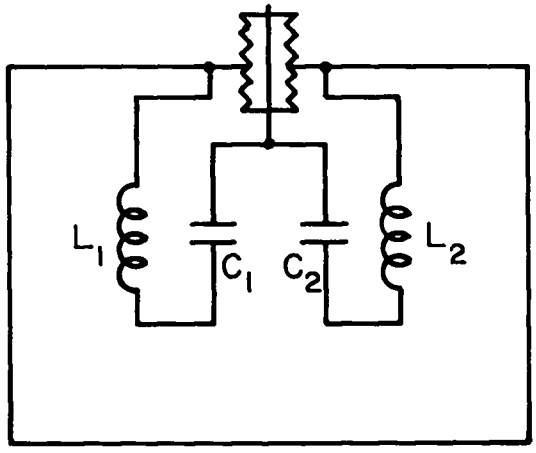

Fig. 12. Type-C Guillemin-Marx circuit.

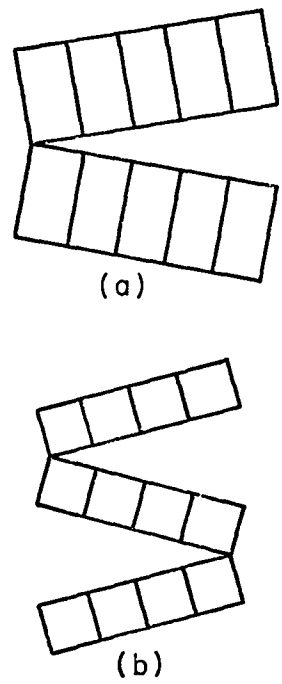

Fig. 13. Folded Marx generator configurations.

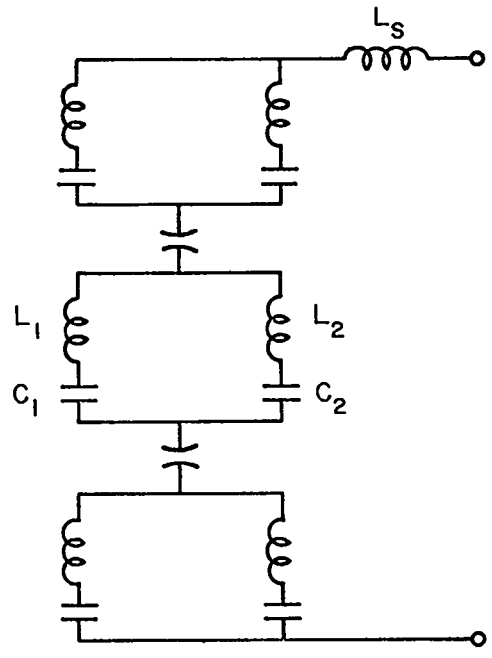

Fig. 14. Schematic of pulse-forming capacitor for Type-C Guillemin-Marx circuit.

For the range of pumping-system parameters, the number of parallel PFNs is either 24 or 36 (one for every six anodes or four anodes, respectively). The incremental cost per PFN is ~ $40 000, covering tank, oil, support structure, circuit connections, local trigger generator, local control system, assembly, and test. A shorter pumping pulse, which requires 36 PFNs, will increase the cost of the energy storage system by ~ $500 000.

Energy Transmission System -- Several means have been considered for transporting the energy from the energy storage capacitor to the laser amplifiers: polyethylene coaxial cables, high-pressure gas-insulated coaxial lines, and solid dielectric insulated strip lines. Because polyethylene coaxial cables are commercially available, they are economically most attractive. Such cables are used for high-voltage ac power transmission, but life data for pulsed operation are not available. However, scaling laws allow us to estimate the electrical fields for reliable performance. The lifetime of solid dielectric systems (capacitors) is related to voltage by

$$L \propto V^{-n}, \qquad (6)$$

where n can be between 5 and 8.

A typical ac cable has an electric field at the center conductor of 250 V/mil and must last at least ten years, or 2×10^{10} cycles at 60 Hz. According to the above scaling law, this cable would last 10^5 to 10^7 shots at 1 kV/mil. Thus, a conservative design figure for the cable would be 1 kV/mil, or 4×10^7 V/m.

We will perform accelerated tests on coaxial cables using a low-energy Marx generator, at 0.5 Hz up to 1 MV, to determine the scaling parameters and to estimate life.

Electron-Gun System -- The energy requirements for the pulsed electron-gun power supplies are relatively light. The power requirements for the electron gun for one power amplifier module are about 10 kA at 500 kV in a 3-μs pulse. The energy delivered is ~ 15 kJ, and the impedance is 50 Ω. These specifications are compatible with pulse transformers. Discussions with manufacturers of high-voltage pulse transformers indicate that a transformer with leakage inductance of 50 μH (viewed from the secondary) can be built with standard technology and oil insulation. Such units will provide a risetime of ~1 μs. Lower inductance can be attained by using solid insulation and thus closer spacing. A pulse transformer will allow energy storage, switching, and transmission at relatively low voltages (50 to 100 kV), with attendant increase in reliability and maintainability.

Optical Engineering

Optical Analysis -- The optical-analysis effort in support of the HEGLF program aims at developing optical designs and computer codes for the evaluation of various parameters of the HEGLF optical systems. Code development has continued on FERMAT, our geometric-optics ray-tracing code, to extend its capabilities to nonstandard optical elements such as the two-mirror Schwarzschild aplanatic focusing systems and linear axicons (i.e., mirrors that are full surfaces of revolution). The second generation of this code, FRESNEL, is capable of calculating the diffraction field near the focal point.

Applied to a specific problem these codes can determine, e.g., the relative sensitivity of vari-

ous focusing systems to misalignment of the input beam. Using FERMAT, a bundle of rays is passed through the system and the rms spot size in the focal plane is determined. As various perturbations are applied, aberrations cause the spot size to increase. The magnitude of unacceptable perturbations can thus be found. The study indicated that the aplanatic focusing system could offer diffraction-limited performance with misalignments of the input beam on the order of 10^{-3} rad. These misalignments were one-hundred times larger than those that could be tolerated in some off-axis parabolic focusing systems considered. Similar studies of power-amplifier optical systems have shown variations of several orders of magnitude in the alignment tolerances. Such information is critical when choosing a practical design.

In a related field, the ray-tracing codes can be used to determine the sensitivity of the position of the focal spot to misalignment of elements in the optical system. Such an analysis is important to determine the spot "jitter" caused by environmental microseismic effects. We aided MRI, a consultant on this problem, by verifying that the correct coefficients were input for these sensitivities.

Some optical designs being considered for HEGLF reduce the size of the output beam of the power amplifier. This allows the use of a smaller vacuum tube between the amplifier and the target chamber, and keeps the size of the turning mirror within fabrication constraints. We compared the performance of a pair of linear axicons to that of a confocal parabolic pair when these systems are used to reduce the dimensions of a collimated beam. The output beam was focused with an idealized focusing system, and the rms spot radius of the ray bundle was used as the merit function of system performance. This study revealed that the misalignment tolerances of axicon pairs are small, both with respect to each other and with respect to the input beam. However, axicons are probably much easier to fabricate at UCC's Oak Ridge Y-12 facility than confocal parabolic mirrors, because they require only a single axis of motion in fabrication.

Mechanical Design and Vibration Analysis -- The vibration analysis contracted to MRI was completed. The study indicates that the stability of the optical system would be affected more seriously by the mechanical equipment of the building (e.g., heating, ventilating, and air-conditioning systems) than by the vibrations natural to the site (e.g., subseismic earth motions and local vehicular traffic). These conclusions aid us in pinpointing the physical areas in which to concentrate on vibration isolation and damping.

The study also identified some supporting structures in the optical system that will require stiffening: the supports for the target-area turning mirrors and for the power amplifiers. A preliminary design on the turning-mirror support structure has been initiated, using the MRI results on the initial design as a basis for comparison. Finite-element analyses have been prepared for the lower structure (x-y translation stage), the upper yoke, and the gimballed ring for the mirror mount. These analyses allowed us to assess the stiffness characteristics for the individual structural members, together with the bearing and actuator elements that provide pitch and yaw. The natural frequency and mode-shape characteristics for the upper structure were determined and compared with the results for the MRI-improved baseline. For the yoke substructure, we obtained a fundamental frequency of 40 Hz as compared to 36 Hz for the improved baseline structure.

As a next step, we will combine this structure with the other substructures and will repeat the determination of frequencies and mode shapes. The structural characteristics will be evaluated for both a massless support structure (350-kg mirror) and for the structure weight consistent with present design.

Mirror Design -- We have begun to design the large mirrors for the HEGLF optical train. Major constraints are:

- Weight limitations. The weight of mirror blanks plus checking fixture for the Y-12 Excello lathe is limited to 680 kg.
- Distortions. Distortion of a mirror due to its overweight while held stationary in the horizontal lathe, while mounted in a frame for testing, and while mounted in HEGLF must be held to dimensional toler-

ances of ~ 10^{-7} m. Distortions of the mirrors due to centrifugal forces while turning must be axisymmetric.

Cost eliminates many materials, such as beryllium, that are highly desirable as to their thermal distortion, rigidity, and stiffness-to-weight ratio. Our studies show that lightweight metal mirrors made from, e.g., aluminum alloys, copper-base alloys, stainless steels, and low-expansion alloys such as Invar, will not be too costly. The weight limitation of 680 kg indicated above includes fixtures to hold the mirror blank while turning, as well as the mirror. If we assume that the machined mirror weighs about one half of this weight, we can calculate the void fraction we need to achieve a 340-kg mirror. Comparative results are summarized in Table II.

TABLE II

VOID FRACTION REQUIRED TO ACHIEVE 340-kg MIRRORS

	Aluminum	*Copper*	*Stainless Steel*
Weight of solid ring, kg	*1300*	*4300*	*3800*
Void fraction for 340-kg ring	*0.70*	*0.92*	*0.90*

Mirror blanks can be fabricated from brazed or welded box structures. Mirror faces can be clad with copper either by electroplating or by brazing copper sheet to the substrate. Our investigations show that industrial facilities and expertise are available for all aspects of blank fabrication.

The basic configuration for an annular mirror, such as the rear mirror in the power-amplifier module, is a box structure with a stiffened face plate and diagonal stiffeners. This arrangement approaches an optimum stiffness-to-weight ratio for all bending modes. Several methods for supporting a ring structure with a horizontal axis have been studied; two show allowable distortions. These designs are illustrated in Figs. 15 and 16. In Fig. 15 the ring is supported vertically by equispaced tangential springs, which apply tangential, sinusoidally varying forces to the centroidal circle of the structure. With 12 or more springs, calculations show negligible distortion. Figure 16 illustrates support by vertically acting, equally loaded springs attached to equispaced points on the centroidal circle. With 12 or more springs, distortion is even less than with tangential springs. Axial restraint in both arrangements would be at three equispaced points on the mirror.

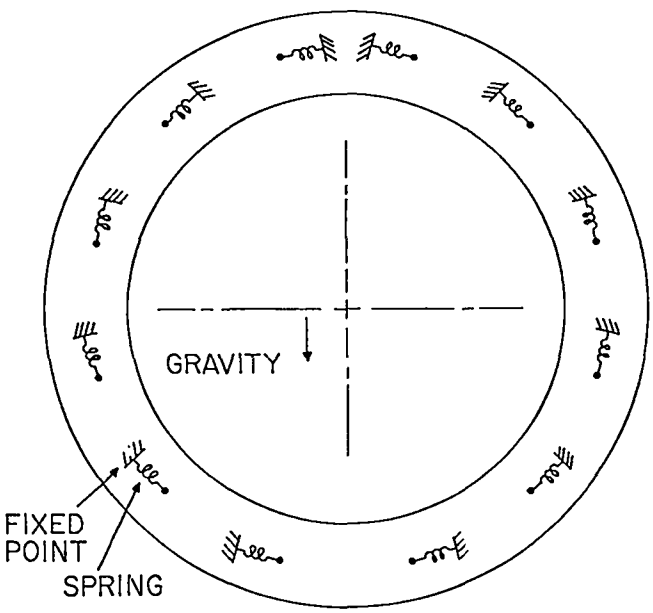

Fig. 15. Schematic of tangential spring support for mirrors.

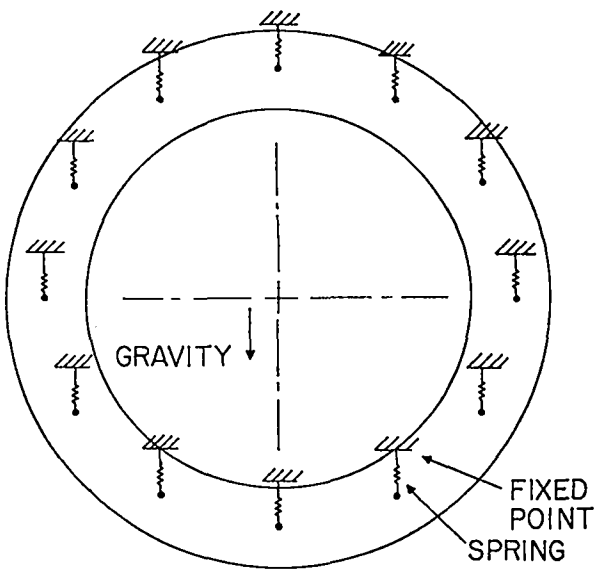

Fig. 16. Schematic of vertical spring support for mirrors.

Mirror chucking in the Y-12 Excello lathe is under study. The static-distortion problem is complicated by vibration and by differential centrifugal expansion. For example, at the preferred spindle speed of 3.3 rps, the inner radius of an annular steel blank will expand $\sim 12 \times 10^{-6}$ m whereas a solid disk with an outer diameter of 1.4 m will expand only 1.2×10^{-6} m. The chucking problem has not been analyzed in sufficient detail to suggest a solution.

Large-Mirror Fabrication -- The number and size of optical components for laser-fusion systems present a procurement problem, particularly under the time constraints imposed by scheduled completion dates. The components required for HEGLF are large; the largest power-amplifier mirrors are 2 m in diameter. A typical beam line will incorporate at least six mirrors with diameters larger than 1.4 m, and there are six beam lines. Given these sizes and time constraints, we have actively supported the diamond-turning development program at UCC's Y-12 plant. We intend to develop this technology to such a state that it can be used in the fabrication of large mirrors. In addition to providing an efficient production technique, diamond-turning also provides a flexibility not found in conventional fabrication methods: axicon-type components can be turned, as demonstrated in the Air Force laser programs.

Several machine capabilities have been discussed earlier (see, e.g., LA-6245-PR). Briefly, two machines are available: The Moore lathe with a diameter and weight limit of 66 cm and 180 kg, respectively, and the Excello lathe with corresponding limits of 198 cm and 680 kg. Our mirror program requires more than one machine to provide the required production capability. Consequently, special emphasis is being placed on upgrading several Excello machines. The first of them is nearly complete as demonstrated in Fig. 17, which is a recent photograph of an elliptical 198-cm-diam test blank mounted and turned on the Excello lathe.

Control of the surface figure could be improved if the figure were determined while the mirror is still mounted on the machine. The Optical Sciences Center of the University of Arizona and Y-12 are therefore developing in situ interferometric methods that will determine the surface figure after turning. Analysis of the interferograms will provide a correction signal that will be entered into the machine-control computer; recurring machine errors can thus be determined and eliminated. The system will be tested in the production of 12 off-axis parabolas used in the target chamber of our Eight-Beam System.

Deformable Optics -- Each optical train in HEGLF contains about 75 optical surfaces. To optimize the energy on anticipated target configurations, individual surface figures must be controlled to tolerances marginally achievable with diamond turning. We wish to preserve the design and fabrication flexibility offered by diamond turning; we are therefore investigating the use of deformable mirrors to provide wave-front correction and thus to minimize system aberrations. The problem of deformable optics for use at a wavelength of 10 μm has been addressed successfully in several Air Force-sponsored programs. Their requirements are more severe than ours, and their system re-

Fig. 17. Elliptical 198-cm-diam test blank mounted and turned on the Excello lathe.

sponses must be fast, whereas ours are effectively steady state. Based on Air Force experience, deformable optics provide an attractive alternative to conventional polishing in accommodating a reasonable number of errors.

NaCl Windows -- Polycrystalline NaCl or KCl, and ZnSe are prospective window materials for use in HEGLF. Based on materials technology, damage thresholds, and cost, we have selected NaCl. At present, 40-cm-diam polycrystalline NaCl windows are in use in the TBS and will also be employed in the EBS. Our experience indicates that the segmented, 12-windowed, annular structure envisioned for HEGLF is feasible. Each of the 12 windows is roughly equivalent to a 40-cm- diam window; however, present production capability for these large windows is incompatible with the scheduled completion date, and we are investigating methods to increase production.

The laser-system design is constrained by the damage threshold of NaCl. We have selected an average flux density of 2 J/cm^2 for nanosecond pulses based on experimental data obtained several years ago. Recent similar measurements with a well-characterized beam on present-day materials indicate peak damage fluxes of > 6 J/cm^2 for uncoated NaCl and of > 8 J/cm^2 for AR-coated NaCl. Diffraction effects in the power-amplifier system could increase peak intensities to about three times the average intensity. We could therefore increase our design value of 2 J/cm^2 somewhat by installing AR-coated materials, provided that beam focusability is maintained.

Instrumentation and Control

Microprocessors -- The computer control system for HEGLF will consist of a supervisory minicomputer in the control room and of microprocessors throughout the facility. Each multiprocessor will handle one or two dedicated tasks. These tasks include communications to the supervisory computer, data acquisition, control, sequence timing, and system-parameter monitoring.

Two software development stations are being established to support microprocessor development. The first station consists of a stand-alone microcomputer having the capability of generating M-6800 object tapes from a mnemonic source code and to edit any source code with a line and character editor. This station is operational, and several small codes have been written and assembled on it. One of these codes is a test-diagnostic program written to test the memory of the station.

The second software development station consists of a terminal connected by telephone to a PDP-10 computer at another location. The PDP-10 contains a high-level language for microprocessor code development, which was adapted for the M-6800 microprocessor from IBM's PL/1 language. The high-level code should greatly increase the coding efficiency because each of its statements is usually the equivalent of ten to twenty assembly-language statements. The code includes a relocatable linking loader which assembles a set of separately compiled, relocatable programs into a single, absolute one.

A stand-alone programmable read-only memory (PROM) programmer was designed, which provides programming capability for Intel's 2708 and 2404 PROMs. The PROM is the memory device in which the microcomputer's program will reside. After a code is written and checked out it is transferred into a PROM for implementation in the system. The PROM programmer is the device that transfers the code to the PROM. The programmer contains an M-6800 microprocessor and firmware (a program loaded in a PROM) that controls the PROM programming. The firmware transfers the object code from a cassette tape into the PROM programmer and then controls the programming sequence for programming the PROM. The contents of the PROM are checked for errors after the programming operation.

Fiber Optics -- The HEGLF control system requires low-cost fiber-optic data and communication links of high reliability. Many components and circuits for these data channels have been evaluated.

In its earliest use, fiber optics provided an optically coupled timing interface in the TBS. Obviously we must know when the power supplies are discharged during laser operation. However, because the stored energy is discharged through gas gaps, which convert the electrical signal to light, it is only necessary to conduct this flash of light to a screen room and to reconvert it to an electrical timing pulse. This is done with a fiber-optic

cable ~ 50 m long and with a PIN diode-amplifier combination. A four-channel interface between fiber optic and timing pulse has been built and is being tested. Also, a fiber-optic monitor of similar design is being used in the EBS.

The HEGLF fiber-optic communications receiver circuit has been tested over a 50-m-long bundle and over a short, single, optical fiber. Operation was satisfactory with a signal-to-noise ratio of ~ 8 dB. Improved connectors and the use of low-loss fiber will improve this ratio to ~ 20 dB. The cost of a 50-m-long data link between these components and circuits is less than $150.

Serial Bus Stepping-Motor Controller -- We have designed a stepping-motor controller which uses an 8-bit serial-coded word for its stepping commands. The controller accepts the coded command serially transmitted either over a pair of wires or over a single fiber-optic cable. The serial configuration (as compared to a parallel bus) greatly simplifies the cabling of multiple stepping-motor systems.

The serial-to-parallel, parallel-to-serial conversion and error checking of the coded command are accomplished with Motorola's asynchronous communications interface adaptor, MC-6850. A logic circuit decodes each command and steps the motor either clockwise or counterclockwise as determined by one bit in the code. The other seven bits are used to select a given motor on the serial daisy-chain bus. In this manner, 128 motors can be controlled on a single bus.

Immediately after receipt of command, the addressed controller will transmit an 8-bit coded word confirming the received command and transmitting the limit-switch information from that motor.

HEGLF Building Design and Construction

Introduction -- Five buildings will house the HEGLF laser system and related activities. These five buildings will be located near existing laser facilities and are briefly described as follows:

Laser Building -- This building includes a large, open laser hall in which the six power amplifier modules are located; a basement for the optical front end; a control room; machine and high-voltage shops; target-preparation, optical, and electronic laboratories; and operations offices.

Target Building -- This building houses the target chamber, turning mirrors, and target diagnostic equipment. Six-foot-thick normal concrete walls and a 5-ft-thick roof provide the shielding against anticipated neutron fluences. Artists' renditions of this building as well as of the laser building are shown in Figs. 18 and 19.

Mechanical Building -- This building consolidates most of the mechanical equipment required for heating, ventilating, air conditioning, and building services for both the Laser and the Target Buildings.

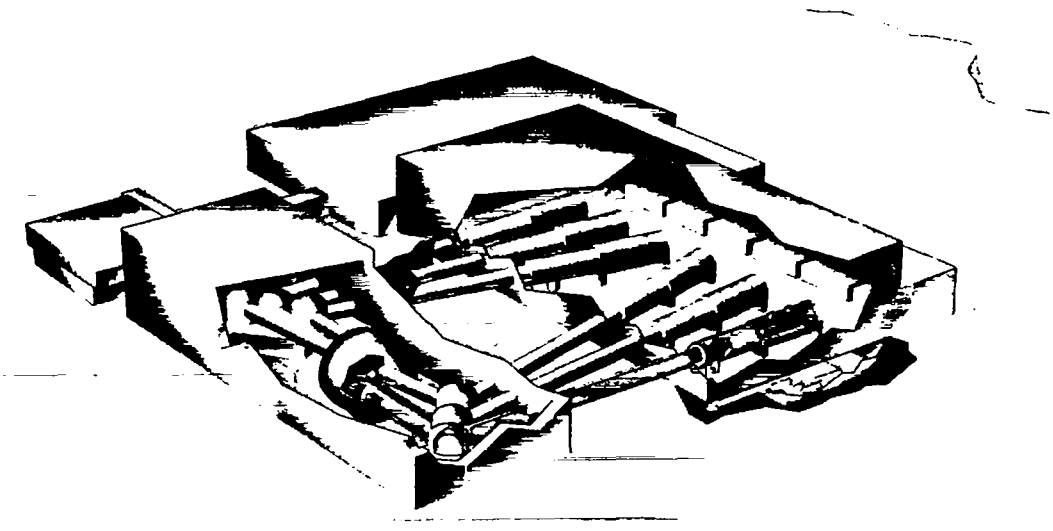

Fig. 18. HEGLF conceptual layout.

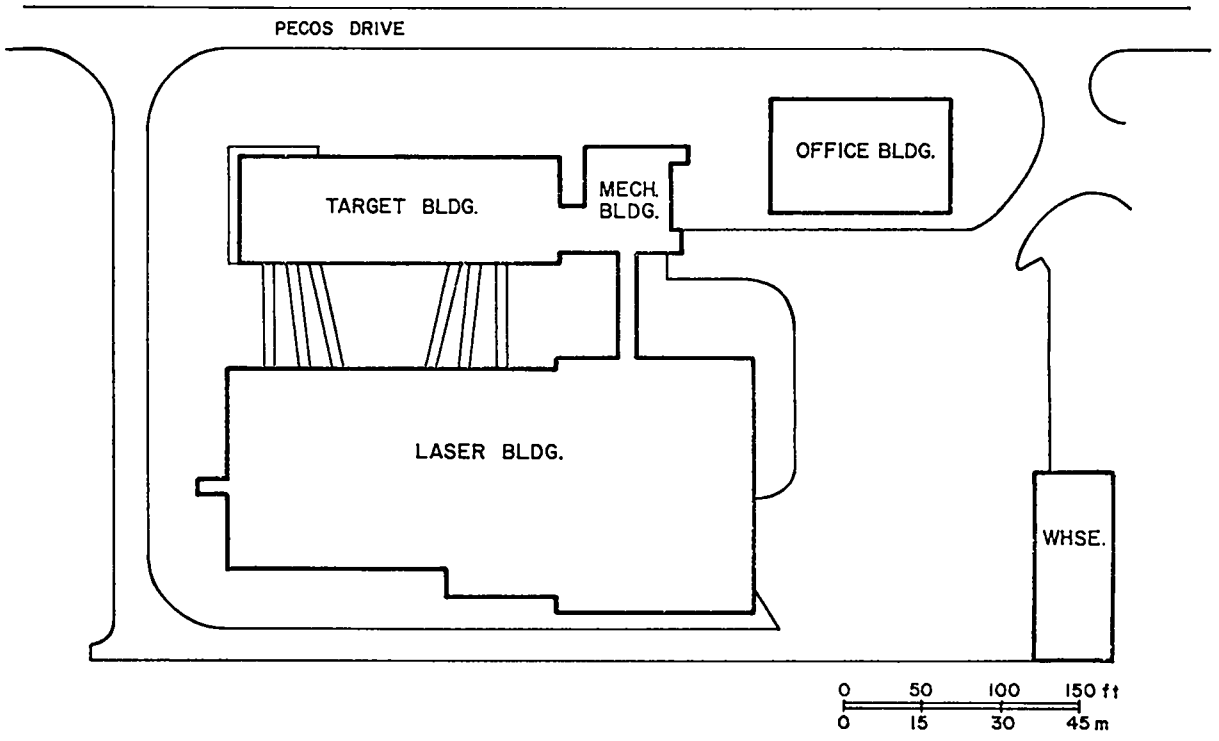

Fig. 19. HEGLF site plan.

Office Building -- Office space is provided for the 35 persons directly concerned with operation of, or experiments in, the facility.

Warehouse -- This building has 6000 ft^2 of unheated storage area.

Description of Function -- Details of the laser and target buildings are shown in Figs. 20 and 21. The optical beam proceeds as follows. A single, short pulse is generated in the front end (basement) room of the target building, is amplified, and is split into six individual beams. Each of these six beams is then amplified further, is steered through a tunnel below its power amplifier, and is turned by a mirror in a manhole upward to the power-amplifier input optics. The input optics expand the beam to the power-amplifier diameter and direct it through the amplifying medium to the back reflector. After back reflection the beam again traverses the amplifying medium and continues beyond the input optics through the amplifier salt windows to a pair of beam-compression mirrors located in a vacuum. From the compressor the beam travels down the evacuated, buried beam line to the turning-mirror chamber in the target building and is directed to the focusing optics inside the target chamber. An aplanatic pair of mirrors and a folding mirror focus the beam onto the target.

The 24 PFNs shown at the rear of the power amplifiers are triggered by the Marx high-voltage networks which supply electrical energy to the power amplifiers. Not shown in the figures are the 24 coaxial cables that connect each power amplifier to four PFNs. The laser hall is serviced by an overhead crane.

The control room is the point from which all laser-system control is exercised for normal shots. There are two computers in the room: one for laser-system control and the other for target diagnostics. Data links between various parts of the system and the control room are, for the most part, provided by fiber optics.

The optics laboratory will be used for receiving and inspecting optical components, assembling mirrors in their mounts, checking mirror drives, and for maintenance of optical components that cannot be performed in place. It has partial crane coverage.

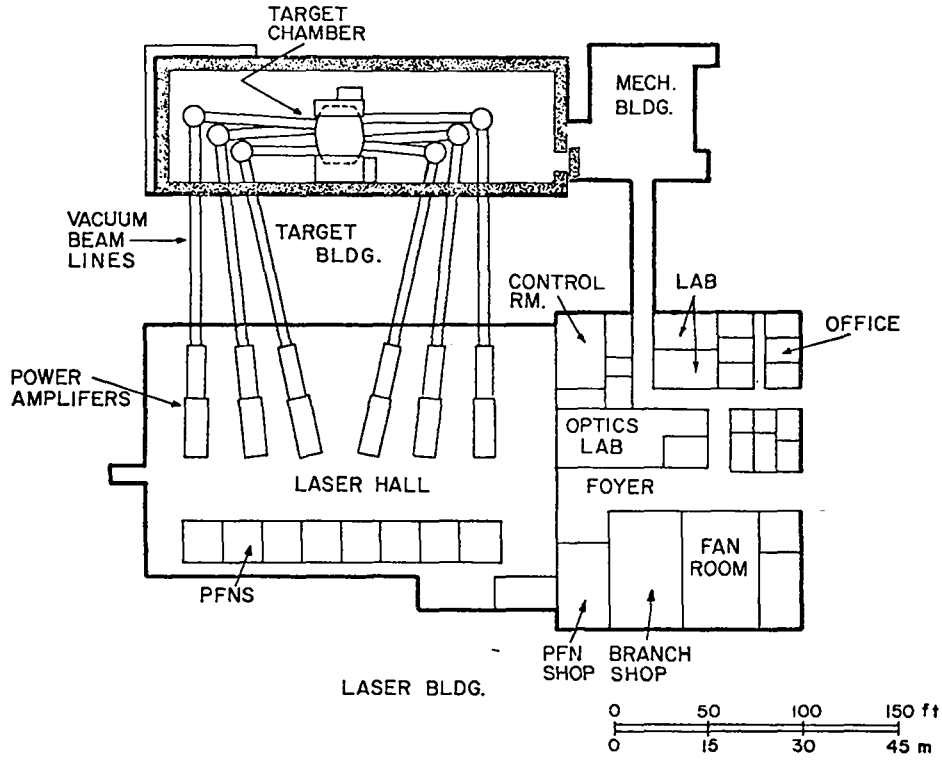

Fig. 20. HEGLF floor plan.

The branch shop is a machine shop with a normal complement of medium-size machine tools for maintenance of mechanical components. It has partial overhead crane coverage.

A PFN shop will allow maintenance of high-voltage components, which are primarily the power-amplifier PFNs. Malfunctioning PFNs will be replaced by operable ones and moved on air pallets from the laser hall to the PFN Shop. This shop has full crane coverage.

The electrical and electronics shop will be used for maintenance and some development of electrical and electronic components and systems.

The target building, in addition to housing the target chamber, beam-line segments, and turning-mirror chambers, makes space available near the target chamber for experimental operations, for storage of beam-line segments and target-chamber heads during maintenance operations, and for a target diagnostics screen room.

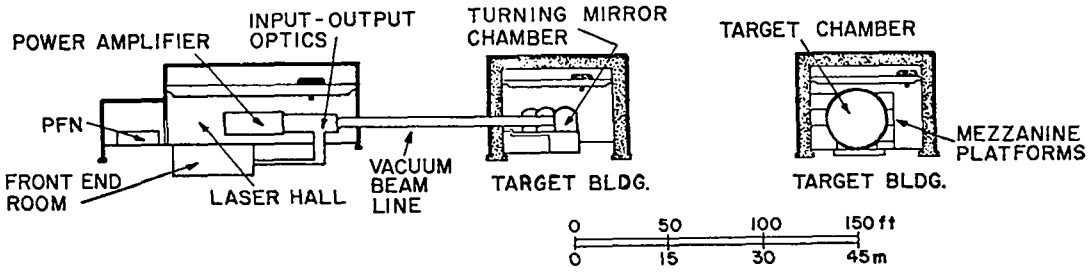

Fig. 21. HEGLF vertical section.

Environmental Control -- Special provisions are made for control of environmental factors in various areas of the facility.

- Temperature: Maximum seasonal range in the laser and target buildings is 68 to 78°F. Maximum departure from the set point in the front-end room and optics laboratory is ± 1°F and in the laser hall and target building is ± 2°F.
- Humidity: A relative humidity of < 40% will be maintained in the front-end room and in the optics laboratory.
- Air Cleanliness: Well-filtered ventilating air will circulate in the laser and target buildings. Class-100 000 conditions will be established in the optics laboratory.
- Vibration: Vibration will be controlled to the extent that optical pointing and focusing requirements can be met.

Architect-Engineer -- A pre-Title I study was completed in June, 1975, by the architect-engineer, Norman Engineering Co., Los Angeles, CA. This study delineated the major features of the site, buildings, and services and resulted in a cost estimate believed to be correct to within ± 15%. The account of the facility in semiannual Progress Report LA-6245-PR was based on this pre-Title-I study. However, since then, several changes have been made either to reduce costs or to satisfy different technical requirements. Major changes are:

- Substitution of thicker concrete walls and of a concrete ceiling for earth covering as neutron shielding in the target building.
- Addition of a mechanical building to house most of the mechanical functions previously to be accommodated in the laser and target buildings.
- Enlargement of the optical laboratory.
- Addition of a PFN maintenance shop.
- Additional crane coverage in several areas.

Shielding -- The buildings will be shielded as needed to protect site personnel as well as the general public outside the immediate site boundary. Shielding against bremsstrahlung radiation from the power-amplifier electron guns is relatively straightforward and will be provided by normal concrete walls and by excluding all personnel from the laser hall during electron-gun firings.

Shielding from neutrons and from induced gamma rays is a difficult design problem. The first step toward such shielding was made by separating the laser and target buildings and transmitting the laser beam through buried beam lines. The HEGLF Monte Carlo neutron-shielding studies required a significant effort before we obtained meaningful results, with acceptable variances and within reasonable computing times. The target building geometry was described in realistic detail and a calculation was performed to determine the external neutron doses for an all-concrete (2.33-g/cm^3) shield. Sidewalls of 1.83 m (6 ft) and a 1.52-m (5-ft)-thick roof were specified as shielding. For a neutron source of 9 x 10^{19} n/yr, the neutron doses at the shield-wall surface and at a distance of 33.5 m (110 ft) were 0.65 and 0.064 rem/yr, respectively, including both the direct and the skyshine components. One-dimensional (spherical) transport calculations were also made for a 1.83-m-thick ordinary concrete shield, which predicted both the neutron and the gamma-ray doses external to the shield. We used the ratio of neutron-to-gamma ray dose thus obtained to infer a total dose (neutrons plus gamma rays) from the Monte Carlo results. From this ratio, the total doses at the wall surface and at a distance of 33.5 m were 1.1 and 0.11 rem/yr, respectively. Work is in progress to examine the streaming of neutrons through the laser flight tubes and their effect on doses at the control room and in other occupied areas adjacent to the power-amplifier area in the laser building.

Preliminary calculations have provided some indication of the activation levels to be expected in the target building. We computed the radiation dose at 1 m from 1-cm^3 samples of material irradiated at a distance of 0.305 m from a pulsed source of 4.5 x 10^{17} 14-MeV neutrons. Dose rates from samples of 304 stainless steel, 6061 aluminum, and pure copper vs shutdown time are shown in Table

TABLE III

ACTIVATION OF MATERIALS IN HEGLF[a]

Shutdown Time	Activation (rem/n cm^{-3} at 1 m from sample) 304 Stainless Steel	6061 Aluminum	Pure Copper
0	4.28E-04[b]	3.48E-03	1.48E-02
1 h	3.20E-04	2.16E-04	2.83E-04
5 h	1.13E-04	1.41E-04	2.95E-05
10 h	3.28E-05	1.12E-04	2.03E-05
1 d	3.30E-06	5.84E-05	9.15E-06
2 d	1.31E-06	1.93E-05	2.52E-06
5 d	6.91E-07	6.98E-07	6.73E-08
7 d	5.93E-07	7.97E-08	1.88E-08
30 d	4.01E-07	2.12E-09	1.47E-08
50 d	3.20E-07	1.77E-09	1.46E-08
365 d	5.78E-08	6.13E-10	1.31E-08

[a] *Irradiation by pulse of 4.5 x 10^{17} neutrons; sample was located at 0.305 m from source.*

[b] *Read as 4.28 x 10^{-4}.*

III. Gamma-ray transport problems were also investigated to obtain an estimate for the dose rates external to the target chamber after a 14-MeV neutron pulse of 4.5 x 10^{17}. Assuming one pulse every two days, we found that the dose rate after ten pulses was 6 mrem/h at 1 m and one day after shutdown. The corresponding values for 100 and 1000 pulses were 20 and 30 mrem/h, respectively.

CO_2 LASER TECHNOLOGY

Introduction

Each of our CO_2 laser systems described earlier represents a significant advance in the state of the art of reliable CO_2 laser subsystems, components, and diagnostics. The design, construction, and improvement of the systems require, therefore, basic support of CO_2 laser technology. Some important areas are: the development of short-pulse multifrequency oscillators, amplifier optimization, development of subsystems for the prevention of system self-oscillation and removal of prepulse energy, improvement of the transverse profile of the amplified laser pulses, and basic measurements, e.g., of the optical damage thresholds in system components.

Oscillator Development

General -- Future laser-fusion target-interaction experiments at 10.6 μm will require subnanosecond pulses. We are therefore actively pursuing the design, testing, and construction of a 250-ps oscillator system capable of operating on multiple vibrational-rotational frequencies of the CO_2 molecule. This short-pulse requirement has led to the development of new methods of short-pulse generation in gas lasers and of techniques for obtaining multifrequency performance from CO_2 laser systems. Results have been most encouraging; we are now able to generate temporally smooth pulses containing a single rotational line or containing several rotational lines in one or both bands of the CO_2 laser. This multifrequency capability is essential for efficient energy extraction by subnanosecond pulses in 1800- to 2000-torr CO_2 amplifiers. Related results in the generation of ultrashort (50-ps) pulses by optical free-induction decay (FID) are discussed later in this section.

CW Smoothing-Tube-Stabilized Single- or Multiline Oscillator -- The typical output from an atmospheric-pressure CO_2 laser contains considerable temporal structure often described as self-mode-locking. For experiments, this temporal structure must be eliminated (or smoothed). To this end we used the method first discussed by Gondhalekar, et al.,[3] in which a temporally smooth 50-ns pulse can be generated when the pulsed laser cavity also contains a low-pressure CO_2 discharge tube. The flowing gas was a 10:10:80::CO_2:N_2:He mixture at a total pressure of 20 torr. The combination of two gain media in the cavity results in a composite gain curve on each rotational line, which has a wide pressure-broadened gain curve with a narrow peak due to the low-pressure discharge. The extra gain in the peak will cause the laser oscillation to build up in a single longitudinal mode, yielding a smooth temporal output. This technique can be used for either multiline oscillators, or, as shown in Fig. 22, for grating-tuned single-line oscillators. The depicted single-line oscillator has a

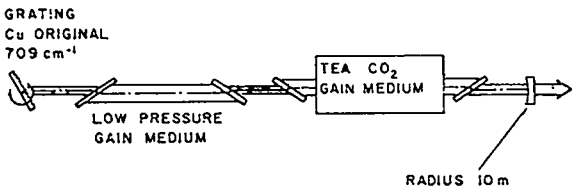

Fig. 22. Single-line cw smoothing-tube stabilized CO_2 oscillator.

micromachined original copper grating. By tuning the grating, temporally smooth pulses were obtained in the 10-μm band from R(4) to R(32) and from P(6) to P(38), as well as in the 9-μm band from R(4) to R(32) and from P(8) to P(40).

Pulsed Smoothing-Tube Stabilized Single- or Multiline Oscillator -- The cw smoothing-tube controlled oscillator had several drawbacks, e.g., water cooling and an expensive regulated dc power supply were required for operation. We have therefore developed a low-pressure discharge tube that alleviates the above complications and provides the additional benefit of permitting multiline operation.

The oscillator is similar to the one shown in Fig. 22, but with a flat mirror replacing the grating. The pulsed smoothing tube is excited by a 2-μs, 80-kV pulse, with the same gas mix and pressure as the cw tube. When only the smoothing tube was pulsed, the laser output consisted of a 20-μs spike followed by a 140-μs tail. Seven rotational lines [P(14) → P(26)] appeared each time the smoothing tube was pulsed; the lines began to lase at different times, but late in the pulse all lines were present simultaneously. The percentages of the total energy in the various transitions were: 0.5, 26, 2, 3, 66, 2, 0.5% for P(14) through P(26) of the 10-μm band. In contrast, only one line [usually P(20) of the 10-μm band] was observed with the cw smoothing tube.

The effect of the pulsed smoothing tube depends upon the delay time between the smoothing-tube pulse and the main discharge.[4] For delays of 0 to 1 ms, the output pulse is well smoothed. With discharge delays of 0 to 100 μs, we obtain single-line smoothed pulses, and with delays of 300 to 600 μs, multiline temporally smoothed pulses. Even at delays so long that temporal smoothing has ceased, multiline generation is still induced. At the operating point of interest, a 500-μs delay generates a seven-line pulse with relative line energies of 2, 7, 14, 14, 46, 15, and 2% for P(12) through P(24) of the 10-μm band. All but the two weakest lines were time-resolved and their time histories appeared identical. Figure 23 shows the temporal behavior of a typical multiline pulse. The slight ringing in the tail of the pulse can be completely removed by reducing the nitrogen content in the 580-torr discharge. With a grating replacing the flat cavity mirror, we obtain smooth single-line oscillation on 65 different lines with a relatively short delay between smoothing-tube discharge and TEA medium discharge. Figure 24 shows the measured single-line output energies.

When a 2-cm-long SF_6 cell is included in the laser cavity, we have some control over which transitions lase. Results at cell pressures of 0.5 and 10 torr are given in Table IV. Lines from the 9-μm band appear at higher SF_6 pressures.

In conclusion, the pulsed smoothing-tube-stabilized TEA laser offers simplicity of operation, requires no gratings in the cavity, no cooling water, and its cavity is easier to align. Temporally smooth multiline pulses are readily and repeatably obtained. This capability will be important for multiline extraction of the stored energy by subnanosecond pulses in large CO_2 laser amplifier systems.

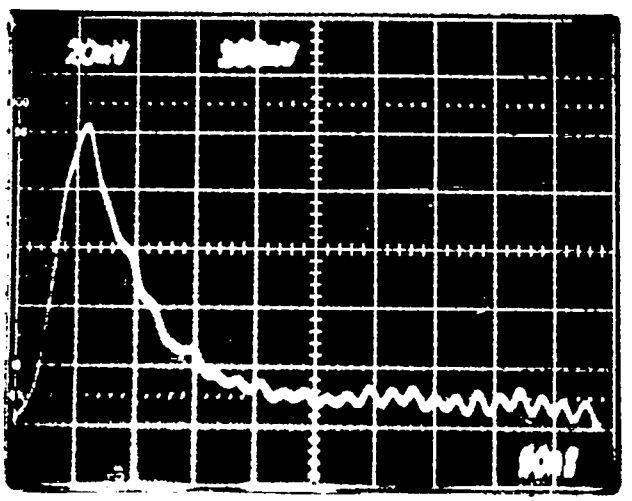

Fig. 23. Oscillogram of multiline output from TEA laser with pulsed smoothing tube. The ringing tail can be completely removed by reducing the N_2 in the atmospheric discharge.

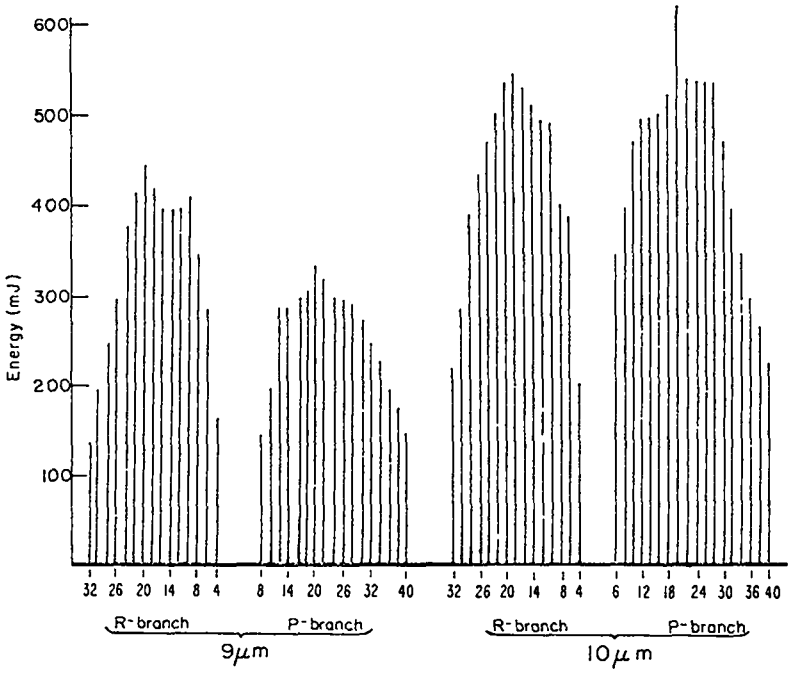

Fig. 24. Output energies of single-line cw smoothing-tube stabilized CO_2 oscillator.

Short-Pulse Generation by Optical Free-Induction Decay

Introduction -- The optical analog of nuclear magnetic-resonance FID was first discussed independently by McCall[5] and by Burnham and Chiao.[6] Recently, Yablonovitch and Goldhar[7] demonstrated the use of FID to generate subnanosecond CO_2 laser pulses. A long CO_2 laser pulse was sharply terminated by optical breakdown and then was passed through a gaseous absorber. Sharp termination of the input pulse caused the absorber to reradiate a short FID pulse. Because of the interest in short pulses for laser-fusion research, we have thoroughly examined this effect.

TABLE IV

RELATIVE INTENSITIES OF MULTILINE SMOOTHED OSCILLATOR CONTAINING A 2-cm-LONG SF_6 CELL

	Transition	Relative Strength (%)
0.5 torr in SF_6 cell	*R(14)*	*22*
	R(16)	*32*
	R(18)	*16*
	R(20)	*5*
	P(20)	*14*
	P(22)	*11*
10 torr in SF_6 cell	*R(12)*	*10*
	R(14)	*40*
	R(16)	*33*
	R(18)	*11*
	R(20)	*6*

By using FID, we have developed a reliable system for the generation of ultrashort (50-ps) CO_2 laser pulses. This capability is important because it provides a direct means of examining the time responses of detectors, oscilloscopes, optical upconverters, and other instruments. This will permit a confident diagnosis of quarter-nanosecond CO_2 systems by using instruments with accurately calibrated response functions. These ultrashort pulses could also be used to test severely our theoretical models of pulse propagation in large CO_2 laser amplifier chains. In addition, such pulses may be useful to measure fast molecular processes.

Experimental Results -- Using an oscillator stabilized by a pulsed smoothing tube, as described earlier, we generated a temporally smooth pulse (50 ns FWHM, 0.5 J) in the setup shown in Fig. 22. The pulse entered a breakdown cell (0.5 to 600 torr) containing a pair of high-quality F/1 lenses. For best operation, a small amount of room air was added to 1 atm of clean, flowing N_2. The beam was then spatially filtered and passed twice through a 2.4-m-long cell of hot CO_2. This setup is shown schematically in Fig. 25. The FID pulses were de-

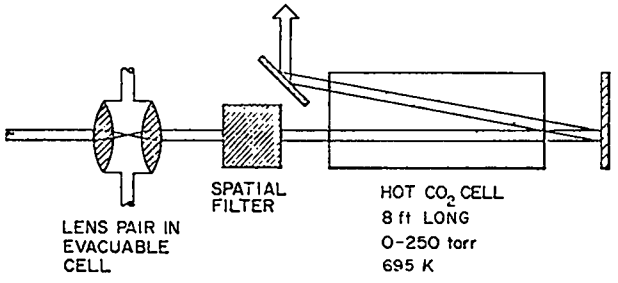

Fig. 25. System used to generate ultrashort FID pulses. The gas mix and the pressure in the lens pair cell are adjusted so that spontaneous optical breakdown occurs at the peak of the input pulse.

tected with conventional electronics and by using the CS_2 Kerr shutter described later in this section.

Pulses shorter than 50 ps have been recorded. An ultrashort pulse is shown in Fig. 26. When the beam came to a focus in the hot CO_2 absorption cell, the risetime of the FID pulse was longer than linear theory would predict. Because results indicated possible saturation of the hot CO_2 absorber, we have measured the saturation flux of hot CO_2 as a function of pressure. With collimated beams of larger diameter in the hot cell, pulse risetimes are shorter and pulse durations are in good agreement with theory when saturation is taken into account.

Linear Modeling -- At sufficiently low pressures, hot CO_2 is Doppler-(inhomogeneously) broadened, whereas above 25 torr it is predominantly pressure-(homogeneously) broadened. We restrict our attention to the homogeneously broadened case in which, for linear propagation, the transfer function $T(\omega)$ is

$$T(\omega) = \exp\left\{\left[i\frac{\omega}{c} - \frac{\alpha_0}{2(1-i\Delta\omega T_2)}\right]\ell\right\}. \qquad (7)$$

Here α_0 is the absorption coefficient at line center, ℓ is the length of the sample, and $\Delta\omega$ is the difference between the light frequency and the center frequency of the absorber; T_2 is the homogeneous lifetime, and is related to the line width through $T_2 = \lambda_0^2/(\pi c\Delta\lambda)$, where λ_0 is the free-space wavelength of the light on resonance and $\Delta\lambda$ is the wavelength difference between half-intensity points. We define the normalized absorber offset as ΩT_2, where Ω is the difference between the center frequency of the laser and the center frequency of the absorber.

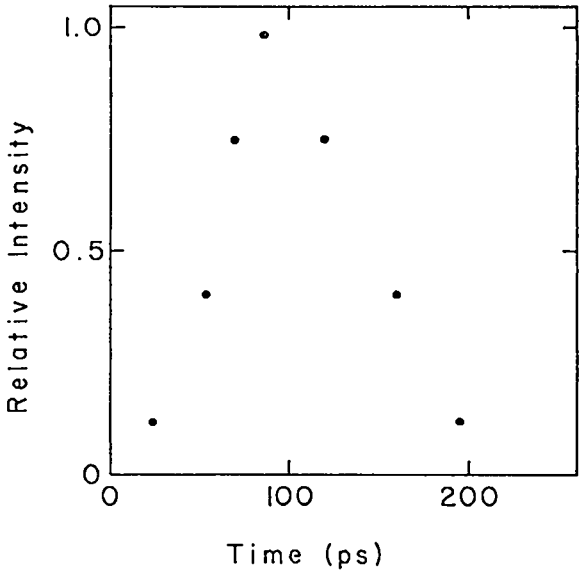

Fig. 26. An ultrashort FID pulse. This is the streak-camera record corrected for the nonlinearity of the CS_2 Kerr-cell upconverter. Camera response characteristics are still present.

In the linear regime, the output pulse $E_{out}(t)$ exiting the hot CO_2 cell can be calculated from the input $E_{in}(t')$.

$$E_{out}(t) = \frac{1}{2\pi}\iint_{-\infty}^{\infty} d\omega dt' E_{in}(t')T(\omega)\exp i[\omega(t'-t)]. \qquad (8)$$

This expression is evaluated by fast-Fourier transform techniques. As an input pulse we first generate a temporally "square" pulse sufficiently long that the transient to the turn-on has died out. The on-resonant calculated FID signal has an oppositely phased second lobe; for small nonzero ΩT_2 the instantaneous phase makes rather smooth transitions between the lobes, yet the lobes are still predominantly out of phase with each other. Although the curve of FID intensity versus time is not very sensitive to ΩT_2, the prepulse energy feedthrough is. In a calculation of the passage of the FID signal through a typical amplifier chain (again retaining only the linear response of the amplifier), the finite amplifier bandwidth increases the risetime of the leading edge while emphasizing the secondary lobe which was already on the FID signal. If the pulse cutoff is suitably

short, we see temporal modulation at the reciprocal of the interline spacing.

Pulse spectra have been generated at all stages of the calculation. The FID spectrum exhibits a deep minimum on line center, consistent with the area theorem. After amplification in a broadband linear amplifier, the spectrum narrows and the single deep minimum remains. For $\Omega T_2 \neq 0$, the FID spectrum develops asymmetry toward the offset side of the resonance.

We have numerically studied the dependence of the FID pulse duration upon propagation distance. Results are shown in Fig. 27. Note that the 1/e and 1/2 intensity durations vary (as predicted by Ref. 7) as $1/\alpha\ell$. The rms duration varies far less with increasing $\alpha\ell$. The distinctly different behavior of the rms duration can be understood in terms of "zero pi" pulse propagation, in which the narrow-band absorption has removed nearly all the central spectrum of the pulse, and in further propagation the pulse therefore has little spectral energy to lose to the absorber.

Nonlinear Modeling -- We have modeled nonlinear pulse propagation by numerically solving the density matrix equations of motion (descriptive of CO_2) coupled with Maxwell's equations. Multiline and multiband pulse propagation have been studied in low-pressure absorbers and in high-pressure amplifiers. In the saturation regime, we investigated pulse reshaping resulting from optical nutation and finite rotational relaxation effects. When a multifrequency oscillator is used, we find that the significance of the secondary lobe of the FID pulse diminishes after amplification.

Pulse-Shortening by Germanium Saturable Absorbers -- As discussed previously (see LA-6245-PR), p-type germanium behaves as a saturable absorber. Proper matching of short-pulse peak intensity to the saturation intensity of a germanium absorber can cause the pulses to be shortened by passage through the germanium absorber.[8]

Using a Brewster-angle pair of germanium plates, as described under isolators, below, we have measured pulse compression. The results are shown in Fig. 28.

Gigawatt Test Facility (GWTF)

The Gigawatt Test Facility (GWTF), as shown in Fig. 29, provides 1.0 J or more in a 1.0-ns CO_2 laser pulse. This laser is capable of operating on single lines in the 9- and 10-μm bands, as shown in the tuning curve of Fig. 24. The output energy is obtained in the following manner: A pulsed, smoothing-tube-controlled oscillator generates a

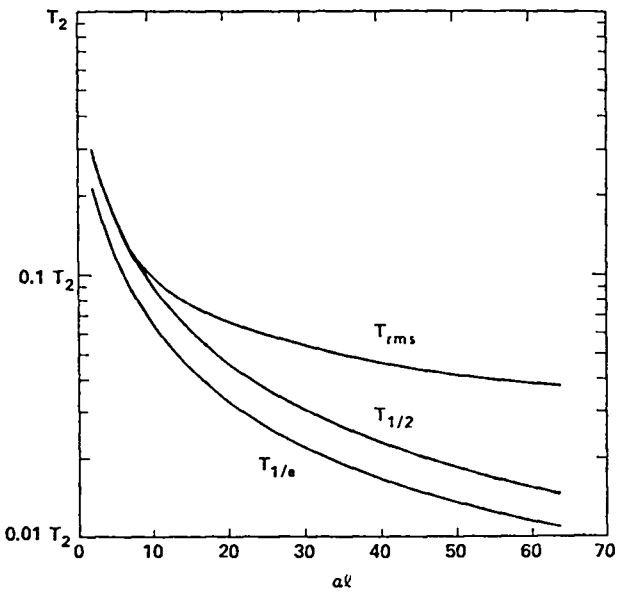

Fig. 27. Calculated absorption-length dependence for FID pulse durations. Shown are the rms duration, the half-intensity duration, and the 1/e intensity duration.

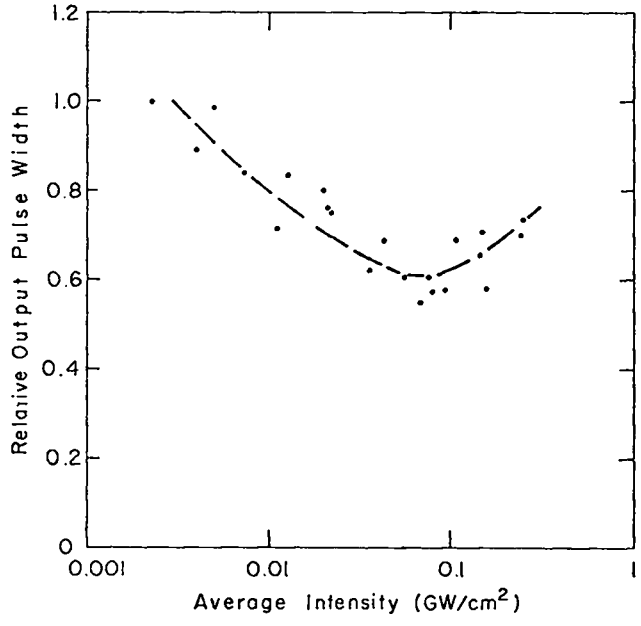

Fig. 28. Pulse shortening measured in p-type germanium. The horizontal axis is intensity in the air just prior to the Brewster-angle sample.

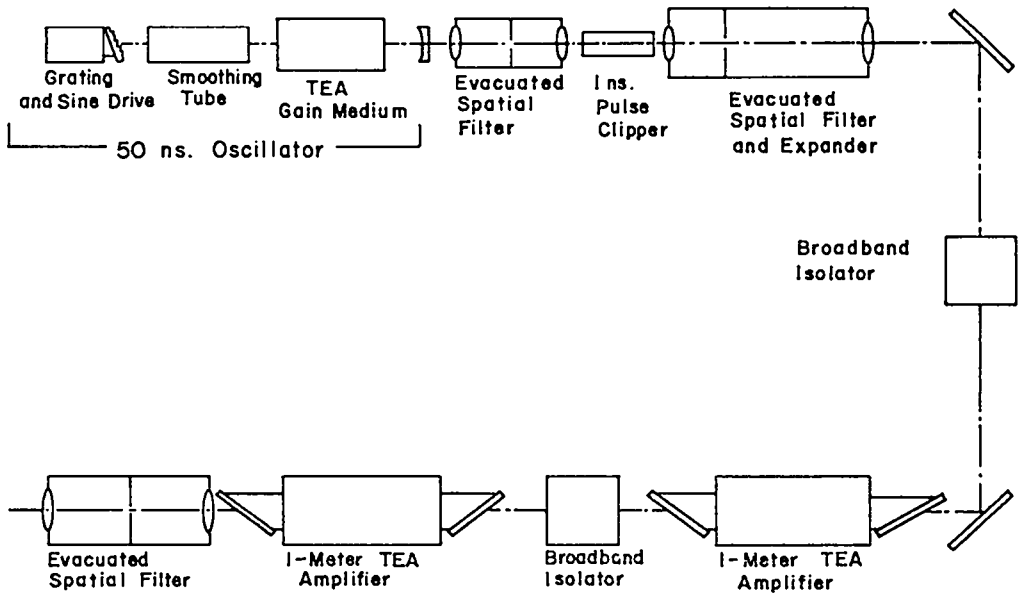

Fig. 29. Schematic layout of broadband Gigawatt Test Facility.

50-ns pulse. A laser-triggered Blumlein[9] electro-optical gate switches out a 1-ns portion of the 50-ns pulse, and the short pulse is directed through a beam expander and a spatial filter. The 1-ns pulse then proceeds through two stages of amplification. The small-signal gains of amplifiers 1 and 2 are approximately 0.04 cm^{-1}. We intend to use this system for studying properties of optical isolators and damage thresholds of optical materials.

We are completing the characterization of the beam after Amplifier 2.

Spatial Filters

Introduction -- Maximum brightness is a parameter of fundamental importance in characterizing lasers for fusion applications because it determines the amount of the beam which can be focused by a lens onto a laser-fusion target. Loss of brightness can be caused by optical aberrations in elements of the optical train, by diffraction from hard apertures, by scattering, and by nonlinear propagation effects (such as self-focusing). Bright beams with uniform, compact far-field patterns are highly desirable for laser-fusion experiments and other related applications.

All the above detrimental effects can be minimized by including in the beam train a small number of spatial filter telescopes.[10,11] The simplest such device is a Galilean telescope with a limited field of view defined by a focal-plane iris. In telescopes designed to pass more than a few milliwatts of optical power, optical damage to the focal-plane iris is usually avoided at the expense of usable f number; this restriction limits the compactness of the device. In solid-state laser systems, this f-number penalty is especially severe because of long propagation lengths in materials with a high nonlinear index of refraction (n_2); yet even in CO_2 systems (where self-focusing is not expected to limit operation) this f number restriction must always be considered.

Theory of Operation -- The spatial-filter telescope depends for its operation on the Fourier-transform relationship between the transverse spatial frequency distributions of the collimated input and the focal-plane fields of an ideal parabolic focusing optic in the Fresnel approximation.[12,13,14]

This situation is illustrated in Fig. 30. Here x and y are Cartesian coordinates and $\bar{r}$ the position vector in the input (I), output (O), and focal (f) planes. The units of transverse spatial frequency in the input beam plane are $1/w$, where w is the characteristic beam radius (the $1/e^2$ intensity radius if the beam is a Gaussian distribution).

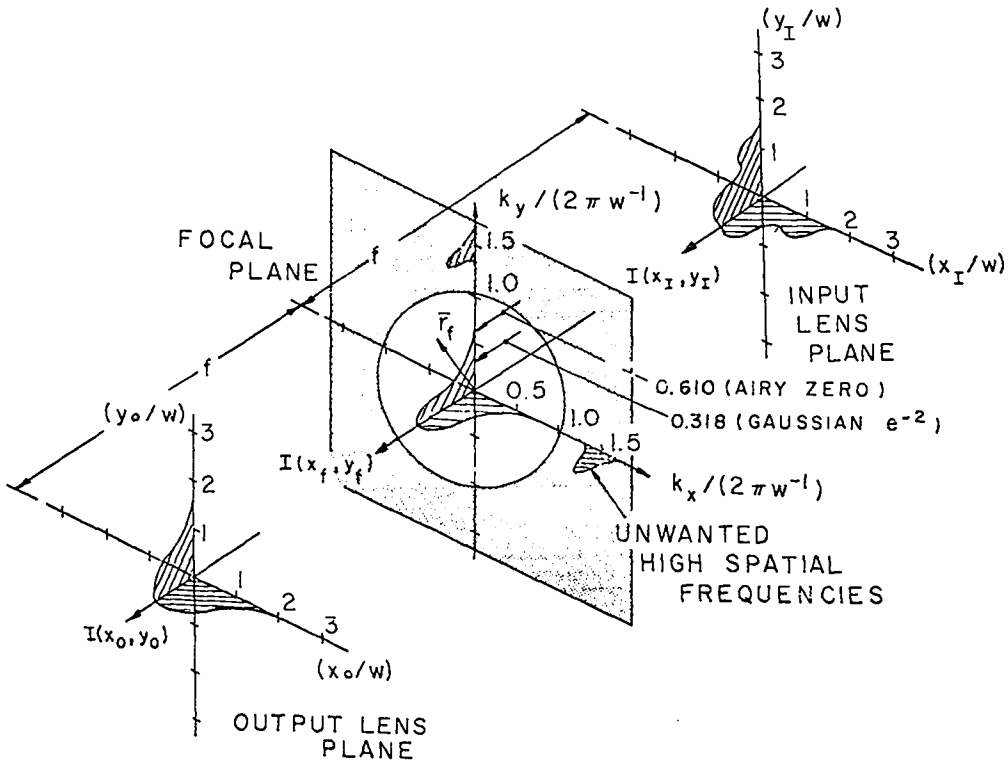

Fig. 30. Spatial filtering with spherical optics.

An input Gaussian beam with waist radius w is transformed into a focal-plane distribution whose $1/e^2$ intensity radius falls at $k_x=k_y=0.318(2\pi/w)$, whereas uniform input illumination of radius w produces an Airy distribution with zone radius $k_x=k_y=0.610(2\pi/w)$.

The unwanted high spatial frequencies in the input beam intersect the focal plane away from its origin, and do not pass through the small iris. In the case shown in Fig. 30, transverse electric-field frequencies greater than $2\pi/w$ are rejected when the iris diameter is π-times larger than the $1/e^2$ intensity diameter of the focal spot for a Gaussian input beam. This choice means that the low-pass iris will interact very little with the fundamental low-frequency components of the input beam. For example, for an ideal Gaussian input beam, only 5×10^{-3}% of the peak focal intensity strikes the aperture. However, the fine structure responsible for bad beam quality is well discriminated against.

System Applications -- Eight spatial filter units have been designed for the low- and intermediate-energy portions of the EBS and the GWTF. EG&G is assisting us with the mechanical design of several telescope assemblies; a typical spatial-filter telescope is shown in Fig. 31.

Optical Design Considerations -- Refractive Telescopes with Spherical Optics -- Six lens materials for the refractive telescopes (Ge, ZnSe, KCl, NaCl, BaF_2, and CdTe) have been considered; the selection criteria are discussed below.

Acceptable Peak Focal Intensity -- One of the most stringent limits on spatial filters is optical damage to the iris in the focal plane. Realistic damage thresholds of iris materials and analysis of accidental misalignment led to a criterion of minimum f number for the spatial-filter telescope. It can be shown,[15] for either Gaussian or uniform illumination, that a lens concentrates the peak incident intensity by a factor η, which depends upon the characteristic diameter of the incident beam, D = 2w, on f number, and on wavelength:

$$\eta = \frac{I_{wo}}{I_w} = D^2/(\frac{4}{\pi} f_\# \lambda)^2 , \qquad (9)$$

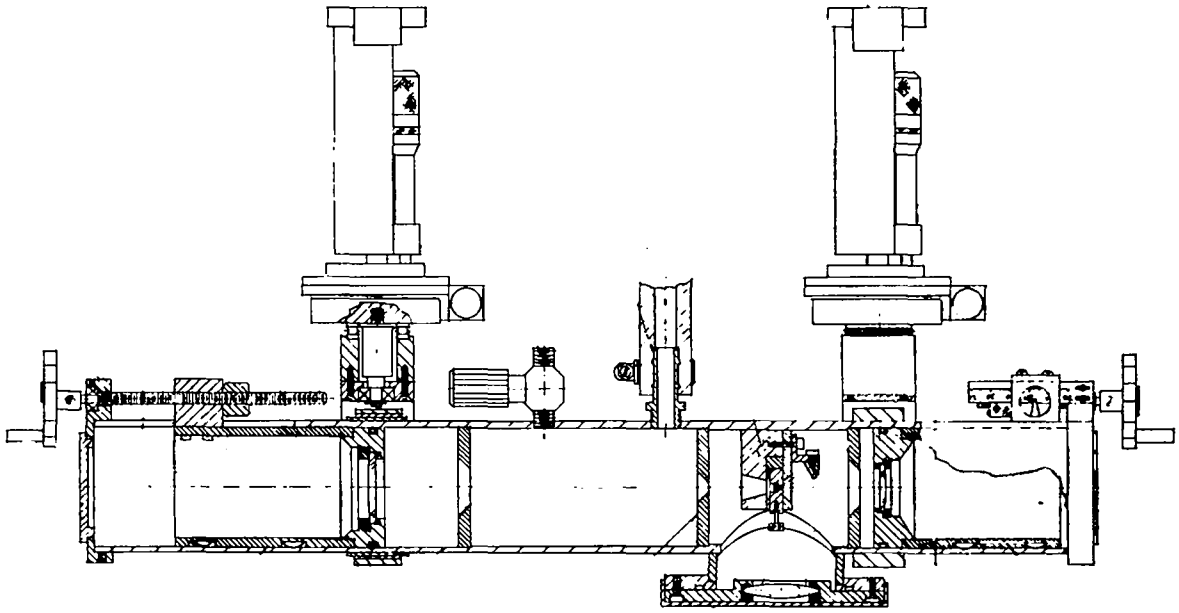

Fig. 31. EG&G mechanical design for a typical spatial-filter telescope.

where $f_{\#} = f.\ell./D$, $f.\ell.$ is the focal length of the lens, and D is either the lens diameter (for uniform illumination) or D = 2w (for a Gaussian beam).

Engineering considerations then give

$$f_{\#min} = 4.7\ [\tau_p(ns)]^{1/4}\ D(cm)\ \sqrt{I(MW/cm^2)}. \quad (10)$$

Here, $I(MW/cm^2)$ is the peak incident beam intensity, D(cm) = 2w is the characteristic diameter of the incident beam, and $\tau_p(ns)$ is the pulse duration.

Satisfaction of the Fresnel Approximation -- The impact of the Fresnel approximation on the Fourier transform properties of coherent imaging can be described by the inequality (see Ref. 13):

$$f_{\#} >> 3.65\ D(cm)^{1/3}\ . \quad (11)$$

For practical applications to high-power spatial filtering, this limit is difficult to violate.

Acceptable Spherical Aberration -- Spherical aberration is the deviation from ideal imaging, which results from the use of spherical rather than parabolic reflecting or refracting surfaces. To establish a lower limit on lens f number under this design criterion, we assumed a Gaussian transverse profile for the collimated telescope input, with $1/e^2$ intensity radius w. The deviation half angle due to spherical aberration at this radius was then equated to the diffraction-limited divergence half angle corresponding to Gaussian illumination with beam waist w.

Two cases were considered. In the first, we used the optimum combination of front- and back-surface radii giving minimum spherical aberration for a given lens refractive index. In the second case, we assumed a plano-convex configuration.

These two limits are compared in Fig. 32. Note that the penalty for using the plano-convex configuration is essentially constant and that there is a strong penalty in either case for using a refractive index smaller than 2.0.

Acceptable Chromatic Aberration -- Because of the broadband character of the CO_2 laser system now envisioned, the chromatic change in focal length of a refractive telescope should cause no more than a $\pm$ 10% variation in peak intensity at the 10.0-μm focal plane as the wavelength of the incident beam is varied from 9.2 to 10.8 μm.

Acceptable Deformation Under 1-atm Pressure Loading -- To reduce the cost of the overall design, we decided to use the input-output lenses

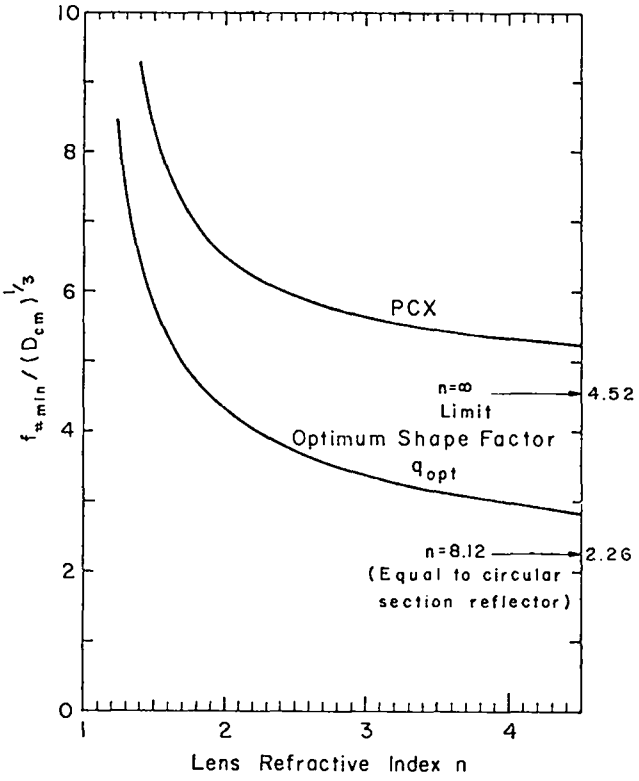

Fig. 32. Refractive-index dependence of spherical-aberration-limited f number for a spherical collimating lens at λ = 10.6 μm.

as the atmosphere-to-vacuum mechanical interface, with iris ablation damage to the lenses to be minimized by the internal mechanical design of the telescopes. This decision introduced the requirement for sufficient lens edge thickness to withstand atmospheric pressure loading with no more than 3 μm deformation at the lens center.

Visible Transparency -- To permit coarse alignment of the telescopes by a visible laser, we retained visible transparency of the lens material as a desirable design criterion.

Optical Design Conclusions -- Refractive Telescopes with Spherical Optics -- Plano-convex ZnSe lenses are the best choice among the six materials considered; in addition to satisfying all the design criteria, they offer several additional advantages. With this choice, the peak focal-intensity criterion was the most severe lower limit on f number for all telescope designs. Germanium or CdTe gave somewhat less spherical aberration and much less chromatic aberration, but ZnSe was quite adequate and transmits visible light. In general, BaF_2, KCl, and NaCl were unsatisfactory because their chromatic aberration was the most severe limit on f number. Zinc selenide has the further advantage that high-power antireflection coatings for the 10-μm region are commercially available.

Dispersion does not permit direct visible-wavelength alignment with fixed focus; however, visible alignment is possible with either the temporary insertion of correcting lenses or with temporary refocusing of the telescope.

Optical Design Considerations -- Cylindrical Reflective Telescopes -- We have developed a two-step cylindrical-optics spatial-filter concept. This new device permits a large reduction in physical length and offers many other advantages in comparison to the conventional spherical-optics telescope discussed above. Because the Fourier-transform relationship, which forms the basis for filtering, can be expressed in Cartesian coordinates, the x- and y-filtering operations may be performed sequentially. This approach is illustrated in Fig. 33. For an input beam of circular symmetry, the average characteristic width of either line focus is the same as the characteristic spot diameter produced in a spherical-optics telescope having the same f number.

In a cylindrical-optics telescope, the concentration of input-beam intensity varies linearly (instead of quadratically) with f number, which permits more compact devices for the same input in-

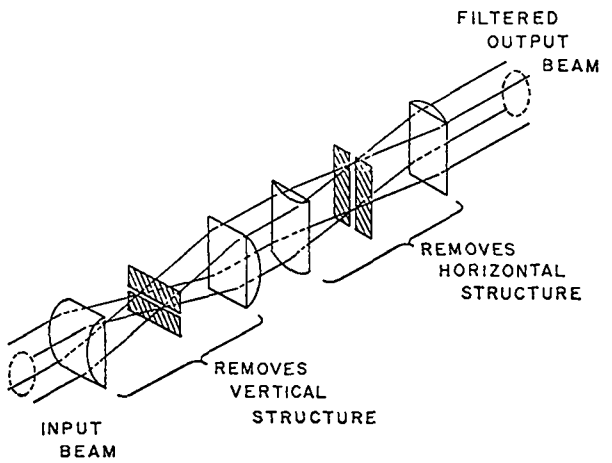

Fig. 33. Schematic of two-step cylindrical-optics spatial filter.

tensity, wavelength, and iris damage limit I_{wo}. For this case, Eq. (9) becomes

$$n(CYL) = \frac{I_{wo}}{I_w} = D/(\frac{4}{\pi} f_{\#} \lambda) , \quad (12)$$

Eq. (10) becomes

$$f_{\#min}(CYL) = 0.014[\tau_p(ns)]^{1/4} D(cm) I(MW/cm^2) , \quad (13)$$

and the aberration criterion for cylindrical optics becomes

$$f_{\#min}(CYL) = 2.30\ D(cm)^{1/3} . \quad (14)$$

For input powers higher than a few gigawatts, cylindrical systems are the only practical spatial filters.[14] For example, if spatial filtering were to be provided for a 20-J beam with a pulse duration of 1 ns and a diameter of 10 cm, a cylindrical telescope would require an f number of 70, whereas a spherical-optics telescope would require an f number of 1000.

Isolator Development

Introduction -- Interstage isolation is one of the major concerns in laser oscillator-amplifier systems used for target experiments. Amplifier systems with small-signal gain higher than 10^{10} are being considered. At such high gain, parasitic oscillations can occur with only minor optical imperfections present.

Isolation problems occur in three areas: prepulse amplification, parasitic oscillations, and amplification of target reflections.

- Prepulse amplification is a problem because a plastic laser-fusion target will melt if more than 50 μJ of light is focused upon it before the main pulse arrives. In our oscillator systems, the short pulse to be injected into the amplifier chain is electro-optically switched out of a longer smooth or mode-locked pulse. When the electro-optic switch is opened, transmission is quite close to unity, but before the switch is "opened" it does not entirely block the beam: about one-thousandth of the incident intensity is transmitted. It is this feedthrough that must be controlled. The feedthrough is neither broadband nor intense; it therefore experiences the peak of the amplifier's unsaturated gain and may grow to contain an appreciable fraction of the total energy output of the system.
- Parasitic oscillation must be avoided prior to amplification of the short pulse; it can melt the target, and it can deplete the gain of the amplifier system before the desired pulse arrives.
- Amplification of target reflections is a serious problem because of residual gain in the amplifiers after passage of the main pulse. As the target reflections are amplified and contracted in diameter, they may damage optical elements in the amplifier chain or in the oscillator.

P-Type Germanium Isolators -- P-type germanium (gallium-doped or indium-doped) is an optically bleachable absorber for wavelengths ranging from 9 to 11 μm. As an isolator for large CO_2 amplifiers, this broadband behavior is its chief advantage over gaseous bleachable absorbers. Because p-type germanium is a solid, it is simple to use and is physically compact. Small-signal absorption coefficients up to 10 cm^{-1} are readily obtained in monocrystalline germanium.

Although previously considered expensive, germanium isolators cost only ~ \$6.00/cm^3 -- twice the cost of NaCl and one quarter the cost of ZnSe. We have recently obtained samples with sufficiently good surface quality that optical damage is no longer a problem. By using a 1-ns CO_2 laser pulse, we have measured the single-event damage threshold for a Brewster-angle sample; this threshold occurs at 6.0 GW/cm^2 in the incident beam, which is comparable to the damage threshold for NaCl.

While germanium isolators are primarily intended to prevent parasitic oscillations, they also alleviate the target-reflection problem and may even solve all three of our isolation difficulties.

We have designed, built, and successfully tested a Brewster-angle germanium isolator. The

device is shown in Fig. 34. The two isolator plates were single-crystal p-type germanium with a resistivity of 1.43 Ω•cm. The experimental setup is shown in Fig. 35. The oscillator and the first two amplifiers of the SBS generated a 2-J, 1.5-ns CO_2 laser pulse. The pulse was spatially filtered, and intensities in excess of 1 GW/cm^2 were directed at the isolator. By monitoring input and output beam intensities and energies with pyroelectric detectors and calorimeters, the spatially averaged transmission of the isolator was measured as a function of incident intensity. The pyroelectric detectors were covered by small irises, whereas the calorimeters were not, so as to test for self-focusing, which did not occur. The operational parameters and the performance of the isolator are shown in Table V.

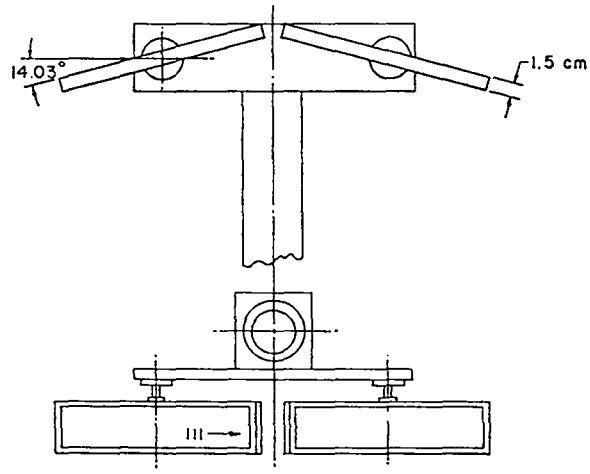

Fig. 34. A two-piece Brewster-angle isolator. Each piece of p-type germanium is single-crystal with a resistivity of 1.43 Ω-cm.

Note that the device was operated conservatively; more complete bleaching could be obtained with higher intensities or with a more uniform spatial profile. These demonstration tests were highly successful and indicate that p-type germanium will perform well as a bleachable isolator to address the self-lasing and reflected-pulse problems.

Electrically Driven Plasmas -- A high-density laser-induced plasma has been shown[16] to be highly effective in attenuating 10-μm radiation and could be useful for retropulse isolation. The plasma would act as an inducible rather than a bleachable absorber, i.e., its transmission would decrease with increasing incident intensity. Burnett and Richardson have suggested[17] that an electrically induced plasma could provide significant attenuation for 10-μm laser beams. In their experiments they obtained a thousandfold intensity reduction in the retropulse whose beam path included a line focus along the axis of an electrical spark (in air) that was triggered after the outgoing laser pulse.

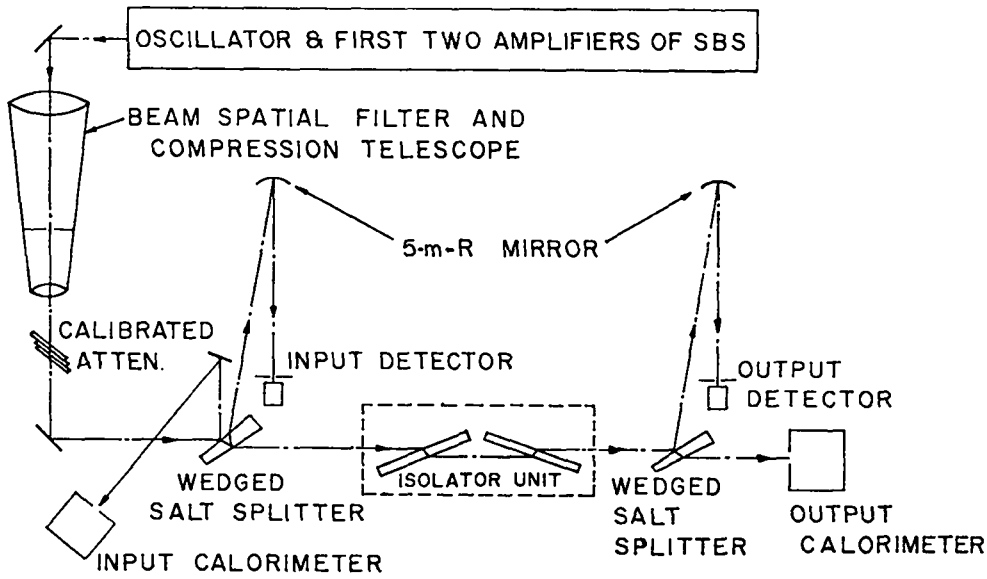

Fig. 35. Experimental setup for characterization of isolator properties.

TABLE V

GERMANIUM ISOLATOR EXPERIMENT -- OPERATING CONDITIONS AND RESULTS

Germanium Isolator Operating Conditions:

Total plate thickness, cm	*3.0*
Total optical path length, cm	*3.09*
Germanium resistivity, Ω·cm	*1.43*
10.6-μm absorption coefficient, cm^{-1}	*1.60*
Small-signal transmission (measured)	*8.84×10^{-3}*
Peak incident beam intensity, GW/cm^2	*1.0*
Input beam quality	*Diffraction-limited*

Germanium Isolator Performance:

Energy transmission at peak intensity, %	*40*
Maximum observed pulsewidth reduction, % (5% transmission point)	*40*
Damage	*none*
Observed self-focusing	*none*

Our studies are directed toward understanding the practical tradeoffs involved in scaling this electrically induced plasma to a larger physical size and in attenuating and refracting laser beams of higher intensity. Our objective is a plasma-based absorber which would transmit 10-μm laser energies on the order of 10^5 J while limiting the target-reflected pulse to ~1 J. In other words, the more power we have, the more attenuation we need.

Initially, we determined the physical scale of the critical density region within small sparks in air between pin electrodes. The setup shown in Fig. 36 was used. A laser-triggered spark gap (LTSG) initiated the discharge, which was driven by closely coupled $BaTiO_3$ capacitors charged to 50 kV. Electrical energy of 1.7 J was delivered to the pin-electrode array, with a risetime-to-peak current of 30 ns. The pin-array gap could be adjusted longitudinally from 2 to 8 mm, whereas the transverse spacing of the four pin-electrode pairs was fixed at 2 mm. As can be seen in Fig. 37, streak photographs of the spark array revealed a relative jitter of 5 ns between the formation of the several sparks. The TEA CO_2 laser used to illuminate the resulting spark curtain (and to trigger the LTSG) generated a passively modelocked train of 20-mJ pulses with a total duration of 100 ns. Ninety percent of the CO_2 beam energy was used to illuminate the spark curtain, and was delayed 70 ns relative to the portion used to trigger the LTSG. The measured half-power radius of the illumination spot at the spark curtain was 0.7 mm.

Initial results of these measurements performed with a beam energy of 20 mJ showed that the transmission of the spark curtain was 2.5% and did not change appreciably when the plane of the four sparks was rotated between 35 and 17° with respect to the propagation direction of the input CO_2 beam. A time-integrated photograph of this spark curtain is shown in Fig. 38(a), with a view of the electrode geometry in Fig. 38(b). Our initial results implied that an insignificant part of the area of the beam was intercepted by plasma of a density exceeding the 10.6-μm critical density.

Detailed measurements of the spatial absorption profile and of the effect of refraction by

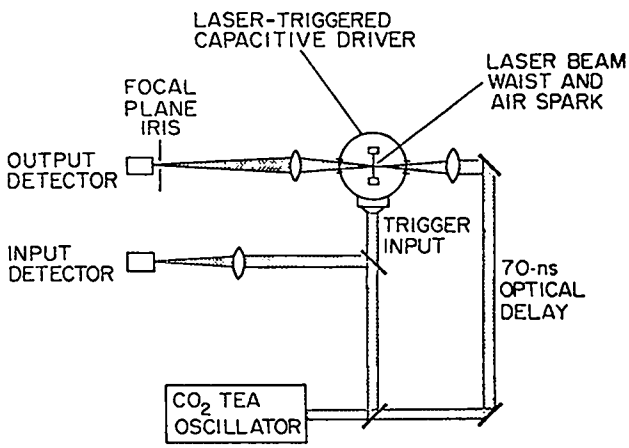

Fig. 36. Setup for studying electrically driven plasmas.

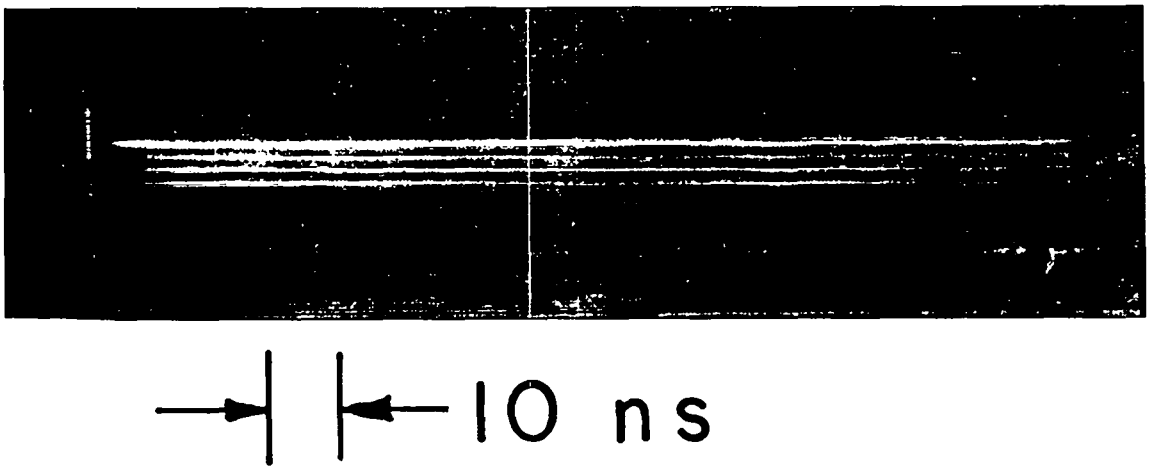

Fig. 37. Streak photograph displaying the relative jitter in a multiple-point gap.

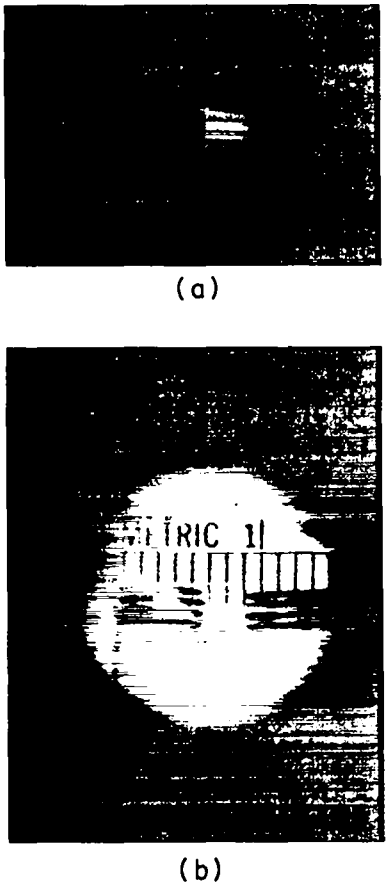

Fig. 38. Electrically driven spark-curtain beam isolator. (a) Time-integrated photograph of spark curtain. (b) Electrode set as seen by the beam. The plane of the electrodes forms a 20° angle with the k-vector of the 10.6-μm probe.

plasma channels were subsequently initiated. The beam was focused to a small spot so as to probe a single spark. A combination of a detector array and magnifying lens was used to provide about 40-μm resolution in the plane of the spark. The results strongly indicate that if the core of the spark exceeds critical density, its diameter is less than 40 μm. Furthermore, the measured attenuation varied with input laser energy. Only 0.3% of a 200-mJ beam was transmitted through a single spark, and decreasing the probe-beam energy increased the amount of transmission. Our experiments are continuing with special attention to the scaling of attenuation and refraction with respect to input power.

These results indicate that the spark plasma acts as a "seed" for further ionization by the laser, yielding increased attenuation at higher laser energy densities.

Saturable Polyatomic Gases -- The gases that have been proposed as saturable absorbers for high-gain CO_2 laser amplifiers do not saturate completely at high flux. The absorptions of several gases at high and low energy fluxes for a 1.5-ns pulse are shown in Table VI. The small-signal absorption coefficient is given by α, and the absorption coefficient at high flux by γ; E_{in} is the laser-pulse energy at which γ was measured. The ratio of these absorption coefficients is a first-order figure of merit for these gases. For larger values of γ/α, we suffer a smaller absorption of our main pulse

TABLE VI

SATURATION CHARACTERISTICS OF GASES FOR 1.5-ns, 10.59-μm LASER PULSES

	SF_6	SF_6	C_2H_4	C_2H_4	NH_2D
P (torr)	5.	5.	5.	10.	2.
L (cm)	2.	2.	122.	122.	122.
P_{He} *(torr)*	0	600.	0	1200.	1300.
α *(torr^{-1}cm^{-1})*	0.5	0.5	0.0008	0.0029	0.0038
E_{in} *(mJ/cm^2)*	200.	120.	220.	220.	200.
α/γ	16.	2.2	8.2	1.6	4.2

for a given value of small-signal loss. In addition to this figure of merit, limitations on usable lengths, L, of absorber cells require that α be large.

To ensure that the pulse will neither damage the cell windows nor suffer loss in the absorber, the saturation energy of the absorber should be small.

Saturable Triatomic Gases -- The polyatomic gases we have thus far investigated with intense 1.5-ns CO_2 laser pulses (SF_6, NH_2D, and C_2H_4) do not exhibit classical two-level saturation. Instead, at high pulse powers they fail to saturate completely, due principally to multiple photon absorption by each complex molecule. Simpler molecules such as carbonyl sulfide (OCS)[18] exhibit more nearly classical two-level saturation behavior. We expect that triatomic molecules, in general, will be more attractive because of the smaller possibility of excited-state absorption.

A literature search has identified several interesting triatomic gases with ir absorption bands coincident with CO_2. We have found coincidences with the fundamental band of oxygen difluoride (OF_2, ν_1 = 928 cm^{-1}) and the difluoroamino radical (NF_2, ν_3 = 931 cm^{-1}), and coincidences with the difference bands of nitrous oxide (N_2O, $\nu_3 - \nu_1$ = 939 cm^{-1}), carbon diselenide (CSe_2, $\nu_3 - \nu_1$ = 935 cm^{-1}), and CO_2 ($\nu_3 - \nu_1$ = 961 cm^{-1}). We are at present more interested in the difference bands because they are less likely to absorb from the excited state.

Induced Infrared Absorbers -- The frequencies of molecular normal modes of vibration change when the molecule is electronically excited. Thus, a suitably chosen molecule could serve as the basis for an ir light switch.

The energy cost of this process could be excessive because many uv photons may be needed to cause the attenuation of one ir photon. However, recent experiments[19] show that multiple photon absorption at 10.6 μm occurs in ground-state SF_6. The principles involved, although not completely understood, indicate that the same process should occur in the vibrational manifold of electronically excited molecules.

The molecules of interest may be either gaseous, or in bulk, or thin-film liquids. The excitation may be effected by a uv light source (flashlamp or laser) or by electron-beam pumping. The excited molecule may dissociate or remain in a bound state. Finally, the transition from unexcited to excited state may increase or decrease the ir absorption of the molecule.

Organic molecules in liquids offer wide latitude, because many are uv-sensitive. Induced dissociation of molecules may yield ir-absorbing radicals, e.g., the photolysis of the perfluoralkyl iodides yields perfluoralkyl radicals that absorb from 8 to 10 μm.

A preliminary search has identified CS_2 as meriting further consideration. The normal mode frequencies in the ground electronic state, ν_1, ν_2, and ν_3, are 658, 397, and 1533 cm^{-1}, respectively.[20] This enables the unexcited CS_2 to transmit

10.6-μm radiation with no attenuation. In the lowest excited state, $^3A_2$ at 26 200 cm^{-1} above ground, the normal modes are 691, 311, and 940 cm^{-1}, respectively.[20] Because the ν_3 mode is ir-active, excited CS_2 will attenuate at 10.6 μm.

Our preliminary analysis of this approach has been encouraging and we are considering some experiments in the near future. We envision, for example, a form of ir switch that can be combined with a capillary waveguide to produce a compact retropulse attenuator.

Gaseous Absorbers for 10-μm Branch of CO_2 -- Sulfur-hexafluoride cells in present use do not absorb sufficiently on all the R-branch transitions in the 10-μm band of CO_2 to prevent parasitic oscillations. We are therefore searching for other gases that absorb these R-branch transitions but do not absorb the P(20) (10.6-μm) transition. It is not necessary that these gases saturate.

We have measured small-signal absorption coefficients on the high-gain CO_2 laser lines and found three attractive gases among several we investigated.

Hexafluoroacetone (CF_3COCF_3) exhibits peak absorption at the 10.4-μm R(12) line, and has a ratio of absorption coefficients $\alpha_{R(J)}/\alpha_{P(20)} \geq 80$ for all R-lines with $J \leq 22$. This is an improvement over the corresponding ratio for chloropentafluoroethane (CF_3CF_2Cl, FC-115), the gas we are presently using to prevent R-branch oscillation in the SBS.

Dichlorodifluoromethane (CF_2Cl_2, FC-12) exhibits strong absorption of 10.6-μm P-branch lines at $J \geq 30$, having an absorption ratio $\alpha_{P(30)}/\alpha_{P(20)} = 20$.

Octafluorocyclobutane (C_4F_8, FC-318) exhibits strongest absorption near the center of the 10.6-μm band with $\alpha_{P(10)}/\alpha_{P(20)} = 12$. This capacity offers isolation protection against the P(10) parasitic oscillation observed in the SBS.

Determination of the saturation behavior of these gases is under way. We are particularly interested in studying the saturation of the finite absorption at the 10.6-μm P(20) line.

Reduction of Prepulse Transmission by Narrow-Band Gaseous Absorbers -- The use of FID for the generation of ultrashort (50-ps) CO_2 laser pulses was described earlier. There is still another application for linear absorption effects in laser-fusion systems, namely, their use to reduce prepulse transmission to acceptable levels. In CO_2 laser systems driven by short (~ 250-ps) electro-optically switched pulses, our studies indicate that linear absorption can reduce prepulse transmission by several orders of magnitude.

In our approach we utilize the narrow-band absorption properties of hot CO_2. A low-pressure hot-CO_2 cell is placed in the beam after the electro-optic switch. The narrow-band feedthrough is absorbed by the CO_2 gas according to Beer's law, whereas the broadband switched-out pulse is transmitted through the narrow-band absorber with little attenuation. The calculated enhancement in contrast ratio for a 250-ps pulse through a 30-torr sample of hot CO_2 gas vs absorption length is shown in Fig. 39. Note that this isolation technique does not rely on the saturation properties of the gas, but only on the different frequency characteristics of the prepulse energy and the main pulse. The effect discussed here is linear, independent of laser intensity, and consequently does not lead to spatial beam distortion.

Diagnostics Development

Introduction -- Our work demands that the spatial shapes, temporal histories, and spectral distributions of CO_2 laser pulses be measured accurately. Techniques are being developed to help examine the properties of our short CO_2 laser pulses in various phases of experiments and amplifier-system development. In addition to the two devel-

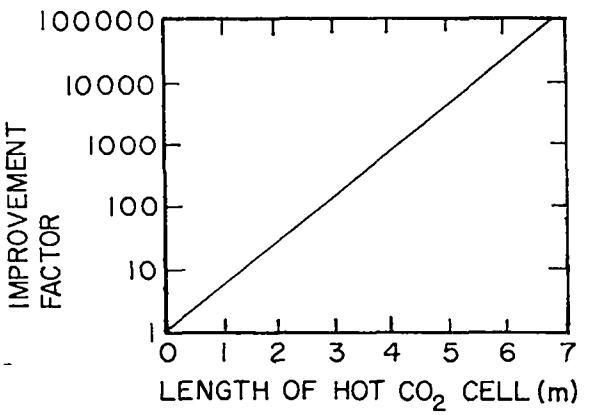

Fig. 39. Calculated improvement in contrast ratio of CO_2 laser pulse through linear absorption in hot CO_2 cell.

opments described in detail below (CO_2 laser-driven CS_2 Kerr shutter and 5-GHz oscilloscope), we have begun the construction of a ruby-laser-pumped parametric upconverter to be used with the 1-ps-resolution streak camera that will be delivered soon. A video system is being designed to read the signal from the new streak camera directly and to display it on an oscilloscope. This will extend our real-time CO_2 pulse-measuring capability down to 5 ps.

CS_2 Kerr Shutter Driven by CO_2 Laser -- In a scheme similar to that discussed by Duguay and Hansen,[21] a CS_2-filled cell imposes the CO_2 pulse shape onto an argon-ion laser beam. The CO_2 light partially aligns the CS_2 molecules, and the temporary birefringence modulates the visible beam. The argon-ion laser beam (containing the CO_2 pulse-shape information) is then directed into a LASL-developed streak camera.

When we first received the streak camera, we tested its temporal response with a 5-ps Nd:glass laser pulse. The streak camera exhibited a 40-ps risetime (10 to 90%), a FWHM of 70 ps, and a streak width of 2 mm. We have subsequently modified the internal circuitry to reduce the streak width to 0.3 mm; this increases the camera sensitivity by a factor of 7 and reduces the minimum detectable power to 2×10^{-4} W at 5145 Å. We have also introduced an additional Pockels cell into the Kerr shutter system as shown in Fig. 40. This improved the signal-to-noise ratio by changing the shutter transmission from $\sin^2(AI)$ to $\sin^2(AI + \theta/2)$, where A is a constant, I is the CO_2 intensity, and θ is the phase delay added by the Pockels cell. For a constant background noise (film fogging, shot noise), this arrangement increases the signal amplitude by a factor of $[\sin^2(AI+\theta/2)-\sin^2(\theta/2)]/\sin^2(AI)$.

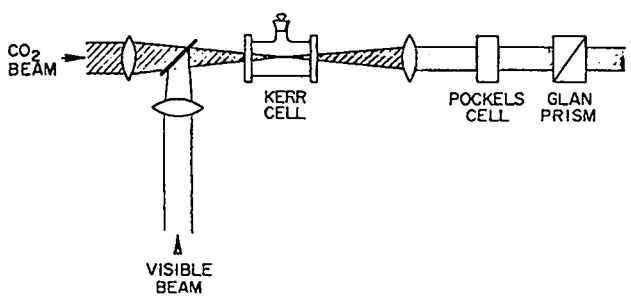

Fig. 40. CS_2 Kerr-cell shutter.

The high current in the streak tube presently limits the temporal resolution; the resolution will be improved markedly after installation of an SIT vidicon camera in place of the photographic film. Video conditioning circuitry between the vidicon and the oscilloscope will compensate for the nonlinear behavior of the CS_2 Kerr gate to provide real-time pulse-measuring capability.

The present Kerr shutter system has been used to measure the 50-ps FID pulses discussed earlier. One typical pulse is shown in Fig. 26.

5-GHz Oscilloscope -- We have developed a 5-GHz single-sweep oscilloscope that uses a TMC-4 cathode-ray tube obtained from the French Laboratoires d'Électronique et de Physique Appliquée, Limeil. Vertical sensitivity is 0.1 V/div, and sweep speed varies from 0.1 to 10 ns/div. Full-scale vertical deflection is 0.6 V. The cathode-ray tube contains a microchannel plate intensifier that eliminates writing-rate problems at these ultrafast sweep speeds. In Fig. 41 we show an ultrashort FID pulse (as discussed earlier in this section) detected by a Molectron P500 pyroelectric detector and recorded on this ultrafast oscilloscope. From both theoretical considerations and our complementary streak-camera observations, this FID pulse has a width of 70 ps FWHM and a risetime of less than 25 ps. From the response observed in Fig. 41, we determined that the detector-oscilloscope combination has a risetime of 70 ps (10 to 90%) and a 100-ps FWHM response to a temporal δ-function input.

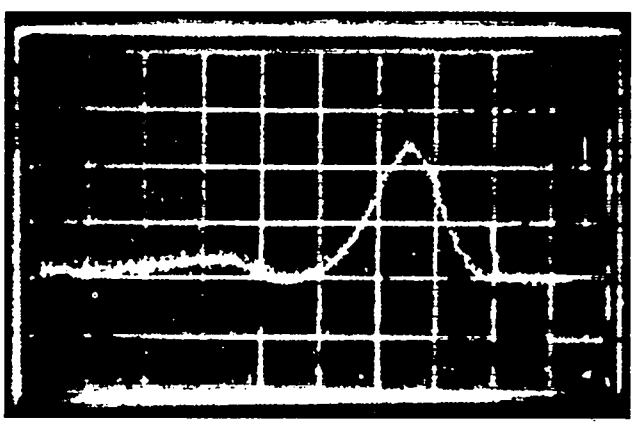

Fig. 41. Free-induction decay pulse displayed by 5-GHz oscilloscope.

Optical Damage with 1-ns Pulses

The oscillator-preamplifier system of the Two Beam System is occasionally available for damage experiments on window and mirror materials and for other experiments that require a 1-ns, 1-J pulse of good beam quality.

We have measured the damage threshold of high-power-laser-finish (HPLF) salt windows with single-layer antireflection (AR) coatings. The commercial AR coating tested increased the damage threshold from 5 J/cm^2 for uncoated windows to 10 J/cm^2. The effect is not well understood (it may be due to a smoother surface), but the result is encouraging. At present, almost 15% of the output energy of the dual-beam module of the Two Beam System is lost because the windows are not available in sizes large enough to mount at Brewster's angle. With AR coatings, we expect that the energy delivered onto the target will increase by ~10% without any change in dual- beam module operation. However, presently installed windows will be coated only after a sufficient number of extra windows is on hand to ensure that operations will not be interrupted, and after successful coating of these large windows has been demonstrated.

Comparison tests of damage to both NaCl and copper surfaces were performed in air and in vacuum; the results are summarized in Table VII. The damage threshold in vacuum did not decrease substantially.

We also conducted damage tests on a new mirror sample supplied by Westinghouse. This mirror uses sintered SiC as a substrate with polished, electroplated copper as the mirror surface. The sample has a damage threshold equal to that of bulk copper. The stiffness-to-weight ratio of sintered SiC is 6.5 times that of aluminum (the present substrate material of our large mirrors), 11.4 times that of copper, and 4.8 times that of molybdenum. In addition, SiC can be machined quite easily in its unsintered state.

Beam-Splitter Development

Plastic films, including polyethylene, Mylar, cellulose acetate, and Teflon, have been evaluated for use as beam- splitting pellicles. The damage threshold of polyethylene was substantially higher than that of any other material, ranging from 1 to 2 J/cm^2 independent of thickness. The internal absorption is low: 1-mil material absorbs less than a few percent of the transmitted beam. The reflectivity of all commercial polyethylene foils tested was highly variable because of poor control of film thickness. Fresnel interference between the two surface reflections causes variations in the reflectance from 1 to 10% in areas separated by only a few inches. Polyethylene pellicles are thus useful primarily when uncalibrated measurements are being made (e.g., pulse-shape measurements) or when in situ calibration can be carried out whenever the pellicle is replaced, moved, or realigned.

TABLE VII

MEASURED DAMAGE THRESHOLD FOR 10.6-μm, 1.2-ns PULSES

Material	*Test Condition*	*Damage Threshold (J/cm^2)*
NaCl (HPLF)	*Normal, uncoated, air*	*5.7*
NaCl (HPLF)	*Normal, uncoated, vacuum*	*5.4*
NaCl (HPLF)	*Normal, AR-coated, air*	*9.9 ± 0.5*
NaCl (HPLF)	*Normal, AR-coated, vacuum*	*7.1 ± 1.0*
Cu (micromachined)	*45°, air*	*9.25 ± 0.5*
Cu (micromachined)	*45°, vacuum*	*7.3 ± 0.3*
Cu (micromachined)	*Normal, vacuum*	*11.9 ± 0.6*
Cu (laser polish)	*45°, vacuum*	*10.5 ± 0.5*
Ge	*70°, vacuum*	*4.4 ± 0.3*

Optical Design and Analysis

The eight-beam, 10-kJ laser facility will require hundreds of optical components. Because of their cost and long procurement time, the optics ordered must perform as desired without significant modification. Therefore, computer programs capable of simulating a proposed optical train are desirable to evaluate the optical design. No existing program can perform this task with sufficient precision. However, some codes can handle parts of the problem and efforts are under way to obtain a code that would perform a complete analysis.

We have recently acquired ACCOS V, a commercial ray-tracing code, which has been incorporated into our computing system. The code is powerful in both design and ray-tracing analysis, but is poor in handling diffraction and off-axis systems. We are, therefore, developing additional in-house design codes to provide more flexibility in problems peculiar to laser-fusion systems; e.g., spatial filtering and beam propagation in high Fresnel-number regions.

We have used ACCOS V to examine critically the individual sections of our optical train. For example, we were uncertain of the magnitude of the aberration introduced by the Brewster-angle salt flat placed after the spatial filter in the modified triple-pass optics. The code showed that an astigmatic wave-front error of $\sim 0.5\ \lambda$ would be introduced. This aberration is unacceptably large and the window will therefore be installed at near-normal incidence.

Rotational Transitions in Ar-CO_2 Collisions

To optimize the performance of short-pulse CO_2 lasers in which the duration of the pulse may be equal to or shorter than the rotational relaxation time and, in particular, to optimize the choice of lines for multiline energy extraction, it is important to understand both the average rotational relaxation rate and its detailed mechanism. Detailed state-to-state cross sections and rate constants are therefore needed. Because the CO_2 rotational energy levels are very closely spaced, most experiments give only average rates. Relaxation experiments at best select the initial or final state but not both. Molecular-beam experiments yield much more detailed differential and integral cross-section data but still involve Boltzmann averages over initial state distributions. Final state information must be extracted from averages over energy spreads, beam widths, and other apparatus effects.

We are thus led to calculate the detailed rate constants needed and have constructed potential energy surfaces for the He-CO_2 and Ar-CO_2 systems.[22,23] Before calculating the He-CO_2, CO_2-CO_2, and N_2-CO_2 collisions that are important in the CO_2 laser, we tested the reliability of our methods. Accordingly, due to the availability of recent molecular-beam studies,[24,25] we have chosen the process,

$$Ar + CO_2(j) \rightarrow Ar + CO_2(j') , \qquad (15)$$

using classical trajectory methods. The classical results should be quite accurate; classical and quantum-mechanical calculations on rotationally inelastic Ar-N_2 collisions gave excellent agreement,[26,27] and the rotational and translational motions of CO_2 are both more nearly classical than those of N_2. In trajectory calculations the CO_2 was treated as a rigid rotor, which should be adequate at thermal energies where the probability of a vibrational transition is small.

Two different potential-energy surfaces were used. Both assume a short-range repulsive potential calculated with electron-gas methods[28,29] and a semiempirical long-range attractive van der Waals potential. The surfaces differ in the way the two are joined at intermediate distances. The overall agreement of the classical-trajectory results obtained from both surfaces with Loesch's[24] experiments is a good indication that the surfaces are basically correct and of useful accuracy.

The quasi-classical trajectory method[30,31] as modified for the rigid rotor[32] was used. The initial rotational state of CO_2 was included in the Monte Carlo sampling. Even-numbered states from 0 to 30 were chosen from a Boltzmann distribution at a temperature of 30 K to simulate Loesch's experimental conditions.[24]

Figures 42 and 43 present the integral cross sections and compare them to Loesch's experimental data.[24] These are not true individual cross sections, but represent averaged or apparent cross sections. The most striking feature of this com-

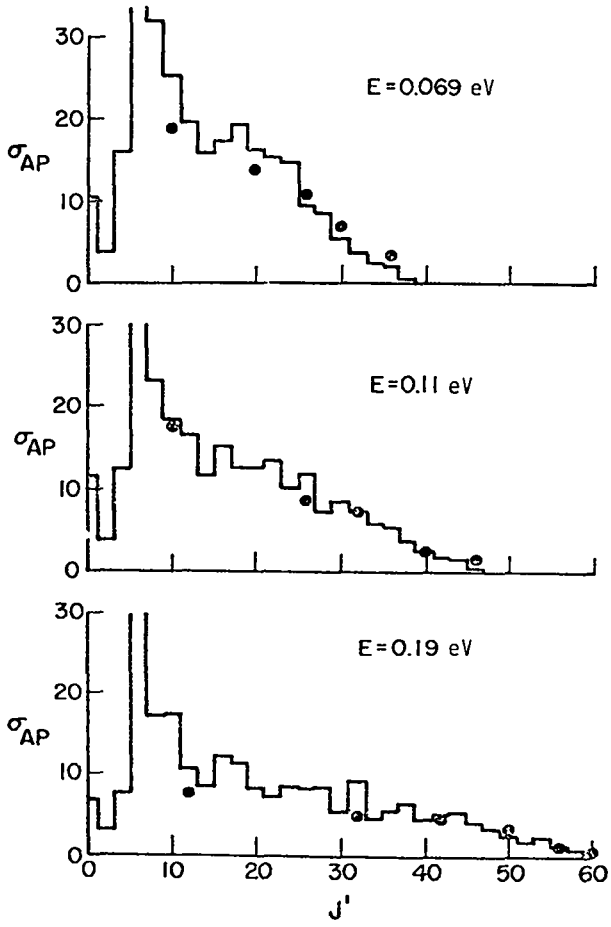

Fig. 42. Integral cross sections. Experimental data are shown as circles, whereas theoretical predictions for Surface 1 are shown in the histograms. The theoretical values are absolute cross sections, whereas the experimental values are relative cross sections.

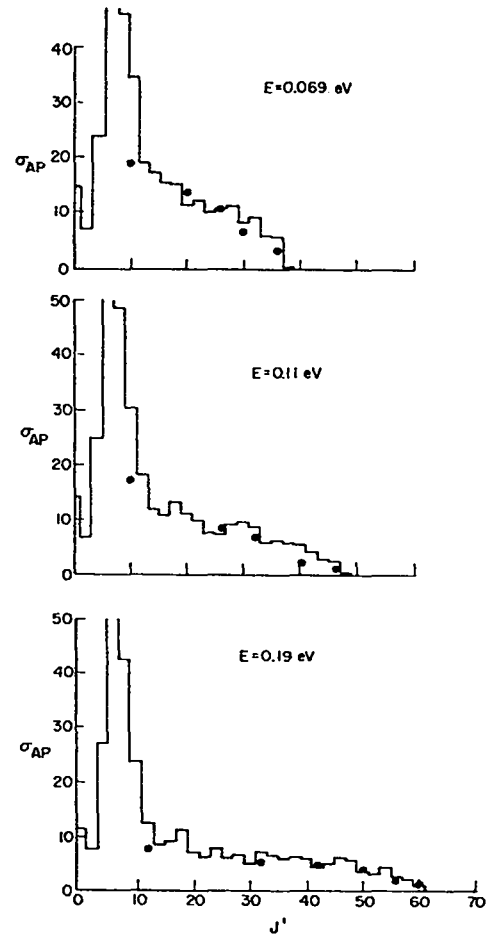

Fig. 43. Integral cross sections from Surface 2. Other notation and scaling are the same as in Fig. 42.

parison is the overall good agreement. The results for both of our surfaces as well as for Loesch's pairwise Lennard-Jones potential are in good agreement with experiment.[24,25]

The classical trajectory results for the two Ar-CO_2 surfaces used herein are in excellent qualitative agreement with detailed molecular-beam experiments. We also obtained good quantitative agreement for integral inelastic cross sections and (with Surface 1) for the angular distributions at most changes in rotational quantum number, Δj. The only significant discrepancy occurs for small Δj angular distributions where the results inferred from experiment may be unreliable.

We thus conclude that the highly anisotropic Ar-CO_2 surfaces obtained from the electron-gas model are giving rather good representations of the interaction, and are certainly accurate enough to be used in explaining the rates and mechanisms of rotational relaxation in CO_2 lasers.

REFERENCES

1. Dale B. Henderson, "Electron Transport in Gas Discharge Laser," J. Appl. Phys. 44, 5513-5516 (1973).

2. K. Boyer, D. B. Henderson, and R. L. Morse, "Spatial Distribution of Ionization in Electron-Beam-Controlled Discharge Lasers," J. Appl. Phys. 44, 551-5512 (1973).

3. A. Gondhalekar, E. Holzhauer, and N. R. Heckenberg, "Single Longitudinal Mode Operation of High Pressure Pulsed CO_2 Lasers," Phys. Lett. 46A, 229 (1973).

4. A. Javan, MIT, private communication.

5. S. L. McCall, "Self-Induced Transparency by Pulsed Coherent Light," Ph.D. Thesis, University of California, Berkeley (unpublished) 1968.

6. D. C. Burnham and R. Y. Chiao, "Coherent Resonance Fluorescence Excited by Short Light Pulses," Phys. Rev. 188, 667 (1969).

7. E. Yablonovitch and J. Goldhar, "Short CO_2 Laser Pulse Generation by Optical Free Induction Decay," Appl. Phys. Lett. 25, 580 (1974).

8. B. J. Feldman and J. F. Figueira, "Generation of Subnanosecond CO_2 Laser Pulses at 10.6 μm by Pulse Compression Techniques," Appl. Phys. Lett. 25, 301 (1974).

9. J. F. Figueira and H. D. Sutphin, "Generation of Multiband 1-ns Pulses in CO_2 Lasers," Appl. Phys. Lett. 25, 661 (1974).

10. C. R. Phipps, Jr., "A Study of Optical Scattering Methods in Laboratory Plasma Diagnostics," Stanford University Institute for Plasma Research report 281 (February 1969).

11. W. W. Simmons, S. Guch, Jr., F. Rainer, and J. E. Murray, IEEE/OSA Conference on Laser Engineering and Applications, Digest of Technical Papers, IEEE J. Quantum Electron. QE-11, 30 (1975).

12. A. Papoulis, Systems and Transforms with Applications in Optics (McGraw-Hill, New York, 1968).

13. J. W. Goodman, Introduction to Fourier Optics (McGraw-Hill, New York, 1968).

14. M. Born and E. Wolf, Principles of Optics (Pergamon, Oxford, 1975), 5th ed.

15. W. Magnus, F. Oberhettinger, and F. G. Tricomi, Tables of Integral Transforms (McGraw-Hill, New York, 1954), Vol. II.

16. E. Yablonovitch, "Spectral Broadening in the Light Transmitted through a Rapidly Growing Plasma," Phys. Rev. Lett. 31, 877 (1973).

17. N. H. Burnett and M. C. Richardson, "A Spark Gap Optical Isolator for High-Power Infrared Lasers," Rev. Sci. Instr. 47, 241 (1976).

18. R. V. Ambartzumian, V. S. Letokhov, E. A. Ryabov, and N. V. Chekalin, "Isotopic Selective Chemical Reactions of BCl_3 Molecules in a Strong Infrared Laser Field," ZhETF Pis. Red. 20, 597 (1974) [JETP Lett. 20, 273 (1974)].

19. J. L. Lyman, R. J. Jensen, J. Rink, C. P. Robinson, and S. D. Rockwood, "Isotope Enrichment of SF_6 in S^{34} by Multiple Absorption of CO_2 Laser Radiation," Appl. Phys. Lett. 27, 87 (1975).

20. G. Herzberg, Molecular Spectra and Molecular Structure, Vol. III. Electronic Spectra of Polyatomic Molecules (D. Van Nostrand Co., Princeton, 1966).

21. M. A. Duguay and J. W. Hansen, "An Ultrafast Light Gate," Appl. Phys. Lett. 15, 192 (1969).

22. R. T. Pack, "Van der Waals Coefficients Through C_8 for Atom-Linear Molecule Interactions, I. CO_2-Noblegas Systems," J. Chem. Phys. 64, 1659 (1976).

23. G. A. Parker, R. L. Snow, and R. T. Pack, "Intermolecular Potential Surfaces from Electron Gas Methods, I. Angle and Distance Dependence of the He-CO_2 and Ar-CO_2 Interactions," J. Chem. Phys. 64, 1668 (1976).

24. H. J. Loesch, "Rotationally Inelastic Wide Angle Scattering: The Anisotropy of the Repulsive Interaction Between Ar and CO_2," Chem. Phys., in press (1976).

25. J. M. Farrar, J. M. Parson, and Y. T. Lee, "Rotational Excitation of Linear Triatomic Molecules: Ar + CO_2, Ar + N_2O," Proc. 4th Int'l. Conf. on Molecular Beams (Cannes, France, 1973).

26. M. D. Pattengill, "An Application of the Semiclassical Approximation of the Generalized Phase Shift Treatment of Rotational Excitation: Ar-N_2," J. Chem. Phys. 62, 3137 (1975); "A Comparison of Classical Trajectory and Exact Quantal Cross Sections for Rotationally Inelastic Ar-N_2 Collisions," Chem. Phys. Lett. 36, 25 (1975).

27. R. T. Pack, "Close Coupling Test of Classical and Semiclassical Cross Sections for Rotationally Inelastic Ar-N_2 Collisions," J. Chem. Phys. 62, 3143 (1975).

28. V. I. Gaydaenko and V. K. Nikulin, "Born-Mayer Interatomic Potential for Atoms with Z=Z to Z=36," Chem. Phys. Lett. 7, 360 (1970); V. K. Nikulin and Yu. N. Tsarev, "On the Calculation of Repulsive Interatomic Potentials by the

Statistical Theory. Pairs of Positive Alkali Metal Ions and Noble Gas Atoms," Chem. Phys. 10, 433 (1975); and references therein.

29. R. G. Gordon and Y. S. Kin, "Theory for the Forces Between Closed-Shell Atoms and Molecules," J. Chem. Phys. 56, 3122 (1972); Y. S. Kim and R. G. Gordon, "Study of the Electron Gas Approximation," J. Chem. Phys. 60, 1842 (1974).

30. M. Karplus, R. N. Porter, and R. D. Sharma, "Exchange Reactions with Activation Energy, I. Simple Barrier Potential for (H,H_2)," J. Chem. Phys. 43, 3259 (1965); D. L. Bunker, "Trajectory Studies," in Int'l. School of Physics, "Enrico Fermi," Course 44 Molecular Beams and Reaction Kinetics (Academic Press, New York, 1970).

31. Henry H. Suzukawa, "A Quasiclassical Study of the Energy Transfer of CO_2-Rare Gas Systems," Ph.D. thesis, University of California, Irvine (1974). In this thesis, a classical trajectory study of Ar-CO_2 was described. The primary focus was on vibrational energy transfer. The results indicated that, at low energies, the rigid-rotor approximation should be reasonable for the description of rotational energy transfer.

32. R. A. LaBudde and R. B. Bernstein, "Classical Study of Rotational Excitation of a Rigid Rotor: $L_i^+ + H_2^*$," J. Chem. Phys. 55, 5499 (1971).

II. NEW LASER RESEARCH AND DEVELOPMENT

New types of lasers must be developed to provide the desired energy per pulse, pulse length, pulse shape, wavelength, and efficiency for laser-fusion applications. Our advanced laser research has focused on rare-gas oxides and on Hg_2 excimers.

INTRODUCTION

We have continued our efforts to investigate promising, efficient lasers operating in the visible and uv spectral region, and to identify new lasers for fusion research. Major emphasis has been placed on the study of rare-gas oxides and molecular mercury; the methods of excitation of these laser systems have also been investigated, as has been discussed extensively in previous reports. The experiments are complemented by a related theoretical support effort.

The experimental effort during this reporting period comprised experimental hardware construction, modification, and upgrade, as well as data acquisition and analysis. We anticipate that the construction phase of this effort will be finished within a few months.

In direct support of new laser research, we have continued our studies of optical damage to laser components.

EXPERIMENTAL STUDIES OF RARE GASES AND RARE-GAS OXIDES

General

We have concentrated (1) on upgrading an electron-beam-controlled electrical-discharge device to permit initial investigation of kinetic and stability processes at high gas pressures in the rare-gas oxides such as ArO; (2) on continuing our kinetics studies of the rare gases and rare-gas oxides by using high-power optical pumping techniques; and (3) on installation and testing of a new electron-beam accelerator, Cassandra, as well as on the development of related equipment needed to utilize this device for laser studies.

Electron-Beam-Controlled Electrical Discharges

Efforts are continuing to modify and upgrade our electron-beam-controlled electrical-discharge testbed which had previously been used for CO_2 laser experiments. The device has been operated with demonstrated electron-beam control at a gas pressure of 10 atm and a discharge-current density of 80 A/cm^2. The discharge-current risetime has been reduced from 300 to 50 ns. A new electron-beam supply crowbar operating at 200 kV permits the production of a well-controlled electron-beam pulse whose duration can be varied from 200 ns to 2 μs.

The experiments to be performed require a detailed characterization of the device parameters, such as electron-beam energy and current density. Most of the specialized diagnostic equipment we will need has been constructed. A series of detailed diagnostic measurements indicated that the beam energy transmitted through the foil window into the laser chamber is considerably below the beam supply voltage. The transmitted beam current density is also low, as expected. This behavior is not yet completely understood. This level of performance will prevent the electron beam from completely traversing the discharge cathode-anode gap, which will lead to a nonuniform electric-field distribution, thus preventing any clear interpretation of experimental discharge data. We are continuing to diagnose the cause of this behavior, and several solutions to the problem have been proposed. Suggested modifications will be incorporated into the

device, and initial experiments with rare gases and ArO will begin in August, 1976.

Kinetics Studies in Rare Gases

Short-pulse optical pumping has proven to be a powerful technique for the investigation of kinetic processes in high-pressure gases, and is being rapidly adopted by other investigators. The technique, the experimental apparatus, and results of studies in ArO have been described in previous progress reports and in the literature.[1] Our present effort is concentrated on kinetics investigations in pure krypton and xenon in an attempt to identify and quantify the important intermediate reactions that occur during the formation of rare-gas oxides.

Our short-pulse optical pumping system employs a Febetron-706 electron accelerator to excite high-pressure argon or krypton; the resulting dimer radiation provides an intense short-duration burst of uv light to irradiate a second test cell which contains the gas under study. The response time and the spectral range of the photomultiplier detection system have been increased through the addition of a new Varian photomultiplier tube with a sapphire input window. The photomultiplier has a characteristic rise and fall time of 0.3 ns, and exhibits high sensitivity over a spectral range of 140 to 800 nm. The Tektronix transient digitizer-computer data-processing system programs have been updated and are a valuable asset in these experiments. We are now able to operate with high sensitivity from the vuv region up to the near ir with a system response time of 0.8 ns. Background noise in this high-noise environment is less than 1 mV into a 50-Ω load. The programming now includes baseline correction, noise subtraction, data-interval selection, signal integration, linear and logarithmic plots, and routines based on simple physics models to fit experimental data.

Optical pumping techniques have been used to investigate the atomic and molecular excited-state kinetics of xenon and krypton. The experiments on these systems described in the literature are often difficult to interpret, largely because of the effects of electron collisions, ion recombination, and uncertainty in the deposition energy density. Unfortunately, it appears that published data have frequently been interpreted incorrectly because of the complexity of the experimental conditions. Optical pumping simplifies the situation because no charged-particle reactions occur. In addition, specific initial conditions such as initial-state identity and excited-state number density can often be attained and readily varied. In the case of xenon either the $^1P_1$ or $^3P_1$ state can be pumped by using the molecular continuum emission from argon or krypton, respectively.

Xenon data have been obtained as a function of gas pressure from 10 torr to 3 x 10^4 torr. Many kinetic processes are important over this pressure range even though the total number of kinetic processes is reduced through the use of optical pumping techniques. Figure 44 indicates an extremely simplified model for treating the data from low-pressure xenon. A correct model, Fig. 45, is much more complicated. Optical pumping is followed by fine-structure relaxation (Processes 1 through 6) -- the reverse reactions may also be important -- and by three-body molecular formation (Processes 7 and 8) of the vibrationally excited 0_u^+ and the 1_u and 0_u^- states, respectively. Because the 1_u and 0_u^- states are nearly degenerate and are in thermal equilibrium at all but very low pressures, we will refer to them as though they were a single state designated $1_u{:}0_u^-$. Vibrational relaxation must follow and, even if Process 8 is followed exclusively rather than Process 7a, redistribution must occur between the 0_u^+ and $1_u{:}0_u^-$ states during vibrational quenching. The redistribution determines the branching ratio and is independent of pressure if the vibrational relaxation is fast compared to

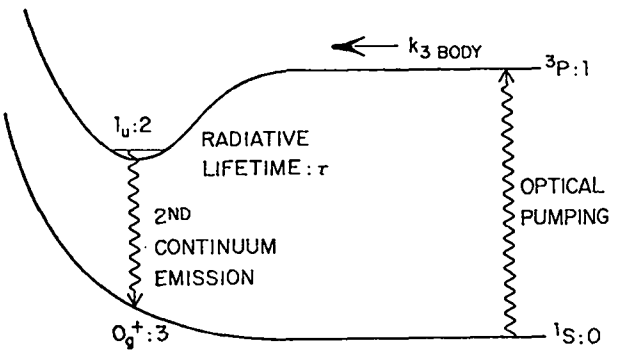

Fig. 44. Simplified kinetics model showing the various processes and state designations.

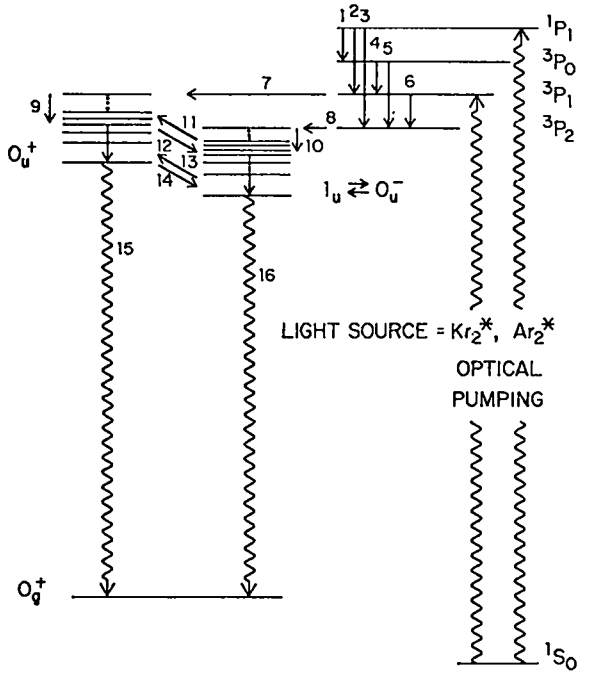

Fig. 45. Detailed kinetics model for rare gases.

the radiative lifetimes of the excited electronic and vibrational states. The branching ratio may be important for several reasons, including the consideration that the 0_u^+ state has a much shorter radiative lifetime and may be the only one that has a stimulated-emission cross section greater than the photoionization cross section for all the rare gases. After vibrational relaxation and redistribution, the ground vibrational states of 0_u^+ and 1_u:0_u^- are collisionally mixed. The rate for Process 12 is expected to be less than for Process 13 because of the 3:1 degeneracy and the thermal Boltzmann factors. Finally, radiative coupling to the dissociative ground state 0_g^+ completes the cycle. Other processes that may be important include quenching to the ground state from all the states shown, three-body processes associated with $^1P_1$, and radiative loss from the atomic states.

Although the rare gases are highly complicated systems, some reaction rates can be assumed to be zero and others to be very fast over particular pressure ranges. In addition, it should be possible to measure directly the branching ratio, the 0_u^+ and 1_u:0_u^- radiative lifetimes, and the 1_u:0_u^- mixing rate into 0_u^+, and k_{12}. The simplified model shown in Fig. 44 can be used under the following conditions: At low pressure, the two-body fine-structure relaxation times should be much faster than the three-body molecular formation times. Therefore, one could assume that $^1P_1$ and $^3P_1$ are strongly coupled into a single source state, defined as ^3P in Fig. 44. The three-body Process 7 in Fig. 45 is expected to be much slower than the two-body Process 6. Molecular formation is followed by radiation to the ground state.

The differential equations governing the temporal character of the system shown in Fig. 44 are determined by

$$dn_1 = (\text{pump} - n_1 n_o^2 k_{3B})dt \, , \tag{1}$$

$$dn_2 = (n_1 n_o^2 k_{3B} - \frac{n_2}{T_2})dt \, . \tag{2}$$

where n_1 and n_2 are the number densities of the excited atomic and dimer states, respectively. If we define $T_1 = (n_o^2 k_{3B})^{-1}$ and assume a delta-function pump pulse, then the solutions to these equations are.

$$n_1 = n_{10} e^{-t/T_1} \, , \tag{3}$$

$$n_2 = n_{10} \left(\frac{T_2}{T_1 - T_2}\right)\left(e^{-t/T_1} - e^{-t/T_2}\right) \tag{4}$$

where n_{10} is the initial atomic excited-state density. For the special case $T_2 = T_1 = T$,

$$n_2 = n_{10} \left(\frac{t}{T}\right) e^{-t/T} \, . \tag{5}$$

The time to the peak of the fluorescence signal for the general case is

$$t_{pk} = \left(\frac{T_1 T_2}{T_1 - T_2}\right) \ell n \left(\frac{T_1}{T_2}\right). \tag{6}$$

In this model we have neglected some important processes, such as fine-structure relaxation, vibrational relaxation, and electronic-state mixing.

However, the general form of Eq. (4) can be expected to provide a good fit if one uses "effective" radiative and three-body formation times. Figure 46 shows a computer-generated plot, based on the analytical function given in Eq. (4), and the signal observed. Here we have subjectively picked the "radiative" and "formation" times to fit the data. The "radiative" lifetime depends on the xenon pressure due to vibrational and fine-structure two-body processes when operating at pressures below 500 torr.

The preliminary three-body formation rate determined from these data was 2×10^{-31} $cm^6 s^{-1}$.

Data taken in high-pressure xenon, using a short optical pulse generated by electron-beam excitation of a mixture of argon and hydrogen by the Febetron 706 (pulse duration, 2.5 ns) indicated a systematic dependence on H_2 pressure, probably because of secondary pumping of the excited xenon. An investigation conducted to determine the spectral character of the pump source revealed that the spectral character was quite complicated and that the temporal character was dependent on wavelength. Window fluorescence was also observed and may set an upper limit on pulse energy for this kind of experiment. A dependence on window exposure to xenon was also noted. In any event, it is clear that wavelength selectivity is necessary to remove secondary pumping and the resulting ambiguities in the measurements. Figure 47 is a schematic of the present apparatus. The entrance and exit slits to Monochromator 218-1 have been removed and the optical pumping-source chamber and target chamber are bolted to the device with their MgF_2 windows near the position the slits occupied previously.

The reduced solid angle and added losses due to the introduction of additional optical elements reduced the optical transmission in the system by a factor of 100, but we are still able to see strong signals from the optically pumped xenon in the target chamber. Figure 48a shows the signal produced by a short optical pump pulse. A natural-log plot of the signal is shown in Fig. 48b. An obvious two-component exponential decay is observed. Note that only digital noise of ~ 200 μV is present. Secondary pumping is not observed. A plot of $1_u:0_u^-$ lifetime versus xenon pressure is shown in Fig. 49. The rate for

$$Xe^*_2(1_u:0_u^-) \rightarrow \text{PRODUCTS} \qquad (7)$$

is

$$(1.07 \pm 0.06) \times 10^{-14} \text{ cm}^3\text{s}^{-1} . \qquad (8)$$

There is substantial disagreement in the literature about this rate: Gleason, Keto, and Walters[2] obtained 7×10^{-15} $cm^3 s^{-1}$ and Gerardo and Johnson[3] obtained 4.3×10^{-14} $cm^3 s^{-1}$. Therefore, our work

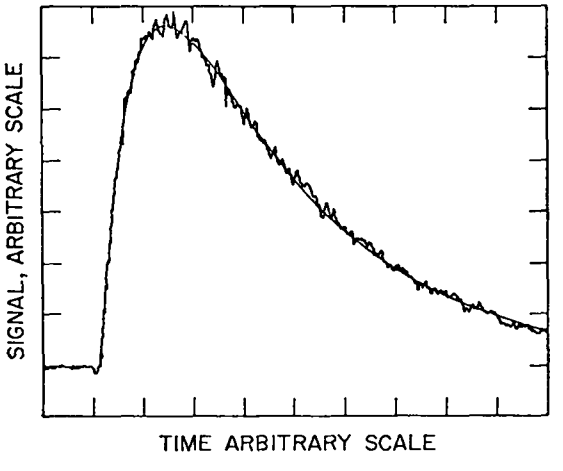

Fig. 46. Photomultiplier signal and computer calculation using $S(t) = a \exp(-t/T_1) - \exp(-t/T_2)$ for 80-torr xenon.

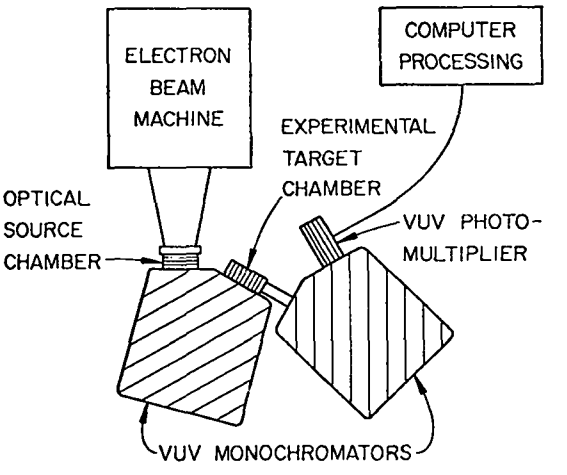

Fig. 47. Schematic of apparatus to ensure no secondary optical pumping occurs.

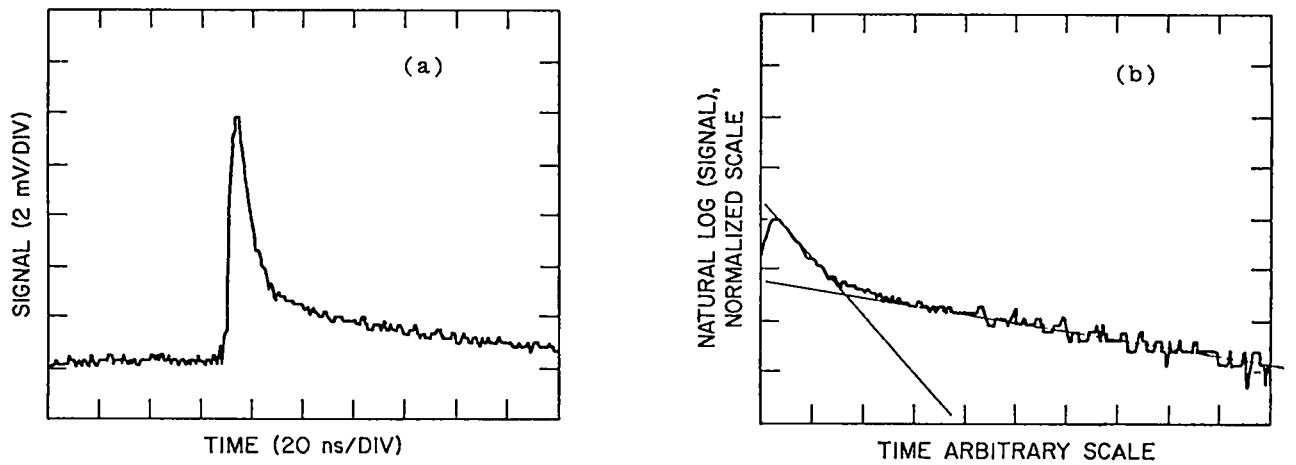

Fig. 48. Photodiode signal for 200-psia xenon using a 1500-psia Ar:150-psia Kr:1200-torr H_2 mix to fill the optical source chamber to 1000 psia; (a) linear scale; (b) logarithmic scale.

clearly supports the former result. Impurities are an unknown factor and the result of these three investigations must be regarded as an upper limit to the rate in question.

Optical pumping of krypton has been initiated and preliminary results indicate that the 0_u^+ decay time is typically 5 ns. The krypton work will continue and the techniques used will be extended to other systems of interest.

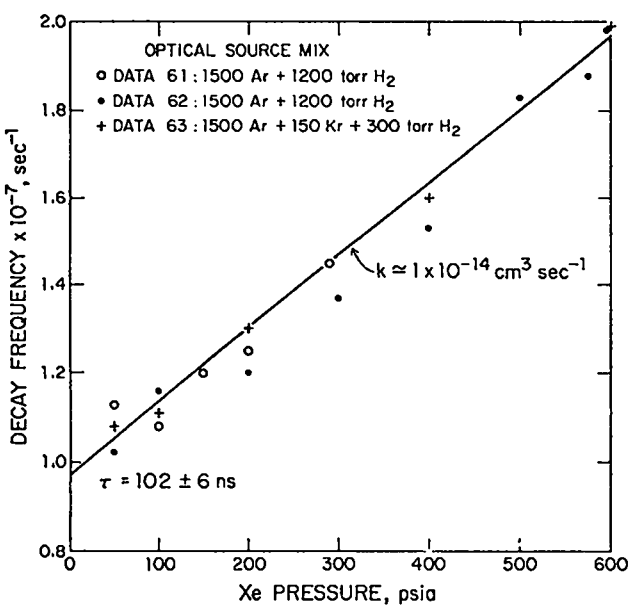

Fig. 49. Decay frequency of $I_u:0_u^-$ vs xenon pressure.

High-Energy Electron-Beam Experimental Facilities

The Cassandra electron-beam accelerator is a large device particularly suited for pumping a high-pressure gas-laser system. The characteristics of the machine, manufactured by Maxwell Laboratories, Inc., are a 2-MeV beam energy, a 50- or 100-cm cathode in a transverse-excitation geometry, an 11-ns current risetime, a duration of 20 to 40 ns, and a total energy delivery of 15 kJ. Modifications to the unit include both a 5- and a 10-Ω transmission line.

Substantial building modifications to install the machine are essentially complete. The 5-Ω configuration was installed and was tested satisfactorily. The 10-Ω line has since been installed and specification testing is about to begin. Design, procurement, and fabrication of a high-pressure stainless steel chamber are under way. This part of the experimental system should be operational by September 1976. The large chamber can be used to study direct electron excitation with gas pressures as high as 100 atm. Two smaller chambers can be optically pumped by the emission from the large chamber. One of the smaller chambers has a 100-cm-long array of MgF_2 windows to admit fluorescence from the large chamber. The input window to the other chamber acts as a high-transmission output coupler for laser oscillation in the large chamber. Techniques for mounting large-area foils are being

investigated. Ultrahigh-strength steel foil (Vasco 300) has been welded successfully to a flange and has been vacuum- and pressure-checked. In another test, a stainless steel foil was attached to a stainless steel flange by high-temperature pressing with Teflon acting as a glue. This foil assembly also passed the vacuum pressure check.

A conduit system is being installed. We expect that a large variety of experiments can be performed on this machine. Experiments on rare-gas oxides will be initiated immediately after installation and checkout of the chamber. Because of the large volume and high gas pressures employed, up to 100 ℓ/atm of rare gas could be used per pulse. Although a high vacuum is maintained throughout the system, contamination of the rare gas is inevitable. For gases such as xenon and krypton, these experiments become very expensive if the gas is not recycled. A gas-purification system is in the design stage. A closed-loop design will be used, with bulk gettering stages in the loop. A quadrupole mass spectrometer has been received and will be installed to analyze the gas and eventually to (1) identify impurities, (2) qualify various bulk gettering techniques for impurity removal, and (3) diagnose the gas during ordinary operation of the purification system.

METAL-VAPOR LASERS

Introduction

Some promising new laser systems, for both fusion and isotope separation, use low-pressure corrosive-metal vapors as the active species. Among these species are "association" laser molecules in which the molecule exists in a bound excited state but has no stable ground state. The rare-gas dimers and rare-gas halides are examples of this type of molecule that have been made to lase. Among these metal vapors are the group IIB dimers (Zn_2, Cd_2, and Na_2), the alkali group IIB excimers, alkali-rare-gas excimers, and group IIIA rare-gas excimers (e.g., Tℓ-Xe). The alkali dimer molecules, in addition, offer the possibility of laser action due to the phenomenon of "displaced potential," which allows a strong population inversion, as in the case of bound-free radiation, and is the mechanism responsible for the lasing of H_2 molecules. Finally, optical pumping of discharge-produced alkali resonance levels can generate ir lasing at several discrete wavelengths.

We are investigating the most promising of these systems and are investigating the possibility of using the heat pipe for containing these vapors.

In our basic investigations, we are studying these systems with excitation provided by an electrical discharge. In almost all proposed metal-vapor lasers, the initial excited state, from which the laser upper level is generated (either by optical pumping or through intermolecular recombination), is a low-lying level of the metal atom ($\lesssim$ 5 eV above the ground state). Such states, in general, have large cross sections for excitation by the low-energy electrons in electrical discharges. With appropriately chosen values of E/N (electric field/gas density), very large fractions of the input energy can be channeled into the states of interest. In the case of mercury, our calculations predict that the rates of electron production of the $^3P_1$ and $^3P_0$ states, which give rise to the molecular bands proposed for laser operation, can be four times higher than any other electron-production rate for values of $E/N \simeq 2$ to 3×10^{-16} V·cm^2. Similar behavior is expected for the other metal vapors. Furthermore, the levels are very low relative to the ionization potentials of the rare gases. Thus, in an electric discharge in a mixture of metal vapor and rare gas, virtually all the energy will be deposited in the excited states of the metal atom. Very little energy will be channeled into the buffer-gas ions, even at very large density ratios of buffer gas to metal vapor. Optical pumping and relativistic electron-beam pumping offer special advantages in terms of interpreting the operative mechanisms (optical pumping) and in terms of coupling large amounts of energy into the gas (electron-beam pumping), but both techniques are severely limited as to achievable conversion efficiency. We feel, therefore, that discharge excitation offers the best hope of building a scalable, high-power, high-efficiency device.

Of all known discharge schemes, transverse-discharge pumping, either preionized or electron-beam-sustained, allows the greatest amount of energy to be deposited per unit volume.

In addition to work on electron-beam-sustained techniques, we have developed a flashboard constructed of tungsten deposited on an alumina substrate, which is compatible with the vapors and temperatures encountered in our work. Discharge apparatuses of several sizes using these flashboards have been or are being constructed. Experiments are planned for the study of discharges in cesium rare-gas mixtures in heated cells, of sodium dimers and sodium rare-gas mixtures in large-aperture heat pipes and of mercury dimers in both heated cells and heat-pipe devices. The apparatuses for the first two systems are in preliminary stages of testing. The main experimental work has been performed in mercury discharges.

Electrical Discharges in Mercury

The Hg_2 dimer was proposed some time ago as a potential high-power laser medium.[4] It was initially suggested that the 485-nm band be investigated because it appeared most prominently in mercury discharges. A study of this band[5] excited by a relativistic electron beam showed net absorption at all wavelengths and seemed to eliminate Hg_2 from future consideration. However, further spectroscopic studies carried out under contract by NBS[6] revealed more detail about the band structure of mercury and, according to present interpretation, the trimer, Hg_3, is responsible for the 485-nm radiation. Furthermore, it was shown that the states responsible for the 485- and 335-nm bands were in thermal equilibrium, with an activation energy of ~ 6500 cm^{-1}. In superheated vapors, therefore, the dominant emission shifts from the blue to the uv band. This development revived interest in Hg_2, with emphasis shifted to the 335-nm band. In recent results, gain on the 335-nm band has been observed under electron-beam excitation.[7]

The apparatus used in our study is shown schematically in Fig. 50. The chamber can accommodate up to 50-cm-long electrodes. All seals are of the knife-edge type equipped with nickel gaskets to minimize the attack by mercury vapor. The feedthroughs are of all ceramic-metal construction with no precious-metal brazes, and the windows are of similar construction with sapphire optical flats. The sapphire windows are maintained at the temperature of the cell and are isolated from ambient air by vacuum buffer zones terminated in quartz windows at Brewster's angle. The mercury is contained in a reservoir appendage heated by an oven that is controlled independently from the main cell.

Initial discharge studies were performed with the electrode structure shown, having an active discharge area of 11.5 x 1.5 cm and an electrode spacing of 9.6 mm. The entire apparatus is capable of temperatures up to 823 K and pressures up to 5 atm. A stainless steel capacitance manometer is used to monitor the chamber pressure.

The discharge parameters were monitored under conditions of long pulse duration and low-current density, and short-pulse duration and high-current density. In the first case, the discharge apparatus consisted of a thyratron switch in series with a capacitor and a $CuSO_4$ load resistor. With this apparatus, stable glow discharges were obtained at current densities of ~ 100 mA/cm^2 for pulse lengths of ~ 60 to 70 μs before arcing occurred. The preionization consisted of discharging a 0.05-μF capacitor charged to ~ 16 kV across the tungsten-alumina flashboard. A delay generator was used to vary the delay between the preionization pulse and the main discharge. However, the discharge would not begin at voltages below ~ 4 times the stable glow value, without application of the preionization. Furthermore, delays of up to ~ 15 μs between preionization and discharge could be tolerated, although the discharge was better behaved for small delays (1 to 2 μs). A plot of the data obtained with this apparatus for E/N as a function of mercury density is shown in Fig. 51. Experimental

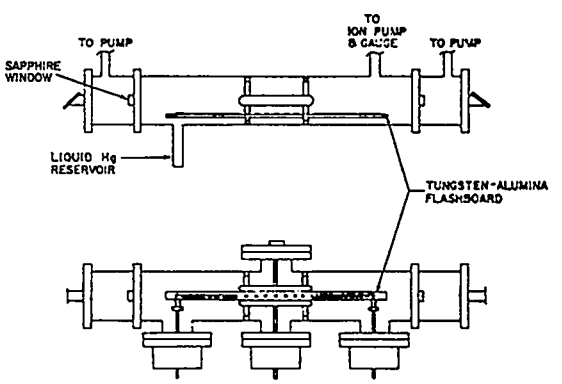

Fig. 50. Schematic for electrical discharge-heated cell configuration in mercury.

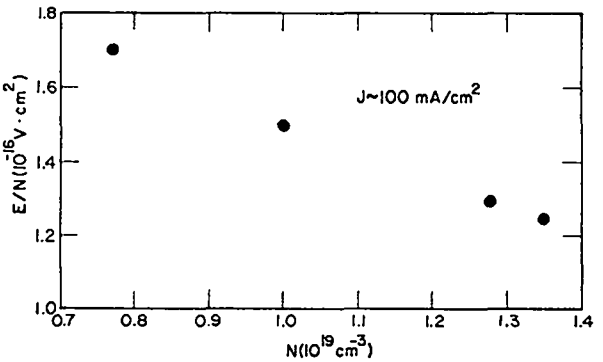

Fig. 51. E/N as a function of mercury density at constant current density.

difficulties prevented extension of the data to pressures above 965 torr.

Having established the basic integrity of the flashboard technique for producing stable discharges, we removed the load resistor in order to deposit more energy into the gas and obtained very uniform glow discharges at much higher current densities. The best discharge parameters we achieved are listed in Table VIII. By using the calculated drift velocity of 8.5×10^5 cm/s for this value of E/N, we estimated that the electron density is $\sim 4 \times 10^{13}$ cm^{-3}. To obtain an upper bound on the density of mercury excimers in the ^3l_u state, which radiates at 335 nm, we balanced the $^3P_1$ production rate ($\sim 3 \times 10^{-11}$ cm^3/s) with the excimer formation rate (which at these pressures should dominate the radiative rate) and the excimer formation rate against its radiative lifetime ($\sim$ 200 ns). This simple model neglects quenching collisions but should yield an order-of-magnitude estimate of the excited-state densities in the plasma. For the discharge conditions described above, we calculate an atomic density $N(^3P_1) \simeq 10^{14}$ cm^{-3} and an excimer density $N(^3l_u) \simeq 10^{15}$ cm^{-3}. The stimulated-emission cross section, σ, for this transition is estimated to be $\sim 3 \times 10^{-18}$ cm^2, and the upper limit on the expected small-signal gain therefore is $\sigma N(^3l_u) \simeq 0.003$ cm^{-1}.

TABLE VIII

DISCHARGE PARAMETERS IN MERCURY

Current density, A/cm²	*6*
Voltage pulse halfwidth, μs	*1.4*
E/N, V cm²	*2×10^{-16}*
N, cm⁻³	*10^{19}*
Pressure, torr	*750*
Cell temperature, K	*683*
Energy deposition, J/ℓ	*15*

An attempt was made to measure the small-signal gain in this apparatus by using a helium-cadmium laser operating at 325 nm as a probe beam because this wavelength lies approximately at the 65% point on the 335-nm emission profile of Hg_2. The maximum gain in the device was expected to be ~2.5%. Measurement of such a small gain on the present apparatus was expected to be marginal, and the results were inconclusive.

To circumvent some gain-measurement problems, we are installing 50-cm-long electrodes in the cell, are replacing sapphire windows with Brewster-angle quartz windows, and have purchased narrow-band interference filters at 325 nm to limit any interference from the broad-band spontaneous emission. These improvements should increase the anticipated gain to a more significant value of 10%. In addition, even if further gain-measurement problems arise, the new Brewster-angle windows should reduce the cavity losses to a level sufficiently low that direct lasing action can be obtained. Data from this apparatus are expected in the near future, which should resolve the question of whether the Hg_2 dimer can be made to lase.

Heat-Pipe Evaluation

The heat-pipe development program has been directed toward determining the feasibility of using such devices to contain high-pressure corrosive gases at high temperatures while maintaining the medium at a homogeneity and optical quality adequate for propagation of a visible or near uv light beam. We have built heat pipes ranging in diameter from 1.7 to 9.8 cm, which have been operated with working fluids of mercury, water, and sodium.

In the small-diameter device, four heat-pipe arms extended radially from a central cell that

could be operated in a superheated mode. This device is shown in Fig. 52; a detailed description was given in the previous progress report (LA-6245-PR). The cell was operated with mercury as the working fluid at pressures up to ~ 3 atm. This device produced reasonably well-defined interface zones between the metal vapor and the buffer gas at pressures up to 1 atm, which, although not perfectly vertical or planar, were at least temporally stable. The aberrations introduced by such interfaces could, in principle, be corrected by external optics. However, at pressures above 1 atm, the boundary layers showed signs of turbulence. In addition, we observed some streaming of mercury vapor through the boundary layer, as evidenced by condensation on the cell windows. No raining or cloud formation was seen at any time.

The design of this four-armed device did not allow the installation of a large electrode structure nor easy study of the discharge characteristics of small discharges. We therefore decided to build the largest device consistent with the maximum wicking height of a reasonable screen for mercury. Such a device, we felt, would permit the installation of a reasonably sized discharge apparatus and, simultaneously, would provide data on heat pipes scaled to the larger sizes required for high-power laser applications. The device was a 7.5-cm-o.d. by 90-cm-long tube with an unwicked, superheated 30-cm-long zone in the center and 30-cm-long heat-pipe zones at both ends. The initial study was to be done with mercury as the working fluid, but problems were encountered during initial attempts in obtaining adequate wetting of wicks. We therefore decided to study the heat-pipe characteristics initially with a more tractable fluid, water.

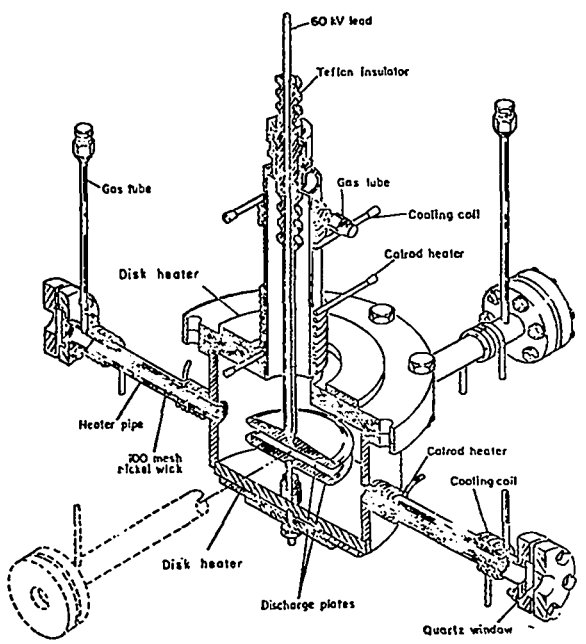

Fig. 52. Four-arm heat-pipe apparatus for initial investigation of electrical discharges in mercury.

Although the wicks were clearly saturated with water and pumping well, we had to match the density of the buffer gas to that of the saturated water vapor at the interface zone very carefully. Whenever these two densities became significantly different, severe stratification of the gases occurred, causing the interface to incline sharply from the vertical, permitting water vapor to stream through the interface barrier. We also observed that the vertical interfaces were not maintained by matching the buffer-gas molecular weight to that of the water, but rather by using a gas mixture of lower molecular weight. This implies that the temperature of the buffer gas at the interface is either somewhat lower than that of the saturated water vapor or is a function of the radial position in the pipe. In addition, changes in temperature (and therefore in vapor pressure) require different mixtures. Finally, even when the densities were precisely matched, condensation fronts and rain were observed, which seriously distorted the optical path. The large temporal fluctuations could be monitored by observing the pressure fluctuations at the buffer-gas reservoir.

We finally obtained reasonable wetting with mercury on plated (nickel followed by copper) stainless steel wicks, and the results were similar to those with water. Streaming of mercury vapor through the interface occurred at temperatures as low as 458 K (~ 3 torr mercury vapor pressure) with an overpressure as high as 325 torr. When the condensation front moved outward from the center of the cell, it did so only at the bottom of the pipe, with the upper half of the pipe showing only the temperature drop due to pure thermal conduction. Complete stratification of the heavy mercury vapor

at the bottom and of the less dense buffer gas at the top occurred in all cases -- again with evidence of strong turbulence and rain. No convenient gas with a density near that of mercury vapor exists and, hence, no vertical interfaces could be obtained.

The large-diameter (9.8 cm) heat pipe has been filled with sodium, but the data obtained to date are insufficient to determine whether its behavior parallels that of the 7.5-cm-o.d. device. Experiments are in progress to study the behavior of this heat pipe.

We tentatively came to the conclusion that state-of-the-art heat pipes are not promising devices for horizontal, large-aperture lasers. It appears that a reasonably stable high-pressure interface should not exceed a diameter of ~ 2 to 3 cm. This restriction would appear to rule out the use of heat pipes (and thereby of metals with either extremely high corrosiveness or very low vapor pressures) in lasers of very high power. However, only work with other fluids and geometries would prove or disprove this conclusion. In particular, it would be valuable to quantify the behavior of the interface zone inside the pipe.

THEORETICAL SUPPORT

Introduction

Theoretical support for new laser research has been concentrated in 3 areas: (1) assessing the effect of electron-collisional excited-state kinetics in argon and mercury electrical-discharge lasers; (2) performing semi-empirical calculations of electron-impact cross sections for the argon lasers; and (3) performing ab initio calculations for the electronic structure of KrO and XeO, and calculating the relevant transition probabilities.

Excited-State Kinetics in Argon and Mercury

The effect of electron collisions on atomic and molecular excited-state population densities can be significant in high-power electrical discharges and electrically excited lasers. The processes involved include impact ionization of excited states and collisions of the second kind (superelastic collisions). Because the cross sections for these processes are large, the interaction of electrons with excited states could be expected to modify significantly the electron-energy distribution function in the discharge, which is particularly important if the ratio of excited-state population to ground-state population is large.

To evaluate these effects, we compute the rate for the inelastic processes by averaging the inelastic cross section with the electron-distribution function. The latter is obtained from a solution of the Boltzmann transport equation, which includes the inelastic cross section for the ground and excited states weighted by the excited-state population fractions. The excited-state population fractions are, in turn, determined from a kinetics model that describes the energy flow in the excited states and the ion chemistry of the atoms and molecules in the discharge. The complete theoretical description, therefore, requires a simultaneous solution of the transport and kinetic equations. For a pulsed electrical discharge, this process requires solutions of the coupled equations at each time during the discharge sequence. Because very effective numerical techniques have been developed at Los Alamos to solve either the Boltzmann transport equation or the kinetics equations individually, the coupling of the two procedures is, in principle, straightforward. In practice, however, considerable computation time and expense are involved for typical discharge and laser systems of interest. To circumvent this procedure, we have used the Boltzmann equation in a parametric study to evaluate the effect of excited-state population fractions on the electron-distribution function. This method is simple and provides physical insight into the fundamental processes involved. The particular species investigated are argon and mercury; they were selected because both are being considered for laser systems, and because inelastic electron-impact cross sections for transitions to and from the excited states are available from the literature.

In our argon studies we included cross sections (taken from the literature) for 12 allowed electronic transitions and one lumped cross section for the forbidden transitions; only one inelastic process for ionization from the $^3P_2$ state was considered. The inelastic processes in mercury in-

cluded transitions from the ground state to the $^3P_0$, $^3P_1$, $^3P_2$, and $^1P_1$ states, as well as ionization. Ionization from the $^3P_0$ and $^3P_2$ levels was also considered.

In general, published data on electron-impact cross sections for electronic transitions in rare gases are very incomplete. However, theoretical laser modeling requires a complete set of accurate values for these electronic cross sections. We have therefore initiated cooperative experimental and theoretical efforts with outside contractors to obtain the needed data for argon and krypton, as described below.

The threshold energy levels for the lowest excitation processes in argon and mercury are shown schematically in Fig. 53. In argon, a large isolated cross section, due to the ionization from the $^3P_2$ metastable state, is apparent at 4.2 eV, well below the threshold energy for ground-state transitions to the ^3P levels. This process is expected to affect significantly the ground-state excitation rate to the ^3P levels at high population densities. Because the ^3P energy levels in all the rare gases are approximately 4 eV lower than the ionization level, the parametric behavior in He, Ne, Kr, and Xe should be qualitatively similar to that in argon.

The ^3P levels in mercury have about half the ionization energy. The net effect of ionization from the ^3P metastable levels is to cluster a number of inelastic processes at a threshold energy of 5 eV. Because of this near energy coincidence, any effect on the primary electron-distribution function and on the excitation rates from the ground state should be minimal. The results of our calculation illustrate this behavior qualitatively.

We have performed parametric studies over the range $0.5 \times 10^{-16} \leq E/N \leq 9 \times 10^{-16}$ V·cm^2. The fractional metastable densities chosen were 10^{-1}, 10^{-2}, 10^{-3}, and 10^{-4}. The electron-distribution function for argon is shown in Fig. 54 for $E/N = 3 \times 10^{-6}$ V·cm^2. Similar distribution functions have been obtained at other values. As indicated in the figure, a fractional population of 10^{-2} for the $^3P_2$ state can affect the electron-distribution function significantly, which is also reflected in the ground-state electron-excitation rate. Changes in the population fraction of the excited state change the excitation rates plotted in Fig. 55. The largest changes occur for the higher lying states, particularly at values of E/N near threshold for the ground-state excitation process. This behavior results from the fact that the low-energy cross section, i.e., $^3P_0 \rightarrow$ ionization, controls the tail of

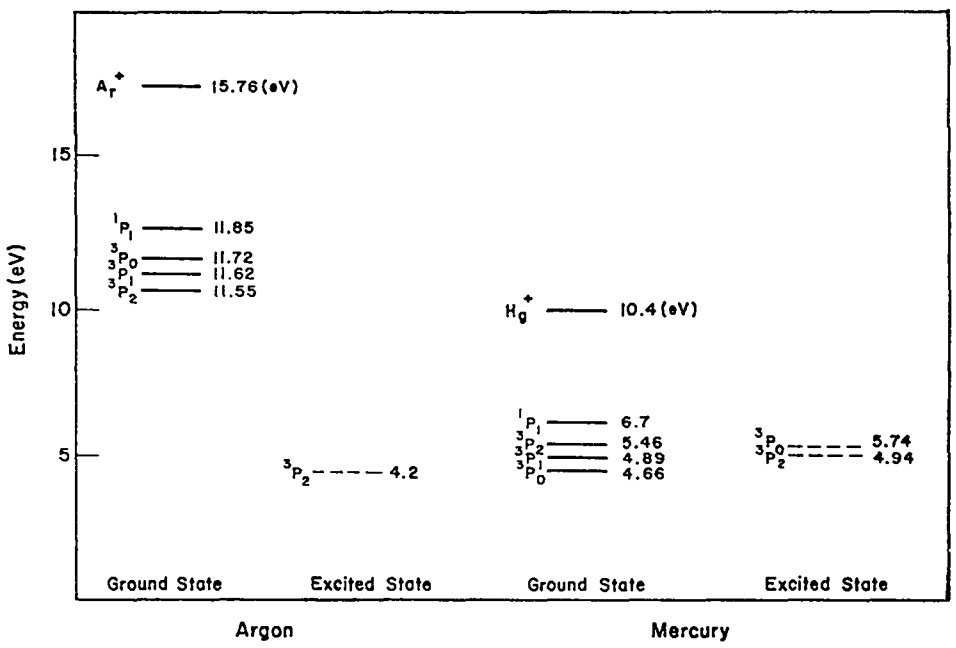

Fig. 53. Partial energy-level diagrams for argon and mercury.

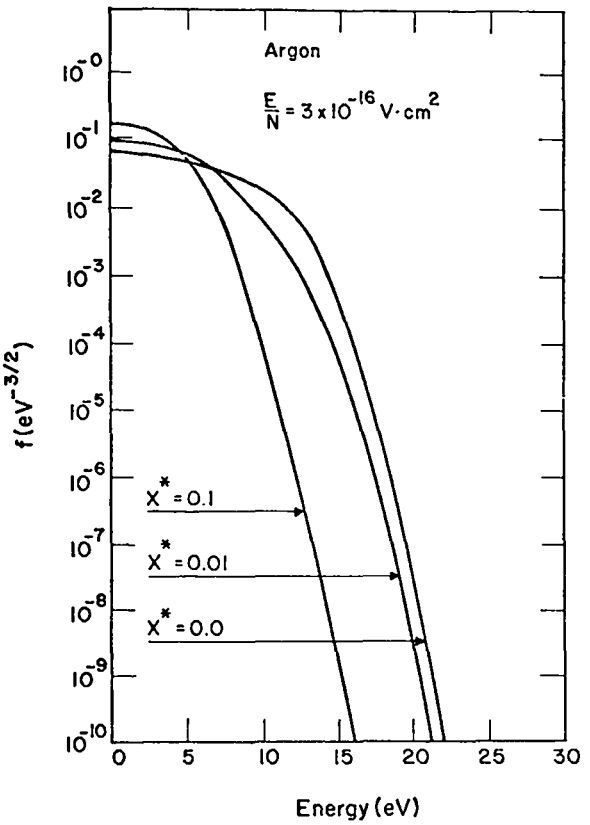

Fig. 54. Electron energy-distribution functions in argon for several values of the $Ar(^3P_2)$ excited-state population fraction X.

the electron-distribution function, which, in turn, dominates the behavior of the ground-state excitation rates. A quantitative example of this behavior is shown in Fig. 55. Plotted is the excitation rate for the $^3P_1$ level from the ground state as a function of E/N for several assumed population fractions of the $^3P_2$ state. Near threshold, the rate appears to decrease substantially as the population fraction increases. The onset for this interaction occurs at a $^3P_2$ fractional population, X*, of 10^{-4}. As $X^* \rightarrow 10^{-3}$ the rate decreases by a factor of 10.

The qualitative conclusion from this study is that as the ^3P excited-state population fractions approach 10^{-4}, electron-impact-induced transitions from these states to higher lying states or to the ionization continuum result in a change in the electron-distribution function, which reduces the excitation rates to these states. The magnitude of this effect, particularly important for values of E/N near threshold, increases as X* increases.

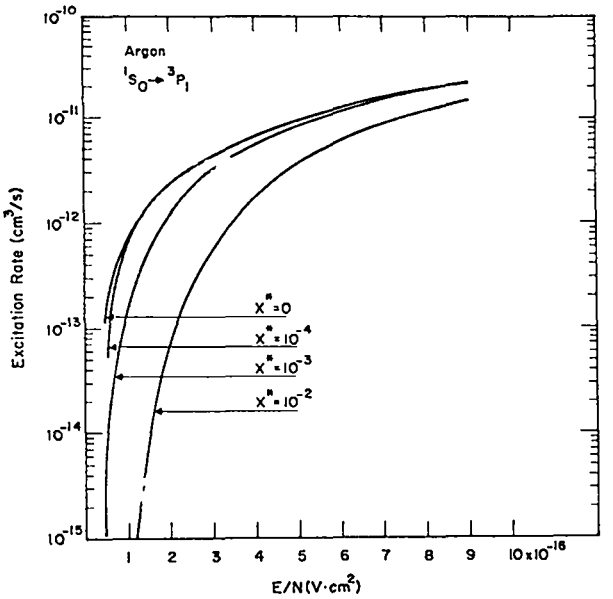

Fig. 55. Effect of $Ar(^3P_2)$ population fraction on $^1S_0 \rightarrow ^3P_1$ excitation rate.

The calculated distribution function for mercury is shown in Fig. 56 for E/N = 3 x 10^{-16} V·cm^2.

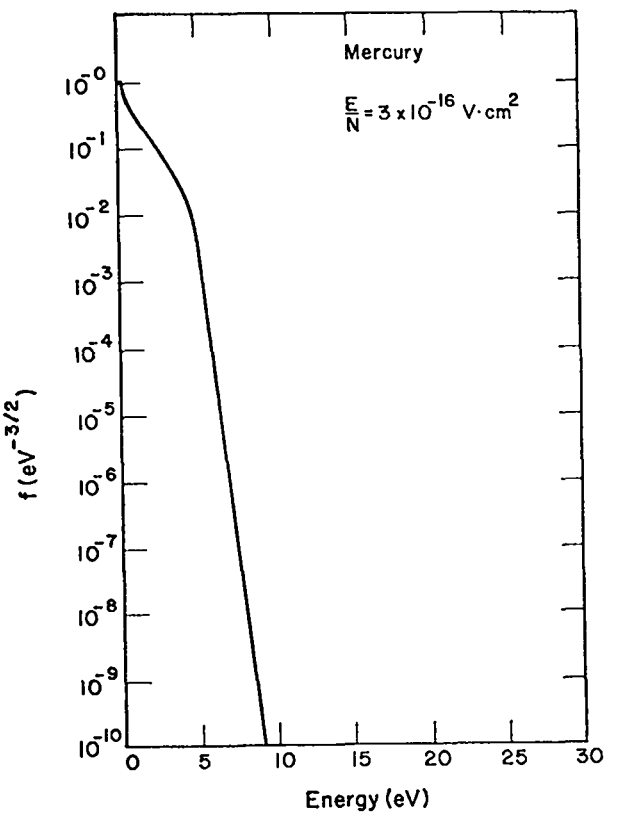

Fig. 56. Electron energy-distribution function in mercury for E/N = 3 x 10^{-16} V·cm^2.

For most practical purposes, the distribution function is unchanged for $X^* \leq 0.01$. Also, no significant variation in these rates is noted. Because the ^3P energy levels are about half the ionization level, all inelastic cross sections are clustered about a threshold value of 5 eV. The effects of inelastic processes for $X^* \leq 0.01$ from the excited states on the distribution function are greatly minimized, and the electronic excitation rates were found to be invariant.

The effect of excited-state population fractions can be illustrated in an alternative manner. The power flow into the i-th excited state, $P_x(i)$, can be written as a product of the inelastic excitation rate ν_{ij}, the electron density, the ground-state density, and the energy of the transition u_{ij}. Similarly, one can obtain the power flow from the i-th excited state to the ionization level, $P_I(i)$. The efficiency for production of a given excited state can then be expressed as

$$\eta_x(i) = \frac{P_x(i)}{P_x(i) + P_I(i)} , \qquad (9)$$

where $P_x(i)$ and $P_I(i)$ are functions of E/N through ν_{ij} (E/N) and X^*. A plot of η_x for the $Ar(^3P_2)$ state as a function of X^* and E/N is shown in Fig. 57. As indicated, the efficiency for producing the $Ar(^3P_2)$ excited state decreases rapidly for $X^* > 10^{-5}$, particularly for $E/N \leq 1 \times 10^{-16}$ V·cm^2. Because X^* is proportional to the energy input to the gas, η_x decreases as the energy input increases. Clearly, it is advantageous to operate at larger values of E/N to maximize η_x for a constant value of X^*.

The results of this study indicate that the effects of electron-induced transitions out of excited states in atoms depend on the level structure of the excited states with respect to the ionization level, on the cross section for transitions out of the excited states to higher lying states, and on the population fraction of the excited states. The dominant effect is the decrease of the average energy in the electron distribution and a consequent decrease in ground-state inelastic electron-excitation rates. These effects are larger in the rare gases than in mercury because of the electronic-level structure assumed in the calculation; in argon, the excitation rates begin to decrease when the excited-state population fraction X^* reaches 10^{-4}, whereas a similar effect in mercury begins when $X^* = 0.01$.

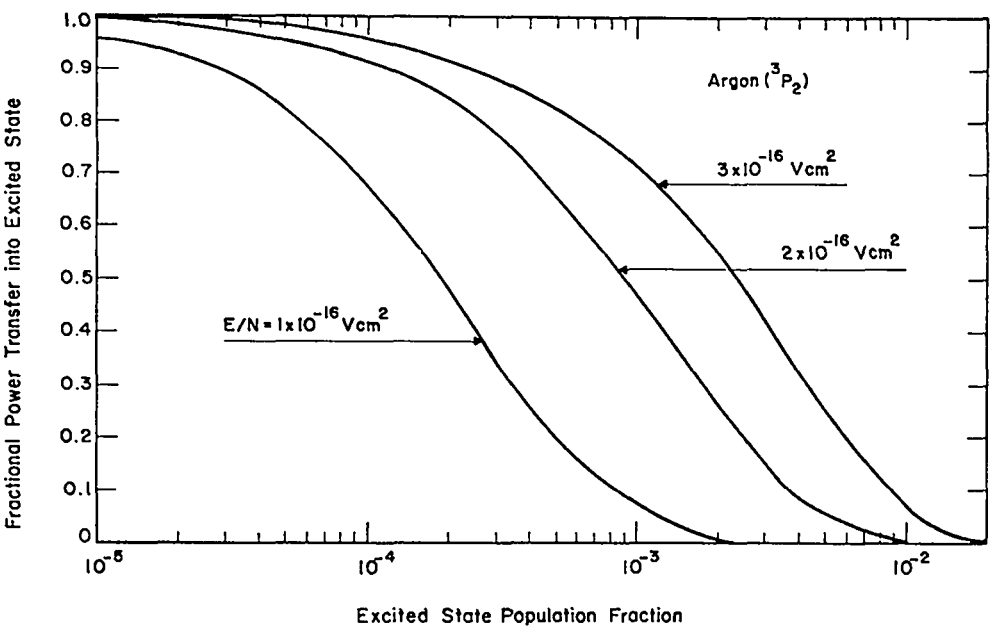

Fig. 57. Fractional power transfer into the $Ar(^3P_2)$ state as a function of X^* and E/N.

The results obtained in this calculation are only qualitatively correct, at best. If we had taken into account transitions from the lowest electronic excited states to the next-higher levels, the results for mercury would probably resemble closer those obtained for argon; also, the value of X* for the onset of the electron-distribution-function modification may be lower than 10^{-4}, depending on the excited-state energy-transfer kinetics.

Calculations such as those described above indicate qualitatively the effect of a high fractional population of the excited electronic states on the electron-distribution function and ground-state excitation rates, and provide a semiquantitative estimate for the value of X* at which these effects become important. The net result of these effects is to limit the fractional population and, consequently, the energy storage in the electronic levels with increased electrical excitation. This behavior may set a fundamental limit on performance of certain electric-discharge-pumped visible and uv lasers in which the rare gases are used to channel energy into a lasing specie. In particular, these effects should be important for lasers using the rare-gas oxides such as ArO and the rare-gas halides such as KrF and XeF. These effects are significantly reduced as E/N is increased.

These deleterious effects may be circumvented by introducing an additional energy channel that competes effectively with the electron-induced transitions out of the excited states. For example, with increased total operating pressure and gas-mixture optimization, two- and three-body collision processes, such as the direct formation of ArO and Ar_2, can compete with the excited-state electron processes. However, deleterious electron collisional processes, which are similar to those discussed for atoms, may also occur in molecules. Unfortunately, few, if any, data are available for reliably estimating the magnitude of this effect in molecules. A realistic evaluation of these processes will require experimental measurements.

Excitation Cross Sections for Argon and Krypton

Although electron impact processes in the inert gases have been studied experimentally since the early 1930's, absolute excitation cross sections for atomic levels higher than the lowest metastable states exist only for helium, and even in this case only for principal quantum numbers $n \leq 3$. Emission cross sections are readily studied experimentally but these cross sections almost always contain cascade contributions from higher excited states. This property of emission cross sections usually renders them only marginally useful for kinetic modeling purposes. More importantly, owing to experimental limitations on the spectral coverage and interpretation of these data, estimates have been obtained for only ~ 15% of the important excited-states cross sections for both argon and krytpon. In addition to a quantitative determination of the density of the excited states that form the upper state for the laser transition, absolute electron-impact cross sections for all the important excited-state transitions are essential for the determination of the electron-distribution function in the laser medium. Because rare gases are an important constituent of most lasers of programmatic interest, we have initiated a program, in cooperation with Jet Propulsion Laboratory, to determine a complete and consistent set of absolute excitation cross sections for argon and krypton. Progress made to date is reported below.

Relative differential excitation cross sections are extracted from electron-energy loss data, taken at fixed incident electron energy, for various scattering angles. Typical energy-loss spectra are shown in Fig. 58 for argon at an incident electron energy of 20 eV and scattering angles of 20 and 135°; and in Fig. 59 for krypton at an incident electron energy of 30 eV and scattering angles of 10 and 135°. Note the dramatic change in relative peak height of the spectra when the scattering angles are increased to 135°. This phenomenon is a manifestation of the fact that, for ℓ-s coupling, the differential cross sections for dipole-allowed and symmetry-forbidden transitions are usually peaked in the forward direction, whereas those for the spin-forbidden transitions are usually peaked in the backward direction.

These electron energy-loss spectra are then analyzed by a nonlinear least-squares technique to extract the relative contribution to each peak in the spectrum by the unresolved contribution from each individual state. Typical results for argon are shown in Fig. 60. The upper curve is the mea-

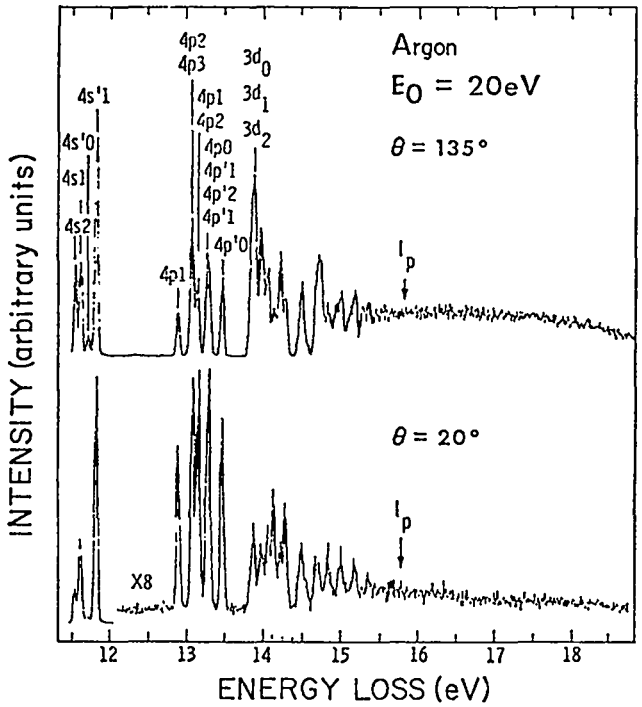

Fig. 58. Electron-energy loss spectra in argon for 20-eV incident electron energy and scattering angles of 20 and 135°. Orbital designations for some excited states are also shown.

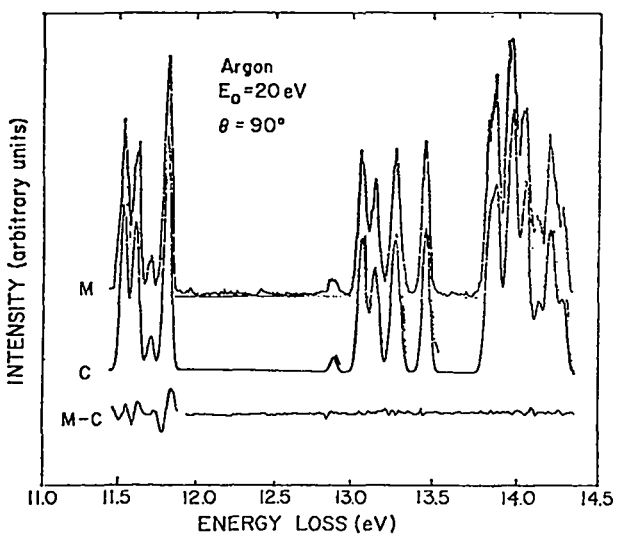

Fig. 60. Typical decomposition of an electron-energy loss spectrum in argon for 20-eV incident electron energy and 90° scattering angle. The upper spectrum is measured (M), the middle is calculated (C), and the lower is the difference spectrum (M-C).

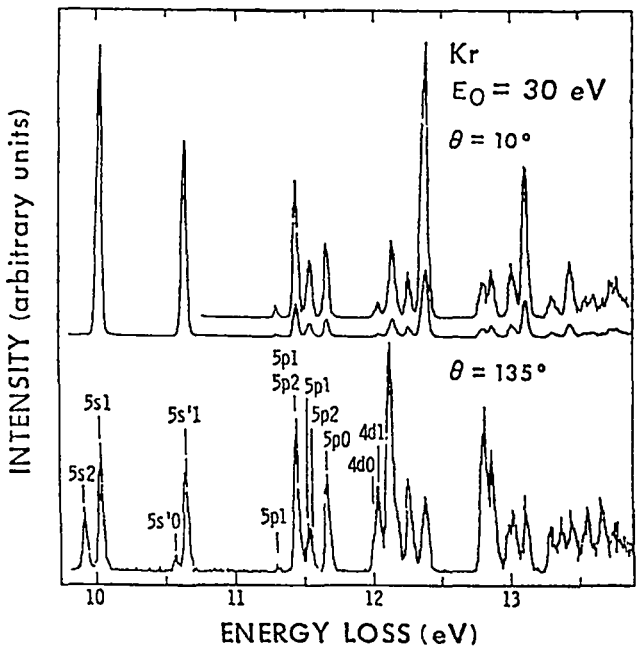

Fig. 59. Electron-energy loss spectra in krypton for 30-eV incident electron energy and scattering angles of 10 and 135°. Orbital designations for some excited states are also shown.

sured (M) spectrum, the middle is the calculated (C) spectrum, and the lowest curve is the difference spectrum. The spectrum is clearly fitted very well by this method which includes 26 different excited states. The computer results are being converted into absolute differential and integral cross sections for excitation of these 26 excited states by incident 20-eV electrons. Analysis of similar sets of energy-loss data at different incident electron energies will yield the energy dependence of the excitation cross sections. These cross sections will then be used to determine the electron-distribution functions in argon.

Electronic State Properties of Krypton and Xenon Oxide

Our work on the ArO molecule (see LA-6245-PR) has been extended to the KrO and XeO systems, with results shown in Figs. 61 and 62. In all these cases, we examined the emission of the $O(^1S) \rightarrow O(^1D)$ line at 558 nm, which is collision-induced by the rare gas. The electronic transition intensity between the relevant molecular states ($2\,^1\Sigma^+ \rightarrow {}^1\Sigma^+$ in the figures) increases in the order Ar < Kr < Xe. This sequence might suggest shorter lifetimes

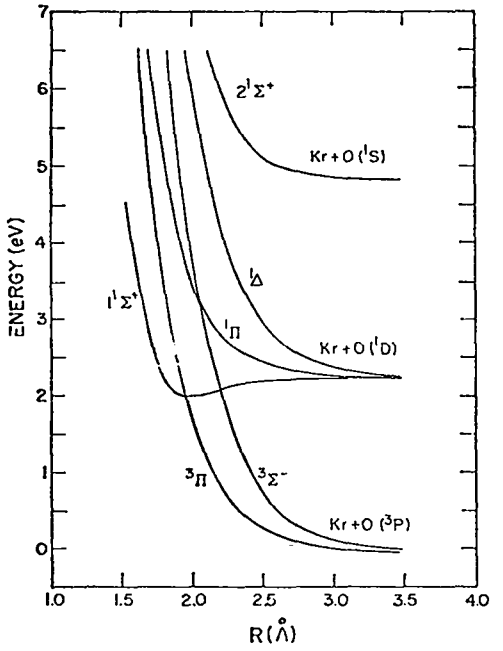

Fig. 61. Potential-energy curves of low states of KrO.

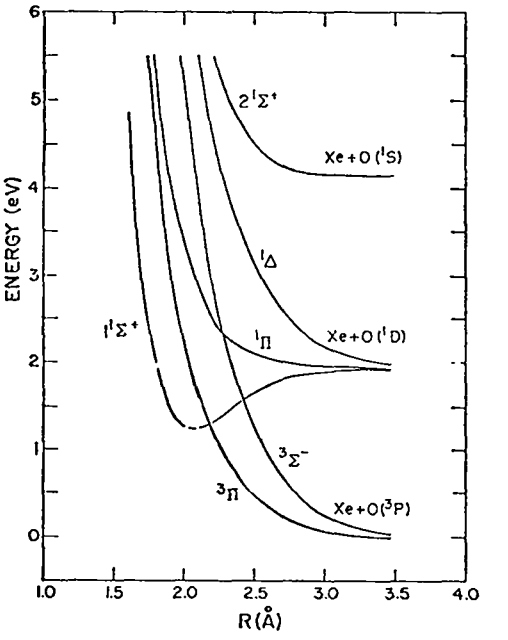

Fig. 62. Potential-energy curves of low states of XeO.

for the heavier systems, but meaningful estimates will require further analyses of the Franck-Condon factors and thermal-energy distributions. In addition, we obtained a pronounced well in the lower state ($1\ ^1\Sigma^+$) of the lasing transition, with well depths increasing again in the order Ar < Kr < Xe. The calculated well depth in XeO (0.7 eV) is twice that previously estimated, and the existence of such wells should lead to enhanced depletion of the lower laser level by quenching the O(^{1}D) population to the O(^{3}P) ground state.

OPTICAL DAMAGE STUDIES

Testing Capability

As discussed in previous reports, optical damage is a major problem in high-power visible and uv lasers. Because of increased interest in the uv and visible wavelength regions for use in laser fusion, we have extended the capability of our laser-damage testing facility. We can now test at 0.532 μm by frequency-doubling a 1.06-μm beam, and have installed a frequency tripler for the production of 0.355 μm; no damage tests have yet been performed at this latter wavelength. We are now well equipped to evaluate coating materials in the uv range, including coatings produced by rf sputtering under contract with Battelle Pacific Northwest Laboratories and Optical Coating Laboratory, Inc. (OCLI), Santa Rosa, CA.

RF-Sputtered Dielectric Films

The development of rf-sputtering techniques for the deposition of damage-resistant films of TiO_2 as laser coatings has been reported previously.[8,9] The coatings have been produced at Battelle Pacific Northwest Laboratories, and several problems have been solved. The best of these coatings are now superior to electron-gun-produced coatings.

The previously observed large radial variation in coating thickness, produced by the sputtering diode head, has been largely eliminated by the use of a glass guard ring mounted in such a way that the substrate sees a more uniform electric field. Thickness uniformity is now limited only by the target-to-substrate shape factor.

Our efforts to define the deposition parameters for SiO_2 films continued. Several coatings of SiO_2 have been received for damage evaluation, but have not yet been tested.

Battelle has produced single-layered sputtered coatings of TiO_2 and SiO_2 that are quarter-wave ($\lambda/4$) thick at 0.532 μm as well as at 1.06 μm. These coatings will be evaluated soon.

New contracts have been initiated with Battelle and OCLI for the development of sputtered coatings. Work at Battelle will concentrate on studying new damage-resistant materials for the uv range. Materials to be investigated include HfO_2, Y_2O_3, and Al_2O_3; sputtering parameters for these materials will be optimized.

Optical Coating Laboratory, Inc., will apply Battelle's results and experience in sputtering TiO_2 under production conditions. They will optimize the sputtering parameters for TiO_2, ZrO_2, and SiO_2, and will produce usable reflectors for 532- and 355-nm laser light. Both contracts begin in July 1976.

Effect of Standing-Wave Electric-Field Configuration on Optical Damage of Multilayer Optical Coatings

Experimental evidence on the effect of standing-wave (SW) electric-field configurations on the damage resistance of single dielectric thin films has been described previously.[8] By using 30-ps laser pulses at 1.06 μm, we found that the damage thresholds for TiO_2 films of odd quarter-wave thickness were higher than for even multiples. This finding correlated well with predicted internal peak fields.

We have extended our investigations to multilayer optical coatings of, e.g., reflectors. Two sets of experiments were performed. The first evaluated the effect of depositing an additional SiO_2 coating onto a 17-layer TiO_2-SiO_2 reflector. Addition of a half-wave thickness of SiO_2 does not change the internal electric-field distribution at the design wavelength of a reflector, except in the extra SiO_2 layer itself (see Fig. 63). However, adding a quarter-wave thickness increased the electric field significantly, by as much as a factor of 2.1. Results of damage tests on two specimens of each of these three coating configurations are listed in Table IX along with the corresponding SW field enhancements.[10]

Although the value of E^2 in the half-wave SiO_2 overcoating for the same incident power was 2.4 times higher than in any other layer in the reflector, the damage threshold was not affected significantly. We therefore conclude that the first high-index layer, TiO_2, fails first. However, adding a quarter-wave SiO_2 layer increased the field maxima in all layers 2.1-fold and reduced the damage threshold correspondingly, by as much as a factor of 2.5. The damage threshold in a reflector thus seems to be limited by the weaker of the two coating materials, i.e., TiO_2, with the breakdown threshold energy reduced by the increased electric field in the layer.

The reflectors used in the preceding experiment were coated in subsequent runs in which slight differences in coating properties could have resulted from small unintentional deviations from nominal fixed deposition conditions. To eliminate these potential sources of uncertainty in comparing

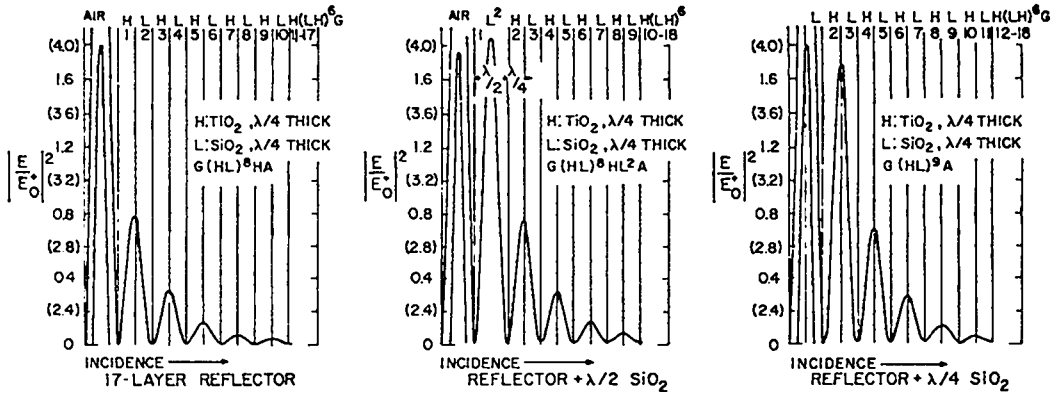

Fig. 63. Standing-wave electric-field intensities in three TiO_2/SiO_2 multilayer reflectors: (a) 17 layers; (b) same as (a) plus $\lambda/2$-thick SiO_2 overcoat; and (c) same as (a) plus $\lambda/4$-thick SiO_2 overcoat.

TABLE IX

DAMAGE THRESHOLDS OF TiO_2/SiO_2 REFLECTORS

Coating	Peak Energy Density (J/cm^2)	Mean Value of Two Samples (J/cm^2)	Standing-Wave Electric-Field Enhancement, $\lvert E/E_o^+ \rvert^2$	
			In TiO_2	In SiO_2
17-layer reflector	2.7 - 4.0 2.2 - 4.0	3.2	0.79	0.79
Reflector + $\lambda/2$ SiO_2 overcoat	3.3 - 4.3 2.2 - 4.2	3.5	0.79	1.89
Reflector + $\lambda/4$ SiO_2 overcoat	1.2 - 1.5 1.0 - 1.3	1.3	1.66	4.00

coatings deposited in different runs, OCLI deposited four different TiO_2-SiO_2 quarter-wave stacks during the same coating run. Sample A was a 9-layer reflector, whereas Samples B, C, and D were 8-layer stacks obtained by eliminating a prescribed single layer by the use of shields. The internal electric-field distributions of these four samples differed greatly as shown in Fig. 64.[11]

Figure 65 shows field patterns that have been normalized relative to the value of the incident electric field corresponding to the energy density at the damage threshold. The two curves shown for each coating correspond to the maximum and minimum measured threshold ranges. The horizontal bar marks the value of the electric field (7.7 MV/cm) in TiO_2, which best fits all four cases. Again, the high-index layer failed first. Apparently, the SiO_2 layer survived at least 13 MV/cm. These experiments show conclusively that laser damage in high-quality dielectric films is limited by the peak internal electric field. Note that in some coatings, e.g., in ZrO_2, the effect of the SW electric field can be masked by coating defects.[12]

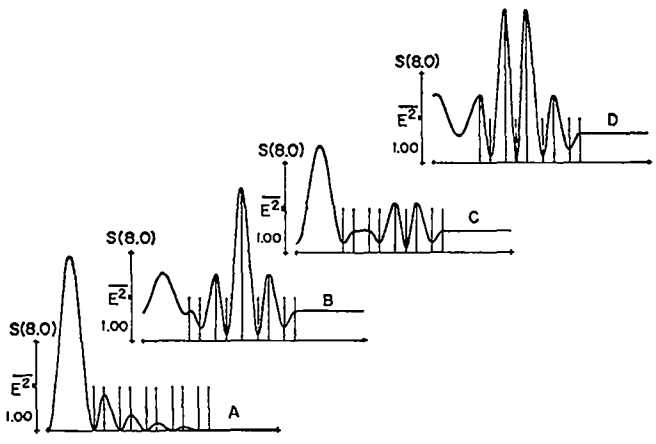

Fig. 64. Electric-field profiles for S-polarized radiation incident at 8° on four multilayer designs.

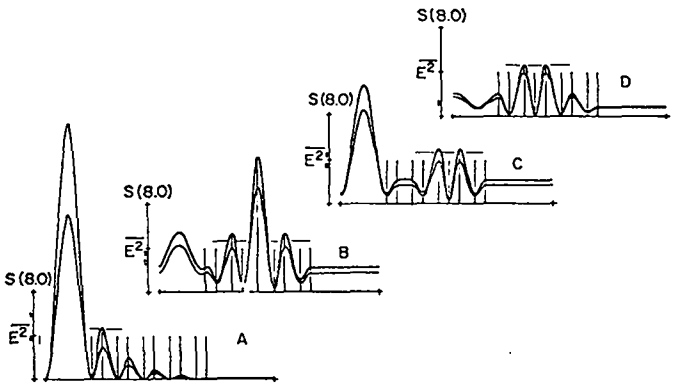

Fig. 65. Electric-field profiles for four designs with incident intensities adjusted to equal the extremes of observed laser damage ranges. The short horizontal lines are placed at the same value on each profile (~ 8 mV/cm).

REFERENCES

1. W. M. Hughes, N. T. Olson, and R. Hunter, "Experiments on the 558-nm Argon Oxide Laser System," Appl. Phys. Lett. 28, 81 (1976).

2. R. E. Gleason, J. W. Keto, and G. K. Walters, "Collisional Mixing of the Lowest Excited States of Xe_2 and Ar_2," 28th Annual Gaseous Electronics Conference, Rolla, Missouri, October 21-24, 1975.

3. J. B. Gerardo and A. W. Johnson, "Formation and Decay of Xenon Dimers in Photoexcited Xenon and Xenon-Noble Gas Mixtures," 28th Annual Gaseous Electronics Conference, Rolla, Missouri, October 21-24, 1975.

4. R. J. Carbone and M. M. Litwak, "Intense Mercury-Vapor Green-Band Emission," J. Appl. Phys. 39, 2413 (1968).

5. R. M. Hill, D. J. Echstrom, D. C. Lorents, and H. H. Nakano, "Measurement of Negative Gain for Hg_2 Continuum Radiation," App. Phys. Lett. 23, 373 (1973).

6. R. E. Drullinger, M. M. Hessel, and E. N. Smith, "Analysis of Optically Excited Mercury Molecules," NBS Monograph 143 (1975).

7. L. A. Schlie, B. D. Guenther, and R. D. Rathge, "Positive Gain Measurements on the 3350 A Continuum Band of Hg_2," Appl. Phys. Lett. 28, 393 (1976).

8. F. Skoberne, "Laser-Fusion Program at LASL, July 1 - December 31, 1975," Los Alamos Scientific Laboratory report LA-6245-PR (July 1976).

9. D. H. Gill, B. E. Newnam, J. S. Hartmann, and W. J. Coleman, "Super-High Damage Thresholds for RF-Sputtered TiO_2 Films," OSA 1975 Annual Meeting, Boston, MA, October 1975.

10. B. E. Newnam and D. H. Gill, "Laser Damage Resistance and Standing-Wave Fields in Dielectric Coatings," OSA Asilomar Conference on Optical Interference Coatings, February 24-26, 1976.

11. J. H. Apfel, J. S. Matteucci, B. E. Newnam, and D. H. Gill, "The Role of Electric Field Strength in Laser Damage of Dielectric Multilayers," 1976 Symposium on Damage in Laser Materials, Boulder, CO, July 1976.

12. B. E. Newnam, D. H. Gill, and G. Faulkner, "Influence of Standing-Wave Fields on the Laser Damage Resistance of Dielectric Film," in Laser-Induced Damage in Optical Materials: 1975, NBS Special Publication 435, pp. 254-271.

III. LASER FUSION -- THEORY, EXPERIMENTS, AND TARGET DESIGN

In an integrated program of theory, target experiments, and target design, we are establishing a fundamental understanding of laser-target interactions, particularly of the relevant plasma physics and hydrodynamics. Both the experimental and the theoretical efforts have concentrated on studying the wavelength-dependence of laser-plasma interactions. The close coupling of theory and experiment has made it possible to eliminate theories that are not supported by experiment. In general, basic studies of laser-plasma interactions have shown that the design difficulties associated with long wavelengths are less severe than believed earlier, and that breakeven target designs are attainable even in the presence of a hot-electron spectrum. These results have given us new confidence that significant yield can be obtained from more efficient, less expensive CO_2 lasers.

WAVELENGTH SCALING IN LASER FUSION

Introduction

Throughout the short history of the laser-fusion program, the wavelength-dependence of laser-target interactions has been a central question. Early theoretical predictions were based largely upon idealized collisionless plasma simulations and hydrodynamic models, but recent experimental and theoretical results disagree with their findings. The crucial measurements for wavelength scaling are hot-electron spectra and fast-ion energies. Below, we review three theoretical models for hot-electron energies and their wavelength scaling, and compare their predictions with experimental results. Only the third model, which predicts a weak or nonexistent wavelength-dependence, is consistent with experimental results.

Suprathermal Electrons

It is well-known experimentally that some suprathermal electrons are created by the laser light interacting with the expanding plasma. These high-energy particles also appear to transfer a significant fraction of their energy to high-energy ions. Because of their large range, these hot electrons can prevent the idealized isentropic target compression by preheating the target fuel. The following recent experimental results indicate at most a weak wavelength dependence of electron and ion spectra:

- The maximum observed fast-ion velocity is approximately independent of wavelength at intensities on target of $\sim 10^{15}$ W/cm^2.[1]
- The effective temperature of hot electrons emitted from the plasma is approximately independent of wavelength.[2,3]
- The maximum velocity of fast ions emitted from the rear of flat targets depends on target thickness identically at both wavelengths.[4]

A fundamental theoretical problem, then, is to determine the energy spectrum of these hot electrons and the dependence of the spectrum on laser intensity and wavelength. An important process, which must be included, is the alteration of the low-density hydrodynamic expansion of the plasma by the electromagnetic pressure of the incident laser light. Previously, hydrodynamic models have neglected this effect.

Models of Hot-Electron Energy

Three classes of models of hot-electron energy exist, which give rise to different scaling laws, generally of the form

$$T_H \propto (I_L \lambda^2)^{\delta} , \qquad (1)$$

where T_H is the hot-electron temperature, I_L is the laser intensity, and δ is the scaling factor. These models are summarized in Table X and are described in detail below.

Model 1: Parametric Instabilities in a Homogeneous Plasma -- This model argues that the hot-electron energy is determined by the oscillating energy of a free electron in the laser electromagnetic field or at least scales with the critical density.[5] This model gives a scale factor $\delta = 1$ in our scaling law:

$$T_H(\text{keV}) = 1.9 \times 10^{-16} I_L \lambda^2 , \qquad (2)$$

where I_L is in W/cm^2 and λ is in μm. Model 1 must be disregarded because of the marked inhomogeneity in fusion experiments and because of the fact that λ^2 scaling is inconsistent with our experimental results.

Model 2: Flux Limit -- This model is obtained by equating the laser power absorbed to the heat flowing away from the absorbing region, assuming that the absorption process is "stochastically thick," i.e., that the electrons are heated in many collisions.[6] As shown below, the latter assumption is the primary problem with this model.

If hot electrons are carrying away all the heat, we have

$$\alpha I_L = \beta n_H m_e V_H^3/2 , \qquad (3)$$

where α is the absorbed fraction of the incident laser flux, V_H is the effective thermal velocity of the hot electrons, n_H is the density of hot electrons, and β is the flux-limit factor. Assuming stochastically thick absorption, we have $\beta n_H = 0.06\ n$, where n is the total electron density and V_H is determined by energy balance. We then find, from Eq. (3), that

$$T_H \propto (I_L \lambda^2)^{2/3} . \qquad (4)$$

However, for a "stochastically thin" process, the hot-electron energy is determined by the details of the acceleration process, so that the product βn_H rather than T_H is determined by energy balance.

TABLE X

MODELS OF HOT-ELECTRON ENERGY SCALING WITH WAVELENGTH

$$T_H \propto (I_L \lambda^2)^{\delta}$$

Model	*Scale Factor δ*
Parametric instabilities	*1*
Flux limit	*2/3*
Resonance absorption	*1/2*

The value of n_H, and hence also of β, is determined, e.g., by target thickness. The "stochastically thin" model thus necessarily must predict a higher electron energy than the "stochastically thick" model and also a lower hot-electron density.

Model 3: Resonance Absorption -- In the process of resonance absorption, the incident laser light couples a portion of its energy resonantly into local Langmuir oscillations in the plasma, which, in turn, are damped by particle heating.[7] At sufficiently high powers, the electrons are accelerated in a very localized region giving rise to a "stochastically thin" behavior. This local acceleration predicts

$$T_H \propto eE_0 L , \qquad (5)$$

where E_0 is the electric-field amplitude of the laser light and L is a scale length for electron acceleration. This result has been verified in extensive particle simulations in one and two dimensions. The major problem then reduces to that of determining the scale length L.

For a speed of sound of $\sim 10^7$ to 10^8 cm/s and a laser pulse length of 0.1 to 1 ns, a typical hydrodynamic scale length would be $L_H \sim c_s t \sim 10^{-3}$ to 10^{-1} cm. With an intensity of 10^{14} W/cm^2, the resonance absorption formula, above, gives $T_H \cong 30$ MeV for $L \cong 0.1$ cm. Experimentally, the hottest electron temperature that is inferred or observed is that of the electrons emitted from the plasma. Their temperature can be as high as ~ 100 keV.[2] Thus, experimental results clearly rule out hydrodynamic models which predict large scale lengths (and neglect ponderomotive forces).

The reflection of the light wave at the critical density results in a large ponderomotive force at that point, which can significantly steepen the local density gradient.[8]

The neglect of the electromagnetic pressure has been justified in the past by Eq. (3), above. For example, using $I_L = 0.06\, n_0 v_H\, T_H/2\alpha$ from the energy equation for "stochastically thick" heating, we have $E_0^2/8\pi n_0 T_H = I_L/2n_0 T_H c = 0.03\, v_H/c\alpha$, which is clearly small compared to unity. More generally, comparing the laser pressure to the cold background, we have

$$E_0^2/8\pi n_0 T_c = \beta v_H n_H T_H/\alpha c n_0 T_c \,, \qquad (6)$$

where n_0 is the critical density at which $\omega = \omega_p$ and T_c is the cold electron temperature, for a two-temperature electron distribution. If $n_H < n_0$ the local pressure gradients result from the cold electrons even if $n_H T_H > nT_c$, where n is the density of cold electrons. Thus, for $n_H T_H > nT_c$, $E_0^2/8\pi nT_c$ can be much larger than originally anticipated, so that the laser radiation pressure cannot be neglected. We will see the consequence of this in a moment. The pressure of a two-temperature electron distribution alters significantly the implications of the energy-balance equation. As mentioned in several earlier progress reports,[3,9] when $E_0^2/8\pi T > 1$, the density profile near critical density can be steepened significantly, which will reduce the hot-electron energy by reducing the scale length in the resonance absorption formula, Eq. (5). For $E_0^2/8\pi nT \gg 1$, there is a sharp interface between the incident laser radiation and the high-density plasma, and for all wavelengths satisfying $E_0^2/8\pi nT > 1$, the laser penetrates to a density given by $n \sim E_0^2/8\pi T$, independent of wavelength. Thus, for a 300-eV plasma, intensities on the order of 10^{15} W/cm^2 will penetrate to a density of 10^{21} cm^{-3} for both 1- and 10-μm wavelengths. This is possible because of the highly nonlinear processes involved. For example, the oscillation amplitude of the driven electrons can be comparable to the length over which the electron density increases from subcritical to several orders of magnitude above critical. Depending on the direction of polarization of the laser electric field, the effective scale length of this sharp density gradient can vary. There are several relevant scale lengths that can determine the gradient. These are summarized in Table XI.

From the resonance absorption formula for hot-electron energy, we use the observed emitted hot-electron energy of ~ 100 keV at 10^{15} W/cm^2 to infer a scale length of ~ 1 μm consistent with the longest scale lengths in Table XI.[6] (More realistically, if we accept the estimated 10- to 20-keV energy of hot electrons within the target plasma, the scale length would be ~ 0.1 to 0.2 μm.)

Experimental measurements of emitted hot electrons as well as x-ray and ion spectra also show at most only a weak dependence on laser power and wavelength. If L_s is used for the scale length and pressure balance is assumed, $E_0^2 = 8\pi nT$, we find that $L_s \sim T_c^{1/2}/I_L^{1/2}$ so that T_H scales as $T_c^{1/2}$ independent of laser power and wavelength! Theoretically, however, it is more plausible that L_ω or L_d is the characteristic length, which would predict $T_H \propto \lambda$. The apparent experimental dependence of the number of hot electrons on wavelength may be due to changes in α and β in the energy-balance expression. The steep density gradients observed in simulations and inferred from experiments reduce the importance of inverse bremsstrahlung and enhance the resonance absorption process. Thus, the

TABLE XI

CHARACTERISTIC SCALE LENGTHS

(T_e = 300 eV; $I_L = 10^{15}$ W/cm^2)

	Scale Length		Wavelength (μm)
	Formula	Value (μm)	
Free-space wavenumber	$L_\omega = c/\omega$	*0.16*	*1*
		1.6	*10*
Skin depth at higher density	$L_s = c/\omega_p$	*0.16*	*1*
		0.16	*10*
Debye length at critical density	$L_d = v_e/\omega$	*0.004*	*1*
		0.04	*10*
Debye length at higher density	$L_D = v_e/\omega_p$	*0.004*	*1*
		0.004	*10*
Electron excursion length	$L_o = eE_o/m\omega^2$	*0.003*	*1*
		0.3	*10*

stochastically thin description of hot-electron energy, Eq. (5), which gives the weakest dependence on wavelength, would seem physically the most appropriate.

Finally, if energy balance results in $n_H > n_o$, we would expect the sharp density gradient to be reduced by the expanding hot plasma because $E_o^2 < 8\pi n_H T_H$. However, because of the rapidly increased scale length, resonance absorption would decrease, so that fewer hot electrons would be created. The hot electrons would then collisionally cool down and the laser pressure would subsequently reshape the sharp density gradient. The time-averaged absorption coefficient would then be smaller than for the case where the sharp gradient is maintained continuously. We would expect from this behavior that the value of α would adjust itself to keep $n_H < n_o$.

In summary, present experiments and theory suggest a weak wavelength dependence of the hot-electron temperature in laser-produced plasmas. The number of hot particles (a secondary question, because the presence of a significant number of "hot" hard-to-shield electrons is difficult to handle in fusion-target designs requiring high isentropic compression) does seem to increase with laser wavelenth. The disagreement with earlier, more naive, models largely originates in plasma-profile modifications due to the ponderomotive force of the light wave. Measurements (both direct and indirect) and more realistic calculations of self-consistent density profiles in laser-produced plasmas should lead to a better understanding of the critical question of wavelength-dependence of laser-plasma interactions.

TARGET EXPERIMENTS AT 1.06 and 10.6 μm

Introduction

Because of the importance of the wavelength-scaling question, we have performed experiments at both 1.0 and 10 μm at nearly equal intensities and pulse lengths. These experiments allow a direct comparison between the effects of these two wavelengths. The experiments examined the spectra of ions and electrons as well as the transport phenomena; all these effects were studied in thin-film experiments. The applicability of vacuum insulation to target design was also investigated.

Suprathermal Electron Measurements

As discussed in the preceding part of this section, the study of suprathermal electrons is essential to the understanding of laser-target interaction physics. Previous measurements[10] have indicated that the energy distribution of suprathermal electrons in the energy range 0.1 to 1.0 MeV emitted from laser-produced plasmas is nearly independent of laser wavelength at laser intensities of $\sim 10^{15}$ W/cm^2. The angular distribution of these electrons has also been measured previously on the laser side of a flat target. Recently, we have repeated these measurements with detectors consisting of a photographic film stack on both the laser side and the back side of a very thin (500 Å) cellulose-acetate foil.

A CO_2 laser pulse at an intensity of 7×10^{14} W/cm^2 was used. We found that structure in the angular distribution of ions from the laser side and the back side of the target were mirror images. The energy carried out the back by the electrons was about one half that carried out the front (i.e., back toward the laser). The energy spectra were comparable above 100 keV, although the spectrum of electrons on the back side was slightly "hotter" due to the loss of the lowest energy electrons in propagating through the foil. According to energy losses expected for a cold material, passage through such a thin foil should not have altered the electron distribution measurably. Yet, distortion of the electron distribution was larger than expected. This anomaly may indicate inhibited flow of the energetic electrons through the target due, perhaps, to the presence of relatively large electric or magnetic fields.

In one experiment, we irradiated a single 3.8-μm-thick (~ 5-mg/cm^2) foil with the Nd:glass laser at an intensity of 6×10^{14} W/cm^2. In this case, the energy carried by suprathermal electrons leaving the rear surface was about one-tenth the energy carried by electrons leaving the front surface. Results were similar for a double-foil target (1000-Å-thick cellulose acetate on the laser

side, 3.8-μm-thick Mylar on the back side, with 500-μm separation between the two) irradiated by a CO_2 laser at an intensity of 7×10^{14} W/cm^2. Again, the spatial distribution was distorted in the rear, without the narrow (~ 1°) structure and peaking observed along the target normal on the front side.

The stacks of photographic emulsions (shielded from visible light) which we used in our measurements were placed 50 cm from the target. Of course, only electrons emitted from the plasma were detected in this experiment. How our results relate to the energy distribution and density of suprathermal electrons within the target plasma is not yet fully understood.

Characterization of High-Energy Ions from Single- and Double-Foil Targets

Measurements of ion spectra yield information on the general features of laser-target interactions, such as absorption of laser energy and energy transport. This can lead to a better understanding of the physics of laser fusion. Measurements on very fast ions with velocities $\gtrsim 5 \times 10^8$ cm/s were carried out using thin-film time-of-flight detectors similar to those described previously.[11] Ion spectra have been measured systematically from flat targets illuminated by both a Nd:glass and a CO_2 laser at an intensity of ~ 10^{15} W/cm^2. The ion emission from single flat-foil targets was recorded simultaneously from both the front and the back surfaces. Double-foil experiments were carried out to investigate the closure velocity, i.e., the speed at which plasma illuminated by lasers of different wavelengths and intensities connects the two foils.

Ion spectra emitted from laser-generated plasmas as observed from the laser side of the targets are shown in Fig. 66. The most striking feature is the steep rise in the leading edge of the ion spectrum, which suggests several important correlations with this rise:

- Its presence implies a sharp leading edge of the laser pulse. This spectral feature can be altered drastically by adjusting the quantity of pulse-shaping dye in the Nd:glass laser system, and is eliminated entirely by any prepulse.
- It is strongly dependent on beam intensity focused on the target.
- With ball-and-disk targets, it indicates implosion, as documented by pinhole cameras.

While information on angular ion distribution is limited, the very fast ions appear to be found within a 20° half-angle cone and to have a distribution similar to the previously reported distribution for lower energy ions.[12] With an intensity of 10^{15} W/cm^2 for Nd:glass and CO_2 lasers, the fastest observed velocity is ~ 1×10^9 and 1.5×10^9 cm/s, respectively, for the front emission. It appears that an increase in absorbed energy does not increase the fastest ion velocity significantly. It does, however, seem to increase the number of these ultrafast ions proportionally.

Ions transmitted through foils of various thickness are exhibited in Fig. 67, which shows two sets of front and back ion spectra from 500-Å and

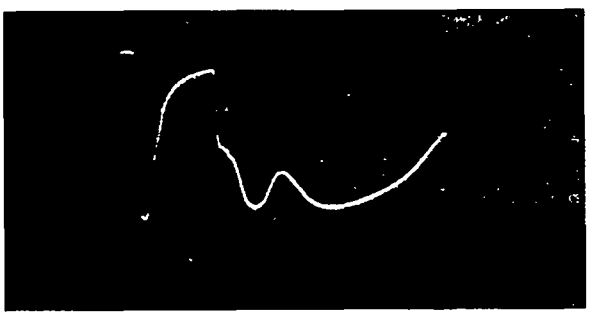

(a)

(b)

Fig. 66. Ion spectra from (a) Nd:glass shot and (b) CO_2 shot.

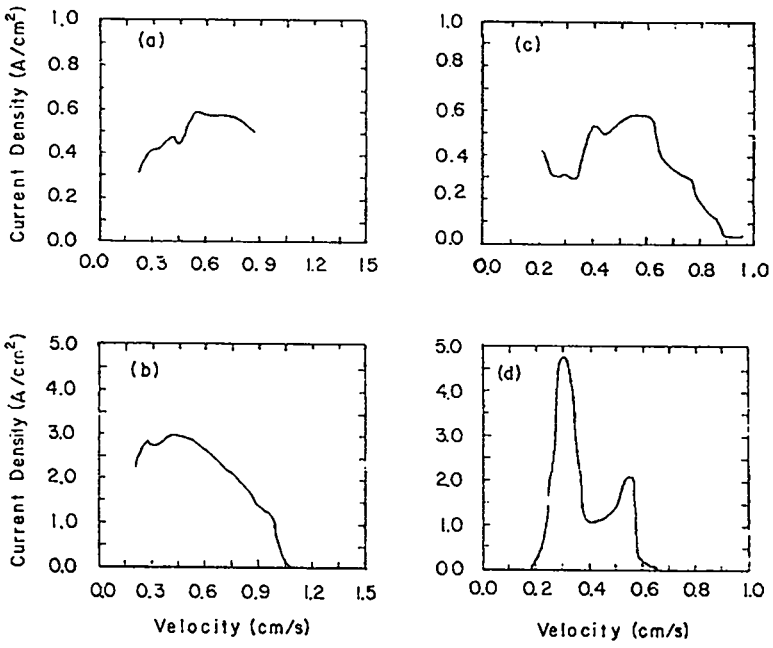

Fig. 67. Computer-reduced emission as a function of velocity, as viewed from the front and back sides, respectively, of a 500-Å foil [(a) and (b)] and of a 25-μm flat target [(c) and (d)].

25-μm-thick plastic foils irradiated by a Nd:glass laser. Note that the transmitted velocity is not substantially reduced even for the thicker foil and that the steep rising feature is preserved.

With the two-foil targets, the transmitted ion spectrum changed, as seen in Fig. 68. The left-hand pair shows the front and back emission for a single 3-μm-thick plastic foil, whereas the right-hand pair shows the emission from a target with a 0.1- to 3-μm-thick pair of foils separated by 75 μm. The transmitted fast ions have diminished abruptly.

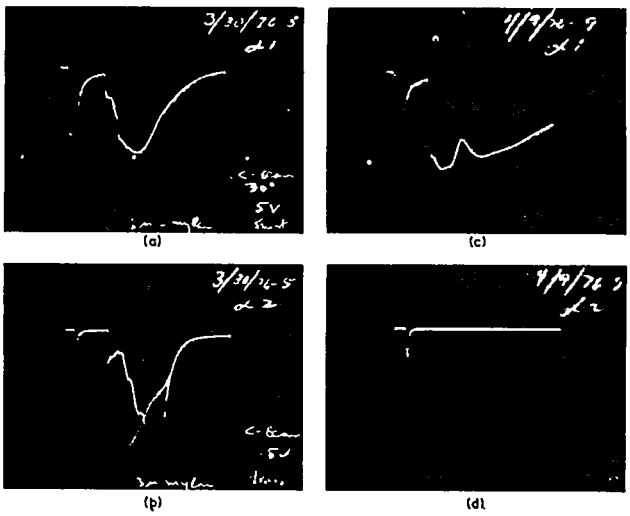

Fig. 68. Time histories of ion emission for single and double foils; (a) and (b) show front and back ion emission, respectively, for a single 3-μm-thick foil; whereas, (c) and (d) show front and back ion emissions, respectively, for a 0.1- to 3-μm-thick double foil separated by 75 μm.

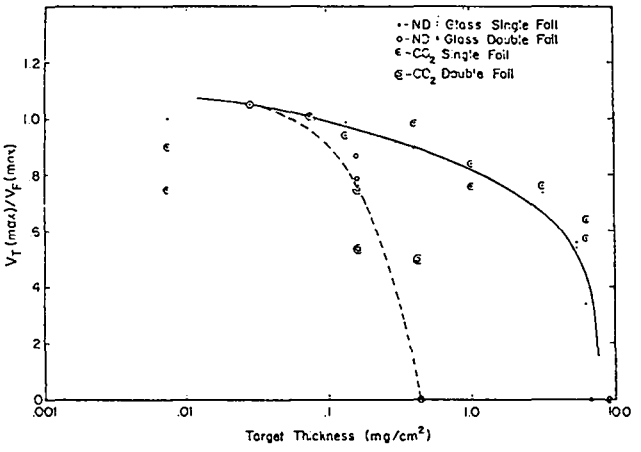

Fig. 69. Ratio of maximum "transmitted" ion velocity to "front" velocity vs target thickness.

In Fig. 69 we have plotted the ratio of maximum "transmitted" ion velocity to "front" velocity versus flat-foil target thickness for both CO_2 and Nd:glass experiments.[2] We observed no significant dependence on atomic number (Z) when platinum and nickel foils were illuminated. Relative fast-ion intensities versus target thickness are shown in Fig. 70. Note that no significant difference exists between the 10.6-μm and the 1.06-μm shots.

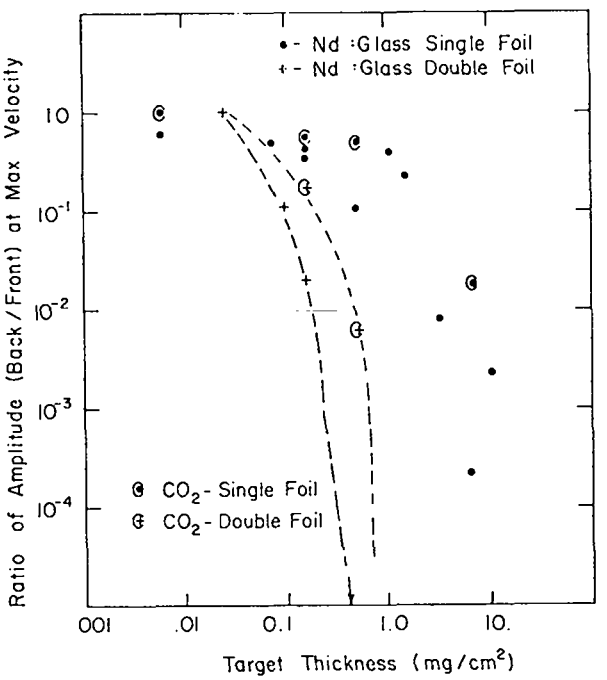

Fig. 70. Ratio of "transmitted" ion intensity to "front" intensity of the fastest component vs target thicknesses.

In results of the double-foil experiment, Fig. 71, the ratio of maximum velocity and amplitude of the fastest ion component is plotted as a function of foil separation distance when illuminated by a CO_2 laser. The transmitted ion velocity appears to be comparable to that of the single-foil experiments until the foil separation reaches a certain distance. Then the ion energy behind the second foil is consistent with that of the fastest ions being generated at the back surface of the first foil and is subsequently degraded in energy when passing through the second foil by an amount given by energy-loss tabulations for cold material. From the pulse length of the laser, the plasma closure time can be estimated. At a power level of $\sim 10^{15}$ W/cm^2, the closure velocity is $\sim 10^8$ cm/s for CO_2 and $< 8 \times 10^7$ cm/s for Nd:glass experiments.

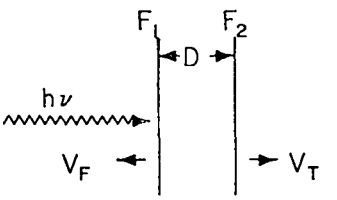

Double - Plastic-Foil Experiment

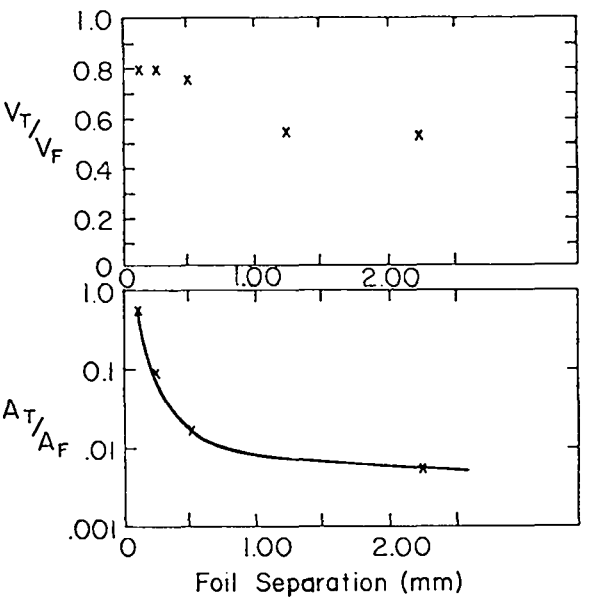

Fig. 71. Experimental arrangement and results for double-foil experiment; (a) target arrangement; (b) and (c) ratios of "back"-to-"front" ion velocity and intensity as a function of foil separation.

We have observed and reported extremely energetic electrons. It is not yet clear how these fast electrons and ions are correlated, and theoretical work is still in progress. However, it can be stated that no strong laser-wavelength dependence exists, contrary to the predictions of some theoretical models.

Target Diagnostics for Two-Beam System

An experimental chamber and associated data-acquisition hardware have been installed and are being brought into use with our two-beam 2- to 4-TW CO_2 laser system. The chamber is a vertical right-circular cylinder of 2.2 m diameter and 0.81 m height with a domed top and bottom (Fig. 72). A horizontal plate at the bottom of the cylindrical portion of the chamber serves as an optical bench for both focusing optics and diagnostic experiments. The two 35-cm-diam laser beams enter the target vacuum system through salt windows and are then turned by micromachined flat mirrors into the cylindrical chamber. There the beams are focused on target by f/2.4 off-axis parabolic mirrors having a focal length of 80 cm. Both beams are 16° from coaxial, i.e., 32° from directly opposing each other. A roughly scaled schematic of the laser and the target chamber is shown in Fig. 73. The focal points of the two beams were placed accurately at the center of the target chamber, 48 cm above the optical bench. The chamber has 64 diagnostic ports, 18 of which are in the horizontal plane of beam incidence. The port flanges are of three standard high-vacuum sizes to facilitate the flexible exchange of experiments.

The targets are held by a mount with one rotational and three linear degrees of freedom controlled by stepping motors with digital motion selection and readout accurate to 10 μm. They are mounted on a rotary holder with one "alignment-control" target and nine actual targets.

Fig. 72. Two-beam target chamber.

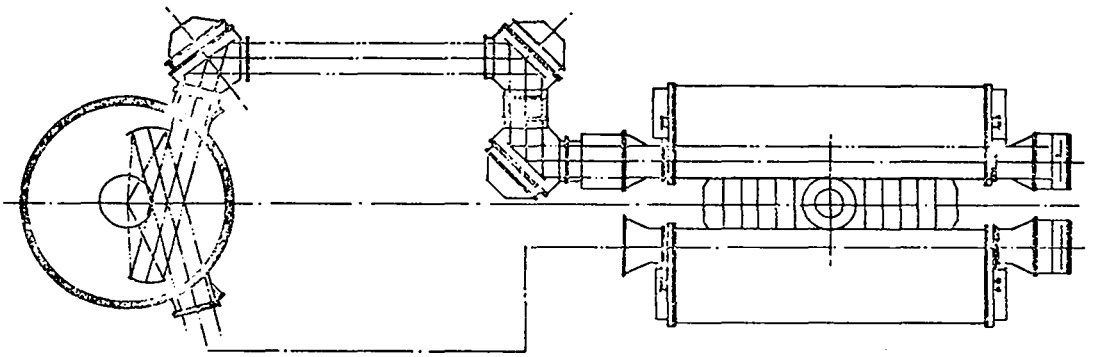

Fig. 73. Schematic of two-beam CO_2 laser and target chamber.

The target chamber is housed in a screen room and is "floated" electrically. Instrumentation cables are run through metal sleeves to another screen room in a trailer. One hundred 50-Ω cables and 20 high-voltage cables are installed. In addition, interfaces for data transmittal to a computer are in place. Trigger signals from the laser control room for tasks such as opening the oscilloscope camera shutters as well as for triggering the scope sweeps in synchronization with the laser pulse are operational.

The target-chamber pumping system has been installed for automatic pumpdown of the chamber to allow rapid replacement of targets in laser-pellet interaction experiments. The system pumps the chamber to a final pressure of 2×10^{-6} torr. Depending on the water-vapor exposure history of the surfaces inside the chamber, this pressure can be attained easily in less than 2 h. The pumping system is back-filled with dry N_2 when the pressure is returned to ambient, to reduce subsequent pumpdown times.

Preliminary Ion Diagnostic Data on the TBS

An ion detector has been placed 100 cm from the center of the target chamber used with the two-beam CO_2 laser system. This detector was installed to gather additional information on the properties of the focused laser beam. Our experience with other CO_2 lasers indicated that the ion current emanating from the laser-produced plasma can be used to ascertain whether the laser beam is properly focused on target and whether the laser energy is deposited in a single short pulse, in multiple pulses, or as a long, self-oscillation pulse; in addition, it can provide a rough evaluation of the laser irradiance on target.[11]

The initial shots were out of focus. After refocusing we found no evidence of multiple pulses or self-oscillation. Preliminary ion data indicate a focal-spot diameter of ~ 175 μm, in rough agreement with predictions based on the quality of the focusing mirror.

Plasma Persistence

Plasma persistence refers to the time interval after arrival of the main laser pulse, during which portions of the plasma are at critical density, or higher. This phenomenon is of interest in 10-μm target experiments for two reasons.

- It permits us to study the basic absorption and reflection properties of a plasma for 10-μm radiation, and
- Plasma formation may serve as a means of optically isolating the target from the laser system.

The interaction of a 1-ns CO_2 laser pulse with targets produces plasma at or above critical density, which persists longer than 50 ns. This phenomenon was observed in time-resolved measurements of 10.6-μm backscatter from a plasma produced by a single 100-J pulse followed by feedthrough pulses. The feedthrough pulses amounted to less than 1 J on

target and were spaced 11.5 ns apart. In these plasma experiments the feedthrough pulses served as probe pulses; we observed the reflection of as many as five such pulses from the plasma created by the 100-J pulse. The backscattered reflection coefficient was about ten times higher for the probe pulses than for the 100-J switched-out pulse, which had been measured previously to be 5%.

We have obtained related information by using a green probe-laser beam synchronized with the CO_2 laser pulse. The green beam had a critical density 400 times that of the 10.6-μm CO_2 laser. These experiments, the first step toward sophisticated study of plasma profiles near the CO_2 critical density, may yield basic information on the effects of ponderomotive forces (radiation pressure) and modification of the electron density profile. They may also be important in developing plasma isolators and short-pulse generators. Initial results indicate that a plasma of sufficient density to reflect or refract the green beam is created near the target. This plasma persists for > 10 ns, a result in agreement with the 10.6-μm backscatter measurements discussed above.

X-Ray Measurements

As indicated earlier, direct measurements of suprathermal electrons emitted from laser-induced plasmas are not sufficient to characterize the plasma itself, because complicated electric and magnetic fields in the plasma influence the spectrum and angular distribution of emitted electrons. Time histories and spectra of x-ray emission from the plasma are our most direct means of characterizing the plasma.

In our measurements we found that the time histories of the soft x-ray continuum emitted by CO_2 laser-produced plasmas at energies less than 1 keV, specifically at 0.85 and 0.45 keV, have decay times considerably exceeding the response time of the scintillator-photomultiplier detection system. On the other hand, the time histories for x-ray continua at energies of 1.5, 2.5, and 4.5 keV were limited by the response of the detection system: the response of the photomultiplier tube and of the NE-111 plastic fluor to 1-ns pulses was 4.5 to 5.0 ns. The x-ray continua at 0.85 and 0.45 keV decayed to half their intensities in 15 ns and exhibited a tail extending to 40 ns. This observation is consistent with the results of our 10.6-μm probe experiments which show that a moderately dense plasma exists for at least 50 ns. The expanding plasma has a low temperature and a low recombination rate.

Previous x-ray measurements have shown that plasma temperatures of ~ 300 eV are achieved with a 1-ns, 100-J laser pulse at 10.6 μm, impinging on a flat target. Also, atomic inner-shell excitation was indicated by the presence of the Kα line in spectra from aluminum targets and by the presence of a more intense Kα line in the spectra from silicon targets. Inner-shell excitation is believed to result from direct excitation by high-energy electrons and, if so, should be Z-dependent. We have recorded x-ray spectrograms during several 80- to 90-J shots on titanium targets and found only one line between 2.1 and 3.1 Å. The measured wavelength of this line agreed to within 0.06 Å with the calculated position of the Kα line of titanium. Although the pointing of the instrument was calibrated, there is sufficient error in the crystal adjustments to prevent positive identification of the Kα line. Further work will determine the nature of the Z-dependence of inner-shell excitation.

THEORETICAL STUDIES OF LASER FUSION

Introduction

In light of most recent experimental data on wavelength-scaling of hot-electron spectra, we have extended our plasma-physics studies of such electrons. First, we have considered their transport mechanism. An examination of return-current resistance as a way of limiting their transport shows that the heat flow of a large fraction of the hot electrons can be inhibited under some conditions, giving rise to fast ions, but still to retain a sufficiently large flux, e.g., 10% of the incident laser flux, to penetrate to high densities. Because of the latter effect and because of large joule heating of the cold background (which destroys the resistance), we have considered using a vacuum to limit the transport of hot electrons.

The electric field produced when a few hot electrons escape turns the bulk of the hot electrons around as they attempt to enter the vacuum region.

As discussed earlier, experimental data on hot electrons and fast ions suggest that the parameter range of interest in laser-produced plasmas leads to a more extreme density gradient in the critical-density region than had been anticipated. Therefore, we have carried out plasma simulations in a very sharp density profile to determine electron spectra and stability properties. Thus far, hot-electron spectra in simulations are much hotter than those inferred from experiments (probably due to high background temperature), but much cooler than if the profile were not steep. In the sharp gradient, most instabilities are damped except for filamentation of the critical surface. As an aid to normalizing our simulations, we have also found an analytical procedure to relate experimental x-ray spectra to the hot-electron distribution.

Hot-Electron Transport -- The role of hot electrons in undesired target preheat is crucial in laser-fusion research. Studies of hot-electron transport have suggested an approach to target design which may help alleviate this problem. In the last progress report[10] we discussed the limit on penetration depth of hot electrons due to the ambipolar electric field and obtained a result that

$$D = 2.9\, T_H^2\, T_c^{3/2}/QZ\,, \qquad (7)$$

where T_c is the temperature (eV) of the cold background plasma and Q is the energy flux of hot electrons (W/cm^2). Note that a reduction in hot-electron flux by two orders of magnitude requires an increase in D by two orders of magnitude. Thus it is possible to inhibit the heat flow of a large fraction of the electrons, giving rise to fast ions, and still to have a sufficiently large flux of hot electrons to preheat the fuel. We have verified this effect by numerical simulations of particle transport where the electric field is given by the resistive drag of the cold return current on the background ions, $E = -\eta j_H$, where η is a constant resistance. These arguments apply even to the case where η arises from collective effects in the plasma.

We have also shown that a significant fraction of the hot-electron energy is deposited in ohmic heating of the background cold plasma. Using the fact that $E \sim T_H/eD$, the energy deposition rate is $T_H j_H/eD$ or Q/D. Thus, a large portion of the incident flux will be deposited in the cold background over a distance D. This has two important results:

- Only a small fraction of the hot electrons will be turned by the ambipolar field, so that only a small fraction of the hot-electron energy can be deposited into fast ions.
- Unless the specific heat of the plasma is very high, corresponding to a large density, the distance D will increase rapidly as T_c increases, resulting in a rapid penetration by the bulk of the hot-electron flux.

These arguments suggest the use of macroscopic magnetic fields or of large vacuum regions as insulation against large hot-electron fluxes.

Vacuum Insulation -- The presence of a tail of high-velocity energetic electrons destroys the performance of many targets because these electrons preheat the fuel and/or the pusher. Several ways of shielding the target from hot electrons are known, the first of which is the use of a high-Z layer. However, the required mass may become too large for the available laser energy. As discussed above, classical or anomalous return-current resistance suffers from the problem of "melting the resistor"; that is, the joule heating of the return current can disable the resistance. Seeded magnetic fields may be an advantageous approach, but our limited experience suggests that ionization of the high-Z material, which provides the large density gradients needed for large magnetic fields on a small scale, may be an impediment in some cases.

We believe that vacuum insulation is a desirable way to prevent electron preheat because it is massless and cannot be heated. In this scheme a few electrons escape into vacuum, setting up a large electric field which prevents the bulk of electrons from escaping. Consider two surfaces:

one from which electrons are escaping and another onto which energetic electrons are impinging. Electrons continue to escape at a rate compatible with the steady-state electric field and the electron emission from the second surface. One might guess that if the separation distance between two surfaces is L, the steady-state electron density between the surfaces is determined by $L = \lambda_D$ where λ_D is the electron Debye length. Detailed simulations indeed verify this to be the case. We expect that the time it takes for the two surfaces to join, in the sense that the vacuum is shorting out so that hot electrons can flow freely between the two surfaces, is the transit time of a fast ion. At this time, we expect that the density in the vacuum region would be comparable to the hot-electron density so that a charge-neutralizing return current can flow. The required energy transport from the laser-heated foil to the other foil would occur via fast or slow ions.

As described earlier in this section, double-foil experiments have shown that vacuum insulation is an effective means to limit energetic electron transport. At intensities in the range of 10^{15} W/cm^2, a separation of ~ 1 μm is needed for each picosecond of pulse. We have not analyzed the effect of supports between the two surfaces, although we expect that fibers are more desirable than sheets.

Assuming that vacuum insulation works as a concept, we can ask whether we can derive target designs in which it leads to a significant increase in yield. Thus far, we have developed some classified target designs for which vacuum insulation is required to attain breakeven for certain assumed hot-electron spectra.

Plasma Stability and Heating in Steep Density Profiles

As discussed earlier, experimental data on energetic electrons and fast ions suggest that the particle energies are nearly the same at equal laser intensities for both 1- and 10-μm wavelengths. This is a surprising result, yet a possible cause may be the severe density-profile modification in the vicinity of the critical density. Some profile modification has been predicted for several years, but the possibility of extreme modification for CO_2 laser wavelengths had not been anticipated. In attempting to understand the experimental results, we need to address the following questions:

- What are the self-consistent laser-produced density profiles at 1 and 10 μm?
- What are the absorption and hot-electron spectra in these self-consistent profiles?
- How stable are these profiles on a long time scale?

Because of computer storage and time limitations, it is extremely difficult to perform a two-dimensional simulation at 1 μm followed by the same simulation in which only the laser wavelength changes to 10 μm. As a first step we can begin by considering simulations in the high laser intensity-low background temperature regime where a very sharp interface develops.

Although plasma simulations are first-principle calculations of the collective behavior of charged particles in the presence of a laser pulse, the answers they provide are for a rather limited range of initial conditions. For example, because of computational limitations, electron temperatures cannot be much below 1 keV, simulation box sizes cannot be much more than a square of a few free-space light wavelengths, and plasma densities are usually not more than a few times the critical density. Severe profile modification arises when $v_o/v_e >> 1$, where $v_o = eE_o/m_e\omega_o$ is the electron oscillating velocity in the laser electric field and $v_e = (kT_e/m_e)^{1/2}$ is the electron thermal velocity. In this regime the self-consistent plasma density can rise from a small fraction of critical density to 10 to 100 times critical density over a distance of less than a micron. This is the regime in which we suspect high-intensity CO_2 lasers are operating -- a regime not easily studied by simulations. Below, we present simulations approaching this high-intensity range.

Before presenting some typical examples, we can summarize our present conclusions about the $v_o/v_e >> 1$ regime:

- The self-consistent profile is that of a sharp laser-plasma interface where laser light pressure approximately balances the plasma pressure with a low-density (a small fraction of critical density) highly supersonically flowing plasma outside the critical surface.
- For polarization perpendicular to the plane of incidence, the critical density surface is unstable to wavelengths comparable to the free-space light wavelength. This instability leads to a severe rippling of the critical-density surface.
- For a laser electric field polarized in the plane of incidence, the absorption is ~ 30% over a wide angular range.
- The hot-electron spectrum is softened in the presence of the sharp density gradient.

We have previously shown[10] that the laser-plasma equilibrium is that of a sharp laser-plasma interface when $v_o/v_e >> 1$. In Fig. 74 we have a near-equilibrium sharp density profile initialized in a simulation box for the following initial parameters: $v_o/c = 0.5$; $v_e/c = 0.2$; $m_i/m_e = 25$; $T_e/T_i = 400$. The light wave is normally incident on the density profile with polarization perpendicular to the plane of the simulation; i.e., there is an incident laser electric field only in the z-direction, where the inhomogeneous direction is in x and the homogeneous-periodic direction is in y. Figure 74 shows the electric-field amplitude of the incident and specularly reflected laser light, whereas Fig. 75 shows the density contours at three subsequent times. Clearly, ripples are growing on the density surface and they only stop growing when nonlinear effects (wave-breaking) smooth out the density protrusions. The linear phase of this instability has been discussed previously. The linear instability saturates when all the incident light is scattered by the density ripples. Subsequently, the density ripples continue to grow secularly until wave-breaking occurs. At this point both the electrons and the ions are heated comparably.

Next, we consider essentially the same problem except that the laser is polarized in the plane of incidence, the x-y plane, and is incident at an angle of 23° to the density profile. The initial density profile is essentially the same as shown in Fig. 74 except that the upper density is slightly lower. Resonant absorption occurs in the region of this steep profile leading to an absorption near 40%. The electric-field structure and the self-consistent density profile at time = $200\omega_o^{-1}$ are shown in Fig. 76. The field structure and the absorption are similar to those obtained in gentler density-gradient simulations, except that there is less enhancement of E_x.

The initial and final electron-momentum (p_x) distributions are shown in Fig. 77. Note that there are significant numbers of electrons above 250 keV ($p_x/mc = 1$), but that the spectrum is still not as hard as when the laser light is incident on a much gentler gradient. The high hot-electron temperature may, in part, be due to the artificially large background electron temperature assumed in the simulations. If a much lower, more realistic,

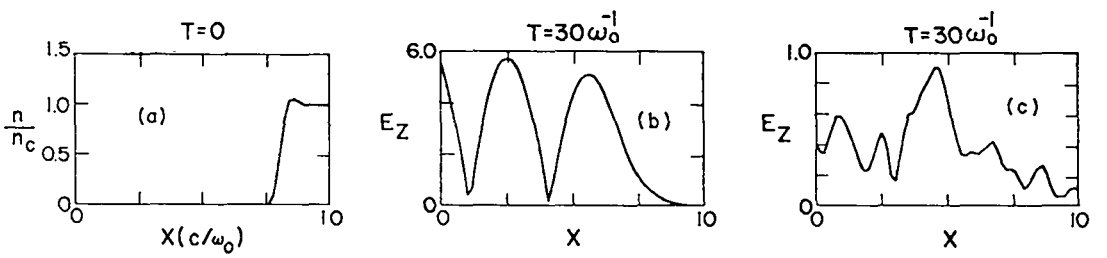

Fig. 74. Two-dimensional particle-in-cell simulation; (a) initial density profile; (b) incident laser electric-field amplitude at $T = 30\,\omega_o^{-1}$, and (c) the most unstable $k_y = 3\,\omega_o/c$ scattered wave.

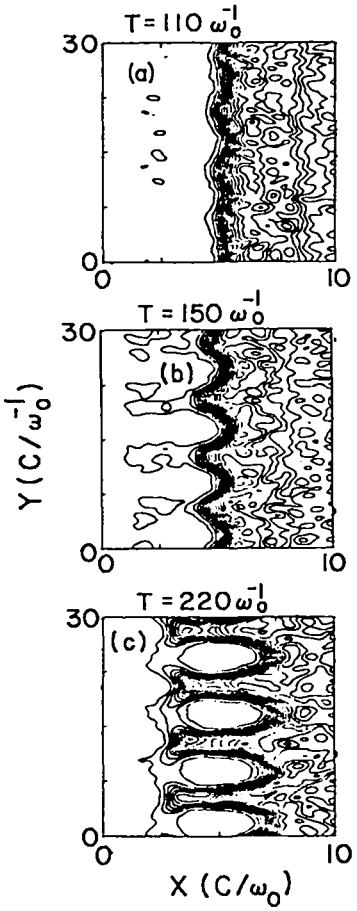

Fig. 75. Plasma density contours at three different times, (a), (b), and (c). Note the formation of density fingers which are smoothed by the heating.

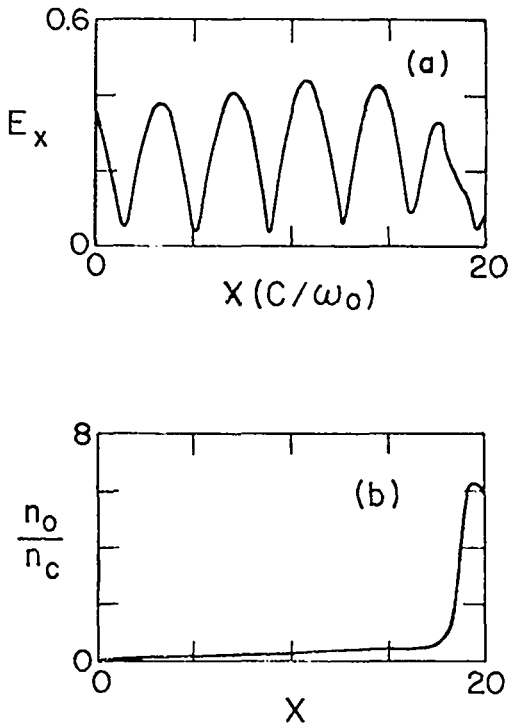

Fig. 76. Results of laser-plasma interaction simulation. Simulation parameters are the same as in Fig. 75, except that the incident laser is polarized in the x-y plane (plane of incidence) at 23° to normal; (a) amplitude of the x-directed electric field at $t = 200\,\omega_o^{-1}$ as a function of position; (b) self-consistent density profile.

temperature had been used, a much sharper density gradient and much higher upper density would have resulted, causing a lower hot-electron temperature according to the formula $T_H \sim eE_0L$, in much better agreement with experiment.

Relation of Experimental X-Ray Spectra to the Number and Energy of Suprathermal Electrons

The number and energy distribution of suprathermal electrons is of extreme importance in laser fusion. Therefore, reliable experimental techniques are highly desirable to measure the distributions of suprathermal electrons. Considerable progress has been made in measuring the x-ray spectra produced in laser-heated plasmas. We will show that these experimental x-ray spectra can be analyzed by the theoretical relations we have derived to determine the distribution of suprathermal electrons.

The exact distribution of suprathermal electrons is still under investigation and is likely to be very complex; however, a particularly simple model[13] can be devised as follows:

- A fraction, f, of the laser energy is absorbed into a suprathermal electron tail characterized by an energy distribution of the form

$$n(\varepsilon) = Be^{-\varepsilon/\alpha kT_e}, \qquad (8)$$

  where ε is the electron energy, α and B are constants, and T_e is the temperature of thermal electrons.

- The remaining fraction, 1-f, of the absorbed laser energy produces a nearly Maxwellian distribution.

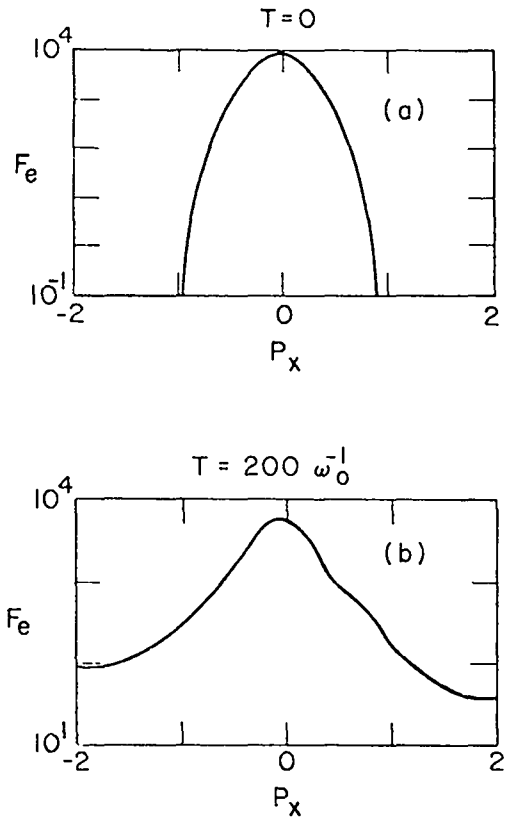

Fig. 77. Electron momentum distributions in x for the simulation of Fig. 76 are plotted at (a) $t = 0$ and (b) $t = 200\ \omega_o^{-1}$.

Brueckner[14] has derived formulae relating experimental x-ray spectra and the number and energy of suprathermal electrons by assuming that collisional drag between the thermal electrons and the suprathermal electrons uniformly dominates other energy losses. However, Brueckner's final results depend sensitively on an inaccurate approximation to an integral in the model. This integral was first evaluated correctly by Brysk,[15] and by Henderson and Stroscio,[16] who found that the x-ray spectrum produced by a suprathermal electron of energy ε_o is given by

$$\frac{d\varepsilon_{rad}}{d(h\nu)} = \frac{\lambda_z}{mc^2}\,\frac{1}{2}\left\{(\varepsilon_o - h\nu)\,\ell n\left[\frac{1+(1-\frac{h\nu}{\varepsilon_o})^{1/2}}{1-(1-\frac{h\nu}{\varepsilon_o})^{1/2}}\right] - \varepsilon_o\left(1-\frac{h\nu}{\varepsilon_o}\right)\right\} \tag{9}$$

where $h\nu$ is the energy of the radiation emitted by the suprathermal electrons and λ_z is a dimensionless constant described in Ref. 16.

To obtain the total emitted x-ray radiation produced by all suprathermal electrons in a typical distribution, $n(\varepsilon)$, one must evaluate

$$\frac{dE_{rad}}{d(h\nu)} = \int_{h\nu}^{\infty} n(\varepsilon_o)\,\frac{d\varepsilon_{rad}}{d(h\nu)}\,d\varepsilon_o\ , \tag{10}$$

that is, one must sum Eq. (9) over all suprathermal electrons present in the distribution. Upon substituting Eq. (9) into Eq. (10) it is apparent that the indicated integration is impossible to perform for all but the most elementary forms of $n(\varepsilon_o)$.

To circumvent this difficulty, we wish to use an approximate kernel that is amenable to Brueckner's differentiation technique (described below) and that retains the logarithmic term of Eq. (9), which is clearly important. Brueckner[14] makes approximations earlier in his development and obtains

$$\frac{d\varepsilon_{rad}}{d(h\nu)} = \frac{\lambda_z}{mc^2}\cdot(\varepsilon_o - h\nu)\ . \tag{11a}$$

As we will see later, the neglect of the logarithmic term in this expression distorts the functional dependence. We have discovered an approximate expression for Eq. (9) which satisfies our criteria:

$$\frac{d\varepsilon_{rad}}{d(h\nu)} = \frac{\lambda_z\varepsilon_o}{mc^2}\left\{0.2\left(4-\frac{h\nu}{\varepsilon_o}\right)+0.5\left[\ell n\left(\frac{4\varepsilon_o}{h\nu}\right)-5+\ell n\ 10\right]\right\}. \tag{11b}$$

This expression is simple enough so that we can differentiate Eq. (10) exactly and obtain results that depend on integrals only through

$$N(\varepsilon>\varepsilon_b) = \int_{\varepsilon_b}^{\infty} n(\varepsilon)d\varepsilon \tag{12a}$$

and

$$E(\varepsilon>\varepsilon_b) = \int_{\varepsilon_b}^{\infty} \varepsilon n(\varepsilon)d\varepsilon\ , \tag{12b}$$

which represent, respectively, the number and the total energy of suprathermal electrons with energies above ε_b. In particular, we obtain

$$\left.\frac{d^2E_{rad}}{d(h\nu)^2}\right|_{\varepsilon_b} = \frac{-\lambda_z}{5mc^2} N(\varepsilon>\varepsilon_b) - \frac{\lambda_z}{2mc^2\varepsilon_b} E(\varepsilon>\varepsilon_b) \quad (13a)$$

and

$$\left.\frac{d^3E_{rad}}{d(h\nu)^3}\right|_{\varepsilon_b} = \frac{\lambda_z}{mc^2}\left(\frac{7}{10}\right) n(\varepsilon_b) + \frac{\lambda_z}{2mc^2(\varepsilon_b)^2} E(\varepsilon>\varepsilon_b) \,. \quad (13b)$$

These results relate the experimentally measured x-ray spectrum, $dE_{rad}/d(h\nu)$, to the suprathermal electron distribution $n(\varepsilon)$, as well as to the number $N(\varepsilon>\varepsilon_b)$ and total energy $E(\varepsilon>\varepsilon_b)$ of suprathermal electrons. From a practical point of view, Eqs. (13a) and (13b) are superior to previous relations[14] that depend on the limit $h\nu \to 0$, which is impossible to measure accurately. Furthermore, these previous results do not contain the important ε_b^{-1} and ε_b^{-2} terms in Eqs. (13a) and (13b), respectively, because the logarithmic dependence in Eq. (9) has been neglected. For the suprathermal electron distribution of Eq. (8), we find that Eq. (13a) reduces to

$$\frac{d^2E_{rad}}{d(h\nu)^2} = -\frac{\lambda_z}{mc^2}\alpha kT_e Be^{-\frac{\varepsilon_b}{\alpha kT_e}}\left[\frac{.7}{10} + \frac{\alpha kT_e}{2\varepsilon_b}\right]. \quad (14)$$

From experimental values of $dE_{rad}/d(h\nu)$ as a function of $h\nu$, one may determine $d^2E_{rad}/d\varepsilon_a^2$ and $d^2E_{rad}/d\varepsilon_b^2$ for any two energies ε_a and ε_b in the experimentally covered range of energy. Thus, with Eq. (14) we find

$$\frac{(d^2E_{rad}/d\varepsilon_a^2)}{(d^2E_{rad}/d\varepsilon_b^2)} = \frac{e^{-\frac{\varepsilon_a}{\alpha kT_e}}\left[\frac{.7}{10} + \frac{\alpha kT_e}{2\varepsilon_a}\right]}{e^{-\frac{\varepsilon_b}{\alpha kT_e}}\left[\frac{.7}{10} + \frac{\alpha kT_e}{2\varepsilon_b}\right]}, \quad (15)$$

which is a transcendental equation for α -- the basic fundamental constant for the suprathermal electron distribution in Eq. (8).

Clearly, Eqs. (13a), (13b), and (15) yield valuable information about suprathermal electrons if used in conjunction with experimentally measured x-ray spectra.

TARGET DESIGN

Introduction

Although most of our target design work is classified, we can mention some of our developmental efforts and some unclassified design calculations. The codes being used and being improved are LASNEX, a two-dimensional Lagrangian code acquired from Lawrence Livermore Laboratory; MCRAD, a LASL-developed two-dimensional Lagrangian code; and CERES, a LASL-developed one-dimensional Lagrangian code.

The multigroup radiation treatment in LASNEX is being improved so that more accurate opacities can be used. Several changes have been made to allow quite accurate three-temperature (3T) calculations including operation with a laser ray-trace code. Because none of our design codes uses a Monte Carlo treatment to describe suprathermal electrons, we have included hot electrons in CERES by a Monte Carlo routine. This inclusion should permit some comparison with the multigroup treatment in LASNEX. The beam-deposition package in LASNEX is being used to study ion-beam implosions, whose energetic ions are created by the laser: An outer low-Z shell receiving spherically symmetric laser illumination explodes, and fast ions emitted from the inside of the shell are used to drive an implosion of an inner DT shell.

Code Improvements

LASNEX -- Modifications to LASNEX are still under way. Because of the radiative-preheat problem, it is important to treat radiation accurately, and this aspect of LASNEX has been under extensive study. For treatment of multigroup radiation, the code uses analytic opacity calculations. However, this routine is being replaced by an interpolation routine that uses more accurate tabular opacities. After implementation, the code will consider the more accurate free-bound coupling between radiation and electrons.

MCRAD -- Development of MCRAD has continued. An implicit three-temperature (3T) algorithm has been incorporated which is superior to the usual explicit 3T treatments. MCRAD can calculate accurately in regions of strong energy cross coupling (1T regions) as well as in decoupled 3T regions.

The new 3T model also accounts for partial ionization. For this revised code we have developed a new routine for calculating the free-bound coupling (which can be much stronger than bremsstrahlung) between the electrons and radiation. In materials of moderate Z-number, this new routine provides much more equilibration than predicted by the standard 3T coupling. In conjunction with 3T thermodynamics, the code now simulates a depleting DT burn with local deposition of α particles.

A mesh-line laser deposition routine has been transferred from LASNEX. It should permit the efficient evaluation of spherical, shell, and thin-foil dynamics without necessary recourse to the more complicated ray-tracing deposition routine. Light can be introduced at any point inside or outside the mesh with a choice of incident direction of the light. The routine models light absorption by inverse bremsstrahlung, by atomic scattering, and by plasma instabilities. The rezoner and the integrator were enlarged so that the full interactive rezoning capability of the code is now available in 3T. Additions have been made for the accurate calculation of transport and hydrodynamics in targets with internal and central voids. Laser ray tracing is now operative in conjunction with 3T.

CERES -- CERES is our one-dimensional Lagrangian code which has a fast Monte Carlo photonics treatment. The code was used, e.g., to elucidate the radiative preheat problem in current glass-microballoon experiments.[17] Fast-electron transport by Monte Carlo techniques is being added. Processes being included are energy loss by collisions, elastic scattering by nuclei, and an electric field generated by a return current of thermal electrons. The first two processes generate almost no feedback on the fast electrons, and an explicit Monte Carlo scheme is satisfactory. An explicit Monte Carlo technique has been incorporated into the code and appears to be working. The return-current electric field produces numerical instabilities except for short time steps. An implicit technique, in which the electric field is adjusted during the time step to obtain a self-consistent value, is being investigated to overcome the numerical instabilities.

Target Design

Laser light at high intensities produces copious amounts of fast ions at energies ranging from 100 to 500 keV. Present experiments in which the laser irradiates a planar foil indicate that the intensity of these fast ions at the front and the rear of the foil can be comparable. As discussed earlier in this section, foil thicknesses appear to be equal to or less than the simple classical range of energetic electrons generated in the laser absorption process. Using laser-produced fast ions directly has already been suggested as a possible approach to target design.[18] We consider isotropic laser illumination of a shell, and the fast ions emitted from the inside of this shell are used to drive an implosion of an inner target, i.e., a DT shell. Summarizing our principal results, we find that if the ions are in the 500-keV to 2-MeV range incident in a linear-ramp pulse with 10 to 50 kJ of energy we obtain a typical yield ratio of 1 to 10%.

In these calculations, performed with LASNEX, we consider that the laser light causes a low-Z shell to explode, creating monoenergetic ions inside and outside the shell. As a first approximation, a one-dimensional calculation of a DT shell is performed with isotropic illumination by ions of a given energy, which are assumed to originate from the inside surface of an outer shell. However, the dynamics of this outer shell are not explicitly included. The impinging ions do not have an actual blowoff profile and deposit only energy, not momentum, in the DT shell.

A typical problem follows. Let us consider a DT shell with an outer radius of 700 μm and an inner radius of 500 μm, i.e., with an aspect ratio of $\sim$3:1. An energy source $\dot{E} = 2(50\ \text{kJ}/2\ \text{ns})\cdot(\tau/2\ \text{ns})$ is used to deposit 1-MeV lithium ions as a function of time τ. The resulting ablation-driven implosion produces a yield ratio of 4%. Although the yields are below breakeven, $\sim$ 1% target performance is rather insensitive to changes in pulse length and energy. Target performance in this regime falls below breakeven conditions because compressions lead to $(\rho R)_{max} < 0.1$, $\rho_{max} < 150\ \text{g/cm}^3$, although ion temperatures reach values above 10 keV. Efforts to achieve higher densities at temperatures of 4 to 5 keV have not been successful, but are proceeding. The general result of inadequate compression with adequate temperature seems to occur also for laser targets of low aspect ratio.[19]

REFERENCES

1. Tai Ho Tan, D. V. Giovanielli, G. H. McCall, and A. H. Williams, "Measurements of High Energy Charged Particles from Laser-Produced Plasmas," 1976 IEEE Int'l. Conf. on Plasma Science, Austin, May 24-25, 1976.

2. D. V. Giovanielli, J. F. Kephart, and A. H. Williams, "Spectra and Angular Distributions of Electrons Emitted from Laser-Produced Plasmas," J. Appl. Phys. 47, 2907 (1976).

3. F. Skoberne, "Laser-Fusion Program at LASL, July 1 - December 31, 1975," Los Alamos Scientific Laboratory report LA-6245-PR (July 1976).

4. D. V. Giovanielli, J. F. Kephart, and G. H. McCall, "Wavelength Scaling Experiments Using CO_2 and Glass Laser-Produced Plasmas," 1976 IEEE Int'l. Conf. on Plasmas Science, Austin, May 24-25, 1976.

5. Lawrence Livermore Laboratory Semiannual report UCRL-50021-72-1, p. 110-111 (1972); W. L. Kruer and J. M. Dawson, "Anomalous High-Frequency Resistivity in a Plasma," Phys. Fluids 15, 446 (1972)(note especially p. 450 where it is pointed out that a typical energetic particle can have energy equal to the zero-order oscillating energy).

6. R. L. Morse and C. W. Nielson, "Occurrence of High Energy Electrons and Surface Expansion in Laser Heated Target Plasmas," Phys. Fluids 16, 907 (1973).

7. D. W. Forslund, J. M. Kindel, K. Lee, E. L. Lindman, and R. L. Morse, "Theory and Simulation of Resonant Absorption in a Hot Plasma," Phys. Rev. A 11, 679 (1975) and references therein; K. G. Estabrock, E. J. Valeo and W.L. Kruer, "Two-Dimensional Relativistic Simulations of Resonance Absorption," Phys. Fluids 18, 1151 (1975).

8. D. W. Forslund, J. M. Kindel, K. Lee, and E.L. Lindman, Los Alamos Scientific Laboratory report LA-5542-PR, p. 67 (1973); E. J. Valeo and W. L. Kruer, "Solitons and Resonant Absorption," Phys. Rev. Lett. 33, 750 (1974); D. W. Forslund, J. M. Kindel, K. Lee, and E. L. Lindman, "Absorption of Laser Light on Self-Consistent Plasma Density Profiles," Phys.Rev. Lett. 36, 35 (1976); K. Lee, D. Forslund, J. Kindel, and E. Lindman, to be published in Phys. Fluids.

9. F. Skoberne, "Laser-Fusion Program at LASL, January 1 - June 30, 1975," Los Alamos Scientific Laboratory report LA-6050-PR (January 1976).

10. F. Skoberne, "Laser Program at LASL, July 1 - December 31, 1975," Los Alamos Scientific Laboratory report, LA-6245-PR (July 1976).

11. Tai Ho Tan, A. H. Williams, and G. H. McCall, "A Thin-Film Detector System for Laser-Fusion Studies," Nucl. Instr. and Meth. 131, 425 (1975).

12. A. W. Ehler, "High-Energy Ions from a CO_2 Laser-Produced Plasma," J. Appl. Phys. 46, 2464 (1975).

13. J. D. Lindl, "Effect of a Superthermal Electron Tail on the Yield Ratio Obtained from DT-Targets Illuminated with a Shaped Laser Pulse," Nucl. Fusion 14, 511 (1974).

14. K. A. Brueckner, "Energy Deposition in Laser-Heated Plasmas," Phys. Rev. Lett. 36, 677 (1976).

15. H. Brysk, "Energy Deposition in Laser-Heated Plasmas," KMSF report KMSF-U488, TA-016T (1976).

16. D. B. Henderson and M. A. Stroscio, "Comment on Energy Deposition in Laser-Heated Plasmas," Los Alamos Scientific Laboratory report LA-6393-MS (1976).

17. G. S. Fraley and R. J. Mason, "Preheat Effects on Microballoon Laser-Fusion Implosions," Phys. Rev. Lett. 35, 520 (1975).

18. D. V. Giovanielli and E. L. Lindman, "Laser Ion Beam Fusion," patent disclosure, Los Alamos Scientific Laboratory, February, 1974.

19. R. J. Mason, "The Calculated Performance of Structural Laser-Fusion Pellets," Nucl. Fusion 15, 1031 (1975).

IV. LASER-FUSION TARGET FABRICATION

Our pellet fabrication effort, supported by extensive theoretical investigations, supplies the thermonuclear fuel in packaged form suitable for laser-driven compressional heating experiments. These targets range from simple deuterated-tritiated plastic films to frozen DT pellets to complex DT gas-filled hollow microballoons, mounted on ultrathin supports and coated with various metals and/or plastics. Numerous quality-control and nondestructive testing techniques for characterizing the finished pellets are being developed.

INTRODUCTION

In our target fabrication effort, we are developing techniques and methods to fabricate spherical targets containing DT fuel in a variety of chemical and physical forms. High-pressure DT gas has been used extensively as the fuel because it can be conveniently packaged in glass or metal microballoons for use as laser-fusion targets. However, the designers and experimentalists would prefer a higher density of DT fuel than can be obtained conveniently in gaseous form. In addition, significantly better yields are predicted if the fuel can be formed as a high-density shell surrounding either a vacuum or a low-pressure spherical core because it is then unnecessary to work against the high pressure of the inner fuel core during the compression of the spherical fuel shell. These considerations have led to our development of methods to condense layers of cryogenic DT, either liquid or solid, on the inside surfaces of microballoons. In addition, we are developing techniques to prepare room-temperature solids containing fuel atoms at high density (e.g., polyethylene, lithium hydride, and ammonia borane, in each of which the hydrogen has been replaced by an equiatomic mixture of deuterium and tritium) and to form these into microspheres and/or microballoons. The nonfuel atoms in these room-temperature solids (carbon, lithium, nitrogen, and boron) must also be compressed and heated to fusion conditions along with the deuterium and the tritium, but, because they do not participate in the fusion reaction, they act as diluents of the fuel. As a result, targets fueled with these room-temperature solids are not expected to perform as well as those with cryogenic DT fuel shells. However, the fuels that are solid at room temperature are considerably easier to work with both in target fabrication and in laser-target interaction experiments, and they also enlarge the parameter space available for exploration in our interaction experiments.

Along with the development of techniques to fabricate the fuel pellets, we also are developing methods to apply a wide variety of coatings to the fuel pellet and to support the pellets for irradiation by the laser beam using thin plastic films or glass fibers so as to introduce a minimum of extraneous material into the system. Finally, we are continuously developing techniques to select, characterize, and measure the various pieces of the target both prior to and after assembly.

HIGH-PRESSURE DT GAS-FILLED TARGETS

General

We have continued the development of techniques and methods to fabricate hollow, multilayered spherical targets to be filled with high-pressure DT fuel gas. These generally consist of a high-Z, high-density, metal pusher shell overcoated with a low-Z, low-density absorber-ablator layer. This

outer layer absorbs energy from the incident laser, heats, vaporizes, and streams away from the pusher shell causing the pusher shell to implode via the rocket reaction forces. The pusher shell can be deposited onto a nonremovable mandrel (e.g., a glass or metal microballoon), but improved performance may be obtained if the pusher shell is fabricated directly as a freestanding metal microballoon. In either case, high-strength pusher shells are desired so that a high DT pressure can be used, minimizing the additional compression required to attain a fusion burn.

Nonremovable Mandrels

Many of our current targets use bare glass microballoons as pusher shells, filled with high-pressure DT gas to serve as the fuel. Therefore, we continued our development of methods for quality selection and characterization of these bare glass microballoons. Many of these techniques should also be applicable to metal microballoon targets, as well as being useful in the selection and characterization of microballoons for use as mandrels for structured, multilayered targets.

Measurement of Microballoons -- We continued our development of optical interferometry techniques for quality selection and wall-thickness measurement of glass microballoons (GMBs). The GMBs are selected for quality by observing the circularity of the interference fringes and their concentricity with the outside surface of the GMB. For a complete assessment of quality the GMBs must be viewed in several orientations, which requires tedious reorientation of the GMB on the microscope slide. This requirement has been substantially reduced by the development of a tilting glass slide holder that allows GMBs on the slide to be rotated through 90° ($\pm$ 45° from the optic axis) without interfering with the microscope optics, thus allowing observation of the GMB through two orthogonal planes.

To improve our understanding of the interference patterns resulting from various defects in the GMBs, we have developed a ray-trace computer program that simulates GMB interferograms as seen in our Jamin-Lebedev transmitted-light interference microscope. In the most advanced version of this code we will be able to calculate patterns for general surface distortions by employing Fourier analysis of the surfaces of the microballoon, expanded in spherical harmonics. We presently consider only refracted rays, but the final version of the code will also treat diffracted and internally reflected light.

We have two versions of the code running; the first treats GMBs consisting of spherical surfaces that are nonconcentric along an arbitrary axis, whereas the second treats the spherical surface case as well as ellipsoidal GMBs in which the axes of the inside and outside surfaces are tilted at arbitrary angles to one another. Examples of the output of this program are shown in Figs. 78 and 79, where we compare patterns calculated for several GMBs by using the wall thickness and nonconcentricity measured in the interference microscope. A circle is drawn around the outside of the pattern corresponding to the outer diameter of the GMB. In both cases, the calculated patterns have one extra fringe near the outer diameter of the GMB, which is thought to have been caused by the neglect of diffraction effects; otherwise, the agreement is good.

We have continued to develop our x-ray microradiographic technique to quality-characterize and measure opaque microballoons. We are using an image-analysis system to analyze the photometric information in the radiograph. Wall-thickness variations of 0.12 μm in 0.6-μm-wall GMBs can now be detected, as compared with the 0.5-μm variations that can be detected with our conventional radiographic technique.[1] Through further refinements, we hope to improve the resolution of this photometric microradiographic technique by an additional factor of 2 to 4.

Plastic-Film Fabrication

For our experiments with thin films and vacuum insulation (see Sec. III), we need thin, freestanding plastic films with a high hydrogen content, and for our ion-spectroscopy experiments we need deuterated films. In response to these needs, we have developed a method of fabricating freestanding films of normal or deuterated polyethylene, $(-CH_2)_n$ or $(-CD_2)_n$, respectively, with thicknesses from ~2 nm to ~1 μm. These films are made by coating glass microscope slides with a solution of polyethylene in hot toluene, evaporating the toluene, and

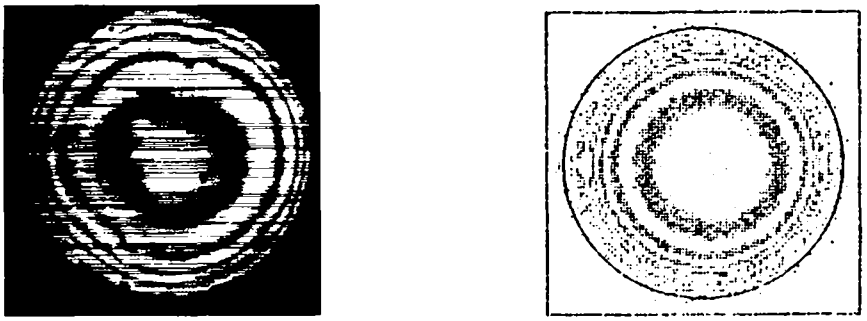

(a) (b)

Fig. 78. Interferograms of a nonconcentric thick-walled microballoon. (a) Photomicrograph from a Jamin-Lebedev interferometer; measured wall thickness, 3.1 μm; measured diameter, 99 μm; measured nonconcentricity, 0.16 μm (i.e., 0.32-μm wall-thickness variation). (b) Computer-generated interferogram calculated from measured parameters.

removing the resultant polyethylene film from the slide by flotation in water. Films as thin as 20 nm can be lifted off the water surface while supported across the 4-mm-diam aperture of our standard target holder; after drying, these films are strong and durable.

The film thickness is varied by adjusting the concentration of polyethylene in the solution as indicated in Fig. 80. Solutions containing up to 6 wt% polyethylene (corresponding to 0.9-μm-thick films) are used at a temperature of 361 K (88°C). Solutions of higher concentrations require higher temperatures for complete dissolution of the polyethylene. At higher concentrations, film thickness is a strong function of bath temperature and is consequently more difficult to control. For these thicker films, it may be more satisfactory to use the slower and more difficult method of Bartle,[2] in which hot polyethylene solution is cast onto glass slides, followed by solvent-evaporation and water-flotation. This latter technique has been used for film thicknesses from 0.5 to 20 μm.

Plastic Microballoon Fabrication

As a continuation of our development of techniques to fabricate structured targets, and partic-

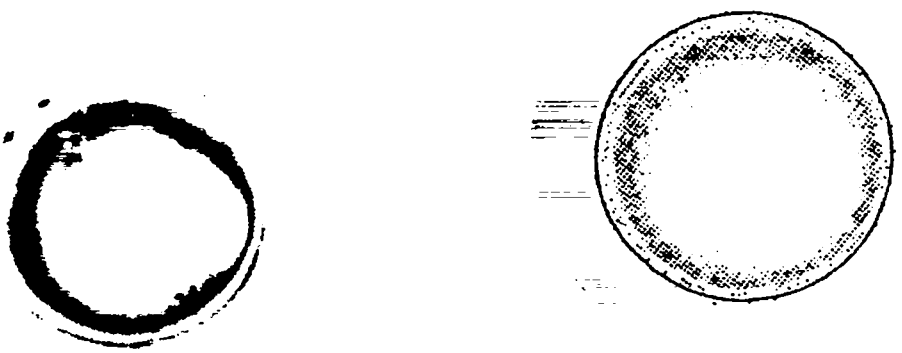

(a) (b)

Fig. 79. Interferograms of a nonconcentric thin-walled GMB. (a) Photomicrograph from a Jamin-Lebedev interferometer; measured diameter, 63 μm; measured wall thickness, 0.55 μm; measured nonconcentricity, 0.06 μm (i.e., 0.12-μm wall-thickness variation). (b) Computer-generated interferogram calculated from measured parameters.

ularly in light of the interest in vacuum insulation, we have developed a technique to fabricate freestanding plastic microballoons. These targets can be lined and/or coated with a variety of metals. In the basic technique, we use our glow-discharge polymerization (GDP) process[3] to fabricate hemispherical shells by depositing polymerized paraxylene onto copper mandrels having machined spherical ends. After coating, the plastic hemispherical shell is separated from the rest of the plastic coating by machining into the mandrel, after which the mandrel is dissolved in nitric acid, leaving a freestanding plastic hemispherical shell. These shells have been lined with metal by physical vapor deposition (PVD) of the desired metal onto the mandrel and then overcoating the metal with plastic by the GDP process. We have thus successfully fabricated plastic shells lined with gold and with aluminum. Metal coatings can also be applied to the plastic hemispherical shells by overcoating the plastic-coated mandrels with metal by PVD.

Spherical configurations are obtained by gluing two hemispherical shells together on either a glass-fiber or a plastic-film support. A DT-gas-filled microballoon can be incorporated in the center of the plastic shell, if desired, and any number of concentric plastic shells can be nested together.

We have made plastic shells with diameters ranging from 300 to 1000 μm having wall thicknesses of 2 to 3 μm, some of which were lined with 0.1 to 2.0 μm of aluminum or gold. A multiple-sample fixture is used in the PVD operation, which rotates 12 mandrels simultaneously, and allows each mandrel to be provided with a uniform coating on the spherical end. A 5-cm-diam electrode is used in the GDP coating step, allowing at least 20 mandrels to be plastic-coated per run. A photomicrograph of a bare, plastic hemispherical shell is shown in Fig. 81.

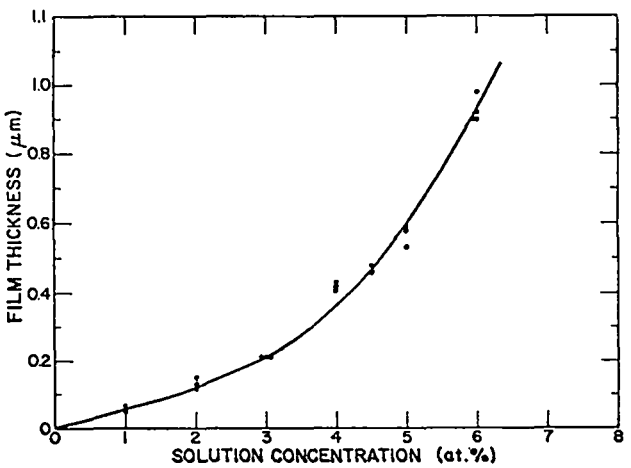

Fig. 80. Parameters for fabricating polyethylene films by coating a slide with polyethylene dissolved in toluene and then evaporating the toluene.

Pusher-Shell Deposition

We have continued the development of methods to deposit uniform layers of high-Z metals onto various types of mandrels for use as pusher shells. The primary objective is the fabrication of high-strength coatings with useful DT permeability.

Chemical Vapor Deposition -- Chemical vapor deposition (CVD) has been very successful in coating microballoon substrates because the gas-fluidized-bed coating apparatus we use in this operation provides good mixing of the substrates and allows metal coatings to be applied to these otherwise difficult-to-handle substrates. We have continued our efforts to improve the control of all the parameters in the CVD process. Flow systems were modified to allow still better control of carrier-gas flows, sensitive mass flowmeters were installed, and experiments were run to determine the constancy of coating-metal feed rates. However, coating repeatability from run to run, especially with the $Mo(CO)_6$ system, is not as good as we would wish, and these general system improvements are therefore continuing.

We continued our efforts to deposit high-quality ~10-μm-thick coatings of molybdenum (or Mo_2C)

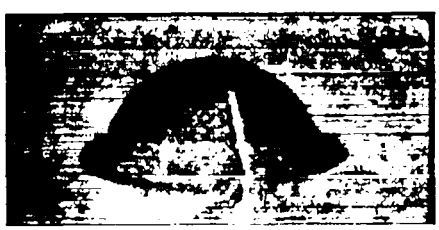

Fig. 81. Photomicrograph of a plastic hemispherical shell. These shells can be used either with the flange, as shown, or with the flange removed. Size: 500-μm diameter by ≈ 3-μm wall.

from $Mo(CO)_6$ onto Solacel substrates. The thermal decomposition of $Mo(CO)_6$ can involve several reactions:

$$Mo(CO)_6 \rightleftharpoons Mo + 6\ CO\ , \qquad (1)$$

$$2\ CO \rightleftharpoons C + CO_2\ , \qquad (2)$$

$$2\ Mo + C \rightleftharpoons Mo_2C\ , \qquad (3)$$

and, in the presence of hydrogen,

$$H_2 + CO \rightleftharpoons H_2O + C\ . \qquad (4)$$

In one set of experiments, we varied the carrier-gas composition and the deposition temperature to determine whether we could produce a deposit of molybdenum metal rather than the molybdenum carbide described previously.[4] We could not suppress the CO_2 disproportionation reaction, Reaction (2) above, neither by the use of low deposition temperatures (475 K) nor by the use of pure CO_2 as the carrier gas [this inability indicates that Reaction (2), as it occurs on the depositing surface, is insensitive to the gas-phase $CO:CO_2$ concentration ratio].

We continue to find it difficult to deposit thick, stress-free, and smooth molybdenum-carbide coatings from $Mo(CO)_6$.[4] Coatings deposited from an argon carrier gas are smooth but stressed, whereas those deposited from a hydrogen carrier are stress-free but have a rough surface, apparently due to gas-phase nucleation of carbon from Reaction (4) and subsequent incorporation of these carbon particles into the surface. We can produce acceptable coatings in an argon carrier gas up to thicknesses of ~ 5 μm, but thicker coatings are so highly stressed that they generally crack. As a result of these difficulties, we have begun to develop techniques to deposit molybdenum metal by CVD from the hydrogen reduction of MoF_6. Initial runs were complicated by the use of a fused-silica coating apparatus that reacted with the HF formed in the MoF_6 reduction. An inert apparatus is being fabricated to solve this problem.

Because tungsten is also a pusher metal of interest, several CVD runs were made to coat Solacels with tungsten by the hydrogen reduction of WF_6. We obtained 8- to 40-μm-thick, smooth coatings that were very strong and exhibited essentially no cracking.

Sputtering -- Sputtering may be useful for coating substrates with metal pusher shells, because it can be used to apply a wide range of metals, alloys, and dielectrics. We have tried previously to coat microspheres by bouncing them on various vibratory support tables to expose their surfaces uniformly to the sputtered vapor, but we were unable to obtain good coating uniformity. We recently installed a small gas-fluidized-bed coater in our sputtering apparatus and sputtered molybdenum onto a bed of Solacels. We found that we could fluidize the bed with a flow of argon gas low enough to provide the pressure appropriate for the glow-discharge sputtering operations (~ 3 Pa); we obtained reasonably uniform coatings.

Electroless and Electrolytic Plating -- We continued to expand our microsphere coating capabilities by perfecting the use of our improved electroless and electrolytic coating apparatus.[5] In pursuit of high-strength coatings, we obtained a commercial nickel-iron alloy bath that we will use to apply electroless nickel-iron alloy coatings to Solacels. In an experiment to apply duplex coatings, we deposited an electroless 2-μm-thick nickel coating to Solacels, overcoated by a 7-μm-thick layer of electrolytic nickel. These are being evaluated.

Several electroless coating runs were made with GMBs as substrates. These GMBs must first be metal-coated by another technique to provide a conductive surface for the electroless process. In one of these experiments the GMBs were precoated with nickel (< 1 μm thick) by CVD from $Ni(CO)_4$, and were then overcoated with thick, uniform coatings of electroless nickel-copper alloy.

In another of these experiments we tried to repeat this CVD-electroless coating sequence on batches of 100 selected GMBs. These samples were mixed with several cubic centimeters of larger GMBs and precoated with nickel by CVD. Four different sets of samples were processed, with recovery in excess of 90% in all cases. However, the subsequent electroless nickel-coating step was not very successful because of apparent bonding problems between the precoated CVD layer and the GMBs. The doubly coated product is being characterized by

scanning-electron microscopy, microradiography, and metallography. After all data are available, we intend to repeat the experiment.

Nondestructive Fuel-Gas Analysis

We have recently completed an initial series of experiments demonstrating the usefulness of a new technique for nondestructive analysis of the fuel-gas content of laser-fusion targets. Beta particles resulting from tritium decay interact with fuel-gas molecules and with the microballoon wall, and cause optical photon emission by means of fluorescent processes. Thus, the number of photons emitted by a DT-filled target should be a function of the amount of tritium contained therein. (The method is useful only for glass or other optically transparent microballoons.)

A preliminary experiment indicated a fluorescent light output of six times the background from a DT-filled GMB, and no light output from a D_2-filled GMB. Encouraged, we filled a series of GMBs of different sizes with 100 atm of pure tritium and counted the photons emitted as a function of GMB radius to obtain the data shown in Fig. 82. Our preliminary analysis of the various processes that can result in visible-light photon emission indicates that the photon output can vary with radius (r) as r^2, r^3, and/or r^4, whereas the data indicate an $r^{3.1}$ dependence, consistent with the analysis. These results demonstrate the usefulness of the method. Next, we intend to determine the wavelength distribution of the emitted light; we hope to be able to distinguish between tritium dissolved in the GMB walls and tritium in the gas phase. We might also be able to differentiate between the deuterium and the tritium contained in the gas space.

CRYOGENIC TARGETS

Laser-fusion targets fueled with cryogenic liquid or solid DT offer the advantage of high initial fuel density without the disadvantage of the diluent atoms present in the room-temperature solids that have a high hydrogen density [e.g., lithium in Li(D,T) or carbon in $(-CDT)_n$]. Calculations indicate that the yields from targets fueled with either liquid or solid DT can be considerably higher than those for targets of the same design fueled with high-pressure DT gas. As a result, we are actively pursuing the development of cryogenic targets in spite of the significant experimental complications that are encountered in the fabrication of such targets and their use in laser-target interaction experiments.

Spherical Geometries

The cryogenic target geometry that is receiving greatest attention is a uniform, hollow shell of solid or liquid DT condensed onto the inside surface of a glass or metal microballoon container that serves as the pusher shell. We are concentrating our efforts on GMBs, simultaneously developing the techniques to (a) condense the DT into a uniformly thick layer on the inside surface of the glass and (b) to measure the thickness uniformity of the DT shell. Two general approaches are being

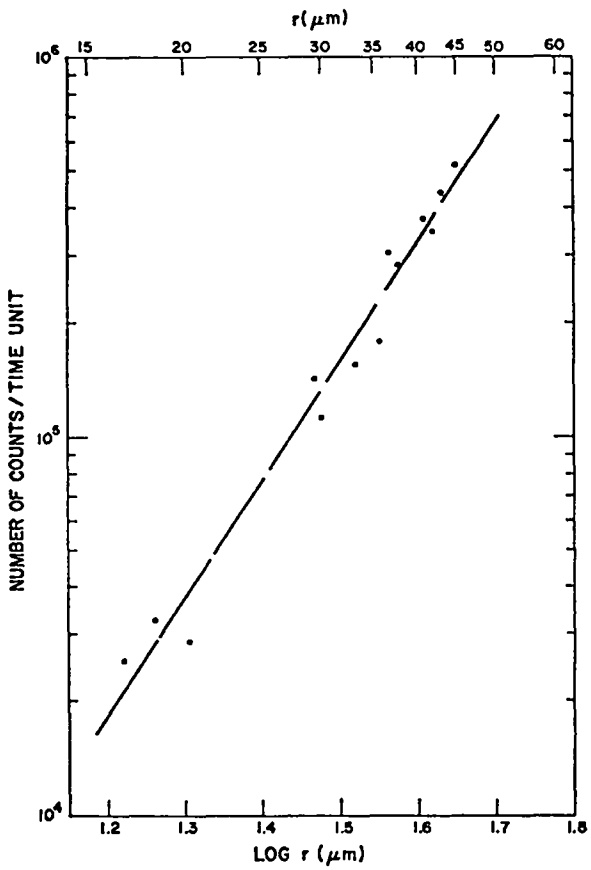

Fig. 82. Light output of tritium-filled GMB as a function of microballoon radius.

examined: (1) we deliberately cool the target non-uniformly in an attempt to counteract the effect of gravitational forces by blowing a jet of cold helium onto the top of the target, or (2) we place the target into an isothermal environment and try to freeze the DT uniformly onto the surface.

Because a combination of heat-removal techniques will probably be required, we performed a series of experiments on GMBs that were filled either with D_2, with DT, or with T_2 to evaluate multiple cooling techniques. The room-temperature fill pressures ranged from 46 to 134 atm, corresponding to uniform solid layer thicknesses ranging from 0.5 to 1.5 μm. Because the qualitative behavior of all the targets was similar (i.e., there was no obvious isotope or thickness effect), we may discuss the results collectively. Each target was cemented onto a glass fiber (1 to 4 μm diameter) which, in turn, was cemented at both ends to a thin brass holder attached to the cryostat ($T \geq 4$ K).

The target was surrounded by a cylindrical radiation shield (also attached to the cryostat) that was perforated by two small holes (on a diameter) for viewing the target. Several hole sizes were used, ranging in diameter from 0.8 to 1.9 mm, resulting in differing image quality and rate of heat input to the target from room-temperature (or illuminator-lamp) radiation incident onto the target through the two holes. Considerable care was required to obtain, and verify the existence of, conditions for observing the target without perturbation by the viewing system.

The target, Fig. 83a, was cooled by four types of heat transfer, in increasing order of cooling rate: (1) radiation to the low-temperature radiation shield; (2) conduction through the glass-fiber support to the cold-metal support; (3) conduction through exchange gas, at pressures of 0.04 to 0.1 Pa (0.3 to 0.8 μmHg), to the radiation shield; and (4) conduction to a stream of cold helium from above. Types (3) and (4) could be controlled during an experiment through operation of a valve. With the target at 24 K and the heat shield at 4 K, the approximate power-removal rates of the four types of heat transfer are: (1) $\sim 6 \times 10^{-10}$ W by radiation to the heat shield; (2) $\sim 10^{-8}$ W by conduction through the glass film; (3) $\sim 5 \times 10^{-7}$ W by conduction to the ^{4}He heat-exchange gas; and (4) although difficult to calculate in detail, $> 10^{-5}$ W for the helium jet heat-transfer method.

The path of heat leaving the target should vary for the four types of heat transfer: Types (1) and (3) should extract heat uniformly over the target surface, whereas Type (2) should act as a cold

Fig. 83. Photomicrographs of DT-filled GMBs (glued to a 4-μm-diam glass fiber) under various cryogenic conditions. Conduction of heat through fiber to heat shield and radiation to heat shield occur at all times. (a) Typical view of gas-filled target before condensation. (b) Primary target cooling via (stagnant) heat-exchange gas. Note thicker layer at bottom. (c) Same target as (a) but cooled by a cold helium jet directed at top of microballoon. Note thicker layer at top of target. (d) Same as (c) but lower helium flow rate. The DT layer now appears to be uniform around the periphery of the target.

point and Type (4) should cool most of the target top. These predictions were supported by observation, except that the fiber contact point did not act as a coagulation point. With small viewing holes (≤ 1.2 mm diam) in the radiation shield, condensation was seen even in the absence of exchange gas or of a cold helium stream. However, one of these two gas-conduction types of cooling had to be used for condensation with 1.8-mm holes in the shield.

In the absence of a known vertical thermal gradient, the condensate was usually thickest at the bottom thinning out toward the top, as might be expected from the effects of gravity and surface tension (Fig. 83b). Some darkening at the top probably was the result of adsorption. Application of a thermal gradient from the stream of cold helium overcame gravity so that condensate either appeared as a uniform layer (Fig. 83c) or could even be made thicker at the top (Fig. 83d).

All our conclusions are based on the assumption that darkening in the image is directly related to condensation. In particular, uniform condensation (the goal) would be expected to create symmetrical darkening, which we did observe under a combination of symmetric and asymmetric heat-transfer techniques (Fig. 83c). Furthermore, the appearance of condensate at various temperatures between 20 and 30 K roughly corroborated the calculations of condensate appearance from the characteristics of the particular target observed, i.e., size, fill pressure, and isotopic vapor pressures. The most informative type of target viewing seems to be with direct, white light. Shearing-plate interferometry with 0.63-μm helium-neon laser light produced rings that generally matched the darkening pattern of the white light.

We will repeat some of these experiments under conditions that will allow higher resolution observation of the target from several directions simultaneously. In addition, we plan to install a second nozzle so that cold helium jets can impinge on the target from above and below. This should allow us to determine the detailed combination of heat-removal techniques necessary to form geometrically uniform liquid or solid DT layers in the GMB targets.

Our second-generation target-freezing apparatus is nearly operational. It provides improved temperature uniformity (to 10 mK), programmed cooling rates from 10 K/s to 10^{-3} K/s, and f/2 optical viewing access on two orthogonal axes through sapphire windows at the cryostat temperature. In addition, an image-intensifier system will be used for viewing the target, allowing a decrease in the required illumination level by a factor of 10^3.

Pressure-Volume-Temperature (P-V-T) Properties of Cyrogenic Hydrogen Isotopes

We have resumed our efforts to measure the P-V-T properties of liquid and solid hydrogen isotopes and isotope mixtures. The apparatus was reassembled and shake-down measurements have started on parahydrogen. We plan to start measurements on deuterium-tritium mixtures as soon as the apparatus can be readied for work with tritium.

REFERENCES

1. F. Skoberne, "Laser Program at LASL, July 1 - December 31, 1975," Los Alamos Scientific Laboratory report LA-6245-PR (July 1976), p. 78.
2. C. M. Bartle and H. O. Meyer, "Improved Technique for the Preparation of Thin Deuterated-Polyethylene Targets," Nucl. Instr. and Meth. 112, 615 (1973).
3. F. Skoberne, "Laser Program at LASL, January 1 - June 30, 1975," Los Alamos Scientific Laboratory report LA-6050-PR (January 1976), pp. 76, 77.
4. F. Skoberne, "Laser Program at LASL, July 1 - December 31, 1975," Los Alamos Scientific Laboratory report LA-6245-PR (July 1976), p. 79.
5. F. Skoberne, "Laser Program at LASL, July - December 31, 1975," Los Alamos Scientific Laboratory report LA-6245-PR (July 1976), pp. 80, 81.

V. TARGET DIAGNOSTICS

The tiny volume and brief duration involved in the laser-fusion process create needs for new diagnostic techniques having spatial and temporal resolutions in the submicrometer and 1- to 100-ps regime, respectively. These needs are being met with a vigorous program of diagnostics in such areas as laser calorimetry, charged particle and neutron detection, x-ray spectrometry, and subnanosecond streak-camera development.

INTRODUCTION

The short duration and minute spatial extent of laser-fusion experiments impose demands on instrumentation that cannot, in general, be satisfied by existing devices. Therefore, our diagnostics development program concentrates on advancing the state of the art in high-speed, high-resolution instrumentation; the development of time-resolved imaging systems in the visible and x-ray spectrum is of special interest.

Because of recent theoretical and experimental results, measuring the density gradient near the critical surface of a plasma has become an important task for determining wavelength-scaling effects. An interferometer is being designed to measure this gradient, and interferogram analysis for high-density plasmas has become an important study area.

X-ray diagnostics have been developed further, because they offer the best means for studying the physics of implosions. Our x-ray streak camera is being perfected, and time and spatially resolved images of microballoon implosions have been obtained. The first x-ray microscope produced by UCC's Oak Ridge Y-12 Plant has been delivered, and testing is in progress; studies of x-ray photographic films and x-ray framing techniques have been continued.

Sensitive and accurate ion calorimeters have been produced, and the design of a 10.6-μm alignment system has been improved. These topics are discussed in detail in the following paragraphs.

OPTICAL DIAGNOSTICS OF CO_2 LASER-PRODUCED PLASMAS

Understanding the interaction of light and plasma in the immediate neighborhood of the critical density for the specific laser wavelength is fundamental to laser-fusion research. We now believe that very steep plasma density gradients near critical values are formed at high laser intensities. Plasmas produced by a CO_2 laser are ideal for plasma studies (the results of which should be essentially wavelength-independent), because visible-light probe beams can easily penetrate to densities well above the 10.6-μm critical density. The diagnostic laser should be synchronized with the CO_2 laser, and should generate a sufficiently short pulse and high spatial coherence to ensure adequate resolution.

We have initiated an effort to synchronize a glass laser with a short-pulse CO_2 oscillator (250 ps $\leq$ pulse width $\leq$ 1 ns). The glass-laser output at 1.06 μm will be frequency-doubled and -tripled by using conventional techniques to produce green (0.53-μm) and blue (0.36-μm) diagnostic beams. The CO_2 and glass lasers with $<$ 20-ps jitter will be synchronized through a LASL-developed fast dielectric switch that will trigger the CO_2 laser when driven by the glass laser.

The green and the blue beams produced from the fundamental frequency of the modelocked near-infrared laser (pulse width, $\simeq$ 20 ps) are ideally suited to two-wavelength holographic interferometry.

We are fundamentally interested in studying the isodensity surface at 10^{19} cm^{-3} (the critical

density for 10.6-μm light), and chose a field of view of ~400 μm for 0.53-μm light and of ~640 μm for 0.35-μm light. These fields are large enough to allow detailed investigation of temporal and spatial developments near this critical plasma density. A spatial resolution of 5 μm should be possible.

This diagnostic apparatus is also capable of schlieren photography. In particular, if we wish to discern density jumps from 10^{19} to 10^{20} cm^{-3} in a distance of 1 μm, then two-wavelength differential schlieren photography would lend itself to at least a qualitative assessment of the major density jumps for the above fields of view.

A glass laser appears best when, e.g., cost, energy, spatial coherence, pulse length, and reliability are considered. A relatively inexpensive 100-mJ modelocked glass laser will provide adequate energy for synchronized two-wavelength multiple-exposure holographic interferometry.

INTERFEROGRAM ANALYSIS

Interferometric probing of high-density, steep-gradient plasmas promises to provide a highly valuable diagnostic tool for the study of laser-target interactions. A means of calculating the fringe patterns to be expected under various conditions is needed in view of the difficult and complex experimental problems faced. This capability is now offered by a computer code called DIVS for media in which the index of refraction is a function of the radial distance. This code performs ray tracing to determine the photon trajectories, ascertains the optical-path differences caused by the medium, and simulates the interferometric fringe-shift pattern that would be observed.

The ray-tracing portion of DIVS iteratively solves the differential equation of light rays. The rays incident on the exit plane at various angles are then projected back to the virtual image plane of the receiving optics (in our case a modified Mach-Zender interferometer). The optical-path differences at the image plane due to the presence of the plasma are then calculated and divided by the probe wavelength to provide the fringe-displacement function for a cylindrical plasma.

After several further mathematical manipulations, phase contours at one-wavelength intervals are plotted as a simulated interferogram. One quadrant of such a simulated interferogram is shown in Fig. 84 for a Gaussian electron-density profile having a standard deviation of 25 μm, a cutoff radius of 100 μm, and the probe-light (532-nm) critical surface at 10 μm. The locus of the termini of the four lowest contour lines is a circle determined by the angular acceptance (assumed to be 15°) of the receiving optics.

The DIVS code is being used to simulate the effect of plasma-profile steepening (caused by radiation ponderomotive forces) on the interferometric probing of a plasma. Initial calculations emphasize the well-known, but often ignored, fact that accurate optical ray tracing requires

$$\frac{1}{n}\frac{dn}{dr} \ll 1 ,$$

where n is the local index of refraction. Even if a probe-laser wavelength is short enough to probe well into a plasma, interferometry is very difficult in steep profiles where dn/dr is large.

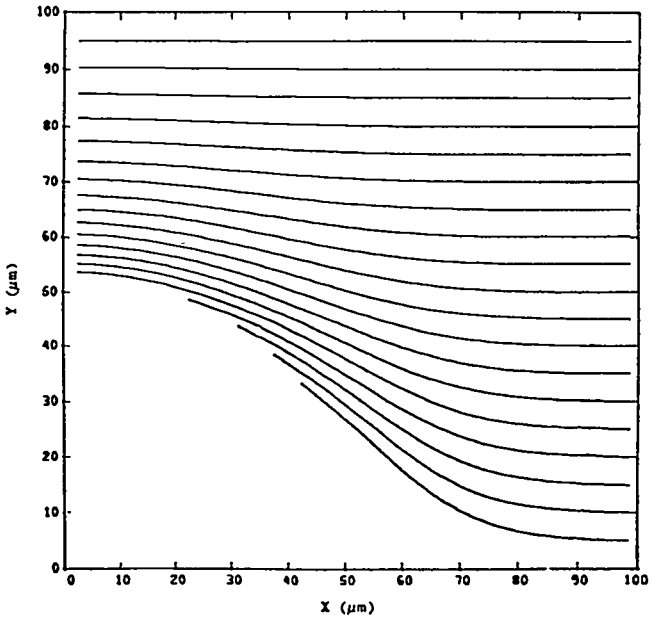

Fig. 84. Simulated interferogram for a Gaussian electron-density profile with the parameter values described in the text.

Fig. 85. Several x-ray streak-camera photographs of nickel microballoon implosions. Time runs from top to bottom in each photograph, with a total time span of 150 ps. Note that trigger jitter is <40 ps.

X-RAY DIAGNOSTICS

X-Ray Streak-Camera Development

Our proximity-focused x-ray streak camera has been used in over 300 shots of the dual-beam Nd:YAG laser system and has proved to be an essential diagnostic tool. The trigger is 98% reliable in producing a streak on each shot. Trigger jitter, as may be seen in Fig. 85, is less than 40 ps. In the figure, which was obtained by irradiating a nickel microballoon, time runs from top to bottom. The entire time span of the image field is ~150 ps.

In its first application we used the camera to synchronize the arrival of the two laser beams on target to within less than 5 ps. These two beams then yielded some of the most symmetric and hottest compressions of a ball-and-disk target we ever obtained. The camera has been used to follow the behavior of many compressions and has produced some intriguing data. Figures 86 and 87 show the compression of an empty 50-μm-diam glass microballoon embedded in a 200-μm-diam disk by a laser pulse of ~70 ps duration. The corresponding x-ray pinhole photograph is shown with the streak. The noise in

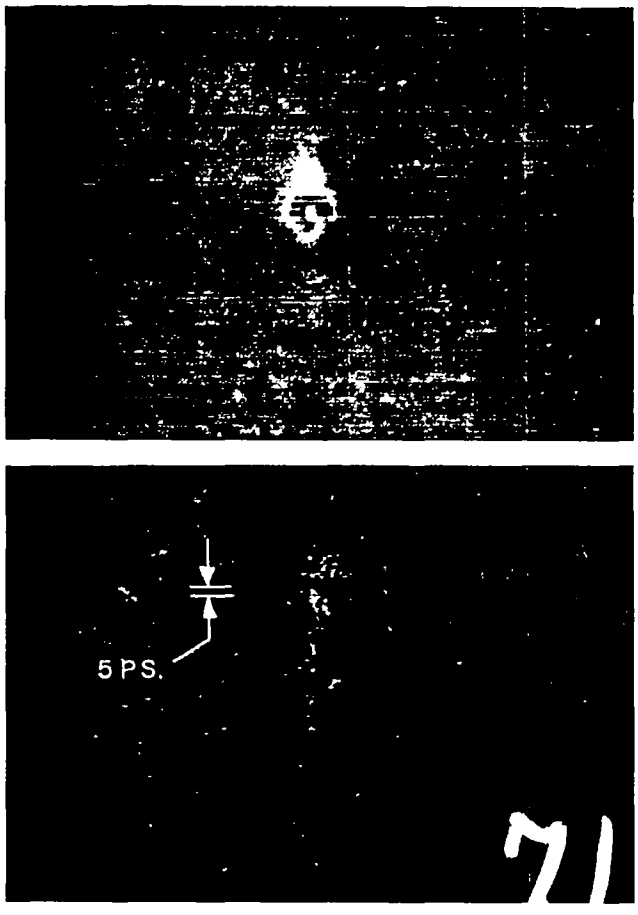

Fig. 86. X-ray streak-camera (bottom) and x-ray pinhole camera photographs (top) of compression of a 50-μm-diam glass microballoon embedded in a 200-μm-diam disk by a ~70-ps laser pulse.

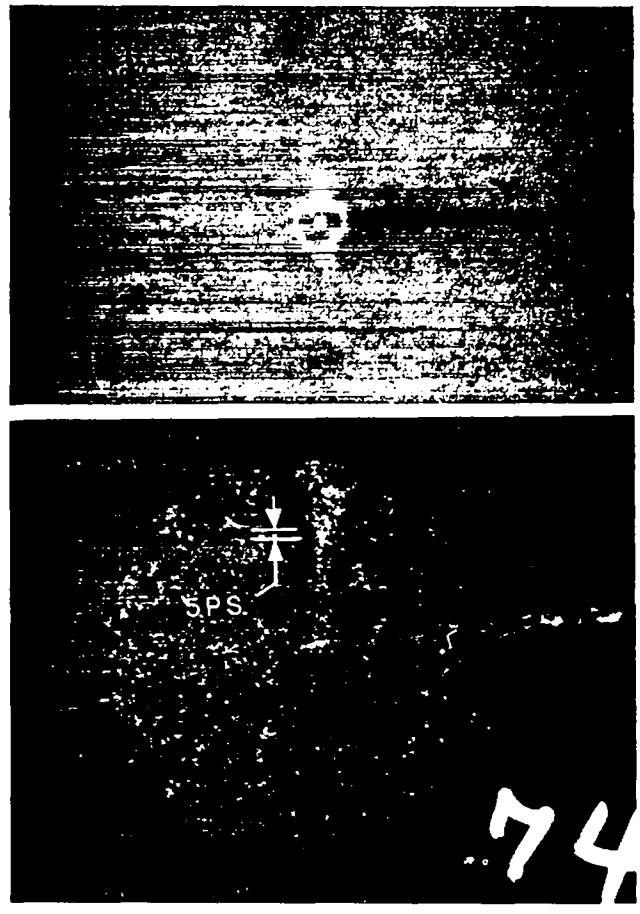

Fig. 87. Compression of glass microballoon similar to that shown in Fig. 86.

the streak photograph is indicative of a vacuum problem with the prototype camera and is not inherent in its design. The compression of the ball may be seen without a bright compression spike. In no case does the streak last much longer than the duration of irradiation. In Fig. 88, we were fortunate to record a feature that confirms the theoretical prediction of 2.7-ps temporal resolution for the prototype camera design (limit, 0.6 ps): the target, after a cold compression (no V-shaped streak), goes through an instability lasting ≤3 ps. This streak photograph supports the need for picosecond x-ray resolution in the study of target compression processes.

All parameters for the construction of a visible-light streak tube based upon the proximity design have been given to the principal engineer on contract with IT&T. An early prototype should be available by December 1976.

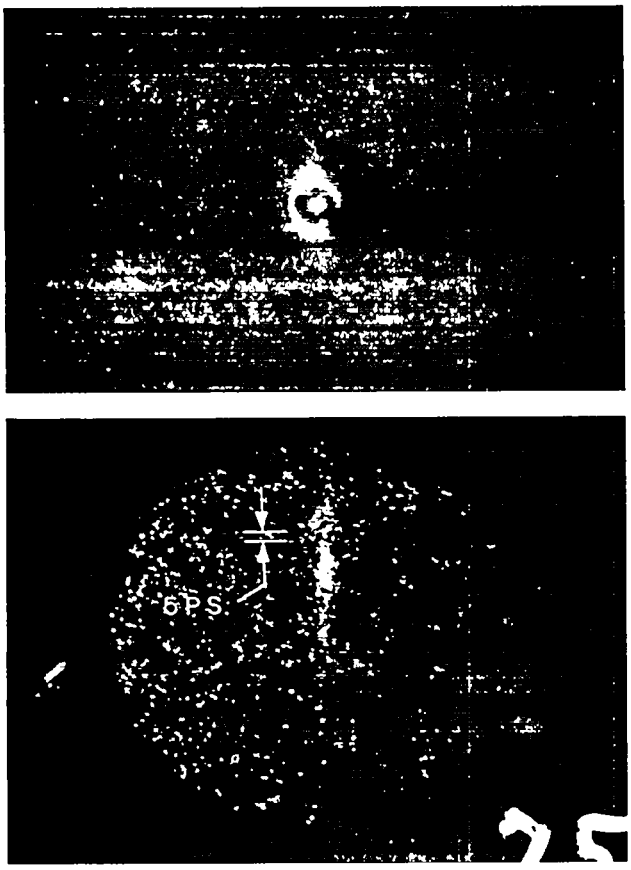

Fig. 88. Compression of microballoon as in Fig. 86; note instability in the streak, which confirms the <3-ps temporal resolution of the streak camera.

X-Ray Microscope Development

Because of the importance of high-resolution x-ray imaging techniques to the laser-fusion program, we are pursuing two approaches. A contract for the design, fabrication, and testing of an x-ray microscope with 1-μm resolution has been awarded to American Science and Engineering (AS&E), who are using the design and the precision hand-finishing methods they had developed previously for their solar x-ray telescopes. However, because optical elements produced in this way are very expensive, we are developing a second method in collaboration with UCC's Oak Ridge Y-12 Plant. By using design techniques described below, we will attempt diamond-point machining to fabricate the optics. The design is based on x-ray scattering measurements obtained by AS&E on flat surfaces produced by Y-12, but there are no data on curved surfaces. If our method is successful, we will be able to produce optical elements for less than 10% of the cost of hand-configured optics. Additional hand finishing, if required, would increase the cost, but significant savings are still possible. The basic design depends critically on surface characteristics, as described below, and the mirrors for some microscope designs, proposed earlier,[1] cannot be fabricated in this way. One element has been fabricated by Y-12, and testing has begun.

The analytical design of x-ray microscopes was described by Wolter,[2] and several microscope designs for laser-fusion research have been proposed recently.[3] For target diagnostics, a microscope consists of a confocal ellipsoid-hyperboloid pair. Wolter showed that the best resolution is obtained when the Abbe sine condition is satisfied at the intersection of the surfaces, but this condition frequently leads to geometries that are difficult to fabricate. Also, the effect of surface errors is not easily assessed analytically, although the resolution is given roughly by the product of surface slope and focal length.

The problems of surface imperfections and violation of the sine conditions are treated most easily by numerical ray-tracing. Although there are many generalized ray-tracing codes, they are cumbersome and costly in computer and setup time. For a system such as the x-ray microscope, where the reflecting surfaces can be specified analytically, these codes are also unnecessary.

An efficient Monte Carlo code which treats surface errors logically and is easily set up has been written. The code traces ~ 100 rays per second of computer time, including surface errors as well as the effects of wavelength and angle of incidence on x-ray reflectivity. The short running time for this code allows microscope design to be performed interactively with a computer graphics terminal, so that both designer and computer time are used most efficiently. This code represents a significant advance in design tools for x-ray microscopes.

Figure 89 shows the calculated ray pattern of a point source located 50 μm off the axis of a microscope that is at a distance of 32 cm from the object and has a magnification of 10. Figure 90 is a simulated densitometer scan of the image. Figure 91 shows a densitometer scan for an on-axis source, assuming that the microscope has a 50-μrad random Gaussian slope (which corresponds to the AS&E measurement); and Fig. 92 shows the same system with a periodic error of 100-Å amplitude and 2-mm period (which corresponds to a Lawrence Livermore Laboratory measurement of a micromachined surface). Clearly, this system should produce good resolution even with fairly large surface errors. (Note that the plots represent the image plane; source resolution is obtained by dividing the distances shown by 10.)

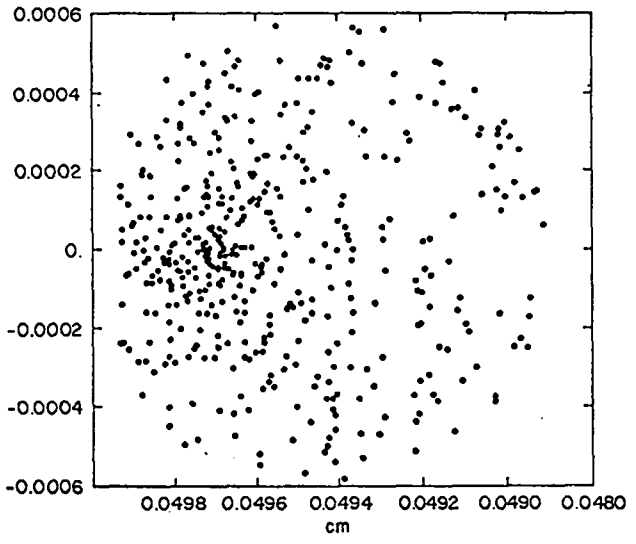

Fig. 89. Calculated ray pattern of an x-ray point source, off-axis.

We have fabricated our x-ray microscope system by using a technique suggested by Y-12. An aluminum mandrel was machined under numerical control on a precision diamond-point lathe. After interferometric measurements had indicated an acceptable slope error of ~ 50 μrad, the mandrel was plated with nickel. The mandrel was then dissolved with sodium hydroxide (NaOH), but the plating on the first unit was unacceptable, and steps had to be taken to correct the problem. Two recent attempts produced surfaces that separated easily from the mandrels without the use of NaOH. Five mandrels have been machined, and work on the plating process is continuing. The high quality of the mandrels indicates that overall cost may have been reduced substantially, but x-ray testing has not yet begun.

The replication method is also being pursued, under LASL contract, by AS&E, who suggested this process independently and are using a somewhat different technique. They will test the process by taking x-ray scattering measurements on replicas of high-quality flat surfaces; the replication process can thus be examined independently of expensive surface finishing. This work will be completed by the end of CY 1976.

X-Ray Collector

We have evaluated a prototype axisymmetric grazing-incidence x-ray lens by using the x-ray

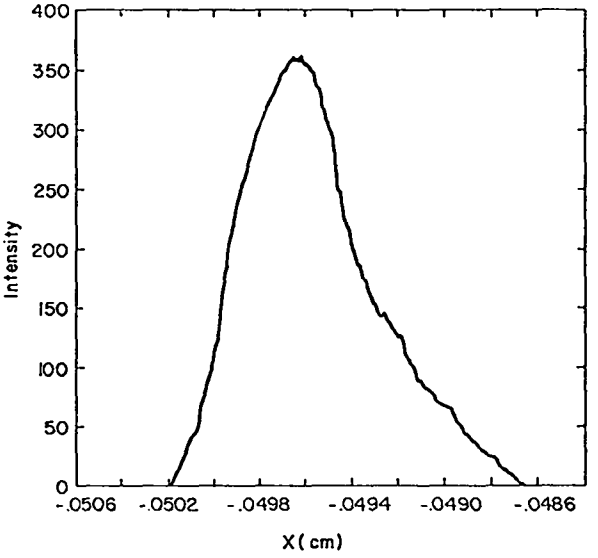

Fig. 90. Simulated densitometer scan.

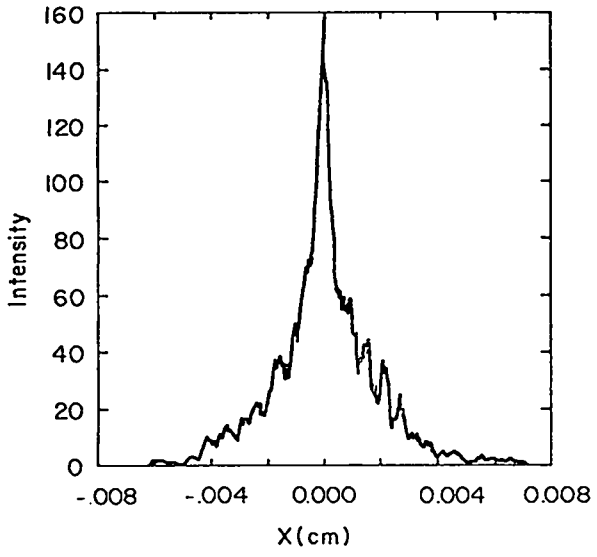

Fig. 91. Densitometer scan for on-axis source.

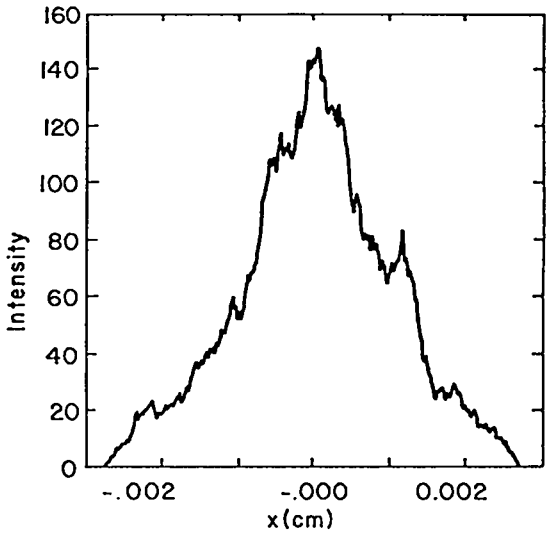

Fig. 92. Same system as in Fig. 91, with a periodic error of 100-Å amplitude and 2-mm period.

emission of a laser-produced plasma on an aluminum slab. The lens had good x-ray transport properties, as evidenced by the fact that an x-ray image was recorded on film 20 cm from the plasma. A calibration experiment was performed as shown schematically in Fig. 93; measured collection efficiency was 0.3%. This instrument may be useful for x-ray calorimetry and for other experiments requiring efficient collection of sub-keV x-rays with modest imaging.

X-Ray Framing

In a series of experiments we are determining the feasibility of using x-ray shadowgraphy for observing laser-fusion targets. To date, our efforts have been devoted to, e.g., the fabrication and alignment of the flash source (laser target), to the target and image system, and to the precise measurement of the resolution.

To test the practicality of the backlighting scheme, we placed a copper mesh between an aluminum laser target and a pinhole camera. Typical spacings were 5 mm from laser focus to the mesh and 5 mm from mesh to pinhole substrate.

The alignment of a system of this type is rather critical, and the technique now in use consists of a He-Ne laser placed with its axis coincident with that of a Questar telescope. A resolution target made of 12-μm-diam crossed gold wires and a flash source consisting of a 100-μm square of 25-μm-thick aluminum were then positioned on the axis. A stereoscopic pair of 5-μm pinholes was

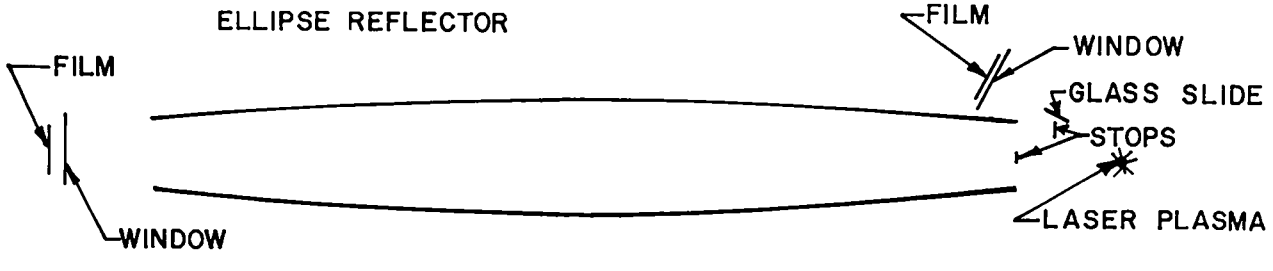

Fig. 93. Schematic of x-ray collector.

iented with one pinhole on the flash source
ıxis. This alignment scheme is straightfor-
i reliable. In Fig. 94 we see the cross
by the intersection of 5- and 7-μm lead
ibers. Both show up clearly, which verifies
: necessary alignment can be achieved and
: apparent resolution of a 5-μm pinhole is
:ter than 5 μm.

:flection Calculations

: practical use of x-ray reflection in an
lorimeter or microscope requires long-term
.ion stability, which, in turn, requires
ms that may accumulate on the reflection
have only a negligible effect on reflect-

study this effect, we have developed a com-
de based on the exact Fresnel equations
's equations across material boundaries)
aces composed of two layers. We then per-
alculations for carbon layers (as a crude
on of oil) on a gold substrate. Thick-
of carbon from 0 to 10 000 Å, photon ener-
om 0.1 to 10 keV, and glancing angles from
25° bounded the parameters of the study.
ause the results exhibit irregular struc-
n plotted against either photon energy or

View of blacklight crossed lead-glass fibers, taken through a 6-µm pinhole, shows a 5-µm fiber (upper right to lower left) and a 7-µm fiber.

angle, they cannot be summarized concisely except in general terms. Generally, for photon energies less than 2 keV the effect of a carbon deposit on the reflectance is noticeable at a thickness of 30 Å and becomes pronounced (in some cases three times higher) at 100 Å. For photon energies above 2 keV, the comparable thicknesses are 100 and 300 Å. In most cases, a carbon thickness of 1000 Å gives a very irregular plot.

X-Ray Spectroscopy

Two multichannel filter-type x-ray spectrometers are being fabricated for target experiments with the TBS. One spectrometer will have ten channels ranging in energy from 0.45 to 8 keV, and the second will have four channels ranging from 0.45 to 1.5 keV. Both systems are designed in modular form so that any one channel may be removed for calibration or interchanged, and both will include channels to measure continuum and line radiation. The signals will be read out on gated charge-sensitive analog-to-digital converters.

X-Ray Film Calibration

The soft-x-ray calibration of Kodak RAR 2490 film has been completed. Relative sensitivities over the measured range of photon energies, 0.28 to 8.04 keV, are plotted in Fig. 95. The characteristic curve (optical density D versus exposure H) was fit to a two-parameter analytic function. A sample of the fit is shown in Fig. 96. Also, we have measured the solarization at 1.49 keV, as shown in Fig. 97, and have thus achieved the sensitometric calibration of a film that can be used for both x-ray spectroscopy and imaging.

AUTOMATIC LASER AND TARGET DATA ACQUISITION

As experiments become more complex, the automatic acquisition and analysis of data become a necessity to take advantage of the large amount of information produced in a single shot. Techniques and instrumentation for these functions are being developed on the NOVA-840 computer.

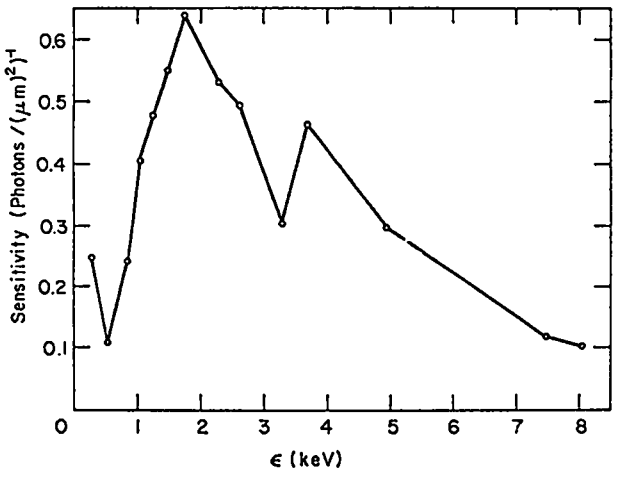

Fig. 95. Relative x-ray film sensitivities.

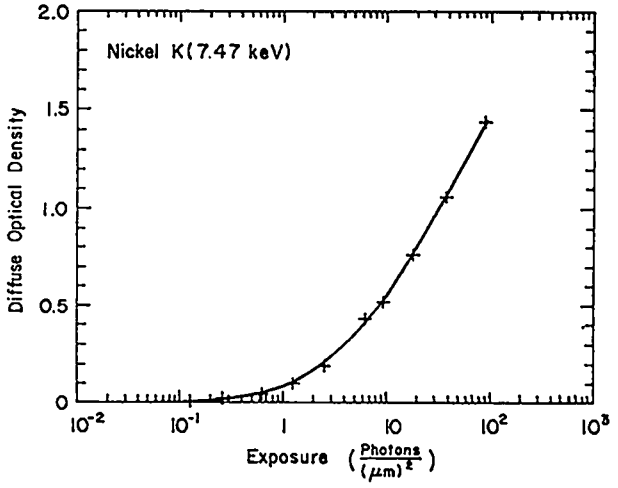

Fig. 96. Fit of a two-parameter function to the characteristic curve (optical density vs exposure) for Kodak RAR 2490 film.

Laser-system data are now acquired, reduced, and displayed by the NOVA computer, without action by an operator. The Wang-600 calculator performs the same task in a less sophisticated manner in parallel, as a backup. Should either controller fail, the calorimeter data-acquisition system may be switched to either the NOVA, the Wang, or both.

Ten channels of 10-MHz, 6-bit, 256-sample transient digitizers and 36 channels of 10-bit peak-sensing analog-to-digital converters may be read automatically on each laser shot for acquisition of target data. The data are stored in disk files, indexed by date and shot number, and may be displayed promptly or on recall. Ion calorimeter data are acquired on spare channels of the laser calorimeter acquisition system.

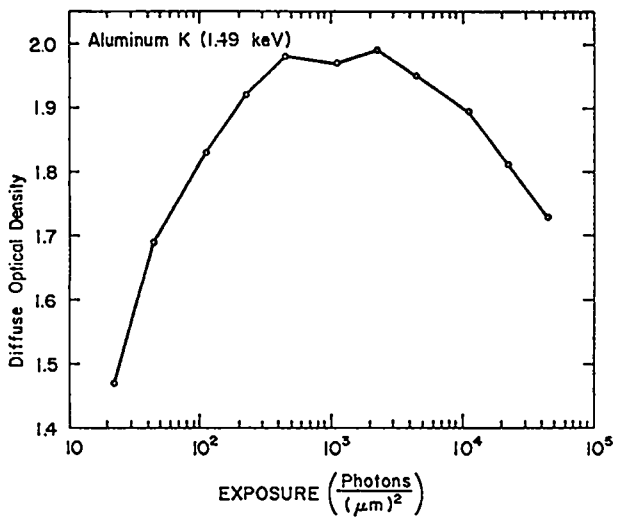

Fig. 97. Solarization of Kodak RAR 2490 film at 1.49 keV.

A second 2.5-Mbyte disk has been installed on the NOVA-840 computer, so that data-analysis programs and real-time programs may expand without competing for disk space. Disks are copied periodically to allow quick recovery from equipment failures.

Our studies indicated that the laser control computer is not cost-effective for the acquisition of data from target experiments. Because of the basic differences in the functions required for laser control and in those required for data acquisition and analysis, it is more efficient and less expensive to separate the functions physically. We have therefore specified a computer system that will handle data acquisition and analysis for all target experiments (one-beam, two-beam, eight-beam, and HEGLF). By combining all the functions in a single computer, substantial computing power can be directed toward a single experiment on a time-shared basis at a cost per laser system that is lower than the cost of increasing the capacity of each laser-control computer.

The design of this dedicated experiments and diagnostics computer data-acquisition system was completed, and bids for the computer have been received from several manufacturers. The new auto-

matic computer station will be installed in the building housing the glass-laser system, because the building is centrally located, is air conditioned, and has dust control appropriate for a computer system. The system will initially provide data-acquisition capabilities for the TBS and for the diagnostics development area. The system is designed to be easily expanded to provide additional data-acquisition and data-reduction capabilities. Provisions are included to allow data to be transferred to LASL's Central Computing Facility via nine-track tape for further processing. System usage standards are being developed. The CAMAC system has been adopted to standardize the interfacing of diagnostic instrumentation to the computer system.

ETCH-TRACK ION DIAGNOSTICS

We have initiated an investigation, under contract to Washington State University, into the use of ion-track diagnostics. This diagnostic method, which has been applied to such diverse problems as the search for quarks and archeological dating, could be useful in our studies of both nuclear reaction products (α,p) and plasma-produced fast ions. Our initial plasma experiments seek to measure the fast-ion spatial distribution (in a manner analogous to "fast"-electron measurements made earlier with photographic film). The Washington State group is using LASL accelerators to determine the characteristics of tracks produced in cellulose-nitrate films by ions of various charge, mass, and energy.

CALORIMETRY

Large quantities of our very successful, convenient, and small differential thermocouple calorimeters have been manufactured. They are being installed in the target chamber of the TBS for light-reflection and absorption measurements at many angles. With these small calorimeters (area of intercepted beam, 1 mm^2), we are able to measure angular distributions accurately without interfering with other diagnostic experiments. We have designed and built amplifiers, now available in quantity, which eliminate the need for costly and inefficient recording with strip charts. The calorimeter signals are entered directly into the NOVA computer during glass-laser experiments.

We are studying modern microcircuitry techniques as a means of assembling even more sensitive and versatile thermocouple and thermopile units. These devices, if successfully developed, should open a wide range of possibilities, such as accurate subkilovolt x-ray calorimetry.

TARGET ALIGNMENT SYSTEMS

Work is under way to improve the target-focusing and alignment of CO_2 laser beams with the use of a pyroelectric-vidicon system. The image of a 65-μm-diam glass microballoon attached to a thin plastic foil, illuminated with 10.6-μm light from a low-power cw CO_2 laser is shown in Fig. 98. After twentyfold magnification, the image was detected by a pyroelectric-vidicon tube and reproduced on a TV monitor.

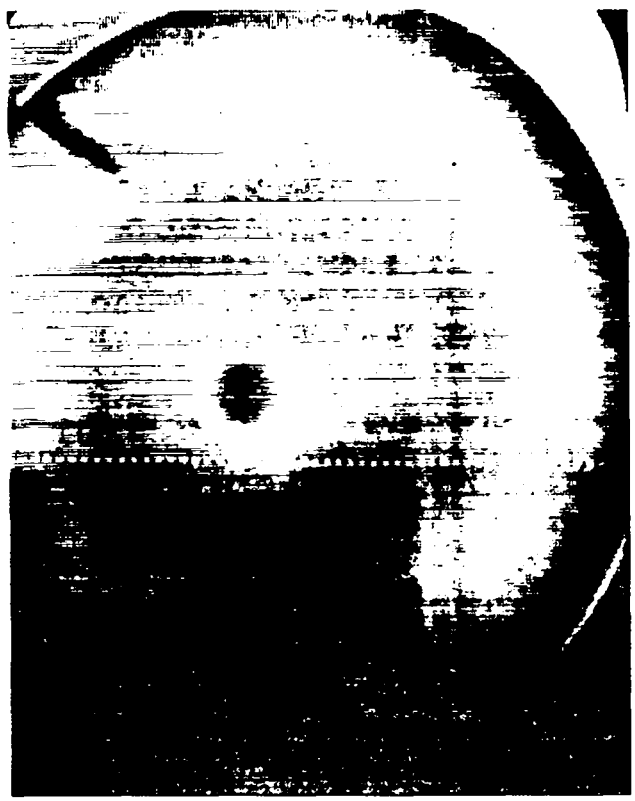

Fig. 98. Vidicon image of 65-μm-diam glass microballoon illuminated by 10.6-μm laser.

We have ordered a lens system specifically designed for use in a target chamber, which should give better resolution. Also, a new state-of-the-art vidicon and a camera with improved resolution and dynamic range will be received soon. This imaging system will allow us to align targets using the oscillator of the CO_2 laser system, and will increase both the shot rate and the alignment accuracy.

REFERENCES

1. P. Kirkpatrick and A. V. Baez, "Formation of Optical Images by X Rays," J. Opt. Soc. Am. 38, 766 (1948).

2. H. Wolter, "Verallgemeinerte Schwarzschildsche Spiegelsysteme Streifender Reflexion als Optiken für Röntgenstrahlen," Ann. Phys. 10, 94, 286 (1952).

3. F. D. Seward and T. M. Palmieri, "A Simple X-Ray Microscope for Photographing Laser Produced Plasmas," Rev. Sci. Instrum. 46, 204 (1975).

VI. APPLICATIONS OF LASER FUSION -- FEASIBILTY AND SYSTEMS STUDIES

Our feasibility and systems studies are being performed to analyze the technical feasibility and economic aspects of various commercial and military applications of laser fusion. The direct production of electricity in central-station power plants is of major concern. The general objectives of these studies are: the conceptualization and preliminary engineering assessment of laser-fusion reactors and generating stations; the development of parametric computer models of power-plant subsystems for economic and technology tradeoff and comparison studies; and the identification of problems requiring long-term development efforts. Applications of laser fusion in the production of fuel for fission reactors, the production of synthetic fuels such as hydrogen, and as a source of high-temperature process heat are also being investigated.

LASER-FUSION REACTOR AND ELECTRIC GENERATING STATION CONCEPTS

Introduction

Several laser-fusion reactor (LFR) concepts are being considered for possible use in central-station generating plants. The two concepts being evaluated at LASL, the wetted-wall and the magnetically protected design, have been described previously in detail.[1,2] The techniques used for the protection of cavity components in these two reactor concepts, and variations of these techniques, have also been adopted by other groups involved in the evaluation of LFRs (see, e.g., Ref. 3).

Wetted-Wall LFR Concept

An artist's rendition of the wetted-wall LFR concept is shown in Fig. 99. The spherical reaction chamber is surrounded by a blanket region consisting of liquid lithium and structural components. The cavity wall is formed by a porous refractory metal through which a coolant, lithium, flows to form a protective layer on the inside surface of the cavity. The protective layer of lithium absorbs the kinetic energy of the pellet debris and part of the x-ray energy resulting from fusion-pellet microexplosions. Part of the lithium layer is evaporated and ablated into the cavity and is subsequently exhausted through a supersonic nozzle at the bottom of the cavity into a condenser. The ablative layer is restored between pellet microexplosions by radial inflow of lithium from the blanket region.

The wetted-wall reactor concept has been investigated in considerable detail (see, e.g., Refs. 1, 4, 5); however, in these studies, the flow of liquid lithium on the inside of the spherical cavity was not modeled in sufficient detail with respect to the treatment of viscous drag and the effects of spherical geometry. We have therefore analyzed in greater detail the gravity flow of a thin

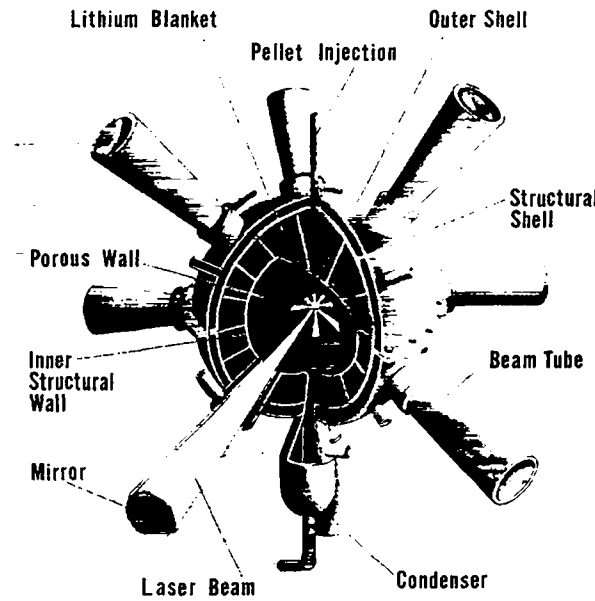

Fig. 99. Wetted-wall laser-fusion reactor concept.

film of liquid along the interior surface of a sphere, as discussed below.

Lithium Flow Model -- The physical problem is stated as follows. Liquid lithium is forced through the porous wall of a spherical reactor cavity at a rate m_s, collects into a layer of thickness δ on the inside of the sphere, flows downward along the wall (positive θ direction) due to the force of gravity, and drains through an opening at the bottom; this opening also serves as an exhaust port for evaporated lithium mixed with the remnants of the pellet microexplosion. We wish to determine the variations in tangential flow velocity, v, and in layer thickness with position on the sphere, θ.

We have previously analyzed the steady-state problem and the detailed methodology, as reported elsewhere.[6] The mass and momentum equations in a form suitable for numerical integration are

$$\frac{dz}{d\theta} = \frac{Rm}{\rho} - \delta \cos\theta \frac{v}{\sin\theta} \qquad (1)$$

and

$$\frac{dv}{d\theta} = g R \frac{\sin\theta}{v} - \frac{200R\mu}{\rho\delta^2} - \frac{Rm}{\rho\delta} , \qquad (2)$$

where
- $z = v\delta$
- R = radius of the sphere
- ρ = fluid density
- v = tangential velocity in the θ-direction
- g = acceleration of gravity
- δ = film thickness
- μ = fluid viscosity, and
- m = difference between mass supplied through the porous wall, $m_s(\theta)$, and that evaporated at the free surface, m_{ev}.

Here we assume turbulent flow with a laminar sublayer of thickness 0.1 δ in which the velocity distribution will be parabolic.

For the singular term of $v/\sin\theta$ at $\theta = 0$,

$$\lim_{\theta\to 0} \frac{v}{\sin\theta} = \frac{dv}{d\theta} , \qquad (3)$$

and Eqs. (1) and (2) become

$$\frac{dv}{d\theta} = \frac{R}{\rho\delta_o}\left\{-\left(\frac{m_o}{2} + \frac{100\mu}{\delta_o}\right) + \left[\left(\frac{m_o}{2} + \frac{100\mu}{\delta_o}\right)^2 + \frac{g\rho^2\delta_o^2}{R}\right]^{1/2}\right\} \qquad (4)$$

and

$$\frac{dZ}{d\theta} = \frac{Rm_o}{\rho} - \delta_o \frac{dv}{d\theta} , \qquad (5)$$

where the subscript zero denotes quantities evaluated at $\theta = 0$.

Results -- Solutions for two forms of the distribution function, $m_s(\theta)$, describing the lithium mass supplied through the porous wall were investigated:

- $m_s(\theta) = m_{os}$(const), $0 < \theta \le \theta_f \le \theta_m = 0$; $\theta_f < \theta \le \theta_m$, and
- $m_s(\theta)$ decreasing linearly from m_{os} at $\theta = 0$ to 0 at $\theta = \theta_f \le \theta_m$.

To facilitate comparison among different solutions, we determined m_{os} in each case so that the mass flow of lithium across the porous wall integrated over the sphere was 2000 g/s.

The quantity m_{ev} is determined by

$$m_{ev} = \frac{E_{ev} P_{rr}}{4 R^2 H} \ (g/cm^2 \cdot s) , \qquad (6)$$

where E_{ev} is the energy absorbed in the lithium layer per pellet microexplosion, P_{rr} is the microexplosion repetition rate, and H is the heat of vaporization.

Results have been calculated for the following set of parameters:

$R = 150$ cm
$H = 2.15 \times 10^3$ J/g
$E_{ev} = 22 \times 10^6$ J/microexplosion
$P_{rr} = 1$
$\mu = 4.5 \times 10^{-3}$ dyne·s/cm^2
$\rho = 0.50$ g/cm^3 .

$m_{ev} = 3.64 \times 10^{-3}$ g/cm^2·s

For $m_s(\theta)$ represented by a step function $m_s(\theta) = m_{os}$, $0 \le \theta \le \theta_f$; $m_s(\theta) = 0$, $\theta_f < \theta \le \theta_m$, we computed three cases corresponding to $\theta_f = \pi/2$, $3\pi/4$, and $15\pi/16$. The results denoted by Curves A-1, A-2, and A-3, respectively, are presented in Fig. 100. As expected, the lithium layer becomes thinner and more nearly uniform as the supply is spread over larger portions of the spherical surface. In all cases, the thicknesses build up rapidly near the bottom of the reactor cavity.

The results for cases in which $m_s(\theta)$ decreases linearly from a maximum m_{os} at $\theta = \theta_f$ are shown in Fig. 101 for $\theta_f = \pi/2$, $3\pi/4$, and $15\pi/16$, denoted, respectively, by Curves B-1, B-2, and B-3. Again the layer thickness decreases and becomes more nearly uniform as the mass supply is spread over a larger portion of the sphere.

The tangential lithium-flow velocities for step and linear mass-supply functions for Cases A-2 and B-2 are shown in Fig. 102. The values increase monotonically with θ and the magnitudes are moderate.

Other variations in the film-thickness function, $\delta(\theta)$, can be obtained by varying the mass-supply function $m_s(\theta)$. Solutions were obtained when the total mass supplied equaled that evaporated, i.e., at 1023 g/s, for the conditions listed at the beginning of this section. Thickness distributions $\delta(\theta)$ for uniform (A) and linearly decreasing (B) mass supplies spread over the top hemisphere are shown in Fig. 103. For uniform mass supply, the layer thickens by 25% toward the equator and then thins to its original value of 1 mm. For linearly decreasing mass supply, the thickness decreases monotonically but remains greater than 1 mm.

Self-Consistency and Stability -- The flow velocity through the porous wall is sufficiently low to resemble diffusion. The highest value of flow velocity through the porous wall in our computations is 0.08 cm/s, which is small compared to typical tangential velocities shown in Fig. 102. Using 15 cm/s as a representative maximum tangential velocity resulting from turbulent-flow calculations, the Reynolds number based on the film thickness is in the range 150 to 500. The Reynolds number resulting from laminar-flow calculations is up to ten times higher. Considering the disturbances to which the film flow will be subjected, the assumption of turbulence over most of the surface appears justified. Thus, the results are consistent with the hypotheses implicit in the formulation of the problem.

A complete transient stability analysis of the lithium film has not been performed; however, as a first step toward establishing stability, a sensitivity analysis has been done. We have shown that the lithium flow is stable at the origin against small perturbations in film thickness, in colatitude component of the lithium velocity, and in rate

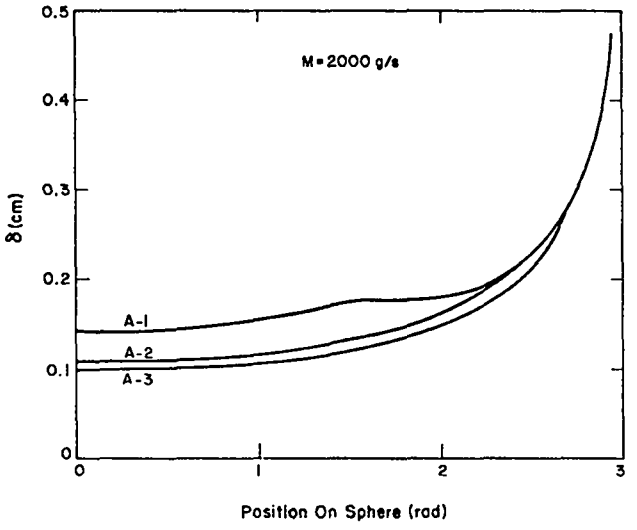

Fig. 100. Lithium layer thicknesses corresponding to different step functions.

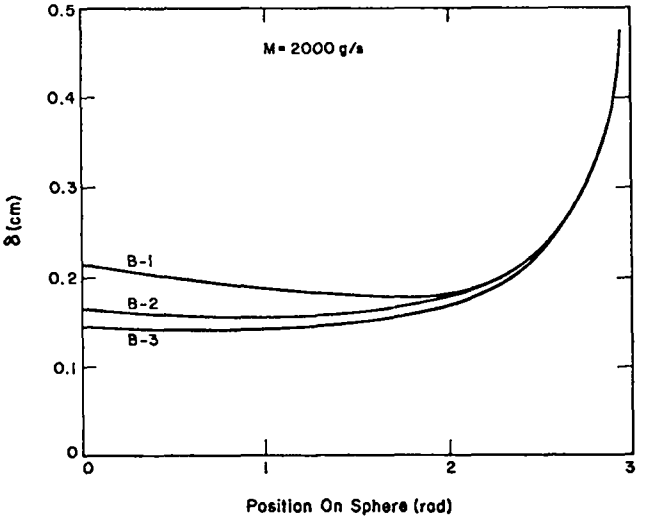

Fig. 101. Lithium layer thicknesses corresponding to different linear functions for lithium mass flow rate, $m_s(\theta)$.

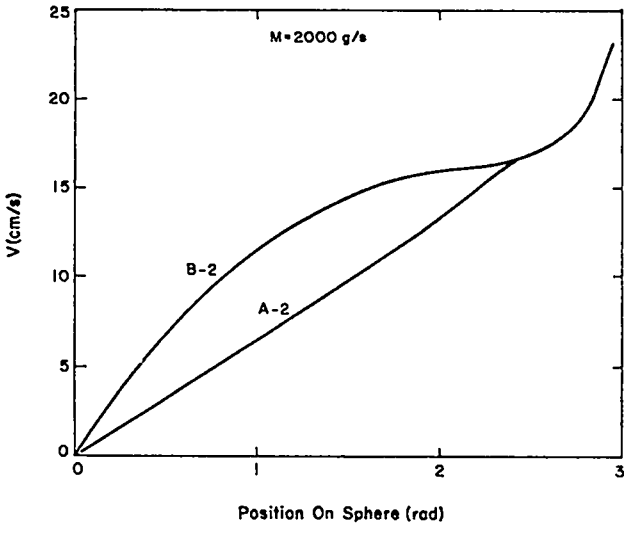

Fig.102. Lithium tangential flow velocity for step and linear mass flow-rate functions, $m_s(\theta)$.

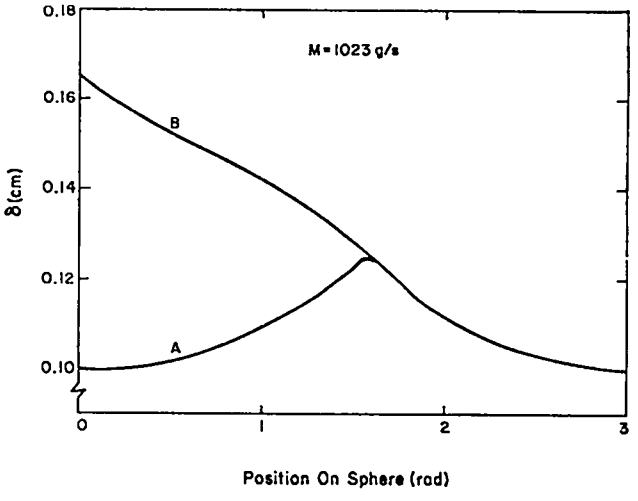

Fig.103. Lithium layer thickness for cases where mass supplied equals mass evaporated.

of mass supply of lithium through the porous wall.[7]

The calculated average flow velocities are ~10 cm/s leading to average residence times for lithium on the cavity wall of ~47 s. Thus, if a steady-state flow as determined by this investigation persisted, the same element of lithium would be subjected to numerous pellet microexplosions. The transient behavior and stability of the lithium film with mechanical and thermal loadings imposed by repeated pellet microexplosions remains to be determined.

Magnetically Protected LFR Concept

Introduction -- The use of magnetic fields to protect the walls of the reactor cavity from energy deposition and erosion by energetic charged particles is an attractive conceptual alternative to ablative cavity liners. The essential features of a magnetically protected reactor concept are shown schematically in Fig. 104. The central portion of the cavity is cylindrical, with an impressed steady-state magnetic field produced by a solenoid located outside, and concentric with a lithium blanket region. The ionized particles in the fusion-pellet debris are diverted by the magnetic field to energy-sink regions at the ends of the cylindrical cavity.

The Computer Program LIFE -- The computer program LIFE (Laser-Induced Fusion Explosion) for simulation of fusion-pellet microexplosions expanding in a magnetic field is one of the principal investigative tools for use in engineering feasibility studies of the magnetically protected LFR concept. This program was originally used in simplified form to investigate the feasibility of magnetically protecting cavity walls from the emissions of pure deuterium-tritium pellet microexplosions. It has recently been modified and expanded to:

- include the physics of plasma expansion and interaction with magnetic fields in the presence of many different charged particles;
- include boundary conditions on electrically conductive cavity component surfaces;
- include a solenoid model of arbitrary design outside the blanket region; and
- transfer information about particle-surface interactions to magnetic tape so that sputtering and temperature fluctuations can be calculated directly without manual data processing.

The program is being used routinely to determine the distributions and angles at which the products of fusion-pellet microexplosions impinge

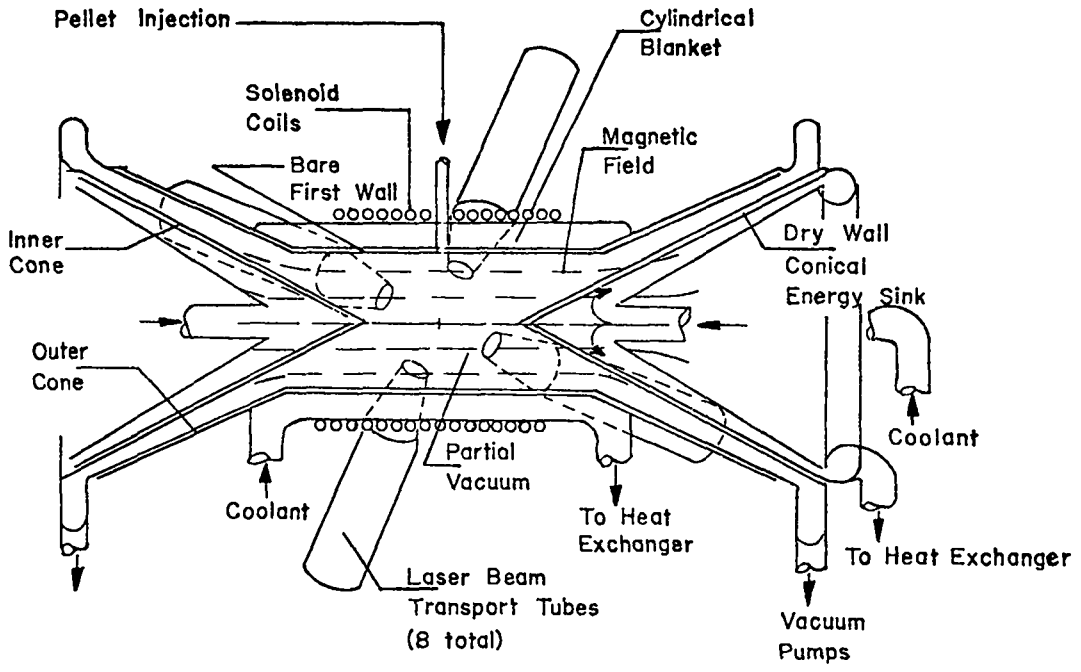

Fig.104. Laser-fusion reactor concept with magnetically protected cavity wall.

on cavity surfaces with different magnetic-field configurations.

Sputtering Erosion of Cavity Component Surfaces -- The principal criterion for optimizing the LFR designs for commercial applications is to minimize power-production costs. For magnetically protected LFRs a cost tradeoff will be performed between the amortization of original capital investment and the cost of component replacement due to damage from pellet microexplosion emissions. One of the damage mechanisms that must be evaluated to permit the prediction of component replacement schedules is sputtering erosion of cavity-component surfaces.

We have completed a survey of experimental data on sputtering of solid materials by energetic ions. From this data survey and from theoretical analyses of sputtering we can predict the dependence of sputtering yields on ion energy and angle of incidence by using derived analytic expressions that possess sufficient accuracy and flexibility for general use. A computer program has been written for use in conjunction with the LIFE code to determine erosion rates of cavity-component surfaces.

Sputtering yields are evaluated in terms of sputtering coefficients, S, which are numerically equal to the number of surface (or subsurface) atoms that escape from a target per incident ion. Sputtering coefficients depend, in general, on mass, charge, energy, and angle of incidence of the impinging ions and on target material, surface finish, crystal structure, and temperature.

The effects of target surface temperature and roughness on sputtering coefficients have not been investigated systematically. Data on temperature dependence appear inconclusive and limited primarily to observations of target temperatures during the investigation of other effects. The effects of surface deviations from a plane have not been closely scrutinized either.

Because sufficient experimental data are lacking and because the current theory is inadequate, we have assumed that the sputtering coefficient, S, is independent of target temperature, surface finish, and crystal structure. Refinements to the model can easily be added as more data become available. We have postulated that S, for a given ion incident on a given material, will be the product of two factors, one describing its dependence

on ion energy and the other on the angle of incidence;

$$S(E,\theta) = S_1(E)S_2(\theta) \ , \qquad (7)$$

where E denotes ion energy and θ the angle of incidence measured from the surface normal.

The dependence of sputtering on ion energy is by far the most extensively studied aspect of sputtering phenomena. The data have been recently summarized and reviewed.[8-10] From these investigations, we have determined the following dependence of S on ion energy:

$$S_1 = 0 \ , \quad \varepsilon < 1 \qquad (8)$$

$$S_1 = \frac{S_o(\ell n\ \varepsilon)^{1+c/\varepsilon}}{\varepsilon^{1+b/\varepsilon}} \ , \quad \varepsilon \geq 1 \ , \qquad (9)$$

where $\varepsilon = E/E_o$; E_o is a threshold energy below which no sputtering occurs; and S_o, b, and c are positive constants to be determined from empirical data. For cases in which the data are inadequate to determine the empirical constants accurately, theoretical considerations are used to supplement the experimental information.

The effect that the angle of incidence, θ, has on the sputtering coefficient, S_2, has been studied by many investigators (see, e.g., Refs. 9, 10). We have determined that the function that best represents the observed and derived properties is given by

$$S_2 = \left[e^{gx^2}(1 - x^2)\right]^h \ , \qquad (10)$$

where $x = 2\theta/\pi$ and the parameters g and h specify the location x_m and the magnitude S_{2m} of the maximum value of $S_2(\theta)$. In terms of these quantities, g and h are given by

$$g = \frac{1}{1 - x_m^2} \qquad (11)$$

$$h = \frac{\ell n\ S_{2m}}{g\ x_m^2 + \ell n(1 - x_m^2)} \ . \qquad (12)$$

For practical purposes, one has to calculate the erosion rate, E_{rr}, given by

$$E_{rr} = \frac{a}{A\rho} \iint S(E,\theta)n(E,\theta)\ dE d\theta \ , \qquad (13)$$

where a is the atomic weight of the target material, A is Avogadro's number, ρ is the target-material density, and n is the flux of ions per unit area of energy E and angle of incidence θ.

Examples of least-squares fits of Eqs. (9) and (10) to empirical data are shown in Figs. 105 and 106, respectively.

We have calculated the erosion rates of the energy sinks in the magnetically protected LFR due to deuterium ions, tritium ions, and alpha particles emanating from a 100-MJ pure (D+T) fusion-pellet microexplosion. Niobium, carbon, and iron energy-sink surfaces were investigated. Typical total erosion rates are $\sim 10^{-9}$ cm per pellet microexplosion for the current design.

Surface Evaporation of Cavity Components -- A second erosive mechanism attacking component surfaces of magnetically protected LFRs, which must be carefully evaluated and controlled, is energy deposition, with possible subsequent evaporation, of reflected laser light; of x rays from laser-generated plasmas and fusion microexplosions; and of energetic particles in the fusion-pellet debris. The energy from all these sources is deposited within a few microns of the surface of incidence in structural materials.

The surface-temperature increase in cavity walls and energy sinks can be modeled mathematically in at least two ways. A surface flux model is described by

$$\frac{\partial T}{\partial t} = \alpha \frac{\partial^2 T}{\partial x^2} \qquad (14)$$

and the boundary conditions by

$$-\alpha\rho c \frac{\partial T}{\partial x} = Q \text{ at } x = 0 \ , \qquad (15)$$

where T is temperature, t is time, x is the space coordinate perpendicular to the surface, α is thermal diffusivity, ρ is density, c is specific heat, and Q is the flux of energy per unit surface area per unit time. The surface-temperature increase at the end of a uniform pulse of duration τ and total

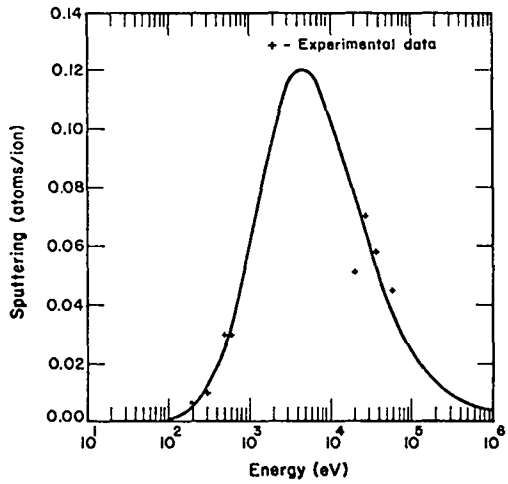

Fig.105. Sputtering of niobium by alpha particles normal to the surface as a function of alpha-particle energy.

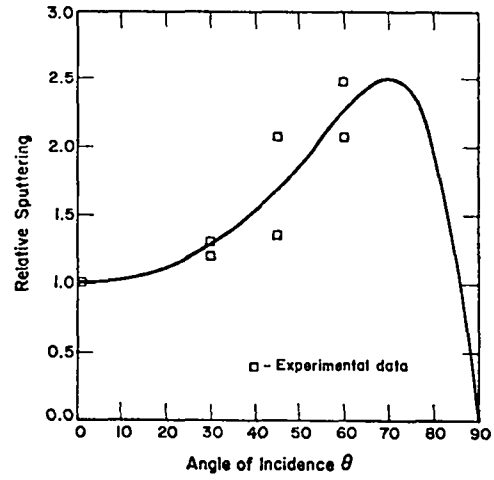

Fig.106. Dependence of sputtering coefficient on angle of incidence of impinging ions.

energy per unit area E, predicted by this model, is given by

$$T(0,\tau) = \frac{2E}{\rho c\sqrt{\pi\alpha\tau}} . \qquad (16)$$

This equation has been used frequently to calculate cavity-wall evaporation rates in fusion reactors (see, e.g., Ref. 10).

We have developed an alternative model that has considerably wider applicability than the surface-flux model. For this model, a volume source of heat energy is specified, the thickness of the wall is explicitly included, and multiple sources of deposited energy with arbitrary time dependence can be specified. The model is described in one dimension by the equation

$$\frac{\partial T(x,t)}{\partial t} = \alpha \frac{\partial^2 T(x,t)}{\partial x^2} + \frac{q(x,t)}{\rho c} \qquad (17)$$

and the conditions

$$T(x,t) = T(x), \; t = 0, \; 0 \le x \le \Delta \qquad (18)$$

$$-\alpha\rho c \frac{\partial T(x,t)}{\partial x} = Q(t), \; x = 0, \; t > 0 \qquad (19)$$

$$T(x,t) = T^*(t), \; x = \Delta \qquad (20)$$

where q is the rate of energy deposition per unit volume at position x, Q is the surface-energy deposition rate, Δ is the wall thickness, and T* is the temperature of the wall surface opposite the source (which is presumably cooled by a flowing fluid).

The problem posed by the volume source model has been solved analytically by Laplace transform techniques. The volume source and the surface flux are approximated by multiple square pulses in space and time, respectively. To obtain an analytic solution, the thermophysical properties must be restricted to constant values. This analytic solution is economical for scoping studies; however, for more accurate results, we have written a computer program to obtain numerical solutions that retain the temperature dependence of thermophysical properties. Surface evaporation is also calculated by the computer program using Langmuir theory,[10] from which the thickness of material evaporated is given by

$$d = \frac{1}{(2\pi R)^{1/2}} \frac{m^{1/2} P_s p_o}{\rho} \int_0^t \frac{\exp[-H/RT(0,t)]}{[T(0,t)]^{1/2}} dt , \qquad (21)$$

where d is the thickness evaporated, R is the ideal gas constant, m is molecular weight, P_s is the sticking coefficient, p_o is the preexponential factor in the Arrhenius expression for vapor pressure, and H is the heat of vaporization.

We have calculated the evaporation rates due to x-ray energy deposition in various materials

that may be used for cavity-wall and energy-sink surfaces in magnetically protected LFRs. The theoretical x-ray spectrum from pure (D+T) fusion-pellet microexplosions consists of relatively energetic photons that are sufficiently penetrating so that they do not seriously heat the surfaces of metal components. However, microexplosions of structured pellets are expected to emit x rays with spectra of lower energy that will be absorbed much closer to the structural surfaces and induce very high surface temperatures.

Examples of calculated evaporation rates of various materials due to energy deposition by x rays with a 600-eV blackbody-equivalent temperature are shown in Fig. 107. For materials with good thermal conductivity, the amount of surface material evaporated by a given amount of x-ray energy depends strongly on pulse width. An example of this dependence is shown in Fig. 108 for a 600-eV blackbody-equivalent x-ray spectrum incident on molybdenum. For pulse widths exceeding 100 ps, the amount of material evaporated per pulse decreases rapidly with increasing pulse width.

Electric Generating Station Concepts

We have recently completed the specification of components and the layout of an electric generating station based on the magnetically protected LFR and CO_2 laser technology. The results of parametric studies leading to the selection of the number of reactor cavities, laser and optical system arrangements, and other plant components were presented previously.[11] An artist's rendition of the generating station is shown in Fig. 109. Four magnetically protected LFRs and a centralized laser system with 100% redundancy of laser-power amplifiers are included in the station.

We have reevaluated the operating characteristics and performance of this generating plant. Significant changes in performance were indicated in a recalculation of the blanket energy-multiplication factor due to exoergic nuclear reactions with lithium and structural materials. The revised value of the factor is 1.08 compared to the previous estimate of 1.25. Also of significance is an updated model of a potassium topping cycle, which better represents the performance and capital costs of current designs. A literature survey of neutron damage to structural materials was conducted in an attempt to more realistically estimate LFR cavity-component lifetimes. We found that the data are insufficient for any judgements of structural materials except, possibly, stainless steel. Based on available information, the life-limiting neutron-

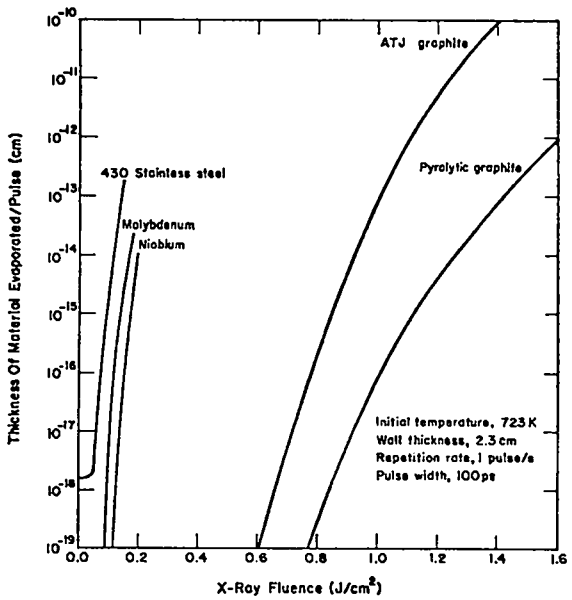

Fig. 107. Evaporation rate of potential cavity-component surface materials due to 600-eV blackbody-equivalent-temperature x-ray spectrum as a function of x-ray fluence.

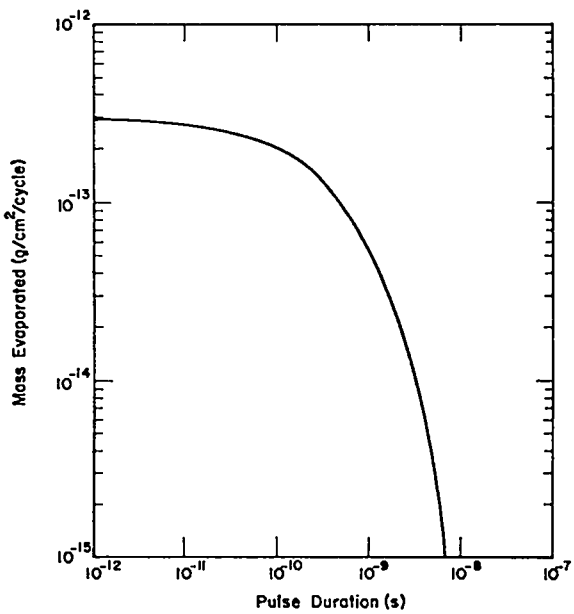

Fig. 108. Dependence of evaporation of molybdenum on x-ray pulse width.

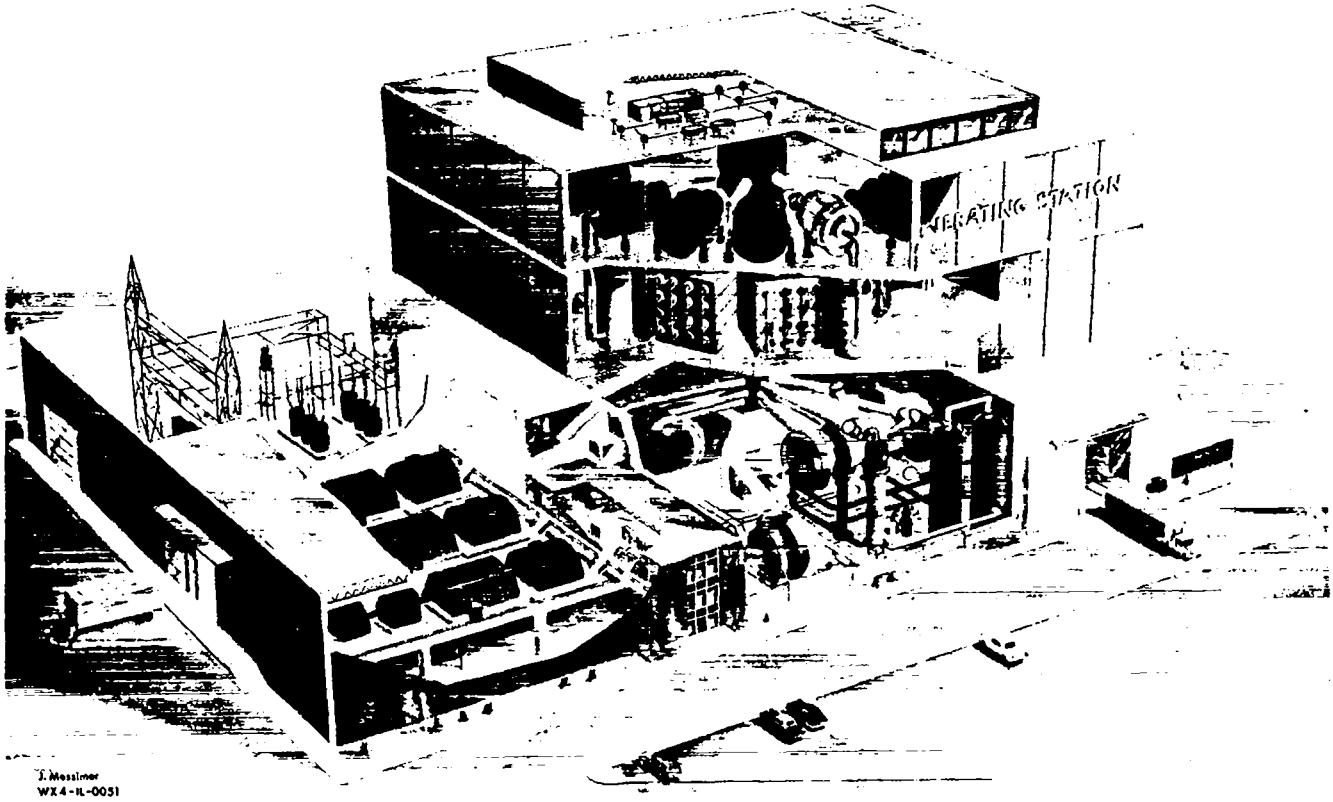

Fig.109. Laser-fusion electric generating station based on the magnetically protected laser-fusion reactor.

damage mechanism for stainless steel apparently is the loss of ductility. We found no reason to change our previous estimate of maximum permissible total neutron fluence of 5 x 10^{22} neutrons/cm^2 for use in determining LFR cavity component lifetimes.

Some generating-station operating characteristics are given in Table XII. Three types of energy conversion systems were evaluated: (1) a low-temperature steam cycle (turbine inlet temperature, 823 K), (2) a high-temperature steam cycle (turbine inlet temperature, 839 K), and (3) a high-temperature steam cycle with a potassium-vapor topping cycle (potassium vapor temperature, 1100 K).

HYBRID REACTOR CONCEPTS

Our evaluation of the ^{239}Pu burner-^{233}U breeder hybrid concept is continuing. Reactor blanket designs investigated in recent studies are spherical shells based on the wetted-wall LFR concept. These designs include a lithium-cooled driver region of stainless-steel-clad rods of $^{238}UO_2$ with the equilibrium concentration of $^{239}PuO_2$ adjacent to the reactor cavity, followed by a region of either ^{232}ThC or $^{232}ThO_2$ rods, also clad in stainless steel and cooled by lithium.

The plutonium in the driver region is continuously recycled in the fuel fabrication and processing cycles and serves only to amplify the neutron population and to produce thermal power. Leakage neutrons from the oxide region are captured in the thorium region and cause the breeding of ^{233}U. Tritium for the fusion fuel cycle is produced by neutron capture in the lithium coolant.

The reactor cavity for these studies has an outside radius of 2 m. We found that the driver region must be at least 20 cm thick for the tritium breeding ratio to exceed unity. Driver regions 30 cm thick were evaluated in this study. The ^{233}U production, in terms of ^{233}U atoms produced per fusion neutron, is shown in Fig. 110 as a function of ThO_2 breeding-region thickness. From these results, a thorium breeding-region thickness of 40 cm was adopted for additional analysis.

We compared thorium breeding regions containing ThO_2 and ThC with a design having a 4-cm-thick beryllium region between the driver region and a ThC breeding region. Some results of this comparison are given in Table XIII. Reactor performance for each of these options is essentially the same. The beryllium region does not appear to enhance performance enough to warrant its inclusion.

TABLE XII

OPERATING CHARACTERISTICS AND COST SUMMARY OF LASER-FUSION GENERATING STATION BASED ON MAGNETICALLY PROTECTED REACTORS

Reactor Cavities	
Fusion pellet yield, MJ	100
Microexplosion repetition rate per cavity, s^{-1}	10
Thermal power per cavity, MW	1077
Number of reactor cavities	4
Reactor dimensions, m	
Cavity radius	2.51
Blanket thickness	0.90
Tritium breeding ratio	1.31
Laser beams per cavity	8
Laser and Beam Transport	
Number of laser power amplifiers	8 (with 100% redundancy)
Beam energy per laser power amplifier, MJ	0.135
Laser efficiency, %	6.3
Pulse rate, Hz	40
Number of mirrors per beam	9
Beam transport efficiency, %	92.7

Overall Plant

	Low-temp Steam Turbines	High-temp Steam Turbines	High-temp Steam Turbines with Potassium Topping Cycle
Net electrical power, MW	903	1194	1423
Generating plant efficiency, %	38.2	45.2	50.8
Net plant efficiency, %	21.0	27.7	33.0
Relative production cost	1.00	0.91	0.82

We conclude from these results that the ^{239}Pu burner-^{233}U breeder concept, producing large amounts of thermal power and fuel for thermal fission reactors, may be attractive as a direct substitute for the liquid-metal fast breeder reactor. The concept could also be adapted to the production of ^{239}Pu from ^{238}U. It does, however, have essentially all the disadvantages of the breeder reactor, except that it does not operate as a critical system. Such reactors would be economically competitive with fission reactors, even with fusion pellets of relatively poor performance, and may provide a useful intermediate phase in the development of fusion power.

SYNTHETIC FUEL PRODUCTION FROM LASER FUSION

We have continued to investigate the possibility of producing synthetic fuel by using the radiation from fusion-pellet microexplosions to decompose H_2O or CO_2 radiolytically into H_2 or CO, and have updated our estimates of product costs from such processes.

The radiolysis of H_2O or CO_2 to produce H_2 or CO commercially in LFRs would undoubtedly be based primarily on the utilization of high-energy neutrons released by thermonuclear reactions. Gamma rays produced during neutron capture in pellet and structural materials may also contribute to the

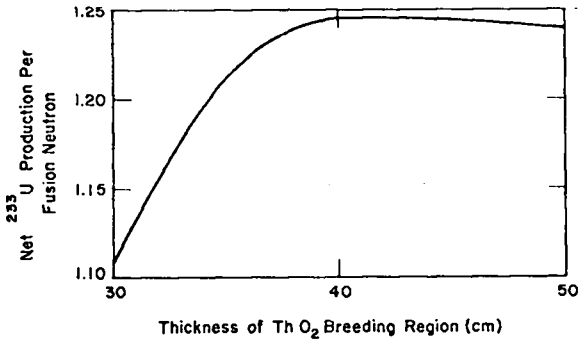

Fig. 110. Net ^{233}U production per fusion neutron as a function of ThO_2 breeder-region thickness. Thorium contains 4 at.% ^{233}U.

process, but the mean free paths for gamma-ray transport in such reactants are too long for any appreciable deposition of gamma-ray energy.

Such a radiolytic system would require the recirculation of a significant amount of electric power, which could be satisfied, in part, by conversion of the plasma and x-ray energies trapped in the reactor cavity, with the remainder provided either by siphoning off part of the neutron energy for conversion or purchase of electric power from another source.

Because the reactor blankets in systems dedicated to synthetic-fuel production would be designed to contain both chemical reactants and the products of radiolysis, lithium for the breeding of tritium would have to be excluded and tritium for the fuel cycle would have to be purchased from an outside source.

A somewhat simplistic model of a production plant has been analyzed to provide estimates of the costs of producing neutrons for radiolytic applications. The plant includes four laser-fusion reactors with magnetically protected cavity components, a common CO_2 laser system with sequential switching of laser beams to successive reactors, and adequate heat-exchanger and power-conversion capacity to generate the electrical recirculating power needed to operate the plant. The reactor blankets consist simply of the structures normally required to contain circulating liquid lithium in power-producing reactors. Except for the wall surrounding the reactor cavity, which consists of niobium, all structures are made of stainless steel. No special apparatus was included for handling chemical reactants or for separation of the products of radiolysis, and estimates of neutron-production costs are therefore conservatively low.

The thermonuclear energy release per fusion pellet was assumed to be 100 MJ, at a pulse repetition rate of 10 per second per reactor. Thus, the total thermonuclear power level is 4000 MW. We assumed that tritium would be purchased from laser-fusion electric generating stations with excess tritium production; costs were determined from the additional costs incurred by the generating station in producing such excess tritium.

Neutron production cost in 1973 dollars is given in Fig. 111 as a function of the cost of supplementary electric power purchased to make up de-

TABLE XIII

PERFORMANCE FOR VARIOUS THORIUM BREEDING REGION OPTIONS

Fuel Form in Breeding Region	*ThO_2*	*ThC*	*ThC-Be*
Equilibrium PuO_2 concentration in driver region, %	*9.62*	*9.50*	*9.80*
^{233}U production per fusion neutron	*1.28*	*1.27*	*1.34*
^{233}U production per year, kg (85% duty cycle)	*451*	*448*	*473*
Thermal power output, MW	*3586*	*3366*	*4095*
Neutron multiplication factor without coolant	*0.92*	*0.90*	*0.94*
Tritium breeding ratio	*1.48*	*1.38*	*1.79*
Thermonuclear power, MW	*95*	*95*	*95*

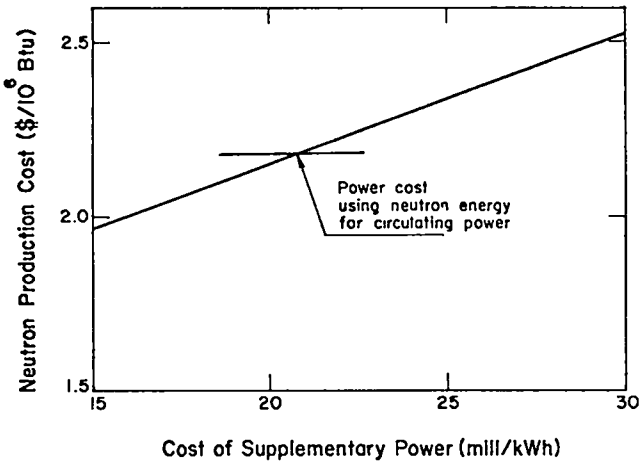

Fig.III. Neutron production cost (1973 dollars) as a function of the cost of supplementary electrical power purchased.

ficiencies in recirculating-power requirements. The cost of neutron production, if neutron energy is converted to electricity in the amount necessary to provide the required recirculating power, is indicated. For the range of electric-power costs considered, neutron-production costs are between 2 and 2.5 dollars per million Btu of neutron energy.

Current estimates of production costs of synthetic fuel from coal (which may be either H_2 or methane) by standard processes range from 1.0 to 1.5 dollars per million Btu (1973 dollars)[12] for commercial operation in the 1980's. Thus, even if the neutron energy is utilized at 100% efficiency for decomposition of H_2O or CO_2, no back-reactions occur, and the H_2 or CO is recovered at 100% efficiency, this form of synthetic-fuel production with laser-fusion reactors would not be competitive within the context of this price structure. In fact, the efficiency of utilization of neutron energy for H_2O or CO_2 radiolysis is not likely to exceed 20 or 30% under most favorable conditions.

These results indicate that synthetic-fuel production from laser-fusion reactors dedicated to this process would not be competitive with standard coal-gasification processes within 1973 market values. Because the overall efficiency of standard coal-gasification (thermochemical) processes ranges from 55 to 70% and demonstrated radiolytic conversion efficiencies are less than 30%, it would appear more reasonable to convert neutron energy to thermal energy for thermochemical cycles than to use it in radiolytic processes.

Radiolysis has been suggested as an attractive method to produce H_2 as a topping cycle in LFRs where the main purpose is the production of steam for process heat or for electrical conversion. A preliminary economic analysis of a system that produces both H_2 and electricity revealed that such a system, although economically more attractive than H_2 production from dedicated plants, offers no incentive per se for this mode of operation. Unless an abnormal price structure (in terms of current relative values) should develop, H_2 production costs are determined by the basic cost of producing neutron energy. There seems to be no reason to seriously consider H_2 production from topping cycles, unless H_2 is produced in copious quantities as an unavoidable byproduct in a system optimized from other considerations.

These conclusions could be reversed by dramatic changes in relative market values, or by scarcities of feed materials such as coal or methane. Note that present-day (1976) coal costs are approaching 1 dollar per million Btu and imported oil is in the 2-dollar per million Btu range.[13] If, because of such developments, new sources of hydrogen are required, the radiolytic decomposition of H_2O in laser-fusion systems would probably be more economical than electrolysis because the inefficiencies associated with conversion to electricity from a primary energy source are avoided. In this case, topping cycles for LFR steam generators offer the best promise for economic systems. Serious consideration of radiolysis for the commercial production of synthetic fuels would have to be supported by an experimental and theoretical program to investigate the effects of radiolytic yields, of the use of scavengers, of increases in temperature and pressure, of two-phase systems, and of the use of additives resulting in combined radiolytic-thermochemical cycles. If fusion sources are to be utilized, these investigations should be done with high-energy neutron and combined neutron and gamma-ray sources.

EXPERIMENTAL INVESTIGATION OF IMPLODING SHELL STABILITY

The stability of imploding shells is an important aspect of fusion-pellet research, but experimental techniques for investigations on the required scale do not exist. We have performed some theoretical calculations to investigate the possibilities of imploding cylindrical shells with high-power lasers. Cylindrical geometry was chosen to allow the viewing of geometrical convergence effects along the inside surface of the shell.

The criteria for an interesting experiment are (1) a driving pressure of 10 to 100 Mbar and (2) a shell that is large enough to permit viewing of the inner surface. A preliminary study indicates that with a 100-kJ, 1-ns laser pulse at 10 μm, it may be possible to obtain a driving pressure of 30 to 40 Mbar for 1 ns in a gold cylinder with a diameter of 0.39 cm and a length of 0.78 cm. Energy intensities would be $\sim 10^{14}$ W/cm^2. At such intensities, some generated impulse is probably lost because of the production of high-energy ions. Impulse measurements at this level of energy and intensity have not been made and would be needed to verify the feasibility of such experiments.

EXPERIMENTAL DETERMINATION OF MATERIALS PROPERTY DATA

We have completed preliminary target designs for opacity and equation-of-state measurements that might be performed with CO_2 lasers at power levels of 10^{12} to 3×10^{14} W. The power level and energy of a 1-kJ laser with a 0.4-ns pulse width are too low for opacity experiments, but marginal equation-of-state measurements could be made and the proof of principle could be established. Experiments with more powerful lasers, i.e., 10 to 100 kJ with 0.3- to 1.0-ns pulse widths, are much more promising. It appears that some opacity measurements would be possible with such lasers, and equation-of-state measurements could be made at pressures up to 100 Mbar.

REFERENCES

1. L. A. Booth, compiler, "Central Station Power Generation by Laser-Driven Fusion," Los Alamos Scientific Laboratory report LA-4858-MS, Vol. 1 (February 1972).
2. T. G. Frank, D. A. Freiwald, T. Merson, and J. J. Devaney, "A Laser Fusion Concept Utilizing Magnetic Fields for Cavity Wall Protection," Proc. 1st Topical Meeting on Technology of Controlled Nuclear Fusion, Am. Nuc. Soc., San Diego, CA (April 1974).
3. J. Hovingh, J. Maniscalco, M. Peterson, and R. W. Werner, "The Preliminary Design of a Suppressed Ablation Laser-Induced Fusion Reactor," Proc. 1st Topical Meeting on Technology of Controlled Nuclear Fusion, Am. Nuc. Soc., San Diego, CA (April 1974).
4. L. A. Booth and T. G. Frank, "Engineering Aspects of Laser Fusion," Proc. Joint ASME/ANS Int'l. Conf. on Advanced Nuclear Energy Systems, Pittsburgh, PA (March 1976).
5. T. G. Frank and L. A. Booth, "Laser-Fusion Reactor Materials Problems Resulting from Fusion Microexplosion Emissions," Proc. Int'l. Conf. on Surface Effects in Controlled Fusion Devices, San Francisco, CA (February 1976).
6. I. O. Bohachevsky, L. A. Booth, and J. F. Hafer, "Lithium Flow on the Inside of a Spherical Fusion-Reactor Cavity," Los Alamos Scientific Laboratory report LA-6362-MS (June 1976).
7. R. A. Axford, "Hydrodynamic Stability of Lithium Flows on Porous Spherical Surface," Los Alamos Scientific Laboratory report, to be published.
8. D. Rosenberg and G. K. Wehmer, "Sputtering Yields for Low Energy He^+, Kr^+ and Xe^+ Ion Bombardment," J. Appl. Phys. 33, 1842 (May 1962).
9. G. Carter and J. S. Colligan, "Ion Bombardment of Solids," Sputtering, Chap. 7, pp. 310-353, Elsevier, New York, NY (1968).
10. R. Behrisch, "First Wall Erosion in Fusion Reactors," Nuclear Fusion 12, 695 (1972).
11. F. Skoberne, "Laser-Fusion Program at LASL, July 1 through December 31, 1975," Los Alamos Scientific Laboratory report LA-6245-PR, (July 1976).
12. H. M. Siegel and T. Kaline, "Technology and Cost of Coal Gasification," ASME 93rd Winter Annual Meeting, Paper No. 72-WA/Fu-2, New York, NY (November 1972).
13. Bertram Wolf, "Some Thoughts on New Energy Sources," Nuclear News 19, 7, 49 (May 1976).

VII. RESOURCES, FACILITIES, AND OPERATIONAL SAFETY

Construction of new laser laboratories was completed. Safety policies and procedures continued to be applied successfully. Additional biological threshold-damage studies are under way to provide the necessary data for regulations being considered for laser users.

MANPOWER DISTRIBUTION

The distribution of employees assigned to the various categories of the ERDA-supported laser-induced fusion research program is shown in Table XIV.

FACILITIES

Laser-Fusion Facility

The Laboratory-Office Building was occupied in April 1976. Occupancy of the Advanced Laser Laboratory was completed in early 1976.

High-Energy Gas Laser Facility (HEGLF)

Norman Engineering Co., of Los Angeles, began Title-I work for the HEGLF in April 1976, with completion expected at the end of August. Work by the Architect-Engineer and LASL has resulted in a more complete definition of the facility and supporting services. Studies by an independent firm, Mechanics Research, Inc. (MRI), also of Los Angeles, provided additional insight into the problems of vibration introduced by background and cultural seismic noise, as well as vibrations initiated by mechanical equipment located within the building.

In the interest of continuity, details of the progress in HEGLF building design and construction are given in Sec. I.

TABLE XIV

APPROXIMATE STAFFING LEVEL OF LASER PROGRAM

June 30, 1976

Program	*Direct Employees*
Glass Laser Systems Development	*4*
CO_2 Laser System Development	*91*
New Laser Systems R & D	*18*
Pellet Design & Fabrication	*41*
Laser-Target Experiments	*44*
Diagnostics Development	*22*
Systems Studies & Applications	*5*
Electron-Beam Target Design & Fabrication	*2*
TOTAL	*227*

OPERATIONAL SAFETY

General

No lost-time accidents have been reported (for 20 months continuous) and there was no incident involving biological damage from laser light.

Corrective lenses of Schott Optical Co. filter glass were developed to cover the uv and visible regions, which will provide laser protective eyewear for specific wavelengths.

Biological Damage-Threshold Studies

Experimental evidence from several investigators has indicated that wavelengths in the near-uv, 400 m, are more injurious to lenticular components of the ocular system than early data indicated. Preliminary discussions have begun with a specialist at the Medical College of Virginia, Virginia Commonwealth University, Richmond, VA, to determine applicability of our experimental uv lasers to a cooperative program of biological damage.

VIII. PATENTS, PRESENTATIONS, AND PUBLICATIONS

PATENTS ISSUED

U.S. Patent 3,935,545, issued January 27, 1976. "Method and Apparatus for Reducing Diffraction-Induced Damage in High Power Laser Amplifier Systems," inventors, Anthony J. Campillo, Brian E. Newnam, Stanley L. Shapiro, and N. James Terrell, Jr.

U.S. Patent 3,940,617, issued February 24, 1976. "Method for Nondestructive Fuel Assay of Laser Fusion Targets," inventors, Eugene H. Farnum and R. Jay Fries.

PRESENTATIONS

The following presentations were made at the 1976 IEEE Conference on Plasma Science, Austin, Texas, May 24-26, 1976:

J. T. Ganley, W. T. Leland, B. F. Bentley, and A. J. Thomas, "Measurement of Potential Distribution and Cathode Fall in Electron-Beam-Sustained Discharges."

D. V. Giovanielli, J. F. Kephart, and G. H. McCall, "Wavelength Scaling Experiments Using CO_2 and Glass Laser-Produced Plasmas."

S. J. Gitomer and J. L. Shohet, "Computer Simulation of Radio Frequency Confinement of a Plasma Near Critical Density."

B. B. Godfrey, W. R. Shanahan, and L. E. Thode, "Computer Simulation of the Auto-Resonant."

A. J. Lieber, H. Dean Sutphin, C. B. Webb, and A. H. Williams, "Time Resolved X-Ray Measurements of Laser-Produced Plasmas."

E. L. Lindman, "Boundary Conditions for Plasma-Wave Interactions."

W. R. Shanahan and B. B. Godfrey, "Stability of a Nonneutral Electron Propagating in an Inhomogeneous Magnetic Field."

S. Singer, J. V. Parker, M. J. Nutter, J. J. Hayden, J. P. Carpenter, and I. Liberman (Westinghouse), "Gain Suppression in High-Gain CO_2 Laser Amplifiers."

Tai Ho Tan, D. V. Giovanielli, G. H. McCall, and A. H. Williams, "Measurement of High Energy Charged Particles from Laser-Produced Plasmas."

The following presentations were made at the Conference on Laser and Electro-Optical Systems, San Diego, California, May 25-27, 1976:

D. H. Gill and B. E. Newnam, "Damage Resistance of Holographic and Ruled Gratings Used as Laser Wavelength Tuning Elements."

I. Liberman (Westinghouse), J. J. Hayden, and S. Singer, "Prepulse Elimination in High Power CO_2 Lasers."

A. J. Lieber, H. Dean Sutphin, C. B. Webb, and A. H. Williams, "Development of Sub-Picosecond X-Ray and Visible Streak Camera."

E. McLellan and J. Figueira, "Generation of Subnanosecond CO_2 Laser Pulses by Electro-Optical Modulation."

B. E. Newnam and D. H. Gill, "Damage Resistance of Antireflection Coatings for Picosecond Pulses."

J. V. Parker, M. J. Nutter, J. J. Hayden, S. Singer, and I. Liberman (Westinghouse), "A Two Beam CO_2 Laser System for Laser Induced Fusion Experiments."

C. Phipps, "A Broadband, Passive Isolator for High Power 10 μm Wavelength Laser Systems."

W. H. Reichelt, "CO_2 Laser Systems for Fusion Studies."

The following presentations were made at the IXth International Quantum Electronics Conference, Amsterdam, The Netherlands, June 14-18, 1976:

I. J. Bigio and R. F. Begley, "High-Power, Visible Laser Action in Atomic Fluorine."

C. J. Elliott and B. J. Feldman, "Multiple Photon Excitation and Dissociation of Molecules with Short Laser Pulses."

B. J. Feldman, R. A. Fisher, E. J. McLellan, and S. J. Thomas, "Free-Induction Decay Generation of 10.6 μm Subnanosecond Pulses."

R. McNair (MIT), S. Fulgurn (MIT), and B. J. Feldman, "Energy Transfer and Relaxation Processes in CH_3F."

The following presentations were made at the Sixth Annual Anomalous Absorption Conference, University of British Columbia, Vancouver, B.C., Canada, May 10-12, 1976:

B. Bezzerides, D. F. DuBois, and D. W. Forslund, "B-Field Generation by Resonance Absorption of E. M. Radiation."

D. F. DuBois, B. Bezzerides, and D. W. Forslund, "Electron Heating in Resonance Absorption of Radiation."

D. W. Forslund, J. M. Kindel, K. Lee, and E. L. Lindman, "Linear and Nonlinear Theory of the Instability of an Expanding Multi-Ion Plasma."

J. M. Kindel, D. W. Forslund, K. Lee, and E. L. Lindman, "Stability and Anomalous Absorption in Laser Light Interactions."

R. C. Malone and R. L. Morse, "Laser Energy Absorption and Subsequent Transport According to the Wild Turbulence Theory."

R. L. McCrory, C. W. Cranfill, and R. L. Morse, "Symmetry and Stability Studies of Thermally Generated B-Fields in Laser Produced Plasmas."

The following presentations were made at the Soviet Nonlinear Optics Conference, Tbilisi, USSR, May 25-28, 1976:

D. B. Giovanielli, J. F. Kephart, and G. H. McCall, "Wavelength Scaling Experiments Using CO_2 and Glass Laser-Produced Plasmas."

R. L. Carman, "Optical Pulse Programing for Laser Fusion."

The following presentations were made at the Meeting of the Society of Photo-Optical Instrumentation Engineers, Reston, Virginia, March 22-23, 1976:

C. Fenstermacher, "High Power, Nanosecond Pulse CO_2 Laser Systems."

R. W. Getzinger, K. D. Ware, and J. P. Carpenter, "Generation and Amplification of Nanosecond Duration Multiline HF Laser Pulses."

In addition, the following presentations were made at various institutions:

R. J. Bohl, "Planning the High Energy Gas Laser Facility," Meeting of the Southwestern and Rocky Mountain Division, American Association for the Advancement of Science, Tucson, Arizona, April 28 - May 1, 1976.

L. A. Booth and T. G. Frank, "Engineering Aspects of Laser Fusion Reactors," Joint ASME/ANS International Conference on Advanced Nuclear Energy Systems, Pittsburgh, Pennsylvania, March 15-17, 1976.

R. L. Carman, "Advanced Laser Technology for Laser-Induced Fusion Applications," invited talk at the Max Planck Institüt für Plasmaphysik, Garching, West Germany, June 7, 1976; and at the Naval Research Laboratory, Washington, D.C., May 18, 1976.

R. L. Carman, "Amplifiers Involving Two-Photon Energy Extraction Schemes," and "Optical Pulse Programming for Laser Fusion," invited talk at the IBM Research Laboratory, Yorktown, NY, May 19, 1976.

D. F. DuBois, "Coupling Saturation in the Nonlinear Theory of Parametric Instabilities," invited talk at the Nobel Symposium on Nonlinear Effects in Plasmas, Aspenasgarden, Lerum, Sweden, June 10-18, 1976.

B. Feldman, R. Fisher, E. McLellan, and S. Thomas, "New Developments in CO_2 Lasers," talk at Optical Sciences Center, University of Arizona, Tucson, Arizona, March 5, 1976.

B. Feldman, R. Fisher, E. McLellan and S. Thomas, "Resonant Optical Transients; Applications for CO_2," talk at University of Illinois, Physics Department, Chicago, Illinois, June 9, 1976; and at City University of New York, Physics Department, New York, New York, June 11, 1976.

B. J. Feldman, R. Fisher, E. J. McLellan, and S. J. Thomas, "Transient Short Pulse Generation in CO_2," talk at Techische Institüt, Munich, Germany, June 30, 1976.

B. J. Feldman and C. J. Elliot, "Multiple Photon Pumping of Anharmonic Oscillators," talk at Culham Laboratory, Culham, England, June 23, 1976.

B. J. Feldman, R. Fisher, E. J. McLellan, and S. Thomas, "Subnanosecond Pulse Generation in Hot CO_2," talk at Culham Laboratory, Culham, England, June 23, 1976.

C. Fenstermacher, "LASL Laser Fusion Program," Santa Fe County Medical Society Meeting, Santa Fe, NM, January 13, 1976.

T. G. Frank and L. A. Booth, "Laser-Fusion Reactor Materials Problems Resulting from Fusion Micro-Explosion Emissions," International Conference on Surface Effects in Controlled Fusion Devices, San Francisco, California, February 16-120, 1976.

S. J. Gitomer and J. L. Shohet, "Computer Simulation of Radio Frequency Confinement of a Plasma Near Critical Density," Annual Meeting on Theoretical Aspects of Controlled Thermonuclear Research, University of Wisconsin Center, Madison, Wisconsin, April 7-9, 1976.

D. B. Henderson, "Laser-Matter Interaction at Los Alamos," 31st Annual Congress of the Canadian Association of Physicists, with the American Physical Society and the Sociedad Mexicana de Fisica, Quebec, Canada, June 14-18, 1976.

R. J. Mason, "Laser Fusion -- Theory and Experiment," Physics Colloquium, New York University, March 8, 1976.

B. E. Newnam, "Laser-Induced Damage to Dielectric Surfaces and Coatings," Optical Coating Laboratory, Inc., Santa Rosa, California, February 17, 1976.

W. H. Reichelt, "Window Limitations for CO_2 Laser Fusion Systems," American Chemical Society, Symposium on Ceramics in the Service of Man, Washington, D.C., June 7-9, 1976.

W. H. Riechelt, "Optical Components for Large CO_2 Laser Systems," Optical Society Workshop, San Francisco, California, February 28, 1976.

K. B. Riepe, "Switching Requirements for Laser Fusion," Electric Power Research Institute Workshop on Switching Problems of Fusion Research, Palo Alto, California, March 24-26, 1976.

S. Singer, "High-Power CO_2 Laser Systems for Fusion Applications," Bell Telephone Laboratories, Holmdel, New Jersey, June 10, 1976.

L. E. Thode, "Plasma Heating by Relativistic Electron Beams: Experiment, Simulation and Theory," American Physical Society Meeting, Washington, D.C., April 26-29, 1976.

PUBLICATIONS

(This list of publications is prepared by computer from a stored data base. It has been checked for accuracy, but there may be typographical inconsistencies.)

Mason, Rodney J.; "Performance of Structured Laser Fusion Pellets."" LASL, 1975. 17P. (LA-5898-MS).

Axford, Roy A.; "Direct Evaluation of Transient Surface Temperatures and Heat Fluxes."" LASL, 1975. 8P. (LA-6051).

Simonsic, Gary A.; "Laser - Fusion Target Fabrication: Application of a Polymeric Ablator Coating to a Ball and Disk Target Design by the Physical Vapor Deposition of Polyethylene."" LASL, 1975. 2P. (LA-6063).

Hoffman, C. Gordon; "Some Effects of Laser Irradiation on Aluminum."" LASL, 1976. 24P. (LA-6189-MS).

Simonsic, Gary A.; "Laser Fusion Target Fabrication: Application of Organic Coatings to Metallic and Nonmetallic Micropellets by the Glow Discharge Polymerization of P-Xylene."" LASL, 1976. 5P. (LA-6207).

Seely, John T.; "Numerical Rate Equation Model for the Helium - Cesium Charge Exchange Laser."" LASL, 1976. 12P. (LA-6298-MS).

Mills, Carroll B.; "Carbon Dioxide Gas Laser Excitation and Gain. Erratum."" J. Appl. Phys., V.47, P.1199. 1976. (LA-UR-73-774-a).

Forslund, David W.; Galeev, A.; "Report of the Working Group on Stimulated Backscatter."" Comments Plasma Phys., V.2, P.97-108. 1976.

Lieber, Albert; Benjamin, Robert F.; Sutphin, Howard D.; Mc Call, Gene H.; "Application of Ultra-Fast High Resolution Gated Image Intensifiers to Laser Fusion Studies."" Abstract published in: Smpte J., V.85, P.17. 1976.

Fisher, Robert A.; "Dispersive Temporal Compression of the Energy in Laser Pulses: A Review."" TIC, 1975. 6P. MN (LA-UR-75-389) Also published in: Energy Storage, Compression, And Switching. 1974. International Conference, Asti-Torino, Italy. Proc., P.405-9. Plenum, 1976. (621.3:E56S).

Godfrey, Brendan B.; Thode, Lester E.; "Ion Acceleration by the Relativistic Two Stream Instability."" IEEE Trans. Plasma Sci., V.Ps-3, No.4, P.201-4. 1975.

Mason, Rodney J.; Morse, Richard L.; "Tamped Thermonuclear Burn of Deuterium -Tritium Microspheres."" Nucl. Fusion, V.15, P.935-8. 1975.

Forslund, David W.; Kindel, Joseph M.; Lee, Kenneth; Lindman, Erick L.; "Absorption of Laser Light on Self Consistent Plasma Density Profiles."" Phys. Rev. Lett., V.36, P.35-8. 1976.

Elliott, C. James; Suydam, Bergen R.; "Self Focusing Phenomena in Air - Glass Laser Structures."" IEEE J. Quantum Electron., V.Qe-11, P.863-6. 1975.

Mason, Rodney J.; "Calculated Performance of Structured Laser Fusion Pellets."" Nucl. Fusion, V.15, P.1031-43. 1975.

Thode, Lester E.; "Energy Lost by a Relativistic Electron Beam Due to Two Stream Instability."" Phys. Fluids, V.19, P.305-15. 1976.

Thode, Lester E.; Sudan, Ravindra N.; "Plasma Heating by Relativistic Electron Beams. Part 2. Return Current Interaction."" Phys. Fluids, V.18, P.1564-73. 1975.

Fisher, Robert A.; Bischel, W. K.; "Numerical Studies of the Interplay between Self Phase Modulation and Dispersion for Intense Plane Wave Laser Pulses."" J. Appl. Phys. V.46, P.4921-34. 1975.

Robinson, C. Paul; "Laser Isotope Separation."" TIC, 1975. 20P. MN (LA-UR-75-642) Also published in: Ann. N. Y. Acad. Sci., V.267, P.81-92. 1976.

Godfrey, Brendan B.; Thode, Lester E.; "Energy Lost by a Relativistic Electron Beam Propagating Along an External Magnetic Field."" Phys. Fluids, V.19, P.316-20. 1976.

Phipps, Claude R., Jr.; Thomas, Scott J.; "High Power Isolator for the 10 Micron Region Employing Interband Faraday Rotation in Germanium."" J. Appl. Phys., V.47, P.204-13. 1976.

Mc Creary, William J.; "Microspherical Laser Targets by Chemical Vapor Deposition."" TIC, 1975. 13P. MN (LA-UR-75-636).

Boyer, Keith; "Laser Fusion: An Overview."" TIC, 1975. 19P. MN (LA-UR-75-660) Also published in: Ann. N. Y. Acad. Sci., V.267, P.117-25. 1976.

Greiner, Norman R.; "Time Resolved Output Spectrum from a Hydrogen Fluoride Laser using Mixtures of Sulfur Hexafluoride and Hydrogen Iodide."" IEEE J. Quantum Electron., V.Qe-11, P.844-5. 1975.

Rockwood, Stephen D.; "Laser Induced Chemiluminescence of Boron Trichloride/Hydrogen Sulfide Mixtures."" Chem. Phys., V.10, P.453-7. 1975.

Antal, Michael J., Jr.; Lee, Clarence E.; "Charged Particle Mass and Energy Transport in a Thermonuclear Plasma."" J. Comput. Phys., V.20, P.298-312. 1976.

De Poorter, Gerald L.; Rofer-De Poorter, Cheryl K.; "Absorption Spectrum of Uranium Hexafluoride from 2000 to 4200 Angstroms."" Spectrosc. Lett., V.8, P.521-4. 1975.

Freiwald, David A.; Kern, Edward A.; "Laser Fusion Sources for Ctr Surface and Bulk Damage Testing."" Radiation Test Facilities For the Ctr Surface and Materials Program. 1975. International Congress, Argonne, IL. Proc., P.749-66. Anl, 1976. (Anl/Ctr-75-4).

Schott, Garry L.; "Pulsed Hydrogen Fluoride Laser Oscillator Amplifier Experiments."" Optical Methods in Energy Conversion, Spie Seminar Proceedings, V.61, P.81-8. Spie, 1975.

Mc Crory, Robert L.; Morse, Richard L.; "Turbulent Pusher Behavior."" Phys. Fluids, V.19, P.175-6. 1976.

Judd, O'Dean P.; "On the Effect of the Addition of Sulfur Hexafluoride to a Nitrogen(2) Electrical Discharge Laser."" IEEE J. Quantum Electron., V.Qe-12, P.78-80. 1976.

Lyman, John L.; Rockwood, Stephen D.; "Enrichment of Boron, Carbon, and Silicon Isotopes by Multiple Photon Absorption of 10.6 Micron Laser Radiation."" J. Appl. Phys., V.47, P.595-601. 1976.

Varnum, William S.; "Electrically Imploded Cylindrical Fusion Targets."" Nucl. Fusion, V.15, P.1183-4. 1975.

Cantrell, Cyrus D., III; Figueira, Joseph F.; Forman, Peter R.; Rink, John P.; Scott, J. F.; Scully, Marlan O.; "Time Resolved Pump Depletion in N -Indium Antimonide Raman Spin - Flip Laser."" Appl. Phys. Lett., V.28, P.398-400. 1976.

Bosler, Gerald E.; "Energy Deposition in a Two Dimensional Lctr Model."" Abstract published in: Trans. Am. Nucl. Soc., V.22, P.15-6. 1975.

Kern, Edward A.; Frank, Thurman G.; Booth, Lawrence A.; "Systems Analysis of Laser Fusion Power Plants."" Abstract published in: Trans. Am. Nucl. Soc., V.20, P.69. 1975.

Freiwald, David A.; Frank, Thurman G.; Kern, Edward A.; Booth, Lawrence A.; "Laser - Fusion Electric Generating Stations Based on the Magnetically Protected Reactor Cavity."" Abstract published in: Trans. Am. Nucl. Soc., V.22, P.68-9. 1975.

Finch, Francis T.; Frank, Thurman G.; Booth, Lawrence A.; Kern, Edward A.; "Radioactive Waste Output from Laser -Fusion Generating Stations during Normal Operations."" Abstract published in: Trans. Am. Nucl. Soc., V.22, P.48. 1975.

Pendergrass, John H.; Finch, Francis T.; "Temperature Dependent Ordinary and Thermal Diffusion of Tritium through Metal Barriers."" Abstract published in: Trans. Am. Nucl. Soc., V.22, P.24-5. 1975.

Figueira, Joseph F.; Ladish, Joseph S.; Schappert, Gottfried T.; Thomas, Scott J.; "Amplification of Multiline/Multiband Carbon Dioxide Laser Pulses."" Appl. Phys. Lett., V.27, P.591-2. 1975.

Judd, O'Dean P.; "Lasers for Laser Fusion."" Abstract published in: Trans. Am. Nucl. Soc., V.22, P.68. 1975.

Giovanielli, Damon V.; Kephart, John F.; Williams, Arthur H.; "Emitted Electron Spectra from Plasmas Produced with Neodymium and Carbon Dioxide Lasers."" Abstract published in: Bull. Am. Phys. Soc., Ser.2, V.20, P.1318. 1975.

Newberger, Barry S.; Gitomer, Steven J.; Morse, Richard L.; "Steady Ablation of Laser Targets in Spherical Geometry. 1. The Model."" Abstract published in: Bull. Am. Phys. Soc., Ser.2, V.20, P.1246. 1975.

Gitomer, Steven J.; Newberger, Barry S.; Morse, Richard L.; "Steady Ablation of Laser Targets in Spherical Geometry. 2. Physical Results."" Abstract published in: Bull. Am. Phys. Soc., Ser.2, V.20, P.1246. 1975.

Sydoriak, Stephen G.; Kohler, David R.; "Freezing and Melting Deuterium in Micro balloons."" Abstract published in: Bull. Am. Phys. Soc., Ser.2, V.20, P.1247. 1975.

Carman, Robert L.; "Generation of Laser Pulses for Optimum Ablative Compressions."" Abstract published in: Bull. Am. Phys. Soc., Ser.2, V.20, P.1286. 1975.

Mueller, Marvin M.; "Beta Absorption in Tritiated Targets and X Ray Counting Corrections."" Abstract published in: Bull. Am. Phys. Soc., Ser.2, V.20, P.1247. 1975.

Farnum, Eugene H.; Fries, Ralph Jay; "External Pressurization as a Means of Upgrading Glass Microballoons."" Abstract published in: Bull. Am. Phys. Soc., Ser.2, V.20, P.1247. 1975.

Maltrud, H. Richard; Farnum, Eugene H.; Fries, Ralph Jay; "Acoustic Measuring System for Determining the Breaking Strength of Microballoons."" Abstract published in: Bull. Am. Phys. Soc., Ser.2, V.20, P.1247. 1975.

Stupin, David M.; Farnum, Eugene H.; Fries, Ralph Jay; Winkler, Max A.; "Quality Selection of Laser - Fusion Target Microballoons."" Abstract published in: Bull. Am. Phys. Soc., Ser.2, V.20, P.1246. 1975.

Benjamin, Robert F.; Lieber, Albert; Lyons, Peter B.; Sutphin, Howard D.; Webb, Clinton B.; "Micro-Channel Plate Collimators for Laser Plasma Diagnostics."" Abstract published in: Bull. Am. Phys. Soc., Ser.2, V.20, P.1294. 1975.

Lieber, Albert; Sutphin, Howard D.; Benjamin, Robert F.; Gitomer, Steven J.; Hall, W. Stanley; "Proximity Focused Ultra-Fast Streak Tube."" Abstract published in: Bull. Am. Phys. Soc., Ser.2, V.20, P.1286. 1975.

Van Hulsteyn, David B.; Benjamin, Robert F.; Lieber, Albert; Mc Call, Gene H.; "X Ray Pinhole Cameras for Laser Plasma Experiments."" Abstract published in: Bull. Am. Phys. Soc., Ser.2, V.20, P.1294. 1975.

Tan, Tai Ho; Mc Call, Gene H.; Williams, Arthur H.; "Development of an Alpha Particle and Proton Detector for Laser - Fusion Studies."" Abstract published in: Bull. Am. Phys. Soc., Ser.2, V.20, P.1318. 1975.

Tan, Tai Ho; Mc Call, Gene H.; Williams, Arthur H.; "Measurements of Alpha Particles and Protons, Produced from Laser Fusion."" Abstract published in: Bull. Am. Phys. Soc., Ser.2, V.20, P.1318. 1975.

Catlett, Duane S.; Fries, Ralph Jay; Mayer, Anton; Mc Creary, William J.; Powell, Billy W.; Simonsic, Gary A.; Fossey, D.; "Recent Developments in Laser - Fusion Target Coatings."" Abstract published in: Bull. Am. Phys. Soc., Ser.2, V.20, P.1230-1. 1975.

Mc Crory, Robert L.; Cranfill, Charles W.; Henderson, Dale B.; "Symmetry and Stability Studies of Thermally Generated Magnetic Fields in Laser Produced Plasmas."" Abstract published in: Bull. Am. Phys. Soc., Ser.2, V.20, P.1285. 1975.

Morse, Richard L.; Mc Crory, Robert L.; "Turbulent Pusher Behavior."" Abstract published in: Bull. Am. Phys. Soc., Ser.2, V.20, P.1265. 1975.

Malone, Robert C.; Fraley, Gary S.; Cranfill, Charles W.; Morse, Richard L.; "Calculation of X Ray Pinhole Photographs."" Abstract published in: Bull. Am. Phys. Soc., Ser.2, V.20, P.1237. 1975.

Taggart, Keith A.; Morse, Richard L.; Mc Crory, Robert L.; Remund, Robert N.; "Two Dimensional Calculations of Asymmetric Laser Fusion Targets using Iris."" Abstract published in: Bull. Am. Phys. Soc., Ser.2, V.20, P.1378. 1975.

Gula, William P.; Kirkpatrick, Ronald C.; "Electron Beam Fusion Pellets."" Electron Beam Research and Technology. 1975. International Topical Conference, Albuquerque, NM. Proc., V.1, P.158-70. Sandia Laboratories, 1976. (Sand76-5122 V.1) abstract published in: Bull. Am. Phys. Soc., Ser.2, V.20, P.1271-2. 1975.

Henderson, Dale B.; Mason, Rodney J.; "Two Dimensional Lagrangian Laser Pellet Simulation Code."" Abstract published in: Bull. Am. Phys. Soc., Ser.2, V.20, P.1378-9. 1975.

Ehler, A. Wayne; "Effect of Secondary Electrons on Charge Collector Measurement of a Laser Produced Plasma."" Abstract published in: Bull. Am. Phys. Soc., Ser.2, V.20, P.1335. 1975.

Mitchell, Kenneth B.; Lyons, Peter B.; "X Ray Continuum and Line Radiation from Plasmas Produced by 10.6 Micrometer Laser Focused on Flat Targets."" Abstract published in: Bull. Am. Phys. Soc., Ser.2, V.20, P.1303. 1975.

Sollid, Jon E.; "Peak Irradiance Measurements on a 10 J, 1 Ns, Carbon Dioxide Laser."" Abstract published in: Bull. Am. Phys. Soc., Ser.2, V.20, P.1336. 1975.

Weiss, Paul B.; Hopper, Gordon L.; "High Speed Digitizing with Camac."" Abstract published in: Bull. Am. Phys. Soc., Ser.2, V.20, P.1369. 1975.

Goldstein, John C.; Dickman, Donald O.; "Diffraction Effects and Optical Quality in the Multistage Amplification of Nanosecond Carbon Dioxide Pulses."" Abstract published in: Bull. Am. Phys. Soc., Ser.2, V.20, P.1238. 1975.

Elliott, C. James; Feldman, Barry J.; "Coherent Multiple Photon Pumping of Simple Quantum Mechanical Systems."" Abstract published in: Bull. Am. Phys. Soc., Ser.2, V.20, P.1282. 1975.

Lindman, Erick L.; Forslund, David W.; Kindel, Joseph M.; Lee, Kenneth; Shanahan, William R.; "Magnetic Fields in Laser Produced Plasmas."" Abstract published in: Bull. Am. Phys. Soc., Ser.2, V.20, P.1378. 1975.

Forslund, David W.; Kindel, Joseph M.; Lee, Kenneth; Lindman, Erick L.; "Ion Wave Turbulence Induced by an Expanding Multi-Component Plasma."" Abstract published in: Bull. Am. Phys. Soc., Ser.2, V.20, P.1377. 1975.

Kindel, Joseph M.; Forslund, David W.; Lee, Kenneth; Lindman, Erick L.; "Electromagnetic Scattering Instabilities in Weakly Inhomogeneous Underdense Plasma."" Abstract published in: Bull. Am. Phys. Soc., Ser.2, V.20, P.1378. 1975.

Comly, Jack C.; Forslund, David W.; Kindel, Joseph M.; Lee, Kenneth; Lindman, Erick L.; "Effect of the Ambipolar Electric Field on the Transport of Energetic Electrons."" Abstract published in: Bull. Am. Phys. Soc., Ser.2, V.20, P.1378. 1975.

Feldman, Barry J.; Elliott, C. James; "Coherent Multiple Photon Excitation of Molecules."" Abstract published in: Bull. Am. Phys. Soc., Ser.2, V.21, P.173. 1976.

Greene, Arthur E.; Elliott, C. James; "Electron Energy Distributions in an E-Beam Initiated Xenon Plasma."" Abstract published in: Bull. Am. Phys. Soc., Ser.2, V.21, P.155. 1976.

Kindel, Joseph M.; "Recent Developments in Understanding the Plasma Physics of Laser Target Interactions."" Abstract published in: Bull. Am. Phys. Soc., Ser.2, V.20, P.1230. 1975.

Freiwald, David A.; Dickman, Donald O.; Goldstein, John C.; "Computer Simulation of a Deuterium -Tritium Pellet Microexplosion in a Magnetically Protected Laser Fusion Reactor."" Abstract published in: Bull. Am. Phys. Soc., Ser.2, V.20, P.1238. 1975.

Newnam, Brian E.; Gill, Dennis H.; Faulkner, George E.; "Influence of Standing Wave Fields on the Laser Damage Resistance of Dielectric Films."" TIC, 1975. 19P. MN (LA-UR-75-1646).

Hughes, William M.; Olsen, T.; Hunter, Robert; "Experiments on the 558 NM Argon Oxide Laser System."" Appl. Phys. Lett., V.28, P.81-3. 1976.

Kim, Kyu C.; "Laser Spectroscopy."" Electro-Optical Systems Design Conference/International Laser Exposition. 1975. Anaheim, CA. Proc., P.191-5. Iscm, 1975. Abstract published in: Electro-Optics/International Laser Conference and Exposition. 1975. Anaheim, CA. Abstracts and Program, Technical Session 5, Paper No.5. The Conference, 1975. (535:E38Ol).

Lyman, John L.; Rockwood, Stephen D.; "Multiple Photon Isotope Separation."" Abstract published in: Electro-Optics/International Laser Conference and Exposition. 1975. Anaheim, CA. Abstracts and Program, Technical Session 5, Paper No.1. The Conference, 1975.

Fenstermacher, Charles A.; "Laser Systems for High Peak Power Applications."" TIC, 1975. 9P. MN (LA-UR-75-1751).

Riepe, Kenneth B.; "Pulse Forming Networks for Fast Pumping of High Power Electron Beam Controlled Carbon Dioxide Lasers."" TIC, 1976. 10P. MN (LA-UR-75-1832) abstract published in: Electro-Optics/International Laser Conference and Exposition. 1975. Anaheim, CA. Abstracts and Program, Technical Session 18, Paper No.3. The Conference, 1975.

Schott, Garry L.; "Optical Methods in Energy Conversion, Spie Seminar in Depth, Rochester, 23-25 June 1975."" Appl. Opt., V.14, P.2784. 1975.

Newnam, Brian E.; Gill, Dennis H.; "Laser Damage Resistance and Standing Wave Fields in Dielectric Coatings."" Abstract published in: J. Opt. Soc. Am., V.66, P.166, 1976.

Gill, Dennis H.; Newnam, Brian E.; Hartman, John S.; Coleman, William J.; "Super-High Damage Thresholds for Rf Sputtered Titanium Dioxide Films."" Abstract published in: J. Opt. Soc. Am., V.66, P.78-9. 1976.

Barnes, Norman P.; Corcoran, Vincent J.; "Parametric Generation Processes: Spectral Bandwidth and Acceptance Angles."" Appl. Opt., V.15, P.696-9. 1976.

Tan, Tai Ho; Williams, Arthur H.; Mc Call, Gene H.; "Thin Film Detector System for Laser -Fusion Studies."" Nucl. Instrum. Methods, V.131, P.425-9. 1975.

Singer, Sidney; Ladish, Joseph S.; Nutter, Murlin J.; "Cold Cathode Electron Guns in the LASL High Power Short Pulse Carbon Dioxide Laser Program."" TIC, 1976. 24P. MN (LA-UR-75-2155) Also published in: Electron Beam Research and Technology. 1975. International Topical Conference, Albuquerque, NM. Proc., V.2, P.274-91. Sandia Laboratories, 1976. (Sand76-5122 V.2).

Rice, Walter W.; Beattie, Willard H.; Oldenborg, Richard C.; Johnson, Stanley E.; Scott, Paul B.; "Boron Fluoride and Aluminum Fluoride Infrared Lasers from Quasicontinuous Supersonic Mixing Flames."" Appl. Phys. Lett., V.28, P.444-6. 1976.

Cantrell, Cyrus D., III; Figueira, Joseph F.; Scott, J. F.; Scully, Marlan O.; "Time Resolved Pump Depletion in N -Indium - Antimony Raman Spin - Flip Laser: Comments."" Appl. Phys. Lett., V.28, P.442-4. 1976.

Getzinger, Richard W.; Ware, Kenneth D.; Carpenter, James P.; "Generation and Amplification of Nanosecond - Duration Multiline Hf Laser Pulses."" TIC, 1976. 5P. MN (LA-UR-76-368).

Bigio, Irving J.; Begley, Richard F.; "High Power, Visible Laser Action in Neutral Atomic Fluorine."" Appl. Phys. Lett., V.28, P.263-4. 1976.

Griggs, James E.; Henke, Michael D.; Aldridge, Jack P.; Kim, Kyu C.; "Design and Performance of a Low Temperature Multiple Reflection Absorption Cell."" Abstract published in: J. Opt. Soc. Am., V.66, P.390. 1976.

Reichelt, Walter H.; "Carbon Dioxide Laser Systems for Fusion Studies."" Abstract published in: J. Opt. Soc. Am., V.66, P.387. 1976.

Parker, Jerald V.; Nutter, Murlin J.; Hayden, James J.; Singer, Sidney; "Two Beam Carbon Dioxide Laser System for Laser Induced Fusion Experiments."" Abstract published in: J. Opt. Soc. Am., V.66, P.387. 1976.

Liberman, Irving; Hayden, James J.; Singer, Sidney; "Prepulse Elimination in High Power Carbon Dioxide Lasers."" Abstract published in: J. Opt. Soc. Am., V.66, P.387. 1976.

Lieber, Albert; Sutphin, Howard D.; Webb, Clinton B.; Williams, Arthur H.; "Development of Sub-Picosecond X Ray and Visible Streak Camera."" Abstract published in: J. Opt. Soc. Am., V.66, P.384. 1976.

Mc Lellan, Edward J.; Figueira, Joseph F.; "Generation of Subnanosecond Carbon Dioxide Laser Pulses by Electro-Optical Modulation."" Abstract published in: J. Opt. Soc. Am., V.66, P.387. 1976.

Gill, Dennis H.; Newnam, Brian E.; "Damage Resistance of Holographic and Ruled Gratings Used as Laser Wavelength Tuning Elements."" Abstract published in: J. Opt. Soc. Am., V.66, P.383. 1976.

Phipps, Claude R., Jr.; Figueira, Joseph F.; Thomas, Scott J.; "Broadband, Passive Isolator for High Power 10 Micron Wavelength Laser Systems."" Abstract published in: J. Opt. Soc. Am., V.66, P.383. 1976.

Barnes, Norman P.; Mace, Phillip N.; Nickle, Richard A.; "Far Infrared Difference Frequency Generation."" Abstract published in: J. Opt. Soc. Am., V.66, P.390. 1976.

Babcock, Richard V.; Liberman, Irving; Partlow, W. D.; "Volume Ultraviolet Preionization from Bare Sparks."" IEEE J. Quantum Electron., V.Qe-12, P.29-35. 1976.

Morse, Richard L.; "Laser Fusion."" High Energy Lasers and Their Applications. 1973. Summer School, Crystal Mountain, WA. Papers, Physics of Quantum Electronics, V.1, P.391-406. Addison-Wesley, 1974.

Hunter, Robert; Shannon, John; Hughes, William M.; "Scaling and Efficient Operation of the 1720 a Xenon Laser."" Abstract published in: Bull. Am. Phys. Soc., Ser.2, V.20, P.238. 1975.

Dudder, H. D.; Henderson, Dale B.; "Ramses, a Two Dimensional, Pic type, Laser Pulse Propagation Code."" Comput. Phys. Commun., V.10, P.155-66. 1975.

Feldman, Barry J.; Feld, M. S.; "Equal Area Property of Narrow Resonances Induced in Coupled Doppler Broadened Systems by Intense Laser Radiation."" Phys. Rev., V.a12, P.1013-8. 1975.

Shapiro, Stanley L.; Kollman, Victor H.; Hyer, Ronald C.; Campillo, Anthony J.; "Streak Camera Studies using Picosecond Pulses of Photosynthesis and Plastic Scintillators."" Abstract published in: IEEE J. Quantum Electron., V.Qe-11, P.5D-6D. 1975.

Jensen, Reed J.; "Hydrogen Isotope Separation from Water."" Filed 1973, Patented Sep.9, 1975. (U. S. Patent 3,904,500).

Robinson, C. Paul; Jensen, Reed J.; Davis, William C.; Sullivan, J. Al; "Explosive Laser."" Filed 1974, Patented Sep. 9, 1975. (U. S. Patent 3,904,985).

Jensen, Reed J.; Rice, Walter W.; Beattie, Willard H.; "Metal Atom Oxidation Laser."" Filed 1974, Patented Oct. 28, 1975. (U. S. Patent 3,916,338).

De Poorter, Gerald L.; Rofer-De Poorter, Cheryl K.; "Oxygen -18 Enrichment Process in Uranium Oxyfluoride Utilizing Laser Light."" Filed 1974, Patented Dec. 2, 1975. (U. S. Patent 3,923,619).

Campillo, Anthony J.; Newnam, Brian E.; Shapiro, Stanley L.; Terrell, James; "Method and Apparatus for Reducing Diffraction Induced Damage in High Power Laser Amplifier Systems."" Filed 1975, Patented Jan. 27, 1976. (U. S. Patent 3,935,545).

Farnum, Eugene H.; Fries, Ralph Jay; "Method for Nondestructive Fuel Assay of Laser Fusion Targets."" Filed 1975, Patented Feb. 24, 1976. (U. S. Patent 3,940,617).

☆ U.S. GOVERNMENT PRINTING OFFICE: 1976—777-018/21